Jürgen Dampf, MSc, BSc

Probability Analysis for Bayesian Direct Position Estimation

DOCTORAL THESIS

to achieve the university degree of
Doktor der technischen Wissenschaften

submitted to

Graz University of Technology

Supervisor

Univ.-Prof. Mag. Dr. habil. Thomas Pany
Institute of Space Technology and Space Applications
Universität der Bundeswehr München

Graz, February 2021

AFFIDAVIT

I declare that I have authored this thesis independently, that I have not used other than the declared sources/resources, and that I have explicitly indicated all material which has been quoted either literally or by content from the sources used. The text document uploaded to TUGRAZonline is identical to the present doctoral thesis.

Date, Signature

Abstract

Bayesian Direct Position Estimation (BDPE) is a novel and promising Global Navigation Satellite System (GNSS) positioning method, which estimates the Position Velocity and Time (PVT) directly from the signal samples. The first novelty of this thesis is to estimate the PVT directly from correlation values, which are generated using two well-known methods, vector tracking and a synthetic multi-correlator. Hereby, the vector tracking loop is closed with the BDPE PVT estimate in order to steer the signal correlation process and the synthetic multi-correlator is used to produce the measurements, massive correlation values in the range and Doppler domain. It was shown in literature, that Direct Position Estimation (DPE) promises a significant sensitivity gain compared to state-of-the-art algorithms and thus, the method fully exploits its benefits in challenging environments. It is known, that in such environments the signal measurements are not Gaussian distributed, thus it is expected, that non-parametric filters will estimate the state more accurately compared to typical used methods, which are based on Gaussian assumptions. Therefore, a natural approach for BDPE is the usage of non-parametric Bayesian filtering techniques. Non-parametric Bayesian filters, such as a Grid-Based Filter (GBF) or Particle Filter (PF), can cope with non-linearities in the system and observation model and are able to cope with non-Gaussian and multi-modal distributed measurements. One essential step with non-parametric Bayesian filters is the measurement update (weight update of grid nodes or particles), where the current state is updated with a new set of measurements. A non-parametric Bayes filter needs for the weight update a probabilistic description of the measurements. Therefore, the second novelty of this work is the derivation of a probabilistic description of the measurements and development of a mathematical framework for an optimal and stable weight update based on correlation values, which can be used for a grid-based filter and a particle filter. The work points out possible instability issues with a grid-based or particle filter when using the derived plain weight update function, especially if User Equivalent Range Errors (UEREs) (orbit, satellite clock, atmosphere or multipath) are not modeled properly. Therefore, the third novelty of the work is the extension of the optimal weight update function to cover unmodeled errors in the range and Doppler domain with Gaussian nuisance parameters. The stabilizing effect of the proposed approach is shown on real-world data with an artificial range error, which is injected at the filter update step when mapping the measurements in the correlation domain to the PVT domain. The

work proposes a computational efficient algorithm to generate the Probability Density Functions (PDFs) of the measurements and perform the weight update on a Central Processing Unit (CPU), which allows to achieve a real-time analysis tool of PDFs in the PVT domain or a real-time capable non-parametric Bayesian filter for DPE. The results include a comprehensive analysis of the PDFs in the PVT domain, which represents the probability distribution of the user position, velocity and time. The developed analysis tool for PDFs of the PVT uses an aided grid-based filter to achieve highly resoluted 2-dimensional subspaces, which are aligned to the 8-dimensional state space using a vector tracking PVTsolution as reference. The resulting probabilities of the user PVT are the basis for a grid-based and particle filter for BDPE and are the result of this work. The PDF of the PVT is analyzed in a simulated environment using a GNSS simulator and in a real-world environment. As degraded signal conditions are of high interest, the real-world analysis focuses on challenging environments in an urban canyon, under-passing a bridge and an indoor scenario. The results show strongly deformed, non-Gaussian and multi-modal PDFs in the PVT domain. The analysis underlines the fact that non-Gaussian as well as multi-modal probability distributions of the GNSS measurements exist under specific conditions, and that a BDPE PF or GBF will provide under these conditions superior performance compared to a Kalman Filter (KF).

Kurzfassung

Bayesian Direct Position Estimation (BDPE) ist eine neuartige und vielversprechende Global Navigation Satellite System (GNSS) Positionierungsmethode, welche die Positions-, Geschwindigkeits- und Zeitlösung (PVT) direkt aus dem digital abgetasteten Signal schätzt. Die erste Neuheit dieser Arbeit ist die direkte Schätzung der PVT aus Korrelationswerten, welche mithilfe zweier bekannter Methoden, Vektor-Tracking und eines synthetischen Multi-Korrelators, berechnet werden. Die Vektor-Tracking Regelschleife wird über die geschätzte PVT Navigationslösung von BDPE geschlossen um den Korrelationsprozess zu steuern. Mit dem synthetischen Multi-Korrelator wird die Messung erzeugt, welche eine hohe Anzahl von Korrelationswerten in der Distanz und Doppler Domäne beinhaltet. Es wurde in der Literatur gezeigt, dass DPE eine signifikante Steigerung der Sensitivität gegenüber konventionellen Methoden ermöglicht, was vor allem einen großen Vorteil in schwierigen Signalbedingungen mit sich bringt. Es ist bekannt, dass bei schwierigen Signalumgebungen keine Gauß-verteilten Messungen vorliegen, daher ist zu erwarten, dass nicht-parametrisierte Filter den Zustand deutlich besser schätzen als typischerweise eingesetzte Methoden, die auf Annahmen von Gauß-verteilten Messungen basieren. Deswegen wird der Einsatz von nicht-parametrisierten Filtern für BDPE als günstig erachtet. Zu den nicht-parametrisierten Bayes-Filtern gehören beispielsweise der Partikelfilter (PF) und der Grid-basierte Filter (GBF). Beide Filter erlauben die Verwendung von nicht-linearen System- und Beobachtungsmodellen, also auch die Verwendung von nicht Gauß-verteilten und multi-modalen Messungen. Ein wesentlicher Schritt von nicht-parametrisierten Bayes-Filtern ist die Neugewichtung der Gitterpunkte bzw. der Partikel, bei dem der aktuelle Zustand mithilfe der vorliegenden Messungen aktualisiert wird. Für nicht parametrisierte Bayes-Filter müssen diese Messungen in einer probabilistischen Form vorliegen. Die zweite Neuheit in dieser Arbeit ist die Herleitung einer probabilistischen Beschreibung der Messungen und die Entwicklung eines mathematischen Gerüstes für eine optimale und stabile Neugewichtung basierend auf Korrelationswerten, welches für einen Partikelfilter und einen Grid-basierten Filter verwendbar ist. In der Arbeit werden mögliche Instabilitätsprobleme bei einem Grid-basierten oder Partikelfilter bei Verwendung der entwickelten direkten und optimalen Neugewichtung diskutiert, welche vor allem bei nicht optimal modellierten UEREs (nicht modellierte Fehler im Orbit-Modell, der Satellitenuhr, der Atmosphäre oder der Mehrwegeausbreitung)

auftreten. Deshalb werden in der Arbeit als dritte Neuheit Gauß-verteilte Fehler bei der direkten und optimalen Neugewichtung eingeführt, um nicht modellierte Fehler bei der Messung in der Distanz- und Doppler-Domäne berücksichtigen zu können. Die vorgeschlagene Methode hat einen stabilisierenden Effekt zur Folge, welcher mit realen Daten und einem künstlich eingeführten Distanzfehler nachgewiesen wird. Dieser künstliche Fehler wird im Filter-Update Schritt beim Zuordnen der Messungen in der Korrelationsdomäne in die PVT-Domäne eingeführt. Weiter wird in der Arbeit ein effizienter Algorithmus für die Erzeugung von Wahrscheinlichkeitsdichtefunktionen (PDFs) der Messungen und die Durchführung der Neugewichtung auf der CPU vorgestellt, welcher ein Echtzeit-Analyse-Tool von PDFs in der PVT-Domäne oder echtzeitfähige nicht-parametrische Bayes-Filter für DPE ermöglicht. Die Ergebnisse beinhalten eine ausführliche Analyse der PDFs in der PVT-Domäne, welche die Wahrscheinlichkeitsverteilung der Benutzer-Position, -Geschwindigkeit und -Zeit darstellen. Das entwickelte Analyse-Tool für die PDFs der PVT verwendet einen gestützten Grid-basierten Filter um hochauflösend 2-dimensionale Teilräume analysieren zu können, wobei das Grid mithilfe einer Vector-Tracking PVT-Lösung im 8-dimensionalen Zustandsraum platziert wird. Die resultierenden Wahrscheinlichkeitsdichtefunktionen der PVT sind die Basis für einen Grid-basierten Filter und Partikelfilter hinsichtlich BDPE und sind die Ergebnisse dieser Arbeit. Die Wahrscheinlichkeitsdichtefunktion der PVT wird in einer simulierten Umgebung mit einem GNSS Signalgenerator und unter realen Bedingungen analysiert. Da vor allem schwierige Signalbedingungen von Interesse sind, wird eine Analyse der PDF in der Stadt, unter einer Brücke und im Innenbereich eines Gebäudes durchgeführt. Die Ergebnisse zeigen eine stark deformierte, nicht Gauß-verteilte und multi-modale Wahrscheinlichkeitsdichtefunktionen der PVT. Diese Analyse untermauert die Annahme, dass nicht Gauß-verteilte sowie multi-modale Verteilungen der GNSS Beobachtungen unter bestimmten Bedingungen existieren und das Partikelfilter sowie Grid-basierte Filter unter solchen Bedingungen einem typischen Kalman-Filter überlegen sind.

Acknowledgements

I would like to express my greatest thanks to Univ.-Prof. Mag. Dr. habil. Thomas Pany, who inspired me to find an interesting research topic and supported me during the whole work. He gave always very helpful guidance, especially in challenging phases of the work and he continuously encouraged me to push forward the exciting topic. Furthermore, his worldwide connections enabled me to get in touch with people working on the same topic, to exchange ideas and gain experience.

The second acknowledgement should go to Ao.Univ.-Prof. Dipl.-Ing. Dr. techn. Manfred Wieser, because he enabled the possibility of the PhD in Graz. I am very thankful for the positive and constructive technical discussions during the studies and I really enjoyed the lectures, seminars and regular meetings. Furthermore, he strongly supported the possibility to finish the curricula and PhD, especially when I moved from Graz to Munich and a regular visit at the University was not continuously possible.

The third acknowledgement should go to Priv.-Doz. Dr.-Ing. habil. Jan Wendel as he accepted the role of the external opponent in the doctorate procedure and doctoral examination. He gave with his deep expertise in GNSS a very constructive feedback to this work.

Moreover, I want to thank my wife Iva Bartůňková for her respect to the short availability of time which comes along with doing a PhD study beside a full-time job. She was always supportive and encouraging, especially during difficult phases of the work. Thanks should also go to my parents Veronika Dampf and Alois Rath as well as to my brother Stefan Dampf for their continuous encouragement to finish the work.

Abbreviations

ADC Analog Digital Conversion
ADS-B Automatic Dependent Surveillance - Broadcast
AGBF Approximate Grid-Based Filter
AGC Automatic Gain Control
AGNSS Assisted GNSS
AGPS Assisted GPS
AltBOC Alternative Binary Offset Carrier
AM Amplitude Modulation
ARM Acorn RISC Machines
ARNS Aeronautical Radio Navigation Service
AS Authorized Service
ASBC Advanced Space Business Corporation
ASIC Application-Specific Integrated Circuit
AWGN Additive White Gaussian Noise
BDCS BeiDou Coordinate System
BDPE Bayesian Direct Position Estimation
BDS BeiDou Navigation Satellite System
BDSBAS BeiDou Satellite-Based Augmentation System
BDT Beidou Time
BER Bit Error Rate
BOC Binary Offset Carrier
BPSK Binary Phase Shift Keying
CAF Cross Ambiguity Function
CDMA Code Division Multiple Access
CGCS2000 China Geodetic Coordinate System 2000
COCESNA Corporacion Centroamerica de Servicios de Navegacion Aerea
CONUS Continental United States
CPU Central Processing Unit
CSK Code Shift Keying
CW Continuous Wave
DFT Discrete Fourier Transform
DGNSS Differential GNSS
DGPS Differential GPS
DLL Delay Locked Loop
DME Distance Measuring Equipment
DOA Direction of Arrival

DOD Department of Defense
DOP Dilution of Precision
DPE Direct Position Estimation
DSSS Direct Sequence Spread Spectrum
EC European Comission
ECEF Earth Centered Earth Fixed
EDAS EGNOS Data Access System
EGNOS European Geostationary Navigation Overlay Service
EKF Extended Kalman Filter
ENU East North Up
ESA European Space Agency
EU European Union
FAA Federal Aviation Agency
FD Fault Detection
FDE Fault Detection and Exclusion
FDMA Frequency Division Multiple Access
FFT Fast Fourier Transform
FLL Frequency Locked Loop
FOC Full Operation Capability
FPGA Field Programmable Gate Array
G2G Galileo Second Generation
GAGAN GPS-Aided GEO Augmented Navigation
GBAS Ground-Based Augmentation System
GBF Grid-Based Filter
GDOP Geometric Dilution of Precision
GEO Geostationary Earth Orbit
GLONASS Globalnaya Navigazionnaya Sputnikovaya Sistema
GLONASST GLONASS Time
GMS Ground Monitor Station
GMT Greenwich Mean Time
GNSS Global Navigation Satellite System
GPS Global Positioning System
GPST GPS Time
GSM Global System for Mobile communications
GST Galileo System Time
HAS High Accuracy Service
HEO Highly Elliptical Orbit
ICAO International Civil Aviation Organization
ICD Interface Control Document
IDFT Inverse Discrete Fourier Transform
IERS International Earth Rotation and Reference System Service
IF Intermediate Frequency
IFFT Inverse Fast Fourier Transform
IGSO Inclined Geosynchronous Satellite Orbit

ILS Instrument Landing System
IMU Inertial Measurement Unit
INLUS Indian Navigational Land Uplink Station
INMCC Indian Master Control Center
INRES Indian Reference Station
INS Inertial Navigation System
IOC Initial Operation Capability
IOT Internet of Things
IOV In-Orbit Validation
IPP Intel® Integrated Performance Primitives
IRNSS Indian Regional Navigation Satellite System
ISRO Indian Space Research Organisation
ITU International Telecommunication Union
JAXA Japan Aerospace Exploration Agency
KASS Korean Augmentation Satellite System
KF Kalman Filter
LAAS Local Area Augmentation System
LAMBDA Least Squares Ambiguity Decorrelation Adjustment
LAN Local Area Network
LBS Location Based Services
LFSR Linear Feedback Shift Register
LIDAR Light Detection and Ranging
LOS Line of Sight
LPV Localizer Performance with Vertical guidance
LPV-200 Localizer Performance with Vertical guidance until a decission height of 200 ft
LSQ Least Squares
LTE Long Term Evolution
LVP Low Visibility Positioning
MC Monte Carlo
MCC Mission Control Centre
MCS Master Control Station
MEO Medium Earth Orbit
MEOSAR Medium Earth Orbiting Search and Rescue
MIMO Multiple Input Multiple Output
MLE Maximum Likelyhood Estimator
MLS Microwave Landing System
MSAS Multi-functional Satellite Augmentation System
MT Multi Threading
MTSAT Multifunctional Transport Satellite
NCO Numerically Controlled Oscillator
NED North East Down
NTP Network Time Protocol
OpenMP Open Multi-Processing

OS Open Service
PDF Probability Density Function
PF Particle Filter
PLL Phase Locked Loop
PNT Position Navigation and Timing
PPP Precise Point Positioning
PPS Precise Positioning Service
PRN Pseudo-Random Noise
PRS Position Report Service
PRS Public Regulated Service
PSD Power Spectral Density
PTP Precission Time Protocol
PVT Position Velocity and Time
PVTA Position Velocity Time and Attitude
QPSK Quadrature Phase Shift Keying
QZSS Quasi-Zenith Satellite System
RAIM Receiver Autonomous Integrity Monitoring
RDSS Radio Determination Satellite Service
RF Radio Frequency
RISC Reduced Instruction Set Computer
RMS Root Mean Square
RNAV Area Navigation
RNSS Radionavigation-Satellite Service
RNSS Regional Navigation Satellite System
RS Restricted Service
RSS Residual Sum of Squares
RTK Real Time Kinematics
SACCSA Solucion de Aumentacion para Caribe Centro y Sudamerica
SAP Synthetic Aperture Processing
SAR Search and Rescue
SAR Synthetic Aperture Radar
SBAS Satellite-Based Augmentation System
SCAT-I Special CATegory I
SDCM System for Differential Corrections and Monitoring
SIMD Single Instruction Multiple Data
SIS Signal-in-Space
SIS Sequential Importance Sampling
SISNeT Signal-in-Space via Internet
SISO Single Input Single Output
SMC Synthetic Multi-Correlator
SMC Sequential Monte Carlo
SMS Short Message Service
SNAS Satellite Navigation Augmentation System
SNR Signal-to-Noise Ratio

SoL Safety of Life
SPAC Satellite Positioning Research and Application Center
SPP Single Point Positioning
SPS Standard Positioning Service
ST Single Threading
TACAN Tactical Air Navigation
TAI International Atomic Time
TTFF Time To First Fix
TTRF Time To Re-Fix
UERE User Equivalent Range Error
UKF Unscented Kalman Filter
UTC Coordinated Universal Time
VOR VHF Omnidirectional Radio Range
VRS Virtual Reference Station
VT Vector Tracking
WAAS Wide Area Augmentation System
WGS-84 World Geodetic System 1984
WLAN Wireless Local Area Network
WLSQ Weighted Least Squares
WRC World Radiocommunication Conference

Contents

1 Introduction

Global Navigation Satellite Systems (GNSS) are satellite-based navigation systems which have the capability to deliver an absolute and accurate Position Velocity and Time (PVT) worldwide. Nowadays GNSSs consist of satellite-based global and regional navigation systems. The unique capability of delivering and absolute position worldwide made GNSS an indispensable backbone infrastructure for a wide range of different applications. Hereby, research and a strong international collaboration as well as knowledge transfer is realized by the Position Navigation and Timing (PNT) community. Existing and new applications have different requirements on the PNT, whereas very strict requirements need to be fulfilled for safety-of-life applications, critical infrastructures and military. The next subchapters discuss briefly existing GNSS, applications which rely on GNSS, GNSS receivers and their performance parameters. The introduction includes also a brief overview of the GNSS market and is concluded with the objectives and the structure of the thesis.

1.1 GNSS Systems and Applications

GNSS are nowadays more important as ever before and the demand for GNSS will further grow in future. The very first satellite-based navigation system Transit was developed by the U.S. Navy and was declared operational in 1964. The system performance is not comparable to nowadays GNSS, but Transit achieved that times a 2-D positioning accuracy of 25 m (RMS) in typically about 10-20 minutes for a stationary or slow-moving user, but up to 100 minutes if the next satellite bypass needs to be awaited for (no continuous availability). The aim of the system was to update the position of ships and submarines, and it was dedicated for military usage and limited maritime civil usage. The equivalent counterpart in the Soviet Union was Parus and Tsikada. Since 1964 satellite-based navigation encountered a tremendous progress. The follow-on program of Transit is the well-known Global Positioning System (GPS), which was declared operational in 1995. The system was designed to have a selective availability, which delivers the full performance to the military users and a reduced performance to civil users. The selective availability aimed to prevent building aided weapons. The counterpart to GPS was

the Russian Globalnaya Navigazionnaya Sputnikovaya Sistema (GLONASS), which was also designed for the military usage, but a subset of the signals was also made available for civil users [Misra and Enge, 2010]. In 2000, the selective availability of GPS was disabled and the civil users where able to obtain worldwide and continuously a 3-D position plus time information with a horizontal positioning accuracy of about 5 m (RMS). This was the breakthrough for GPS and due to the continuous availability and good performance together with the fact that receivers become cheaper with increasing demand, GPS become the standard positioning system for a wide range of different products and applications worldwide. It was rapidly realized by other governments, that GPS was used in safety-critical systems and that GPS became a part of the national infrastructure, but without having its sovereignty. Based on this fact, several countries decided to develop their own satellite-based navigation system, which can be designed to be a GNSS or a Regional Navigation Satellite System (RNSS). Europe contributes to the PNT infrastructure with Galileo (GNSS), China with Beidou (GNSS), India with the Indian Regional Navigation Satellite System (IRNSS) (RNSS), and Japan with the Quasi-Zenith Satellite System (QZSS) (RNSS). Furthermore, all operating countries of a satellite-based navigation system installed a regional Satellite-Based Augmentation System (SBAS), which deliver supplemental information from geostationary satellites to increase the positioning accuracy and availability. North-America is covered with the Wide Area Augmentation System (WAAS) (U.S.), Russia is covered by System for Differential Corrections and Monitoring (SDCM), Europe is covered by the European Geostationary Navigation Overlay Service (EGNOS) (EU), China is covered by the BeiDou Satellite-Based Augmentation System (BDSBAS) (China), India is covered by GPS-Aided GEO Augmented Navigation (GAGAN) and Japan is covered by Multi-functional Satellite Augmentation System (MSAS). This high number of available satellite systems lead to a worldwide significantly increased coverage which allows a fast and accurate position fix with a high availability, even in difficult environmental conditions such as in mountains (if the receiver supports multiple global and regional satellite navigation systems). The navigation systems are operated in the L-Band (frequency range of 1-2 GHz) and S-Band (frequency range of 2-4 GHz), whereas only one signal of the Indian system is placed in the S-Band. Navigation signals are separated from each other by four different orthogonality principles, code division by using different Pseudo-Random Noise (PRN) codes, frequency division by using different center frequencies, phase division by using the 90 deg orthogonality of the In-Phase (I) and Quadrature (Q) component of a signal, and time division by using assigned time slots. Navigation signals are transmitted for military and civil users. Newer signals can have different design criteria and can be optimized to deliver a better ranging performance, have a reduced multipath error envelope, enable higher sensitivity by using data free pilot signals, use short codes for fast signal acquisition, include

encryption or authentication methods or making the signal less sensitive to interference. Navigation signals are affected by different error sources when propagating from the satellite to the user. The most dominant error sources are atmospheric delays caused by the Ionospheric and Tropospheric layer and multipath effects, caused by the environmental conditions. The transmission on multiple frequencies has the benefit, that it allows to estimate Ionospheric delays on receiver side, which is one of the most dominant error sources in GNSS positioning. State-of-the-art receivers support a subset or all of the available satellite navigation systems and depending on the receiver grade, one or multiple frequencies. Low-cost mass-market receivers typically support a single frequency, but dual frequency mass market receivers are currently upcoming, especially in mobile phones and receivers for autonomous driving. High-end receivers for precise positioning or receivers for safety critical applications use typically multiple frequencies and multiple systems. The availability of a wide range of different receiver grades allowed GNSSs to enter many different applications, as shown in Fig. 1.1. GNSS are nowadays a common standard in mobility and transportation. Everybody uses a navigation system in a car to find the fastest way to a destination or keep on track at hiking or bicycling. On commercial side transportation companies use navigation systems for fleet tracking and optimize deliveries in order to facilitate highest flexibility and efficiency. Positioning becomes also standard in mobile phones and thousands of different mobile phone applications use PNT, ranging from taxi apps like Uber to games like Pokemon Go. GNSSs also enabled a significant increase of the degree of automation in the farming industry, which increased the efficiency. GNSSs are the only systems which can deliver a world-wide and continuously available absolute position, which made it also to a standard in surveying and mapping applications. The European Galileo as well as other systems will support in future also Search and Rescue (SAR) in emergency cases, which allows a user to determine and transmit its position.

The characteristics and requirements of a GNSS receiver strongly depend on the application. The performance parameters of a receiver for mass market applications vary significantly in comparison to professional and safety-critical applications. Typical performance parameters of GNSS receivers, as defined in [GSA, 2017], are:

- **Availability** - Percentage of time over a specified time interval that a sufficient number of satellites are transmitting a usable ranging signal within view of the user
- **Accuracy** - The difference between true and computed position (absolute positioning)
- **Continuity** - Ability to provide the required performances during an operation without interruption once the operation has started

Figure 1.1: Today GNSS is a standard application on the road, water, train, air, farm, map, in mobile phones and becomes standard in emergencies to deliver a position message to a search and rescue service. Modern GNSS techniques might allow to extend the field of applications to more challenging environments like woods or indoors. Figure adapted and taken from [GSA, 2017].

- **Integrity** - The measure of trust that can be placed in the correctness of the position or time estimate provided by the receiver
- **Time To First Fix (TTFF)** - A measure of a receiver's performance covering the time between activation and output of a position within the required accuracy bounds
- **Robustness** - A qualitative, rather than quantitative, parameter that depends on the type of attack or interference the receiver is able to mitigate
- **Authentication** - The ability of the system to assure the users that they are utilizing signals and/or data from a trustworthy source, and thus protecting sensitive applications from spoofing threats

1.2 GNSS Market

GNSS is a strongly worldwide growing market, and the growing demand for precise location information in combination with the ongoing evolution of GNSS technology, means that today's GNSS market is bigger than ever. With an estimated 5 billion GNSS devices in use around the world, a number expected to grow to 8 billion by 2020, has made GNSS to a ubiquitous technology [GSA, 2017].

The increasing global coverage and the resulting benefits of a higher availability and accuracy together with competitive companies pushing their GNSS receiver developments to support new systems and signals, enables and supports the development of added-value-services. The sources of the worldwide revenue made by GNSS can be split into two types, *devices and augmentation*

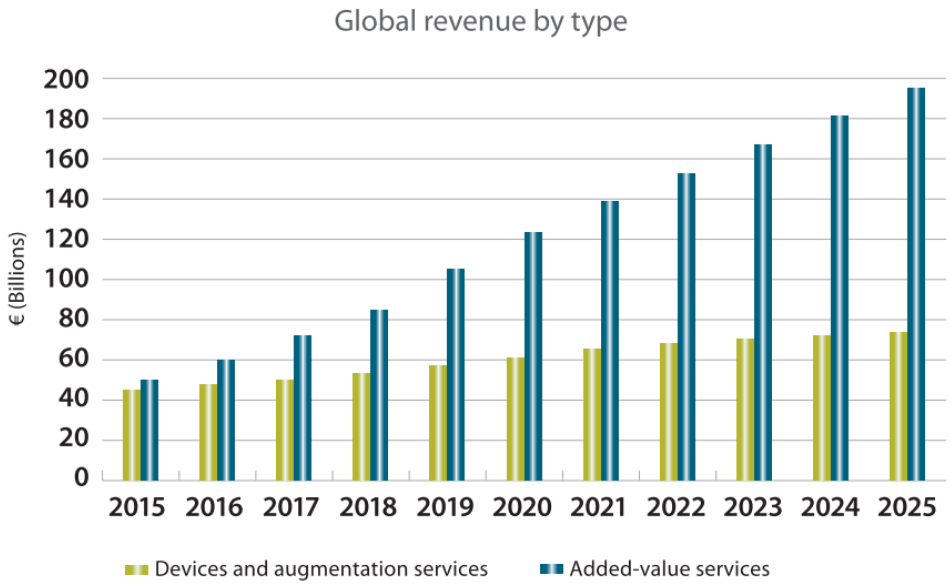

Figure 1.2: Global revenue trend from 2015-2025 made by GNSS and separated by type. [GSA, 2017]

systems (e.g. GNSS receivers) and *added-value services*. As depicted in Fig. 1.2, the revenue made from both types is expected to grow significantly, whereas GNSS as enabling technology brings a rocketing revenue of the added-value services such as navigation services, fleet management applications and many location-aware smartphone apps [GSA, 2017]. Smartphone apps also benefit from the latest developments of a dual-frequency support and access to the raw GNSS measurements of the integrated GNSS receivers, which enable precise positioning techniques such as Real Time Kinematics (RTK) or Precise Point Positioning (PPP) and thus a position accuracy down to the decimeter or centimeter level.

The cumulative revenue split into market segments is shown in Fig. 1.3. It is impressive, that Location Based Services (LBS) and the road segment will dominate the GNSS market together with 93.4% of all revenue made up to 2025. The technological evolutions with connected vehicles and automated driving is expected to be a major driver of growth of GNSS-enabled road applications and services over the upcoming years [GSA, 2017]. The segmentation in Fig. 1.3 clearly shows, that GNSS is available for safety-of-life applications only in (quasi) open sky conditions, whereas non-safety-of-life applications use GNSS also in degraded signal environments.

Initially, the upcoming market of autonomous driving cars brings civil GNSS dependent safety-of-life operations into degraded signal environments. GNSS is a important key element for autonomous driving cars, as it is the only

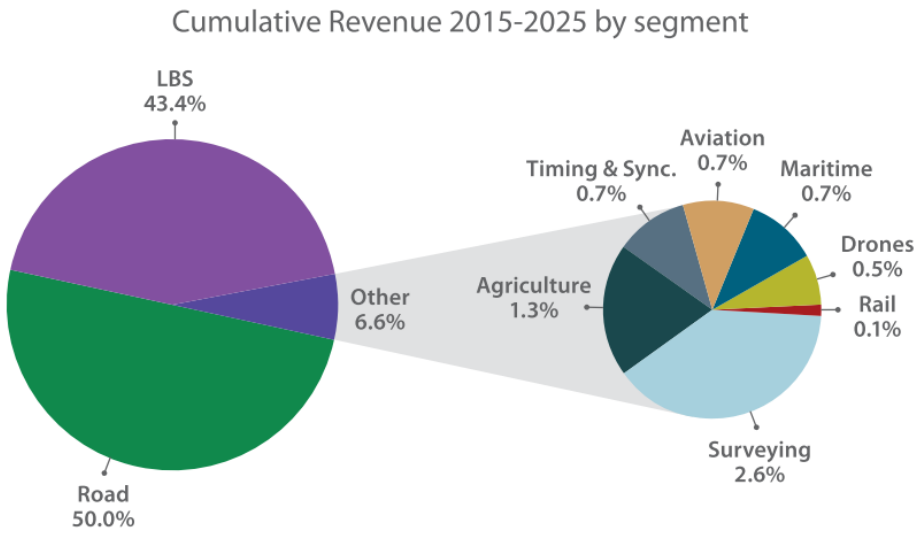

Figure 1.3: Global revenue from 2015-2025 made by GNSS separated by market segment. [GSA, 2017]

global available absolute positioning method, which also achieves accuracies down to sub-dm level. But GNSS relies on very weak signals, which arrive in case of a omni-directional user antenna below the thermal noise floor. This makes GNSS sensitive to signal disruptions and interferences. The market entry of autonomous driving cars is a stepwise approach starting in ideal conditions e.g. on highways where good conditioned roads (broad roads and lines for visual aiding) and open sky for GNSS are available. But the technology for autonomous driving cars need to progress forward to more challenging environments like urban cities or woods, which pushes also the need for high sophisticated GNSS positioning algorithms, whereas this thesis contributes to the development of future advanced GNSS positioning technologies by deriving a PDF of the PVT and by performing an analysis in challenging environments.

1.3 Objectives and Structure of the Thesis

This thesis discusses the implementation of a real-time capable analysis tool for generating PDFs in the PVT domain as well as a real-time capable BDPE software receiver. Therefore, the discussion starts with a summary of today's satellite-based navigation systems in chapter 2. The discussion is continued by placing the investigated method BDPE in context of state-of-the-art positioning technology in chapter 3. Based on the fact, that many state-of-the-art GNSS receivers rely on Bayesian filtering techniques and the implemented

BDPE receiver uses a particle or a grid-based filter for estimating the PDF of the PVT, the basic principles of Bayesian filters are introduced in chapter 4. In order to understand details of state-of-the-art positioning algorithms and fundamental basics for BDPE, the fundamentals of GNSS receivers are discussed in chapter 5. Furthermore, chapter 6 describes the implemented BDPE receiver architecture and shows how the particle and grid-based filter is linked to DPE and how the concept is integrated efficiently into an existing framework of a software-based receiver. Based on the fact, that a probabilistic framework for BDPE is not available, the thesis shows the derivation of a mathematical framework and investigates in an optimal and stable weight update for BDPE in chapter 7. A comprehensive analysis of the obtained PDFs is performed in the correlation domain and in the PVT domain in chapter 8. Furthermore, the resulting PDF is analyzed in challenging real-world scenarios when driving through an urban canyon, underpassing a bridge and going indoors in chapter 8.7. The conclusion in chapter 9 summarizes the obtained results, the lessons learned and gives a short outlook for possible future investigations. The Appendix delivers supplemental material, whereas Appendix A-C contain the complete mathematical derivations to make some chapters more readable, Appendix D extends chapter 8.7 with a time series of the PDFs for the urban scenarios and the indoor case. Appendix E extends chapter 8.5 with a time series of 2D PDFs of the position in order to give evidence, that the proposed approach of introduced nuisance parameters to cover unmodeled UEREs works as expected.

2 Satellite-Based Navigation Systems

This chapter discusses the system architecture of a global or regional navigation satellite system and explains the composition of navigation signals. The discussion is continued with an up-to-date description of all available satellite navigation systems, augmentation systems and transmitted signals. The chapter is concluded with a discussion on the impact of GNSS signal parameters on a DPE solution.

GNSS and RNSS have reserved frequency bands to operate. The frequency bands are assigned by the International Telecommunication Union (ITU) and are located for GNSS in the L-Band and S-Band, whereas today only the Indian system transmit navigation signals in the S-Band. An overview of the allocated frequency bands by GNSSs is shown in Fig. 2.1. All GNSS signals are located in the Radionavigation-Satellite Service (RNSS) band and for safety-of-life applications, some GNSS signals are also located in the stronger protected Aeronautical Radio Navigation Service (ARNS) band. The ARNS band is also used by other radionavigation systems like marker beacons, VHF Omnidirectional Radio Range (VOR), Instrument Landing System (ILS), ILS glideslope, Distance Measuring Equipment (DME), Special CATegory I (SCAT-I), Tactical Air Navigation (TACAN), Automatic Dependent Surveillance - Broadcast (ADS-B) transponders, ground-based radars and associated airborne transponders, and the Microwave Landing System (MLS) [Avila-Rodriguez et al., 2007].

In general, the system operators aim to achieve interoperability of the systems and thus many signals are located at same center frequency and use a common access technique. Hereby, the spectral separation, the spectral shape and modulation types of the navigation signal determine the basic cross-talk (signal interference) properties between the signals and systems. A state-of-the-art overview of all GNSS signals is given in Fig. 2.2, which shows the frequency band and spectral shape of each signal.

2.1 System Architecture

A navigation satellite system consists of three segments, the *Space Segment*, the *Ground Segment* and the *User Segment*. The space segment represents

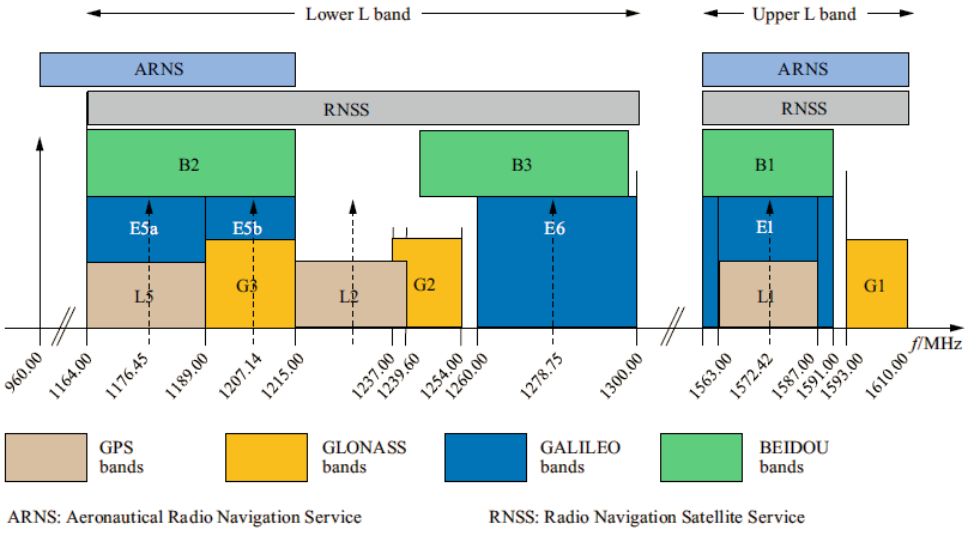

Figure 2.1: Overview of GNSS frequency bands [P. Teunissen and Montenbruck, 2017, Fig. 4.6].

the satellites, which are distributed according to a defined constellation. The ground segment is responsible for the operation of the satellites. The functions of the ground segment, rewritten and adapted from [Misra and Enge, 2010], are

- to monitor satellite orbits,
- to monitor and maintain satellite health,
- to maintain the system time,
- to predict satellite ephemerids and clock parameters,
- to update satellite navigation messages,
- and to command small maneuvers of satellites to maintain orbit, and relocations to compensate for failures, as needed.

Monitoring stations are distributed over the world to achieve a continuous monitoring of all satellites. In case of anomalies satellites are set to unhealthy such that receivers do not use them for positioning. The data of the monitoring stations is used to predict satellite orbits and satellite clock parameters in order to produce a new set of ephemeris data for each satellite, which is uploaded to the satellites on a regular basis (some hours). The user segment consists of the receivers, which receive and process the navigation signals in order to obtain distance measurements to the satellites and calculate a PVT solution. A variety of GNSS receivers emerged in the past decades targeting different user applications. Receivers became that cheap, small and energy efficient such that they are integrated nowadays in every mobile phone.

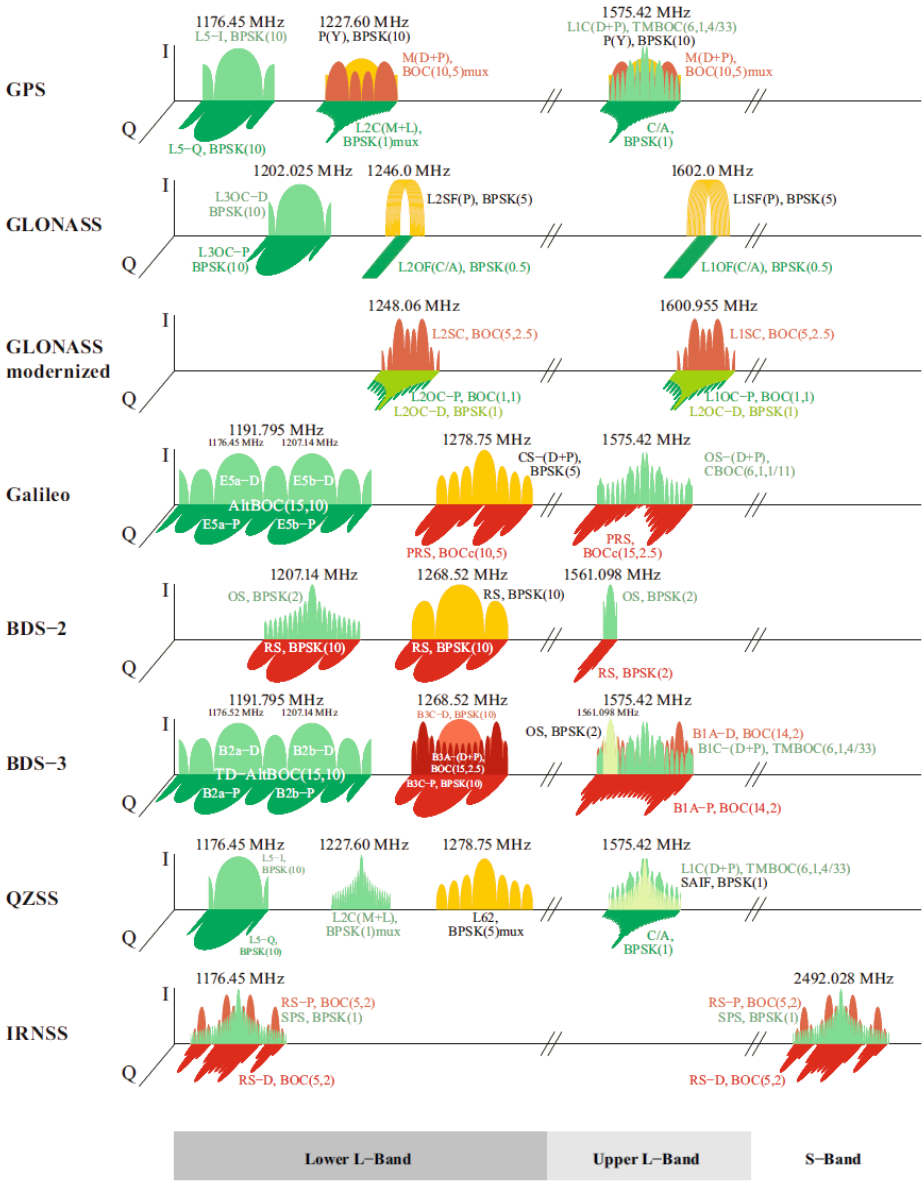

Figure 2.2: Overview of all GNSS signals with modulation schemes - colors indicate open signals (green), authorized signals (red) and restricted access signals (yellow). The figure might differ slightly from the descriptions given by the tables in each subsection, which rely on the latest published ICDs [P. Teunissen and Montenbruck, 2017, Fig. B.1].

2.2 Navigation Signals

A navigation signal is composed of three components, the *carrier*, the *spreading waveform* with a possibly secondary code, and the *navigation data* message, as shown in Fig. 2.3. The spreading waveform is used to generate a Direct Sequence Spread Spectrum (DSSS) signal. At signal generation, the spreading waveform is multiplied with a navigation data message. The resulting baseband signal is mixed to a carrier frequency, typically in the L-Band, is amplified and transmitted.

The spreading code sequence determines the basic characteristics of the navigation signal. The codes have two functionalities, (1) to generate a spread spectrum which allows to recover the signals received below the thermal noise floor and (2) to establish the access technique Code Division Multiple Access (CDMA) and separate the signals from each other. The basic aim of the code sequence is to fulfill the criteria of orthogonality, which is established by generating PRN like sequences allowing to separate the signals by their individual codes. But also a second access technique is used in GNSS, separation of the signals by frequency division, which is called Frequency Division Multiple Access (FDMA). FDMA uses the same PRN code sequences but different carrier frequencies for each transmitted navigation signal, whereas each signal has an assigned frequency slot. There exist different types of PRN codes, but all of them are generated with a Linear Feedback Shift Register (LFSR) or stored as a sequence in memory. Some examples are a Gold Codes, Weil Codes, Kasami Codes or Memory-Codes, whereas a detailed description is not given here. The PRN code together with the modulation scheme defines the spectral characteristics and auto-correlation function of the navigation signal. The higher the code rate, the higher is the occupied spectral bandwidth and the better is the ranging performance. The impact of the code rate and modulation type on the spectral characteristic is briefly visualized in Fig. 2.4, which shows two different modulation types, a Binary Phase Shift Keying (BPSK) and a Binary Offset Carrier (BOC). The BPSK(1) and BPSK(10) have a code rate of $1 * 1.023$ MHz and $10 * 1.023$ MHz, and the $\text{BOC}_{\text{sin}}(10,5)$ has a sub-carrier frequency of $10 * 1.023$ MHz and a code rate of $5 * 1.023$ MHz, all centered at a defined center frequency. The benefit of the BOC modulation is to separate the main lobe symmetrically around the center frequency, whereas the offset between the two main lobes is defined by the subcarrier frequency.

The navigation message contains the almanac and ephemeris data. The almanac data contains a rough description of all satellite orbits and the ephemeris data a precise description of the orbit and clock parameters of the currently tracked satellite. A navigation signal is referred as *data signal*, if the signal carries a navigation message and as *pilot signal*, if no navigation data is modulated onto the navigation signal.

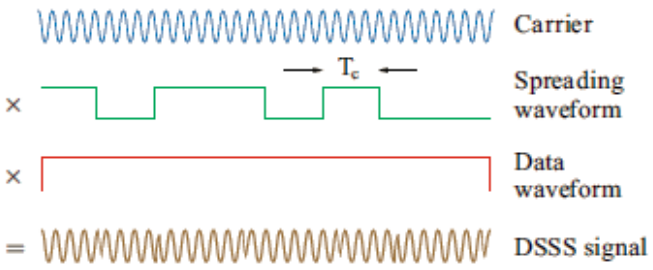

Figure 2.3: The figure shows the composition of a navigation signal consisting of a carrier, spreading code sequence and a navigation data message [P. Teunissen and Montenbruck, 2017, Fig. 7.7].

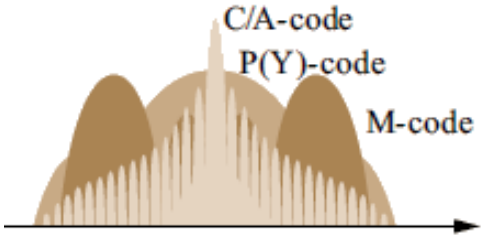

Figure 2.4: The figure shows the spectral shape of three different navigation signals. The C/A-code is a BPSK(1), the P(Y)-code is a BPSK(10) and the M-code a $BOC_{sin}(10,5)$. Figure extracted from [P. Teunissen and Montenbruck, 2017, Fig. 7.8].

2.3 Global Navigation Satellite Systems

There are currently four global satellite navigation systems present, which are operated by the U.S., Europe, Russia and China. All systems and their parameters are discussed briefly in the following subsections. The data is taken from the latest published Interface Control Documents (ICDs), [P. Teunissen and Montenbruck, 2017] and [ESA, 2018].

2.3.1 GPS

The Global Positioning System (GPS) is the GNSS of the U.S. which was developed for the U.S. military, whereas the Department of Defense (DOD) is responsible for operating the system. The deployment of the system started in February 1978 with the first experimental Block I Navstar GPS satellite. The Initial Operation Capability (IOC) with 24 operational satellites in six orbital planes was achieved in December 1993. The full operational capability with Block II / IIA production model satellites was achieved two years later in June 1995. The next generation of satellites was called Block IIR (replenishment) and Block IIF (follow-on). The latest generation of GPS satellites is Block III, produced by Lockheed Martin. The first series of Block III satellites was launched with 4 years of delay in December 2018, whereas the 10th GPS Block III satellite is projected for Q2 2023.

Table 2.1: GPS L1 signal characteristics [P. Teunissen and Montenbruck, 2017], [ESA, 2018], [Kwan, 2019b] and [Kwan, 2019a]

GNSS System	GPS	GPS	GPS	GPS
Service Name	C/A-Q	L1C-I	P(Y)-Code-I	M-Code-I
User Group	civil	civil	military	military
Encryption	no	no	yes	yes
Centre Frequency	1575.42 MHz	1575.42 MHz	1575.42 MHz	1575.42 MHz
Access Technique	CDMA	CDMA	CDMA	CDMA
Signal Component	Data	Data and Pilot	Data	Data and Pilot
Modulation	BPSK(1)	TMBOC(6,1,4/33)	BPSK(10)	2xBOC(10,5) mux
Prim. PRN Length	1023	10230 / 10230	$6.9e^{12}$	N.A.
Sec. PRN Length	-	- / 1800	-	N.A.
PRN Code Family	Gold Codes	Weil Codes	M-seq.	N.A.
Data Rate	50 bps	50 bps / -	50 bps	$\leq$100 bps / N.A.
Min. Rcv. Pwr. 5°	-158.5 dBW	-157 dBW	-161.5 dBW	-158 / -158 dBW

GPS provides two services, the Standard Positioning Service (SPS) and the Precise Positioning Service (PPS). The SPS is a positioning and timing service for commercial and scientific civil users, nowadays transmitted on the L1, L2 and L5 frequency band. The PPS is intended for military usage with encrypted

precision ranging codes for authorized users transmitted on the L1 and L2 frequency band [ESA, 2018].

As shown in Tab. 2.1, Tab. 2.2 and Tab. 2.3, the access technique of GPS is purely based on CDMA. The newer L1C and L5 civil signals deliver a better ranging performance compared to the original C/A code, which is established with the increased code rates. The increased primary PRN code lengths of the new civil signals aim to reduce the cross-talk between the signals. The data free pilot component on the L1C and L5 signal allows for a longer coherent integration time on receiver side which enables a higher sensitivity. The navigation data rates of the new signals have not been increased. Higher data rates would deliver the required ephemeris data faster, but with the tradeoff of a reduced coherent integration time. The coherent integration time needs to be reduced with higher data rates, because the integration period must be aligned to the navigation data bit boundaries. A reduced coherent integration time also leads to a reduced sensitivity and higher Bit Error Rate (BER).

Table 2.2: GPS L2 signal characteristics [P. Teunissen and Montenbruck, 2017], [ESA, 2018] and [Kwan, 2019b]

GNSS System	GPS	GPS	GPS	GPS
Service Name	L2CM-Q	L2CL-Q	P(Y)-Code-I	M-Code-I
User Group	civil	civil	military	military
Encryption	no	no	yes	yes
Centre Frequency	1227.60 MHz	1227.60 MHz	1227.60 MHz	1227.60 MHz
Access Technique	CDMA	CDMA	CDMA	CDMA
Signal Component	Data	Pilot	Data	Data/Pilot
Modulation	BPSK(1) - 2 streams at 511.5 kHz		BPSK(10)	2xBOC(10,5) mux
Prim. PRN Length	10230	767250	$6.9e^{12}$	N.A.
Sec. PRN Length	-	-	-	N.A.
PRN Code Family	M-seq.	M-seq.	M-seq.	N.A.
Data Rate	25 bps	-	50 bps	$\leq$100 bps / N.A.
Min. Rcv. Pwr. 5°	-164.5 dBW (II/IIA/IIR)			-164 / -164 dBW

The new military M-Code comes along with two benefits compared to the original P(Y)-code signal. The signal has an increased ranging performance due to the BOC modulation, which occupies a higher spectral bandwidth compared to BPSK. The higher the occupied bandwidth (Gabor Bandwidth), the sharper is the correlation function and the higher is the navigation signal tracking accuracy [Zhang, Yao, and Lu, 2011]. The second benefit is, that the civil signals can be jammed without hitting the main-lobes of the M-code.

The baseline satellite constellation consists of 24 satellites but supports up to 30 satellites due to a spare slot in each orbit. The orbits are nearly circular with a radius of 26560 km (semi-major-axis), which equals an altitude of about

Table 2.3: GPS L5 signal characteristics [P. Teunissen and Montenbruck, 2017], [ESA, 2018] and [Kwan, 2019c]

GNSS System	GPS	GPS
Service Name	L5-I	L5-Q
User Group	civil	civil
Encryption	no	no
Centre Frequency	1176.45 MHz	1176.45 MHz
Access Technique	CDMA	CDMA
Signal Component	Data	Pilot
Modulation	BPSK(10)	BPSK(10)
Prim. PRN Length	10230	10230
Sec. PRN Length	10	20
PRN Code Family	M-seq.	M-seq.
Data Rate	50 bps	-
Min. Rcv. Pwr. 5°	-157.9 dBW	-157.9 dBW

20200 km and which belongs to the Medium Earth Orbit (MEO). The orbital period is approximately 12 hours and the ground tracks are stationary. The satellites are distributed in 6 orbital planes inclined with 55 deg relative to the equatorial plane. The GPS satellites where launched from Cape Canaveral and the used datum is the World Geodetic System 1984 (WGS-84) [Misra and Enge, 2010] and [ESA, 2018].

2.3.2 GLONASS

The Globalnaya Navigazionnaya Sputnikovaya Sistema (GLONASS) is the Russian counterpart to GPS. The first GLONASS satellites where launched in October 1982, this times in the Soviet Union, with Kosmos-1413, Kosmos-1414 and Kosmos-1415. The system was declared operational in 1993 and its optimal status with 24 operational satellites was achieved in 1995. After 1995 the Russian economy was in a crisis and a full funding for the system was not possible, which caused a disrepair of the system. In 2000 the funding was significantly increased by Vladimir Putin and the restoration become high priority in the government. The original access technique of GLONASS was FDMA ('F'), which delivers a higher robustness due to improved spectral separation and, that times, also a higher protection against narrowband jammers. The original open ('O') and encrypted military ('S') FDMA signals where transmitted on the L1 and L2 band (the L1OF, L1SF, L2OF and L2SF). But two drawbacks came with time, broadband jammers can be produced easily and the spectral separation of each signal increased the complexity on receiver side. The spectral separation induces frequency dependent delays in the satellite hardware, transmission channel and the receiver hardware, which need to be accounted for. Based on these facts, Russia started also to setup

CDMA ('C') signals. The generation of GLONASS-M satellites were initially launched in 2003, which come along with improved clocks and an additional open CDMA signal on the L3 band from 2014 onwards (the L3OC) [Russian Space Systems, 2016d].

Table 2.4: GLONASS FDMA signal characteristics [P. Teunissen and Montenbruck, 2017], [ESA, 2018]

GNSS System	GLONASS	GLONASS	GLONASS	GLONASS
Service Name	L1OF(C/A)-Q	L1SF(P)-I	L2OF(C/A)-Q	L2SF(P)-I
User Group	civil	military	civil	military
Encryption	no	yes	no	yes
Centre Frequency	1602 + n*0.5625 MHz		1246 + n*0.4375 MHz	
Access Technique	FDMA	FMDA	FDMA	FDMA
Signal Component	Data	Data	Data	Data
Modulation	BPSK(0.5)	BPSK(5)	BPSK(0.5)	BPSK(5)
Prim. PRN Length	511	5110000	511	5110000
Meander Seq.	100 Hz	N.A.	100 Hz	N.A.
PRN Code Family	M-seq.	M-seq.	M-seq.	M-seq.
Data Rate	50 bps	50 bps	50 bps	50 bps
Min. Rcv. Pwr. 5°	-161 dBW	N.A.	-161 dBW	N.A.

Since 2007, Russia is providing the civil navigation signals to own and foreign users free of charge and without limitations. A further improvement of the clock was made with the GLONASS-K satellites, which have been initially launched in in 2011. Russia realized that times the rapidly growing demand for high precision services with dual and triple frequencies and thus they placed two more open and encrypted CDMA signals on the L1 and L2 band (the L1OC, L1SC, L2OC and L2SC). The roadmap of GLONASS foresees with the GLONASS-V and GLONASS-KM satellites a encrypted military CDMA signal on the L3 band (the L3SC) as well as interoperable CDMA signals on the L1, L2 and L3 band (the L1OCM, L2OCM and L5OCM) [ESA, 2018] and [Yuri et al., 2011], whereas at the moment only the L1OCM and the L5OCM has been defined [P. Teunissen and Montenbruck, 2017].

GLONASS offers two services, the SPS and the PPS. The SPS is an open civil service without any charge and for worldwide users, whereas the PPS is restricted to authorized users [ESA, 2018].

The space segment of GLONASS consists of nominally 24 satellites distributed in three circular orbital planes. The satellites are operated in the MEO at an altitude of 19140 km, and thus they have a revolution time of approximately 11 hours 15 minutes. Each orbital plane is inclined by 64 deg 8 min and can carry up to eight satellites. Russia uses the launch site in Baikonur/Plesetsk for its satellites and the GLONASS reference datum is the PZ-90.11. The usage of FDMA influenced the satellite constellation, because all FDMA signals transmit the same PRN code. The DSSS code is still necessary due to the

Table 2.5: GLONASS L1 and L2 CDMA signal characteristics [Russian Space Systems, 2016a], [Russian Space Systems, 2016b], [Russian Space Systems, 2016d], [P. Teunissen and Montenbruck, 2017]

GNSS System	GLONASS	GLONASS	GLONASS
Service Name	L1OC-Q	L1SC-I	L2OC-Q
User Group	civil	military	civil
Encryption	no	yes	no
Centre Frequency	1600.995 MHz	1600.995 MHz	1248.060 MHz
Access Technique	CDMA	CDMA	CDMA
Signal Component	Data/Pilot (TM)	N.A.	Pilot/Pilot (TM)
Modulation	BPSK(1)/BOC(1,1)	BOC(5,2.5)	BPSK(1)/BOC(1,1)
Prim. PRN Length	1023	N.A.	10230
Sec. PRN Length	2	N.A.	50
PRN Code Family	Gold Codes	N.A.	Truncated Kasami
Data Rate	125 bps / -	N.A.	-
Min. Rcv. Pwr. 5°	-158.5 dBW	N.A.	-158.5 dBW

Table 2.6: GLONASS L2 and L3 CDMA signal characteristics [Russian Space Systems, 2016b] and [Russian Space Systems, 2016c], [Russian Space Systems, 2016d], [P. Teunissen and Montenbruck, 2017]

GNSS System	GLONASS	GLONASS	GLONASS
Service Name	L2SC-I	L3OC-I	L3OC-Q
User Group	military	civil	civil
Encryption	yes	no	no
Centre Frequency	1248.060 MHz	1202.025 MHz	1202.025 MHz
Access Technique	CDMA	CDMA	CDMA
Signal Component	N.A.	Data	Pilot
Modulation	BOC(5,2.5)	BPSK(10)	BPSK(10)
Prim. PRN Length	N.A.	10230	10230
Sec. PRN Length	N.A.	5	10
PRN Code Family	N.A.	Baker	Neuman-Hoffman
Data Rate	N.A.	100 bps	-
Min. Rcv. Pwr. 5°	N.A.	-158.5 dBW	-158.5 dBW

limited transmission power, which delivers an additional correlation gain when despreading the weak signal on the earth. In order to keep the occupied spectral bandwidth low (L1: 1602.0–1615.5 MHz, L2: 1246.0–1256.5 MHz), 14 frequency channels (almanac slots) are shared with up to 28 satellites. This means that 2 satellites transmit the same code on same frequency at same time. The constellation ensures that these two satellites separated by 180 deg in argument of latitude, which means that they are always at the opposite side of the world [ESA, 2018].

Table 2.7: Planned Interoperability CDMA signal characteristics [Grigoriy Stupak, 2010] and [Yuri et al., 2011], [P. Teunissen and Montenbruck, 2017]

GNSS System	GLONASS	GLONASS	GLONASS
Service Name	L1OCM	L3OCM	L5OCM
User Group	civil	civil	civil
Centre Frequency	1575.42 MHz	1207.14 MHz	1176.45 MHz
Modulation	BOC(1,1)	BPSK(10)	BPSK(10)
Similar to	L1C, E1, B1C	E5b, B2b	L5, E5a, B2a

2.3.3 Galileo

Galileo is the European GNSS, which is an accurate, guaranteed and worldwide available global positioning system under civil control. In 1990 the European Union (EU) decided to set up their own system, whereas the European Comission (EC) together with the European Space Agency (ESA) got the task to deploy the system. The Galileo program consists of three major phases, the IOV (In-Orbit Validation), the IOC (Initial Operation Capability) and the FOC (Full Operation Capability) phase. Prior the IOV phase, two experimental satellites GIOVE-A and GIOVE-B where launched in December 2005 and April 2008 with the purpose to characterize the planned MEO, perform initial tests with the intended satellite payload and to secure the allocated frequency spectrum, which is assigned to Galileo by the ITU in accordance with the World Radiocommunication Conference (WRC) RNSS allocations [ESA, 2018].

The first of four operational IOV satellites was launched with Soyuz VS01 in October 2011 and the satellites where constructed by Astrium GmbH and Thales Alenia Space. The IOV satellites transmit signals on the E1, E5 and E6 band and had the planned SAR feature already installed. First position fixes where reported with the IOV satellites in March 2013. Early in 2014 the IOV tests have been completed and it was clear that Galileo will achieve the expected performance, if the full ground and space segment is installed. The follow-on FOC satellites where produced by OHB Systems and the first two FOC satellites where launched in August 2014. In December 2015 the EC announced the declaration of initial services, which means that Galileo satellites and ground infrastructure is operationally ready, but the high accurate position fix where not available that times, because users cannot always count on four available satellites [GPS World, 2016]. It is expected that Galileo will reach the FOC with 30 satellites (24 satellites plus 6 orbital spares) in 2020. In parallel to deploying the first generation of Galileo satellites, ESA and industry partners are studying already the Galileo Second Generation (G2G) satellites, signals and ground infrastructure [ESA, 2018].

Galileo offers four services, the Open Service (OS), the High Accuracy Service

Table 2.8: Galileo E1 signal characteristics [EU, 2016], [P. Teunissen and Montenbruck, 2017], [ESA, 2018]

GNSS System	Galileo	Galileo	Galileo
Service Name	E1 OS-I	E1 OS-I	E1 PRS-Q
User Group	civil	civil	authorized
Encryption	no	no	yes
Centre Frequency	1575.42 MHz	1575.42 MHz	1575.42 MHz
Access Technique	CDMA	CDMA	CDMA
Signal Component	Data	Pilot	Data
Modulation	CBOC(6,1,1/11)		$BOC_{cos}(15,2.5)$
Prim. PRN Length	4092		N.A.
Sec. PRN Length	-	25	N.A.
PRN Code Family	Random Codes		N.A.
Data Rate	125 bps	-	N.A.
Min. Rcv. Pwr. 10°	-157 dBW		N.A.

(HAS), the Public Regulated Service (PRS) and the SAR service. The OS is accurate to one meter and is freely accessible. The service should support the mass market segment, especially motor vehicle navigation and location-based mobile phone services. The HAS provides an additional navigation signal on a different frequency band for added value services and the signal can be encrypted in order to control the access. The PRS is restricted to government-authorized users. The signal is designed to have a higher robustness against jamming and spoofing and promises a high level of continuity. The signal is intended to be used by critical infrastructure such as energy providers, telecommunications, finance or police forces. The SAR service is worldwide available and establishes also an uplink to the satellites in order to transmit an emergency message including a position. The message can be transmitted with a dedicated SAR beacon. This service extends the Cospas-Sarsat Medium Earth Orbiting Search and Rescue (MEOSAR) program. The SAR center collects emergency messages and relay them to national rescue centers. In some cases it is also possible to feedback a message to the transmitting beacon [EU, 2016], [ESA, 2018], [EU, 2020].

The architecture of Galileo is also divided in a space, ground and user segment. The 30 satellites of the space segment are distributed on three orbital planes in the MEO at an altitude of 23222 km. The planes are inclined by 56 deg with respect to the earth's equator. The satellites are equidistantly distributed in the orbit and need approximately 14 h for one revolution. Each plane has two spare satellites, which are on hold until an operational satellite will have a failure [ESA, 2018].

The transmission frequencies are shown in Fig. 2.1. Galileo transmit all signals E1, E5a, E5b and E6 in the RNSS band, whereas E1, E5a and E5b is additionally located in the ARNS band, which is employed by civil aviation users and

Table 2.9: Galileo E5 signal characteristics [EU, 2016], [P. Teunissen and Montenbruck, 2017], [ESA, 2018]

GNSS System	Galileo	Galileo	Galileo	Galileo
Service Name	E5a-I	E5a-Q	E5b-I	E5b-Q
User Group	civil	civil	civil	civil
Encryption	no	no	no	no
Centre Frequency	1176.45 MHz	1176.45 MHz	1278.75 MHz	1278.75 MHz
Centre Frequency	1191.795 MHz (center E5ab AltBOC)			
Access Technique	CDMA	CDMA	CDMA	CDMA
Signal Component	Data	Pilot	Data	Pilot
Modulation	BSPSK(10)	BSPSK(10)	BSPSK(10)	BSPSK(10)
Modulation	AltBOC(15,10)			
Prim. PRN Length	10230	10230	10230	10230
Sec. PRN Length	20	100	4	100
PRN Code Family	M-seq.	M-seq.	M-seq.	M-seq.
Data Rate	50 sps	-	250 sps	-
Min. Rcv. Pwr. 10°	-158 dBW	-158 dBW	-158 dBW	-158 dBW

allows for dedicated safety-critical applications. The E1 and E5a/E5b bands are dedicated to mass marked OS and Safety of Life (SoL) applications, whereas the E6 band is dedicated to the HAS.

Table 2.10: Galileo E6 signal characteristics [ESA, 2018], [EU, 2016], [EU, 2019]

GNSS System	Galileo	Galileo	Galileo
Service Name	E6 CS-I	E6 CS-I	E6 PRS-Q
User Group	civil	civil	authorized
Encryption	no	no	yes
Centre Frequency	1278.75 MHz	1278.75 MHz	1278.75 MHz
Access Technique	CDMA	CDMA	CDMA
Signal Component	Data	Pilot	Data
Modulation	BPSK(5)	BPSK(5)	$BOC_{cos}(10,5)$
Prim. PRN Length	5115	5115	N.A.
Sec. PRN Length	-	100	N.A.
PRN Code Family	Mem-Seq.	Mem-Seq.	N.A.
Data Rate	1000 sps	-	N.A.
Min. Rcv. Pwr. 10°	-158dBW	-158 dBW	N.A.

2.3.4 BeiDou

The BeiDou Navigation Satellite System (BDS) is the Chinese global navigation satellite system. BeiDou followed a three-step development strategy with BeiDou-1 (BDS-1), BeiDou-2 (BDS-2) and BeiDou-3 (BDS-3). Hereby, BDS-1 is a RNSS planned to cover China and neighbor countries, BDS-2 is also a RNSS and covers Asia-Pacific (roughly East Asia, South Asia, Southeast Asia,

and Oceania) and BDS-3 becomes a GNSS covering the whole world [State Council Information Office Republic of China, 2016].

BDS-1 is a experimental demonstration navigation satellite system consisting of three operational satellites in the Geostationary Earth Orbit (GEO). The first satellite BeiDou-1A of BDS-1 was launched in October 2000 and the system became operational in December 2000. BeiDou-1 is already decommissioned since 2012. The system offered PNT to Chinese users [State Council Information Office Republic of China, 2016].

The project for the second generation BDS-2 started in 2004, whereas the first launch of the BDS-2 satellite Compass-M1 was back in April 2007. BDS-2, also known as COMPASS, became operational end of 2012. The system consists in total of 14 satellites - 5 GEO satellites, 5 Inclined Geosynchronous Satellite Orbit (IGSO) satellites and 4 MEO satellites. BDS-2 was compatible with BDS-1 and provided PNT, wide-area differential services and short message communication services [State Council Information Office Republic of China, 2016].

The last step of the strategic plan is the third generation BDS-3, whereas the project started in 2009. The first BDS-3 satellite was launched in March 2015 and the satellites will offer same passive and active services as BDS-2 and transmit a new set of improved navigation signals. The basic constellation of BDS-3 consists of 3 GEO satellites, 3 IGSO satellites and 24 MEO satellites, whereas the full constellation will have 35 satellites [PhysOrg, 2019], [State Council Information Office Republic of China, 2016], [China Satellite Navigation Office, 2017a]. On 20th October 2020 the constellation consisted of 34 BDS-3 satellites in orbit, with the status that one is in testing and four are experimental [Test and Assessment Research Center of China Satellite Navigation Office, 2020].

The GEO satellites operate in an altitude of 35786 km and are located at 80°E, 110.5°E, and 140°E. The IGSO satellites also operate in an altitude of 35786 km and have and inclination of 55 deg with respect to the equatorial plane. The MEO satellites are operated in an altitude of 21528 km and have also an inclination of 55 deg with respect to the equatorial plane. The coordinate frame is adopted and called BeiDou Coordinate System (BDCS) and is in accordance with the International Earth Rotation and Reference System Service (IERS) as well as with the China Geodetic Coordinate System 2000 (CGCS2000) [China Satellite Navigation Office, 2017a].

The BDS will offer an Open Service (OS) for civil usage, an Authorized Service (AS) for authorized and military usage, a wide-area differential Precise Point Positioning (PPP) service, a regional and global Short Message Service (SMS), a Search and Rescue (SAR) service as well as an augmentation service via GEO satellites and ground based communication infrastructure. An overview

Table 2.11: BeiDou Service Plan [China Satellite Navigation Office, 2019d].

Service Types		Signal(s)/Band(s)	Broadcast Satellites
Worldwide	Positioning, Navigation and Timing (RNSS)	B1I, B3I	3GEO+3IGSO+24MEO
		B1C, B2a, B2b	3IGSO+24MEO
	Global Short Message Communication (GSMC)	Uplink: L Downlink: GSMC-B2b	Uplink: 14MEO Downlink: 3IGSO+24MEO
	International Search And Rescue (SAR)	Uplink: UHF Downlink: SAR-B2b	Uplink: 6MEO Downlink: 3IGSO+24MEO
China and Surrounding Areas	Satellite-based Augmentation System (SBAS)	BDSBAS-B1C, BDSBAS-B2a	3GEO
	Ground Augmentation System (GAS)	2G, 3G, 4G, 5G	Mobile communication networks, Internet
	Precise Point Positioning (PPP)	PPP-B2b	3GEO
	Regional Short Message Communication (RSMC)	Uplink: L Downlink: S	3GEO
Note: China and surrounding areas means 75°E to 135 °E, 10°N to 55°N			

of planned services is given in Tab. 2.11. The OS provides a position with an accuracy of 10 m, time with an accuracy of 50 ns and velocity with an accuracy of 0.2 m/s to civil users worldwide. The wide area differential service is a correction service intended to achieve 1 m positioning accuracy and to allow Cat I approaches with aircraft. Hereby, 30 stations broadcasting corrections via GEO satellites. The short message service is also called Position Report Service (PRS) and allows a user to exchange 120 Chinese characters per message [ESA, 2018], [China Satellite Navigation Office, 2019d].

2.4 Regional Navigation Satellite Systems

Regional navigation systems have a limited aerial coverage and are planned by Japan and India. Both systems are described in the following sections.

2.4.1 QZSS

The Quasi-Zenith Satellite System (QZSS) is the Japanese regional navigation satellite system. The Japanese government initiated the development of QZSS in 2002. At beginning a development team called Advanced Space Business Corporation (ASBC) was set up, which consisted of Mitsubishi Electric Corp., Hitachi Ltd., and GNSS Technologies Inc. This cooperation collapsed in

Table 2.12: BeiDou OS B1 (L1-Band) signal characteristics. The QMBOC(6,1,4/33) is effectively composed of a BOC(1,1) and a BOC(6,1) which are in-phase quadrature. The navigation message D1 is transmitted from the MEO and IGSO satellites, D2 is transmitted from GEO satellites. Data from the ICDs [China Satellite Navigation Office, 2017a], [China Satellite Navigation Office, 2019a].

GNSS System	BeiDou	BeiDou	BeiDou
Service Name	B1C-I	B1C-IQ	B1I
User Group	civil	civil	civil
Encryption	no	no	no
Orbit	MEO, IGSO		MEO, IGSO, GEO
Centre Frequency	1575.42 MHz	1575.42 MHz	1561.098 MHz
Access Technique	CDMA	CDMA	CDMA
Signal Component	Data	Pilot	Data
Modulation	$BOC_{sin}(1,1)$	QMBOC(6,1,4/33)	BPSK(2)
Prim. PRN Length	10230	10230	2046
Sec. PRN Length	1	1800	-
PRN Code Family	Weil	Weil	Gold
Data Rate	100 sps	-	D1: 1kbps, D2:500 bps
Power Ratio	Data:Pilot=1/4:3/4		-
Min. Rcv. Pwr. 5°	-158.5 dBW (MEO), -160.3 dBW (IGSO)		-163 dBW

Table 2.13: BeiDou OS B2 (L5-Band) signal characteristics. Data from the ICDs [China Satellite Navigation Office, 2017b], [China Satellite Navigation Office, 2019b], [China Satellite Navigation Office, 2019b]. Signals and Data with (*) indicates data from [P. Teunissen and Montenbruck, 2017] and might not be according to latest ICDs

GNSS System	BeiDou	BeiDou	BeiDou	BeiDou
Service Name	B2a-I	B2a-Q	B2b-I	B2b-Q*
User Group	civil	civil	civil	civil
Encryption	no	no	no	no
Orbit	MEO, IGSO		MEO, IGSO	
Centre Frequency	1176.45 MHz	1176.45 MHz	1207.14 MHz	1207.14 MHz
Access Technique	CDMA	CDMA	CDMA	CDMA
Signal Component	Data	Pilot	Data	TBD
Modulation	BPSK(10)	BPSK(10)	BPSK(10)	BPSK(10)
Modulation	TD-AltBOC(15,10)*			
Prim. PRN Length	10230	10230	10230	10230
Sec. PRN Length	5	100	-	TBD
PRN Code Family	Gold	Gold	Gold	TBD
Data Rate	200 sps	-	1000 sps	TBD
Pwr. Ratio	Data:Pilot=1/2:1/2		-	TBD
Min. Rcv. Pwr. 5°[dBW]	-155.5 (MEO), -1570.3 (IGSO)		-160 (MEO), -162 (IGSO)	

2007 and the Japan Aerospace Exploration Agency (JAXA) together with the Satellite Positioning Research and Application Center (SPAC) took over the responsibilities for system development and operation. The initial operation phase started in Sept. 2010 and has been completed in summer 2011. During this phase it was verified, that the first quasi-zenith satellite Michibiki and the

Table 2.14: BeiDou OS B2b-PPP and B3 signal characteristics [China Satellite Navigation Office, 2019c], [China Satellite Navigation Office, 2018]. The navigation message D1 is transmitted from the MEO and IGSO satellites, D2 is transmitted from GEO satellites.

GNSS System	BeiDou	BeiDou	BeiDou
Service Name	B2b-I-PPP	B2b-Q-PPP	B3-I
User Group	civil	TBD	civil
Encryption	no	TBD	no
Orbit	GEO	GEO	MEO, IGSO, GEO
Centre Frequency	1207.14 MHz	1207.14 MHz	1268.520 MHz
Access Technique	CDMA	CDMA	CDMA
Signal Component	Data	TBD	Data
Modulation	BPSK(10)	TBD	BPSK(10)
Prim. PRN Length	10230	TBD	10230
Sec. PRN Length	-	TBD	-
PRN Code Family	Gold	TBD	Gold
Data Rate	1000 sps	TBD	D1: 1kbps, D2:500 bps
Pwr. Ratio	-	TBD	Data:Pilot=1:2
Min. Rcv. Pwr. 5	-160dBW	TBD	-163 dBW

Table 2.15: BDS-II AS signal characteristics. Planned BDS-III AS signals cannot be confirmed and thus they are not listed in the table, but Fig. 2.2 contains also planned BDS-III AS signals [ESA, 2018], [Lu and Yao, 2014]

GNSS System	BeiDou	BeiDou	BeiDou
Service Name	B1-Q	B2-Q	B3-IQ
User Group	authorized	authorized	authorized
Encryption	yes	yes	yes
Orbit	N.A.	N.A.	N.A.
Centre Frequency	1561.098 MHz	1207.14 MHz	1268.52 MHz
Access Technique	CDMA	CDMA	CDMA
Signal Component	N.A.	N.A.	Data
Modulation	BPSK(2)	BPSK(10)	QPSK(10)
Prim. PRN Length	N.A.	N.A.	N.A.
Sec. PRN Length	N.A.	N.A.	N.A.
PRN Code Family	N.A.	N.A.	N.A.
Data Rate	N.A.	N.A.	N.A.
Pwr. Ratio	N.A.	N.A.	N.A.
Min. Rcv. Pwr. 5	N.A.	N.A.	N.A.

ground segment was operational and that QZSS+GPS can deliver an improved position performance of more than 10 percent compared to GPS only. The Japanese government decided to accelerate the QZSS development to reach an initial constellation of 4 satellites and targeting a full constellation of 7 satellites [ESA, 2018].

The space segment is planned to have three satellites in a periodic Highly Elliptical Orbit (HEO) and a fourth satellite in a GEO. The perigee altitude

is about 32000 km and apogee altitude is about 40000 km for the HEO satellites, and all of them have the same ground track [ESA, 2018]. The name quasi-zenith arises from the fact, that one satellite has always an elevation of more than 70 deg in Japan. The system is designed to have the highest interoperability with GPS and thus the system has, at least for initial signals, same signal characteristics as GPS. QZSS is designed to transmit 6 signals on the L1, L2, L5 and L6 (E6) frequency band.

QZSS offers a positioning service and a short message delivery service. The positioning services will cover a Satellite Positioning Service similar to GPS [Japanese Cabinet Office, 2018c], a Sub-Meter Level Augmentation service [Japanese Cabinet Office, 2019d], a Centimeter Level Augmentation service [Japanese Cabinet Office, 2019a], [Japanese Cabinet Office, 2018a] and Position Technology Verification Services for purposes to demonstrate position technologies [Japanese Cabinet Office, 2019c], [Japanese Cabinet Office, 2018b]. The short message delivery service aim to provide messages for disaster and rescue management [Japanese Cabinet Office, 2019b].

Table 2.16: QZSS L1 Signal Characteristics for the Satellite Positioning Service. BI and BII are acronyms for Block I and Block II QZSS satellites. Data from [ESA, 2018], [Japanese Cabinet Office, 2018c].

GNSS System	QZSS	QZSS	QZSS
Service Name	C/A-BI:I-BII:Q	L1CP-BI:Q-BII:I	L1CD-I
Orbit	Quasi-Zenith Orbit, GEO		
User Group	civil	civil	civil
Encryption	no	no	no
Centre Frequency	1575.42 MHz	1575.42 MHz	1575.42 MHz
Access Technique	CDMA	CDMA	CDMA
Signal Component	Data	Pilot	Data
Modulation	BPSK(1)	BI: BOC(1,1), BII: TMBOC(1,1)	BOC(1,1)
Prim. PRN Length	1023	10230	10230
Sec. PRN Length	-	1800	-
PRN Code Family	Gold Codes	Weil Code	Weil Code
Data Rate	50 bps	-	100 sps
Min. Rcv. Pwr. 5°	-158.5 dBW	BII:-158.25 dBW	BII: -162.4 dBW

2.4.2 IRNSS

The Indian Regional Navigation Satellite System (IRNSS) covers primary the area of India plus 1500 km of its geo-political boundaries. The IRNSS is developed, maintained and operated by the Indian Space Research Organisation (ISRO) and should deliver an accuracy better than 20 m to its users. The system design criteria was to minimize the Dilution of Precision (DOP), maximize the visibility over the target area, minimize the satellite constellation,

Table 2.17: QZSS L2 and L5 Characteristics for the Satellite Positioning Service. BI and BII are acronyms for Block I and Block II QZSS satellites. (*) Two channels are time-multiplexed into one channel for each chip. All signals in this table refer to the Satellite Positioning Service. Data from [ESA, 2018], [Japanese Cabinet Office, 2018c]

GNSS System	QZSS	QZSS	QZSS	QZSS
Service Name	L2CM-I	L2CL-I	L5-I	L5-Q
Orbit	Quasi-Zenith Orbit, GEO			
User Group	civil	civil	civil	civil
Encryption	no	no	no	no
Centre Frequency	1227.60 MHz	1227.60 MHz	1176.45 MHz	1176.45 MHz
Access Technique	CDMA	CDMA	CDMA	CDMA
Signal Component	Data	Pilot	Data	Pilot
Modulation	BPSK(1) - 2 streams at 511.5 kHz (*)		QBPSK(10)	
Prim. PRN Length	10230	767250	10230	10230
Sec. PRN Length	-	-	10	20
PRN Code Family	M-seq.		Neuman Hofman	
Data Rate	25 bps	-	50 bps	-
Min. Rcv. Pwr. 5°	BII:-158.5 dBW		-157.0 dBW	-157.0 dBW

Table 2.18: QZSS L1 Signal Characteristics for the Submeter Augmentation Service and the L6 Signal Characteristics for the Centimeter Level Augmentation Service. BI and BII are acronyms for Block I and Block II QZSS satellites. (*) Code 1 and code 2 are time multiplexed. The navigation message of the L6 signal is modulated with Code Shift Keying (CSK). Data from [ESA, 2018], [Japanese Cabinet Office, 2019d], [Japanese Cabinet Office, 2018a], [Japanese Cabinet Office, 2019a].

GNSS System	QZSS	QZSS	QZSS
Service Name	L1S	L6-1	L6-2
Orbit	Quasi-Zenith Orbit, GEO	Quasi-Zenith Orbit, GEO	
User Group	civil	restricted	restricted
Encryption	no	yes	yes
Centre Frequency	1575.42 MHz	1278.75 MHz	1278.75 MHz
Access Technique	CDMA	CDMA	CDMA
Signal Component	Data	BI:Data, BII:Data	BI:Pilot, BII:Data
Modulation	BPSK(1)	BPSK(5) - 2 streams at 2.5575 Mcps (*)	
Nav. Msg. Modulation	-	Code Shift Keying (CSK)	
Prim. PRN Length	1023	10230	BI:1048575, BII:10230
Sec. PRN Length	-	-	-
PRN Code Family	Gold Code	Small Kasami Set	
Data Rate	250 bps	2 kbps	BI:-, BII: 2 kbps
Min. Rcv. Pwr. 5°	BII:-158.5 dBW	BI:-155.7 dBW	BII:-156.82 dBW

achieve sustenance in case of one-satellite failure and consider the availability of orbital locations [P. Teunissen and Montenbruck, 2017].

The space segment consists of seven satellites, four in the IGSO and three in the GEO. The orbits are inclined by 29 deg with respect to the equatorial plane.

Table 2.19: QZSS L5S Signal Characteristics for the Positioning Technology Verification service.

GNSS System	QZSS	QZSS
Service Name	I5S	Q5S
Orbit	Quasi-Zenith Orbit, GEO	Quasi-Zenith Orbit, GEO
User Group	civil	civil
Encryption	no	no
Centre Frequency	1176.45 MHz	1176.45 MHz
Access Technique	CDMA	CDMA
Signal Component	Data	Pilot
Modulation	QPSK(10)	
Prim. PRN Length	10230	10230
Sec. PRN Length	-	20
PRN Code Family	-	Neuman Hofman
Data Rate	250 bps	-
Min. Rcv. Pwr. 5°	-157.0 dBW	

Hereby, the GEO satellites are distributed approximately equidistantly in a range of 100 deg in longitude between central Africa and Indonesia. The IGSO satellites cover a latitude range of +/- 30 deg and are centered at 55 deg and 111.75 deg East. IRNSS transmit on the L5 and S-band, whereas the frequencies have been assigned for RNSSs. It was easier to go for the less populated L5-band because the L1 and L2 frequency bands where already intensively used by other GNSSs and interoperability needs to be ensured. In order to achieve better ranging performances with a dual frequency approach, a second frequency in the S-Band was selected, which is up to now unique. The ITU allocated globally a 16.5 MHz slot for Radio Determination Satellite Services (RDSSs) and RNSSs. Furthermore, the S-band is less affected by ionospheric perturbations compared to the L-band [P. Teunissen and Montenbruck, 2017], [Indian Space Research Organization, 2017].

The IRNSS offers a primary and secondary service area, whereas the primary area covers the Indian landmasses plus 1500 km and the secondary service ranges from latitudes 30°S to 50°N and longitudes 30°E to 130°E. The system will offer an open SPS and an encrypted Restricted Service (RS) [P. Teunissen and Montenbruck, 2017].

2.5 Augmentation Systems

Augmentation systems deliver supplemental information to GNSS receivers in order to improve the accuracy, integrity and availability of the PVT solution. There exist different types of augmentation systems, which can be a Ground-Based Augmentation System (GBAS) or a Satellite-Based Augmentation System (SBAS). The GBAS is also often called Local Area Augmentation

Table 2.20: IRNSS L5 and S-Band Signal Characteristics for the SPS and RS. The signal concept adds a fourth interplex signal to achieve a constant envelope signal in order to avoid saturation effects at the high-power amplifier of the satellites. Data from [Indian Space Research Organization, 2017] and signals with (*) from [P. Teunissen and Montenbruck, 2017].

GNSS System	IRNSS	IRNSS	IRNSS	IRNSS
Service Name	L5-SPS-I	L5-RS-IQ (*)	S-SPS-I	S-RS-IQ (*)
Orbit	IGSO, GEO	IGSO, GEO	IGSO, GEO	IGSO, GEO
User Group	civil	restricted	civil	restricted
Encryption	no	yes	no	yes
Centre Frequency	1176.45 MHz	1176.45 MHz	2492.028 MHz	2492.028 MHz
Access Technique	CDMA	CDMA	CDMA	CDMA
Signal Component	Data	Pilot/Data	Data	Pilot/Data
Modulation	BPSK(1)	BOC(5,2)/BOC(5,2)	BPSK(1)	BOC(5,2)/BOC(5,2)
Prim. PRN Length	1023	8192/8192	1023	8192/8192
Sec. PRN Length	-	40/-	-	40/-
PRN Code Family	Gold Code	-	Gold Code	-
Data Rate	50 sps	-/TBD	50 sps	-/TBD
Min. Rcv. Pwr. 5°	-159.0 dBW	-	-162.3 dBW	-

System (LAAS), whereas the International Civil Aviation Organization (ICAO) prefers GBAS. The very first augmentation system WAAS from the U.S. is a SBAS and aim to enable GPS to aircraft in all phases of a flight, including precision approaches to any airport in the covered area. Today's augmentation systems are typically designed to be a SBAS using satellites in the GEO to transmit the correction data. GBAS systems cover only a limited area, typically an airport to enable precision approaches for aircraft. Augmentation systems use typically the same carrier frequencies and spreading techniques as the GNSS signals, with the benefit that receivers need less modifications to enable the service. Augmentation systems rely on data from a network of ground-based reference stations, which continuously observe GNSS signals and calculate the correction data and integrity messages [ESA, 2018]. Other sectors profit from SBAS as well, it is used in agriculture to get a more precise position to reduce fertilizers and pesticides, it is used by the marine in poor visibility conditions and SBAS capability is integrated in nearly all mobile phones. The future trends of SBAS systems is to support multiple systems and multiple frequencies, but with focus on L1 and L5 [P. Teunissen and Montenbruck, 2017].

2.5.1 WAAS

The Wide Area Augmentation System (WAAS) is operated by the U.S. and the service area covers Continental United States (CONUS), Alaska, Canada and

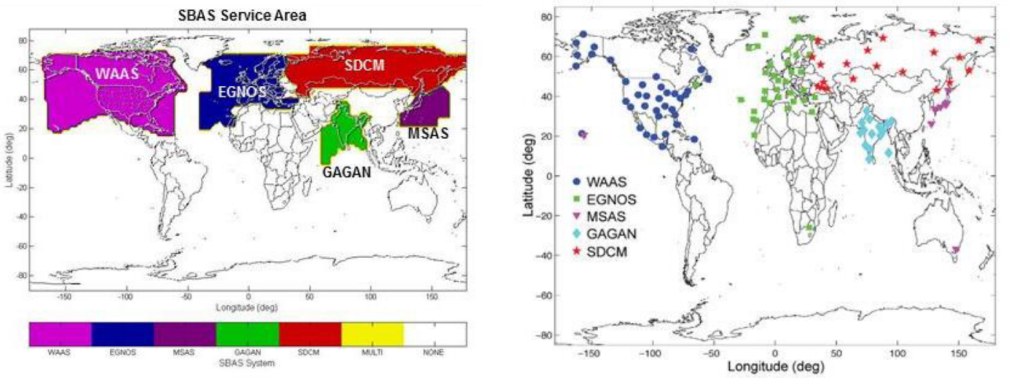

Figure 2.5: The left figure shows the SBAS service areas and the right figure SBAS reference stations from 2015 [Dennis, 2015, Fig. 1 and 2].

Mexico. The system development and operation is performed by the Federal Aviation Agency (FAA), whereas the system became operational in late 2003. The system was developed originally for the civil aviation community and supported already thousands of aircraft instrument approaches on Canadian and U.S. airports. The system supports en-route, terminal and approach operations as well as a full Localizer Performance with Vertical guidance until a decission height of 200 ft (LPV-200) precision approaches (similar to a CAT-I approach capability). The system uses a ground-based network of 38 reference stations to calculate the correction data in 3 master stations. The corrections are transmitted by 6 uplink systems to three geostationary telecommunication satellites. The user benefits in two aspects, because the GNSS receiver can use the three additional geostationary satellites for calculating the navigation solution and can improve the solution by using the correction data [FAA, 2020].

2.5.2 SDCM

The System for Differential Corrections and Monitoring (SDCM) is the Russian SBAS, which is developed as a component of GLONASS. It supports integrity monitoring and generation of correction data for both, GPS and GLONASS. The ground segment consists of 19 prototype measuring points in Russia and 4 outside of Russia, whereas it is planned to add further 27 measurement points inside Russia. The SDCM control center is located in Moscow and the system distributes the correction data using 3 geostationary satellites and a Signal-in-Space via Internet (SISNeT) server. The geostationary satellites where launched between 2011 and 2014. The SDCM development plan foresees regional SDCM data processing centers, enlargement of the reference station

network and enlargement of the transferred data composition [ESA, 2018], [Grigory Stupak, 2012].

2.5.3 EGNOS

The European Geostationary Navigation Overlay Service (EGNOS) is the European satellite-based augmentation system. EGNOS offers three services, the OS, which is freely available to the public of Europe (operational since 2009), the SoL service, which provides the most stringent level of Signal-in-Space (SIS) performance (operational since 2011) and the EGNOS Data Access System (EDAS), which provides access to EGNOS data by other communication channels not using the GEO satellites. The ground segment uses a network of 39 reference stations in Europe, Africa and North America and processes the data in four Mission Control Centres (MCCs). The correction data is distributed by 6 uplink stations and 3 geostationary satellites. From 2011 to 2030 EGNOS supports augmentation for GPS L1 only, but it is planned with EGNOS-V3 to support also the SBAS dual frequency L1/L5 standard, which is forseen to enter into service in 2024 [GSA, 2019]. Since 2015 EGNOS supports LPV-200 aircraft approaches [GSA, 2015], [ESA, 2018].

2.5.4 SNAS

The Satellite Navigation Augmentation System (SNAS) is the Chinese satellite-based augmentation system, which is also called BDSBAS. The SNAS service is compatible the standard of ICAO and is planned for 2020. The full system is planned to have 30 reference stations in China and 20 reference stations in neighbor countries. The space segment consists of 3 geostationary satellites to transmit the correction data [P. Teunissen and Montenbruck, 2017].

2.5.5 MSAS

The Multi-functional Satellite Augmentation System (MSAS) is the Japanese satellite-based augmentation system. MSAS was declared operational in 2007 and supports the augmentation of the GPS L1 signal. The ground segment consists of six Ground Monitor Stations (GMSs) to collect information on the signals and use two Master Control Stations (MCSs) to process the data. The correction data is distributed via two geostationary Multifunctional Transport Satellites (MTSATs), the MTSAT-1R and MTSAT-2. It is planned to perform a system update to support QZSS and Area Navigation (RNAV) with MSAS-V2, add additional GEO satellites and GMSs, support Localizer Performance with Vertical guidance (LPV) aircraft approaches with MSAS-V3 (from 2023

onwards) and support in future dual frequency and multi-constellation SBAS with MSAS-V4 [Saito, 2019].

2.5.6 GAGAN

The GPS-Aided GEO Augmented Navigation (GAGAN) is the Indian satellite-based augmentation system. The system consisted of 15 Indian Reference Stations (INRESs), 2 Indian Master Control Centers (INMCCs) and 3 Indian Navigational Land Uplink Stations (INLUSs) in 2017. The space segment should cover 5 geostationary satellites which distribute the correction data over India. Lateral guidance for aircraft became operational in 2014 and the vertical guidance in 2015 [P. Teunissen and Montenbruck, 2017].

2.5.7 Other SBAS

The Republic of Korea intends to develop its own SBAS system Korean Augmentation Satellite System (KASS). The system should consist of 5 or more reference stations, 2 central processing centers, 4 uplink stations and 2 geostationary satellites. A preliminary service was planned for 2020 [P. Teunissen and Montenbruck, 2017].
South/Central America and the Caribbean intend a SBAS system called Solucion de Aumentacion para Caribe Centro y Sudamerica (SACCSA). SACCSA is an ICAO project with the contributing member states Argentina, Bolivia, Colombia, Costa Rica, Guatemala, Panama, Spain, Venezuela and Corporacion Centroamerica de Servicios de Navegacion Aerea (COCESNA) [ESA, 2018].

3 BDPE in Context of State-of-the-Art Positioning

This chapter gives an overview of state-of-the-art positioning methods, of positioning methods where research is currently ongoing and how DPE is placed in context of the latest methods. All methods aim to improve the user Position Velocity and Time (PVT) estimate, which is corrupted by natural, unintentional or intentional error sources. Thus, the chapter is concluded with a short discussion on error sources in GNSS in context of DPE/BDPE.

3.1 State-of-the-Art Positioning Methods

In the last decades many GNSS signal processing and positioning algorithms have been implemented and proposed to improve one or more of the performance parameters listed in chapter 1.1. Common state-of-the-art and future technological improvements in GNSS are briefly summarized in the next paragraphs.

Single Point Positioning (SPP) is the most common positioning method which is used since GNSS became available. This method relies on the code pseudorange measurement of the GNSS receiver, which is a range measurement from the user to the satellite. Based on triangulation and known position of the satellites, the PVT of the user can be estimated by means of a Least Squares (LSQ) solution. This fundamental approach is discussed in detail in chapter 5.8.1. The positioning accuracy depends on the system UERE budget, which depends on the broadcast clock and ephemeris, on the residual ionospheric and tropospheric delays, on the receiver noise and resolution and on multipath. The 1-σ Residual Sum of Squares (RSS) error is about 7.1 m for the GPS SPS and about 1.4 m for the PPS [Kaplan and Hegarty, 2006, Chap. 7.2.8]. Some well-known concepts can be used to improve the code pseudorange based SPP solution: (1) The code measurements can be smoothed with carrier phase measurements, which reduces the code noise and thus the position noise. (2) Dual frequency measurements allow to eliminate the ionosphere, one of the most dominant error sources. This method removes a bias of the position solution but increases the measurement noise and thus the position noise. (3) Ionospheric and tropospheric delays can be accounted by models

such as Klobuchar, which reduces the position bias caused by the atmosphere. SPP is the most fundamental positioning method and used in every GNSS receiver. [Kaplan and Hegarty, 2006], [Misra and Enge, 2010].

Differential GNSS (DGNSS) is a differential positioning method and is also known as Differential GPS (DGPS), but which considers GPS only. DGNSS aims to improve the accuracy by usage of correction data from a reference station or reference receiver. This method allows to significantly (1) reduce the satellite clock error from 2 m to 0.0 m (RMS), (2) reduces the satellite ephemeris prediction error in LOS from 2 m to 0.1 m (RMS), (3) reduces the error caused by the ionospheric delay (zenith) from 2-10 m to 0.2 m (RMS), and reduces the error caused by the tropospheric delay (zenith) from 2.3-2.5 m to 0.2 m (RMS). Errors caused by multipath (code 0.5-1 m and carrier 0.5-1 cm in a clean environment) and receiver noise (code 0.25-0.5 m and carrier 1-2 mm (RMS)) cannot be removed with DGNSS, because multipath is uncorrelated between antennas and receiver noise is uncorrelated between receivers. The above-mentioned reduction in errors can only be achieved, if the reference station is in proximity of about 10 km regarding the user and the delay of the correction data is below 10 seconds. With DGNSS a position accuracy less than 1 m can be achieved. DGNSS is typically applied in professional survey or aviation receivers, or with applications where an improved and robust position estimate is required [Kaplan and Hegarty, 2006], [Misra and Enge, 2010].

Receiver Autonomous Integrity Monitoring (RAIM) aims to improve the integrity of a position solution by performing a Fault Detection (FD) on processed GNSS signals. With this method the GNSS receiver is able to detect a corrupt signal autonomously, without any external information. Hereby, the method of Fault Detection and Exclusion (FDE) allows to continue the operation even if a faulty signal was detected. RAIM relies on four steps, a (1) preliminary step computing the navigation solution, (2) executing the fault detection mechanism, (3) isolation of faulty satellites and (4) protection level computation. RAIM is typically applied in professional aviation or backbone infrastructure receivers, or other safety-critical applications where a higher level of integrity is required. The development of autonomous driving vehicles pushes also the research for RAIM algorithms in context with carrier-based positioning methods [ESA, 2018].

Assisted GNSS (AGNSS), formerly also known as Assisted GPS (AGPS), aims to improve the TTFF, accuracy and sensitivity. The method should support GNSS receivers in difficult environments like urban canyons or indoors. The architecture is similar to DGNSS with using correction data from a reference receiver, but AGNSS provides a variety of assistance data. AGNSS receivers can be supported with (1) almanac and ephemeris data, with (2) correction data and with (3) navigation data bits. The support with almanac and

ephemeris data allows a receiver to determine all available satellites with just having a rough knowledge about the time. This allows a receiver to reduce the TTFF because the navigation data does not need to be decoded and a receiver in very challenging environmental conditions can focus only on available satellites. The correction data from a reference receiver helps to improve the accuracy of the position estimate, based on the same principle as DGNSS. If the receiver has knowledge about the navigation data bits in near real-time, long coherent integration times up to 2 seconds can be employed by performing a databit wipeoff prior the correlation, which significantly improves the sensitivity of the receiver. The assistance data is typically distributed via the Internet, e.g. using Local Area Network (LAN), Wireless Local Area Network (WLAN), Global System for Mobile communications (GSM), 3G, 4G, 5G or other links. AGNSS was initially applied in mass-market receivers which are integrated in mobile phones or similar devices, but is nowadays also employed in professional and R&D receivers [Misra and Enge, 2010].

Real Time Kinematics (RTK) aims to increase the position accuracy by making use of ambiguous but accurate carrier phase measurements of a GNSS signal. Therefore, RTK follows a DGNSS approach and uses reference data from a nearby real or virtual reference station with known position to resolve this ambiguity, e.g. by using the Least Squares Ambiguity Decorrelation Adjustment (LAMBDA) method [P. J. G. Teunissen, 2014]. It is a relative method with respect to the used reference station. The reference data is typically delivered to the RTK receiver via internet connection, geostationary satellite-link or terrestrial Radio Frequency (RF) links. It is possible to use a Virtual Reference Station (VRS), where the reference data is virtually generated from a network solution (network of GNSS reference stations). The achieved accuracy is in the centimeter range, whereas the convergence time is within some seconds. This method is available with professional or R&D GNSS receivers, whereas proprietary or open commercial services exist to deliver the necessary reference data [Henkel, Mittmann, and Iafrancesco, 2016], [Vollath et al., 2000b], [Vollath et al., 2000a], [Henkel and Sperl, 2016].

Precise Point Positioning (PPP) also aims to increase the position accuracy by making use of carrier phase measurements of a GNSS signal. Therefore, PPP uses precise clocks and orbits (precise ephemeris) and accurate atmospheric correction data (ionosphere and troposphere) calculated from a global network. The correction data can be accessed via an internet connection or commercially available geostationary satellite links. The commercial service of Galileo will also provide PPP correction and authentication data, whereas the correction data is transmitted using all Galileo satellites on the E6-B band. The major benefit compared to state-of-the-art commercial services is, that the necessary correction data is available through MEO satellites with a good worldwide coverage. A worldwide coverage with a good visibility to geostationary satellites is not possible due to the low elevation at high-

latitude regions, which causes easily broken transmission links. The achieved accuracy is in the sub-decimeter level, but the convergence time is typically large compared to RTK with up to half an hour. But the convergence time can be significantly reduced if using a dual- or triple frequency approach, down to the minutes or several seconds level. This method is available with professional or R&D GNSS receivers and proprietary or open commercial services exist and will be deployed to deliver the necessary correction data [Basile et al., 2018], [Leandro et al., 2011], [X. Chen et al., 2011], [Zang, Li, and Shen, 2017].

Sensor Fusion aims to increase the accuracy, continuity, Time To Re-Fix (TTRF) and robustness of the PVT by incorporating additional (ideally complementary) sensor information. The most common approach the fusion of GNSS with relative measurements of an Inertial Navigation System (INS), because it delivers ideal complementary measurements of accelerations and rotation rates with respect to an inertial reference frame [Wendel, 2007; Groves, 2013]. Furthermore, INSs are self-contained systems which are not affected by the outside world, in contrast to GNSS receivers which depend on the received signal quality. GNSS/INS systems can be loosely, tightly and ultra-tightly coupled [Hwang et al., 2011]. A loosely coupled system update the relative Inertial Measurement Unit (IMU) measurements with a PVT solution [Wang et al., 2017], a tightly coupled system uses for the update pseudorange and Doppler measurements [Garc, 2018] whereas an ultra-tightly (deeply) coupled system additionally aid the receiver internal tracking loops using the IMU measurements [Niedermeier et al., 2010; Ban et al., 2014]. But there exist several other sensors which deliver absolute or relative position or attitude information. Some commonly used absolute sensors for positioning are RF signals e.g. from mobile network, WLAN or Bluetooth [Pany, Winkel, et al., 2010]. The most common used sensors for relative positioning are barometric sensors supporting the height estimate, optical sensors for attitude, position and velocity determination, odometer sensors together with wheel angle sensors for relative positioning in cars or sensor fusion with Light Detection and Ranging (LIDAR) systems [Sánchez and Gómez, 2018; Fernández et al., 2010]. The most common method for sensor fusion is a Kalman filter or Extended Kalman Filter (EKF), basically due to its low complexity and computational efficiency. The Kalman filter is discussed in chapter 4.2 and the Extended Kalman filter in chapter 4.3. Sensor fusion is widely used and can be found in the professional GNSS market e.g. for tilted surveying applications or aviation systems as well as in the mass market and R&D segment.

Vector Tracking (VT) aims to improve the accuracy, continuity, and robustness of a GNSS receiver. "The signal tracking is performed using receiver tracking loops which continuously align internally generated replica signals to the received signals. From these tracking loops the signal parameters of interest can be derived, which allow in a further step the estimation of the position,

velocity and time. In vector mode, the navigation processor controls the code and carrier Numerically Controlled Oscillator (NCO) replacing the tracking loops. A major advantage of this method is that once a good PVT solution is available, all GPS signals are continuously tracked even under weak (or no) signal conditions" [Pany and Eissfeller, 2006]. The major drawback of vector tracking is, that the presence of a fault in one channel will affect all the other channels and possibly leads to receiver instability or loss of lock on all satellites [Lashley and Bevly, 2009]. The method exploits its benefits in degraded signal environments and shows an increased robustness during jamming and spoofing attacks. The method is discussed in more detail in chapter 5.9. Beside R&D GNSS receivers it is not totally clear, if the method is generally utilized in professional and mass market GNSS receivers due to less publications of proprietary processing methods. But due to patents it is strongly assumed that vector tracking is applied in ultra-tightly coupled GNSS-INS receivers for integrated aircraft systems [Broderick and Grove, 2006], in professional surveying and non-surveying receivers [Zhodzishsky and Ashjaee, 2001] as well as in military systems.

Beamforming aims to improve the accuracy, continuity, authentication and robustness of a GNSS receiver. This signal processing method generates an antenna aperture which suppresses signals retrieved from an unexpected Direction of Arrival (DOA), such as multipath signals or interference [Viandier et al., 2008; Fernández-Prades, Arribas, and Closas, 2016]. Beamforming can be exploit using antenna arrays or synthetically with a single antenna and known motion. The synthetic beamforming method, also called Synthetic Aperture Processing (SAP), is based on a spatial movement of a single GNSS antenna, same as the principle of Synthetic Aperture Radar (SAR), which stands in contrast to multi-phased array antennas having an instantaneous spatial separation. Whereas multi-phased array antennas need to be well calibrated and accurately know their orientation, the synthetic approach with a single antenna needs a well-known trajectory and time over the beamforming interval. The key step to create a synthetic antenna aperture is to project the retrieved signal on an internally generated and expected phase signature. In a GNSS receiver this step can also performed in the post-correlation domain. This method allows to effectively detect and eliminate multipath and spoofing signals. Based on the fact that the method also allows to discriminate the DOA of GNSS signals, it is also one of the most reliable methods to authenticate GNSS signals, as it is practically impossible to send modified signals from the true spatial direction or generate a modified signal with a faked DOA without knowledge of the exact attitude or motion of the spoofed receiver. SAP was investigated within an ultra-tightly coupled GNSS-INS system in [Dampf, Gruber, and Pany, 2013] and analyzed for multipath and spoofing detection and mitigation using a rotating antenna in [Dampf, Pany, Baer, et al., 2016; Dampf, Pany, Bär, et al., 2017]. It was shown that the method

is capable of removing effectively the multipath on code and carrier phase measurements and thus can be used e.g. for fixed mounted reference stations to deliver reliable and authenticated correction data to all of its clients or using the method to allow RTK/PPP receivers enter multipath prone environments. The method is currently further investigated to bring it to embedded devices and was patented in [Faragher, Couronneau, and Crockett, 2017].

Direct Position Estimation (DPE) is a rather new GNSS positioning technique which aims to improve the sensitivity, continuity, integrity and robustness of a GNSS receiver. The method was introduced in [Closas, Fernández-Prades, and Fernández–Rubio, 2007; Closas, 2009] and in comparison to state of the art receivers, which use a two steps approach for positioning (synchronization and trilateration) and which track each GNSS signal independently, a DPE receiver estimates the PVT in a single step directly from the signal samples [Closas, Fernández-Prades, Bernal, et al., 2008]. The method directly tracks the PVT solution which allows to collectively process all available GNSS signals and thus exploit a significant tracking gain of $G = 10 \log 10(N)$ dB, where N is the number of GNSS signals [Closas and Gusi-Amigó, 2017]. If combined with Bayesian nonlinear filters — like particle filters — the method is called BDPE, which allows for coping with multi-modal probability distributions and avoids the linearization step to convert correlation values into pseudoranges [Dampf, Frankl, and Pany, 2018]. Since the method operates in the PVT domain, the fusion with additional sensors and side information is more intuitive and allows e.g. the incorporation of probabilistic maps to the position estimation process. Due to the significantly increased sensitivity and ability to derive a PDF for the estimated PVT, which allows also for integrity measures, the method is a strong candidate to be exploited in future GNSS receivers. The drawback of the method comes with higher processing complexity, the need of a rough initial PVT and knowledge about the ephemeris data. The method is currently only implemented in R&D GNSS receivers.

The listed methods briefly summarize some major advances in GNSS since the last decades, whereas this work investigates in the realization of BDPE in a commercial software-based GNSS receiver using a particle and grid-based Bayesian filter and perform an analysis on the obtained PDFs.

3.2 Bayesian Direct Position Estimation

As stated in [Dampf, Frankl, and Pany, 2018], the PVT estimate of a GNSS receiver is sometimes not sufficiently accurate, in particular in difficult environments such as urban areas, forests or indoors. In such environments, the observations do not follow a Gaussian distribution. In ideal (open sky)

conditions the PVT solution can be described as closely to Gaussian distributed [Misra and Enge, 2010; Van Diggelen, 1998; Viandier et al., 2008; Bin Ahmad, Sahmoudi, and Macabiau, 2014; Zhu et al., 2018], but deformed and non-Gaussian observations lead to diverge from Gaussian distributed PVT solutions. Thus, the PVT estimation in difficult environments can benefit from Sequential Monte Carlo (SMC) methods because they consider all available statistical information in the estimation process.

Particle filters [Kitagawa, 1996; Kanazawa, Koller, and Russell, 1995] belong to the group of non-parametric Bayesian filters and are an implementation of an SMC method [Arulampalam et al., 2002]. Thus, they allow for nonlinear and non-Gaussian distributed system and observation models. A performance comparison between a particle filter and a EKF operated in a nonlinear and non-Gaussian environment shows, that improved position estimates can be expected when using a particle or grid-based filter, but with the drawback of a computationally intensive processing [Gordon, Salmond, and Smith, 1993]. But this assumption is not generally true, the presence of a performance improvement depends on the non-linearities in combination with the variance of the state estimate and especially, if there are relevant multi-modalities. The application of particle filters in the field of PVT estimation can mostly be found in research. Often, particle filters are applied in tracking multiple objects e.g. [MacCormick and Blake, 1999]. For this purpose, particle filters are used to combine different sensors with the GNSS receiver PVT estimate or the receiver observables, the pseudorange, Doppler and carrier phase. For instance, the shadow matching algorithm is based on a particle filter that aims to improve the positioning results in dense urban areas by fusing three-dimensional geometry information of buildings with the PVT estimates from GNSS signals [Roi and Boaz Ben, 2014]. In [Gentner et al., 2012], the indoor positioning results are improved by a particle filter that fuses PVT estimates from GNSS signals with high power 4G Long Term Evolution (LTE) mobile network signals. Furthermore, in [Hafner, 2015] a particle filter is used to improve the position estimate to support visual impaired people by fusing non-Gaussian distributed probabilistic maps with PVT solutions from GNSS.

Apart from these investigations that combine GNSS PVT estimates with other sensors, particle filters and grid-based filters are also applied in BDPE, that aims to estimate the PVT of a GNSS receiver directly from the signal samples or correlation values. All previous related work on DPE use a summation of the correlation function in the PVT domain, which is a valid approach but not a probabilistic description. Non-parametric filters used for BDPE, like a particle or grid-based filter, require for optimal usage a probabilistic description of the measurements. The development of such an optimal probabilistic description of the measurements and the corresponding mathematical framework is a

part of this work. An overview of previous related work on DPE based on the summation of the correlation function is given in the next chapter.

4 Bayesian Filters

Bayes filters nowadays are a common standard in many scientific areas and applications. In a general description a Bayes filter tries to estimate recursively the PDF of the state estimate, which allows in the next step the estimation of the system state and nuisance parameters. The most often and commonly used subtype of a Bayes filter is the Kalman filter, basically due to its simple implementation and computational efficiency. In the navigation domain Kalman filters are often used for different purposes such as PVT estimation from pseudoranges and Doppler observations, Position Velocity Time and Attitude (PVTA) estimation when doing sensor fusion with additional (ideally) complementary sensors - e.g. an IMU - or using a Kalman filter for ambiguity estimation, when dealing with carrier phase based precise positioning techniques such as RTK or PPP.

This chapter describes some fundamental elements for state estimation when dealing with linear and Gaussian as well as non-linear and non-Gaussian state and observation models. First a brief overview of Bayes filter realizations are given, followed by descriptions of the most common filters in navigation. The focus will be on a grid-based and PF, simply because of the important role within this work and to achieve a real-time capable BDPE GNSS receiver implementation. This chapter is stongly aligned to [Arulampalam et al., 2002] and partial contents have been adapted and rewritten.

4.1 Introduction and Overview

All types of non-parametric Bayesian filters aim to estimate the state of a dynamic system by construction of a posterior PDF of the state estimate. The PDF of the state estimate is from now on abbreviated as PDF, if not stated otherwise. To follow this approach, all models need to be available in a probabilistic form. A target system is described by its *state vector*, which contains all relevant information to describe the dynamics of the system. The system state is propagated in time using the *system model*. Usually, a perfect description of the target system is not available, and the *process noise* is used to describe the system model uncertainties. The information about the system state is updated with *measurements*, which are affected by noise. As the system

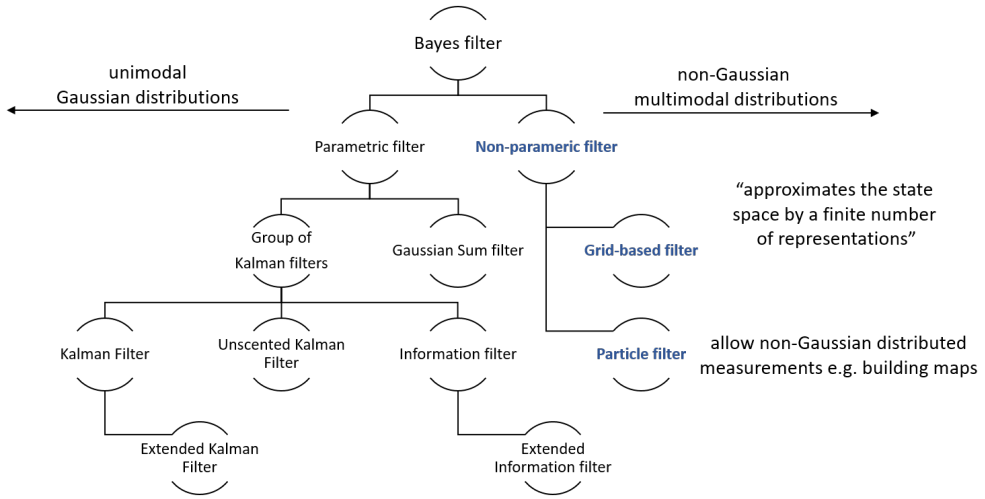

Figure 4.1: Bayes filter realizations which have been redrawn and adapted from [Hafner, 2015, Fig. 3.4]

state mostly cannot be measured directly, the measurements must be related to the system state by a *measurement model*. In most applications it is sufficient to describe the system model and measurement model with linear elements and it is often assumed that all occurring noise is unimodal and Gaussian distributed. The group of parametric filters in Fig. 4.1 covers implementations which follow these assumptions, while the group of non-parametric filters allows also for non-linear system and measurement models and possible non-Gaussian distributed system state and measurements.

The state evolution in time in a discrete form can be described with

$$\mathbf{x}_k = \mathbf{f}_k(\mathbf{x}_{k-1}, \mathbf{v}_{k-1}) \tag{4.1}$$

where $\mathbf{x}_k$ is the state vector of the current epoch, which is propagated from the previous epoch $\mathbf{x}_{k-1}$ using the possibly non-linear function $\mathbf{f}_k(\cdot)$ and the corresponding Independent and Identically Distributed (*i.i.d.*) process noise sequence $\mathbf{v}_{k-1}$, where epoch $k \in \mathbb{N}$. Two different random variables are independent and identically distributed, if they are independent from each other but induce the same probability distribution. The system state is estimated recursively from the measurements using the measurement model

$$\mathbf{z}_k = \mathbf{h}_k(\mathbf{x}_k, \mathbf{n}_k) \tag{4.2}$$

where the measurement for the current epoch $\mathbf{z}_k$ depends on the possibly non-linear function $\mathbf{h}_k(\cdot)$, the current state $\mathbf{x}_k$ and the *i.i.d.* measurement noise

sequence $\mathbf{n}_k$. The Bayesian approach requires to estimate some degree of belief of the state $\mathbf{x}_k$ and thus it is required to construct the PDF $p(\mathbf{x}_k|\mathbf{z}_{1:k})$, where $\mathbf{z}_{1:k}$ contains all measurements up to time k [Arulampalam et al., 2002]. The initial PDF $p(\mathbf{x}_0|\mathbf{z}_0)$ is probably unknown and may be initialized with a Gaussian or uniform distribution under the assumption, that the variance have been chosen large enough to cover the true state. The above described framework allows to estimate $p(\mathbf{x}_k|\mathbf{z}_{1:k})$ in two steps, *prediction* and *update*. Under the assumption that $p(\mathbf{x}_{k-1}|\mathbf{z}_{1:k-1})$ is known, the prediction step allows to estimate the prior PDF at time k using the system model (4.1) by evaluating the Chapman-Kolmogorov equation

$$p(\mathbf{x}_k|\mathbf{z}_{1:k-1}) = \int p(\mathbf{x}_k|\mathbf{x}_{k-1})p(\mathbf{x}_{k-1}|\mathbf{z}_{1:k-1})d\mathbf{x}_{k-1}. \tag{4.3}$$

The first term in the integral $p(\mathbf{x}_k|\mathbf{x}_{k-1})$ refers to the probabilistic model of the state evolution, which is defined by the system model (4.1). If a measurement $\mathbf{z}_k$ at time k becomes available, the prior PDF can be updated using Bayes' rule

$$p(\mathbf{x}_k|\mathbf{z}_{1:k}) = \frac{p(\mathbf{z}_k|\mathbf{x}_k)p(\mathbf{x}_k|\mathbf{z}_{1:k-1})}{p(\mathbf{z}_k|\mathbf{z}_{1:k-1})} \tag{4.4}$$

and with

$$p(\mathbf{z}_k|\mathbf{z}_{1:k-1}) = \int p(\mathbf{z}_k|\mathbf{x}_k)p(\mathbf{x}_k|\mathbf{z}_{1:k-1})d\mathbf{x}_k \tag{4.5}$$

as a normalization constant. The PDF for $p(\mathbf{z}_k|\mathbf{x}_k)$ is defined by the measurement model in (4.2) and describes in a probabilistic form the measurement $\mathbf{z}_k$ in dependency of $\mathbf{x}_k$. After the Bayes update $p(\mathbf{x}_k|\mathbf{z}_{1:k})$ refers to the posterior PDF of the current state. Hereby, the normalizing constant in (4.5) is necessary to normalize the posterior PDF in order to obtain

$$\int p(\mathbf{x}_k|\mathbf{z}_{1:k})d\mathbf{x}_k = 1 \tag{4.6}$$

As stated in [Arulampalam et al., 2002], the recurrence relations in (4.3) and (4.4) form the basis for the optimal Bayesian solution. But the analytical optimal solution is only available in very restrictive cases, for example with the Kalman filter. In case if the analytical solution cannot be evaluated, suboptimal algorithms does exist. Suboptimal approaches such as the Extended Kalman Filter (EKF), Approximate Grid-Based Filter (AGBF) and Particle Filter (PF) approximate the optimal Bayesian solution.

4.2 Kalman Filter

The Kalman filter assumes that both models, the system and measurement model can be written as linear functions and assumes that all occurring noise can be modeled as Gaussian. If these assumptions hold, the posterior PDF can be modeled with the first and second order statistical moments, the mean and variance. As stated in [Arulampalam et al., 2002], this is possible because it was proven that if $p(\mathbf{x}_{k-1}|\mathbf{z}_{1:k-1})$ is Gaussian, also $p(\mathbf{x}_k|\mathbf{z}_{1:k})$ is Gaussian, when following assumptions hold [Ho and Lee, 1964]:

- $\mathbf{v}_{k-1}$ and $\mathbf{n}_k$ are drawn from Gaussian distributions of known parameters.
- $\mathbf{f}_k(\mathbf{x}_{k-1}, \mathbf{v}_{k-1})$ is known and is a linear function of $\mathbf{x}_{k-1}$ and $\mathbf{v}_{k-1}$.
- $\mathbf{h}_k(\mathbf{x}_k, \mathbf{n}_k)$ is a known linear function of $\mathbf{x}_k$ and $\mathbf{n}_k$.

In such a case (4.1) and (4.2) can be rewritten as

$$\mathbf{x}_k = \mathbf{F}_k\mathbf{x}_{k-1} + \mathbf{v}_{k-1} \tag{4.7}$$

$$\mathbf{z}_k = \mathbf{H}_k\mathbf{x}_k + \mathbf{n}_k \tag{4.8}$$

where (4.7) and (4.8) refers to the system model and measurement model, which have been rewritten in a way to include the known linear functions $\mathbf{F}_k$ and $\mathbf{H}_k$ in matrix notation. The Kalman filter assumes that the occurring noise $\mathbf{v}_{k-1}$ and $\mathbf{n}_k$ can be modeled as statistically independent Gaussians with zero mean. This allows to formulate the noise terms $\mathbf{v}_{k-1}$ and $\mathbf{n}_k$ as covariance matrices for the process noise $\mathbf{Q}_{k-1}$ and measurement noise $\mathbf{R}_k$, containing only the statistical second order moment. Both, the linear models and noise terms can be time variant.

Rewritten from [Arulampalam et al., 2002, Eq. (8)-(14)], the Kalman filter defines the following recursive relationship:

$$p(\mathbf{x}_{k-1}|\mathbf{z}_{1:k-1}) = \mathcal{N}(\mathbf{x}_{k-1}; \mathbf{m}_{k-1|k-1}, \mathbf{P}_{k-1|k-1}) \tag{4.9}$$

$$p(\mathbf{x}_k|\mathbf{z}_{1:k-1}) = \mathcal{N}(\mathbf{x}_k; \mathbf{m}_{k|k-1}, \mathbf{P}_{k|k-1}) \tag{4.10}$$

$$p(\mathbf{x}_k|\mathbf{z}_{1:k}) = \mathcal{N}(\mathbf{x}_k; \mathbf{m}_{k|k}, \mathbf{P}_{k|k}) \tag{4.11}$$

where

$$\mathbf{m}_{k|k-1} = \mathbf{F}_k\mathbf{m}_{k-1|k-1} \tag{4.12}$$

$$\mathbf{P}_{k|k-1} = \mathbf{Q}_{k-1} + \mathbf{F}_k\mathbf{P}_{k-1|k-1}\mathbf{F}_k^T \tag{4.13}$$

$$\mathbf{m}_{k|k} = \mathbf{m}_{k|k-1} + \mathbf{K}_k(\mathbf{z}_k - \mathbf{H}_k\mathbf{m}_{k|k-1}) \tag{4.14}$$

$$\mathbf{P}_{k|k} = \mathbf{P}_{k|k-1} - \mathbf{K}_k \mathbf{H}_k \mathbf{P}_{k|k-1} \tag{4.15}$$

and where $\mathcal{N}(x; m, P)$ describes a Gaussian with argument x, mean m and covariance P. By the way, equation (4.12) describes the propagation in time of the previous state $\mathbf{m}_{k-1|k-1}$ to the prior state $\mathbf{m}_{k|k-1}$ using the linear system matrix $\mathbf{F}_k$. Equation (4.13) does basically the same and propagates the previous state covariance matrix $\mathbf{P}_{k-1|k-1}$ via $\mathbf{F}_k$ in time, but additionally add the process noise $\mathbf{Q}_{k-1}$ in order to obtain the prior state covariance matrix $\mathbf{P}_{k|k-1}$. Equation (4.14) and (4.15) depends further on

$$\mathbf{S}_k = \mathbf{H}_k \mathbf{P}_{k|k-1} \mathbf{H}_k^T + \mathbf{R}_k \tag{4.16}$$

$$\mathbf{K}_k = \mathbf{P}_{k|k-1} \mathbf{H}_k^T \mathbf{S}_k^{-1} \tag{4.17}$$

where $\mathbf{K}_k$ defines the Kalman gain, which is the relative weight given to a new measurement. The Kalman gain or weighting is basically derived form the prior state covariance matrix $\mathbf{P}_{k|k-1}$ and measurement noise covariance matrix $\mathbf{R}_k$, which can also be tuned in order to achieve a dedicated filter response. To obtain the posterior state $\mathbf{m}_{k|k}$ in (4.15), the prior state $\mathbf{m}_{k|k-1}$ is updated with the weighted innovation term $(\mathbf{z}_k - \mathbf{H}_k \mathbf{m}_{k|k-1})$, while the innovation term describes the error between the prior state and the current measurement. In (4.15) the Kalman gain is further used to update the state covariance matrix $\mathbf{P}_{k|k-1}$ with a weighted measurement noise covariance matrix in order to obtain the posterior state covariance matrix. As stated in [Arulampalam et al., 2002], if the (highly restrictive) assumption hold, the Kalman filter is an optimal solution an no algorithm can ever do better than the Kalman filter.

4.3 Extended Kalman Filter

If the system model (4.1) and measurement model (4.2) cannot be written in a linearized form as in (4.7) and (4.8), a local linearization may be a sufficient description of the nonlinearity. The EKF is based on this approximation and further assumes that $p(\mathbf{x}_k|\mathbf{z}_{1:k})$ can be approximated by a Gaussian, as given in [Arulampalam et al., 2002, Eq. (22)-(28)], with

$$p(\mathbf{x}_{k-1}|\mathbf{z}_{1:k-1}) \approx \mathcal{N}(\mathbf{x}_{k-1}; \mathbf{m}_{k-1|k-1}, \mathbf{P}_{k-1|k-1}) \tag{4.18}$$

$$p(\mathbf{x}_k|\mathbf{z}_{1:k-1}) \approx \mathcal{N}(\mathbf{x}_k; \mathbf{m}_{k|k-1}, \mathbf{P}_{k|k-1}) \tag{4.19}$$

$$p(\mathbf{x}_k|\mathbf{z}_{1:k}) \approx \mathcal{N}(\mathbf{x}_k; \mathbf{m}_{k|k}, \mathbf{P}_{k|k}) \tag{4.20}$$

where

$$\mathbf{m}_{k|k-1} = \mathbf{f}_k(\mathbf{m}_{k-1|k-1}) \tag{4.21}$$

$$\mathbf{P}_{k|k-1} = \mathbf{Q}_{k-1} + \hat{\mathbf{F}}_k \mathbf{P}_{k-1|k-1} \hat{\mathbf{F}}_k^T \tag{4.22}$$

$$\mathbf{m}_{k|k} = \mathbf{m}_{k|k-1} + \mathbf{K}_k(\mathbf{z}_k - \mathbf{h}_k(\mathbf{m}_{k|k-1})) \tag{4.23}$$

$$\mathbf{P}_{k|k} = \mathbf{P}_{k|k-1} - \mathbf{K}_k \hat{\mathbf{H}}_k \mathbf{P}_{k|k-1} \tag{4.24}$$

and where $\mathbf{f}_k(\cdot)$ and $\mathbf{h}_k(\cdot)$ are nonlinear functions with their local linearization $\hat{\mathbf{F}}_k$ and $\hat{\mathbf{H}}_k$ using the first term of a Taylor series expansion of their nonlinear function, shown as

$$\hat{\mathbf{F}}_k = \left. \frac{d\mathbf{f}_k(x)}{dx} \right|_{x=\mathbf{m}_{k-1|k-1}} \tag{4.25}$$

$$\hat{\mathbf{H}}_k = \left. \frac{d\mathbf{h}_k(x)}{dx} \right|_{x=\mathbf{m}_{k|k-1}} \tag{4.26}$$

$$\mathbf{S}_k = \hat{\mathbf{H}}_k \mathbf{P}_{k|k-1} \hat{\mathbf{H}}_k^T + \mathbf{R}_k \tag{4.27}$$

$$\mathbf{K}_k = \mathbf{P}_{k|k-1} \hat{\mathbf{H}}_k^T \mathbf{S}_k^{-1} \tag{4.28}$$

In general, it is possible to use also higher order terms of the Taylor series expansion, but due to a higher complexity this is not commonly done. The EKF still assumes that $p(\mathbf{x}_k|\mathbf{z}_{1:k})$ can be approximated by a Gaussian. If the true density is a non-Gaussian, the EKF does not perform well and a grid-based or particle filter yield to an improved performance. In case of just significant non-linearities but still Gaussian distributions it is expected, that the Unscented Kalman Filter (UKF) performs better than the EKF.

4.4 Unscented Kalman Filter

The UKF uses a number of deterministic distributed support points (sigma points) selected from the Gaussian approximation $p(\mathbf{x}_k|\mathbf{z}_{1:k})$, which are propagated through the true non-linear functions. These support points are used in a second step to re-estimate the Gaussian approximation. Due to the fact, that the non-linearity of the measurement and state propagation is approximated more accurately, the UKF better estimates the parameters of the Gaussian approximation and perform better as the EKF. For the UKF it is not necessary to build the Taylor series expansion and calculate the Jacobians, which can be difficult or even not possible, if the non-linear functions are not differentiable. More details on the UKF can be found in [Gustafsson and Hendeby, 2012], [Wan and Van Der Merwe, 2000] and [Menegaz et al., 2015].

4.5 Approximate Grid-Based Filter

Grid-based methods use an discrete finite state space $\mathbf{x}_{k-1}^i$ which is decomposed into a grid of N_s cells (or grid-points) $i = 1, \ldots, N_s$, whereas each cell i is represented by a state vector $\mathbf{x}_{k-1}$. From this discrete grid the approximation to the posterior PDF at time $k-1$ is given in [Arulampalam et al., 2002, Eq. (33)] with

$$p(\mathbf{x}_{k-1}|\mathbf{z}_{1:k-1}) \approx \sum_{i=1}^{N_s} w_{k-1|k-1}^i \delta(\mathbf{x}_{k-1} - \mathbf{x}_{k-1}^i) \tag{4.29}$$

where $\delta(\cdot)$ is the Dirac delta measure. Substitution into (4.3) and (4.4) leads to

$$p(\mathbf{x}_k|\mathbf{z}_{1:k-1}) \approx \sum_{i=1}^{N_s} w_{k|k-1}^i \delta(\mathbf{x}_k - \mathbf{x}_k^i) \tag{4.30}$$

$$p(\mathbf{x}_k|\mathbf{z}_{1:k}) \approx \sum_{i=1}^{N_s} w_{k|k}^i \delta(\mathbf{x}_k - \mathbf{x}_k^i) \tag{4.31}$$

where

$$w_{k|k-1}^i \triangleq \sum_{j=1}^{N_s} w_{k-1|k-1}^j p(\overline{x}_k^i|\overline{x}_{k-1}^j) \tag{4.32}$$

$$w_{k|k}^i \approx \frac{w_{k|k-1}^i p(\mathbf{z}_k|\overline{x}_k^i)}{\sum_{j=1}^{N_s} w_{k|k-1}^j p(\mathbf{z}_k|\overline{x}_k^j)} \tag{4.33}$$

Equation (4.32) and (4.33) describe the approximate prior and posterior state probability, where $\overline{x}_{k-1}^j$ denotes the center of the jth cell. In general, for each $\overline{x}_{k-1}^j$ an integral over the region of this cell (grid-point) must be evaluated, as in more detail shown in [Arulampalam et al., 2002, Eq. (36) and (37)]. To simplify and to keep the computational complexity low, $w_{k|k}^i$ is evaluated at the center of each corresponding cell $\mathbf{x}_k^i$ and thus is a discrete approximation to the true continuous state space. In order to get a reasonably good approximation to the continuous state space, a sufficiently dense grid must be used. In case of dealing with higher dimensionality of the state space, the computational cost increases exponentially with the number dimensions. Furthermore, the grid can only cover a finite state space and a drawback of this grid-based method is,

that the grid cannot be distributed unevenly in order to give greater resolution in high probability regions, if no prior knowledge is used. This work uses a grid-based filter for the analysis of the PDF of the state estimate. Grid-based filters are often used in image or map processing applications.

4.6 Particle Filter

The basic idea of a particle filter is to recursively construct the posterior Probability Density Function (PDF) based on a set of random samples with associated weights. From this posterior samples the PDF, statistical parameters as well as the state estimate can be derived. A generic particle filter relies on the concept of Sequential Importance Sampling (SIS) and can be realized with three major steps, *prediction*, *update* and *resampling*.

Sequential Importance Sampling (SIS) As stated in [Arulampalam et al., 2002], the SIS algorithm is a Monte Carlo (MC) method that forms the basis for most sequential MC filters developed over the past decades. This Sequential Monte Carlo (SMC) method is known from literature as bootstrap filtering [Gordon, Salmond, and Smith, 1993], as condensation algorithm [MacCormick and Blake, 1999], particle filtering [Carpenter, Clifford, and Fearnhead, 1999] and survival of the fittest in [Kanazawa, Koller, and Russell, 1995]. The idea of the SIS is to describe the posterior PDF by a set of randomly chosen weighted samples. Thereby, the randomly chosen samples can also follow a defined PDF in order to increase the sample density in regions of interest. If a sufficient large number of samples is used, the Monte Carlo characterization becomes an equivalent representation of the functional description of the posterior PDF [Arulampalam et al., 2002].

In general and as given in [Arulampalam et al., 2002, Eq. (40)], the posterior density at time k can be approximated as

$$p(\mathbf{x}_{0:k}|\mathbf{z}_{1:k}) \approx \sum_{i=1}^{N_s} w_k^i \delta(\mathbf{x}_{0:k} - \mathbf{x}_{0:k}^i) \tag{4.34}$$

if the weights are normalized to $\sum_{i=1}^{N_s} w_k^i = 1$. The equation in (4.34) is the discrete weighted approximation to the true posterior $p(\mathbf{x}_{0:k}|\mathbf{z}_{1:k})$. The approximate posterior filtered density simplifies in the sequential case to

$$p(\mathbf{x}_k|\mathbf{z}_{1:k}) \approx \sum_{i=1}^{N_s} w_k^i \delta(\mathbf{x}_k - \mathbf{x}_k^i). \tag{4.35}$$

An important statement in [Arulampalam et al., 2002] is, that it can be shown that the approximation in (4.35) approaches the true posterior density $p(\mathbf{x}_k|\mathbf{z}_{1:k})$ for $N_s \rightarrow \infty$.

The principle of importance sampling draws a set of samples ξ from a known importance density $q(\cdot)$ such that $x^i \sim q(x), i = 1, ..., N_s$, from which the true posterior density $p(\mathbf{x}_k|\mathbf{z}_{1:k})$ is reconstructed. Hereby, $q(\cdot)$ is used to distribute the samples x^i according to a known distribution, most likely to place more samples in regions of higher interest. For the sequential case with a dependency only on the previous epoch, it was shown in [Arulampalam et al., 2002, Eq. (48)] that the weight update can be rewritten to

$$w_k^i \propto w_{k-1}^i \frac{p(\mathbf{z}_k|\mathbf{x}_k^i)p(\mathbf{x}_k^i|\mathbf{x}_{k-1}^i)}{q(\mathbf{x}_k^i|\mathbf{x}_{k-1}^i, \mathbf{z}_k)} \tag{4.36}$$

where $q(\cdot)$ acts as a normalization step in (4.36) to account for the introduced sampling distribution. This normalization step is required, as the sampling distribution itself influences the resulting posterior PDF.

The idea for the choice of the importance density is to select a probability density, which is close to the unknown but expected posterior PDF. The closer the importance density is to the true PDF, the more samples constructively contribute to the reconstruction, because less samples are wasted in low probability areas. The optimal importance density is defined to be

$$q(\mathbf{x}_k|\mathbf{x}_{k-1}^i, \mathbf{z}_k)_{opt} = p(\mathbf{x}_k|\mathbf{x}_{k-1}^i, \mathbf{z}_k) \tag{4.37}$$

which has the drawback, that it must be possible to resample from $p(\mathbf{x}_k|\mathbf{x}_{k-1}^i, \mathbf{z}_k)$ and to evaluate the integral over the new state, where both steps are typically not straight forward [Arulampalam et al., 2002]. The evaluation of the optimal importance density is only possible for two cases, if (1) x_k is from a finite set and thus sampling from $p(\mathbf{x}_k|\mathbf{x}_{k-1}^i, \mathbf{z}_k)$ becomes possible and (2) if $p(\mathbf{x}_k^i|\mathbf{x}_{k-1}, \mathbf{z}_k)$ is Gaussian. But in many cases an analytical evaluation is not possible and methods exist to construct suboptimal approximations, such as local linearization techniques [Doucet, Godsill, and Andrieu, 2000]. A convenient and common way is to set the importance density to the prior such as

$$q(\mathbf{x}_k|\mathbf{x}_{k-1}^i, \mathbf{z}_k) = p(\mathbf{x}_k|\mathbf{x}_{k-1}^i) \tag{4.38}$$

Inserting (4.37) in (4.36) leads to

$$w_k^i \propto w_{k-1}^i p(\mathbf{z}_k|\mathbf{x}_k^i) \tag{4.39}$$

The choice of the importance density is a crucial design step in a particle filter, whereas (4.39) is commonly used due to its simple implementation [Arulampalam et al., 2002].

Degeneracy and Resampling A common problem of the SIS is the degeneracy problem, as it was shown in [Doucet, Godsill, and Andrieu, 2000] that the variance of the importance weights can only increase. This leads to particles which have almost zero weight and having neglectable contribution to the approximation $p(\mathbf{x}_k|\mathbf{z}_{1:k})$. A measure of the degeneracy is the effective sample size N_{eff}, which was introduced in [Bergman, 1999] and [Liu and R. Chen, 1998] and is given in [Arulampalam et al., 2002, Eq. (50)] as

$$N_{eff} = \frac{N_s}{1 + \mathrm{Var}(w_k^{*i})} \tag{4.40}$$

where $w_k^{*i} = p(\mathbf{x}_k^i|\mathbf{z}_{1:k})/q(\mathbf{x}_k^i|\mathbf{x}_{k-1}^i, \mathbf{z}_k)$ is the 'true weight'. As it cannot be evaluated exactly, an estimate is given in [Arulampalam et al., 2002, Eq. (51)] by

$$\widehat{N_{eff}} = \frac{1}{\sum_{i=1}^{N_s}(w_k^i)^2} \tag{4.41}$$

where w_k^i is the normalized weight from (4.36). It is noted, that $N_{eff} \leq N_s$ and that a small N_{eff} corresponds to severe degeneracy. Basically, there are two methods to overcome this degeneracy phenomenon.

If degeneracy of the particle cloud is observed and $\widehat{N_{eff}}$ drops below a defined threshold, the method of resampling can be applied. The idea of resampling is to eliminate particles with low weights and concentrate on particles with high weight. Therefore, the method generates a new set of $\{\mathbf{x}_k^{i*}\}_{i=1}^{N_s}$ by resampling from an approximate discrete representation

$$p(\mathbf{x}_k|\mathbf{z}_{1:k}) \approx \sum_{i=1}^{N_s} w_k^i \delta(\mathbf{x}_k - \mathbf{x}_k^i) \tag{4.42}$$

such that $\Pr(\mathbf{x}_k^{i*} = \mathbf{x}_k^j) = w_k^i$. The new distribution equals the distribution of $p(\mathbf{x}_k|\mathbf{z}_{1:k})$ using *i.i.d.* samples with reset weights $w_k^i = \frac{1}{N_s}$. In other words, the same probability distribution is represented with another set of *i.i.d.* particles of equal weights, which leads to a dense concentration of particles at higher probabilities. Such a resampling procedure can be implemented with $O(N_s)$ operations [Carpenter, Clifford, and Fearnhead, 1999; Ripley, 1987].

Realization of a Particle Filter A generic particle filter which uses the optimal importance density can be realized in three steps, the

(1) *Prediction* step, which propagates the particle states from the previous state $\mathbf{x}_{k-1}$ to the prior state $\mathbf{x}_k$ and adds the process noise according to the system model given in (4.1)
(2) *Update* step, which updates the weights w_k^i in (4.39) of the prior states according to the measurement model given in (4.2)
(3) *Resampling* step, which is triggered at each iteration or if $\widehat{N_{eff}}$ in (4.41) drops below a defined threshold in order to prevent degeneracy and to keep particles in high probability areas of the true posterior PDF.

It should be noted, that the approximation to the true posterior PDF need to account for both, the weights w_k^i of the particles and their distribution $p(\mathbf{x}_k|\mathbf{z}_{1:k})$, if no resampling step was conducted. Therefore, a weighted histogram is a possibility to retrieve the posterior PDF from weighted samples. The resampling step can be interpreted as shifting the information about the PDF from the weights to the distribution of the samples. After the resampling step, all weights have the same weight and do not contribute to the representation of the PDF. This further means, that after resampling all information about the filter history and PDF is contained in the sample distribution. This implies, that after resampling and a weight update, the weights represent the unfiltered shape of the posterior PDF.

5 Fundamentals of GNSS Receivers

This chapter covers some necessary fundamentals of GNSS and receivers and is strongly aligned to [P. Teunissen and Montenbruck, 2017, Chap. 14]. Sections have been reformulated and figures have been adapted to cover the basic knowledge needed for the implemented BDPE receiver. Detailed explanations and GNSS receiver principles can also be found in [Misra and Enge, 2010; Borre et al., 2007; Kaplan and Hegarty, 2006; Pany, 2010].

5.1 Generic Receiver Architecture

A generic architecture of GNSS receivers is shown in Fig. 5.1. Different realizations of receivers depending on the application exist: Receivers can be fully integrated on a hardware chip to focus on size and power consumption or being purely implemented in software to achieve highest flexibility and processing performance, but all share the same fundamental architecture. As shown in Fig. 5.1, a typical receiver consists of a GNSS capable antenna which gathers the navigation signals transmitted from satellites or pseudolites. In the RF front-end the gathered analog signal r is conditioned, downconverted to a more workable Intermediate Frequency (IF) and digitized to r_{IF}. Then, a receiver performs two steps, synchronization and trilateration. For the synchronization step the digital samples enter a channelized structure, where each signal is acquired and tracked individually. The acquisition block searches for available GNSS signals and deliver coarse synchronization parameters, the code delay $\hat{\tau}$ and Doppler $\hat{f}_d$. The acquisition is performed by doing a serial search (Tong) or applying Fast Fourier Transform (FFT) techniques. These coarse synchronization parameters are used to initialize the tracking loops. The tracking loops keep track on the GNSS signal by using the auto-correlation principle. Hereby the Delay Locked Loop (DLL), Frequency Locked Loop (FLL) and Phase Locked Loop (PLL) track and refine the parameters $\hat{\tau}$, $\hat{f}_d$ and give an estimate of the carrier phase $\hat{\phi}$. The correlation of an incoming signal with an internally generated replica delivers the correlation values P, from which the synchronization parameters can be derived. Furthermore, the correlation values are used to demodulate the navigation message, which contains almanac and ephemeris data delivering information about the position/velocity of the satellites. Data bits and frames are counted

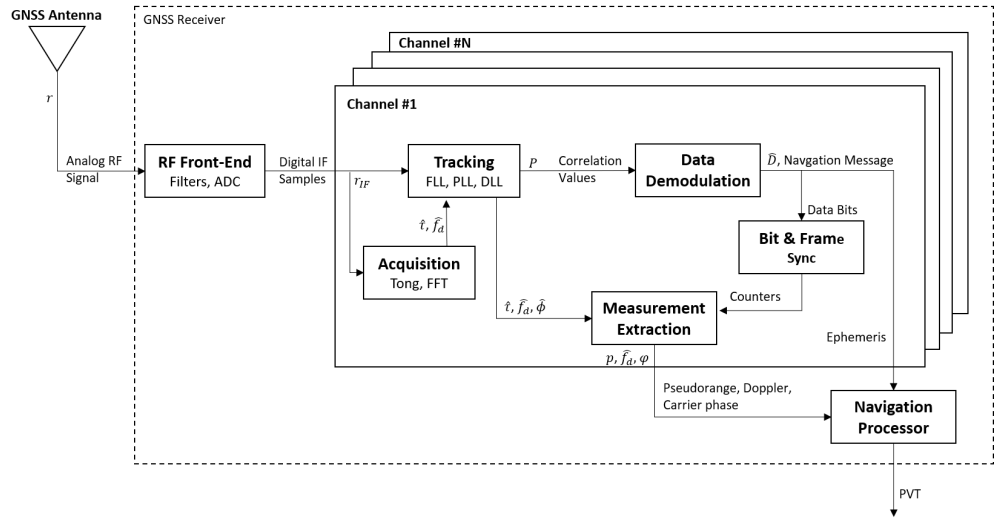

Figure 5.1: Generic architecture of a GNSS receiver showing in detail the tracking channels. Each GNSS signal is tracked in a tracking channel and the maximum number of supported tracking channels N is typically a key performance parameter of GNSS receivers. Redrawn and adapted from [P. Teunissen and Montenbruck, 2017, Fig. 14.3].

to align the integration period of the auto-correlation with navigation data bit boundaries and to obtain the pseudorange p from the code delay estimate $\hat{\tau}$, which include the geometric distance from the satellite to the receiver, the satellite and receiver clock errors, atmospheric delays and hardware delays. The navigation processor uses the code pseudorange, Doppler and the carrier pseudorange estimate from each tracking channel together with the ephemeris data to obtain a PVT solution using the principle of trilateration.

5.2 Transmit and Received Signal Model

The very first step in GNSS is the generation of a GNSS signal on a satellite. Such a GNSS signal with a generic multiplexing scheme based on Quadrature Phase Shift Keying (QPSK) transmitted from the antenna of a satellite in one frequency band can be modeled as given in [P. Teunissen and Montenbruck, 2017, Eq. (14.1)] with a constant power as given in [Misra and Enge, 2010, Eq. (11.1)] with

$$\begin{aligned} s(t) &= \sqrt{2P_{\text{tmt},c}}D_c(t)C_{\text{PRN},c}(t)\cos(2\pi f_L t) \\ &\quad + j\sqrt{2P_{\text{tmt},s}}D_s(t)C_{\text{PRN},s}(t)\sin(2\pi f_L t) \end{aligned} \tag{5.1}$$

where P_{tmt} is the transmit signal power, s and c is the subscript for the cosine (In-phase) and sine (Quadrature) component, $D \in [-1, 1]$ the navigation data symbol with a symbol duration of T_{sym} in (s), $C_{\text{PRN}} \in [-1, 1]$ the PRN spreading code sequence with a chip duration of T_c in (s), f_L the carrier frequency in the L-band in (Hz), t the time at generation in (s) and j the imaginary number. It should be noted, that (5.1) is written in the common complex notation, which allows to apply Euler's identity and represent the signal in an exponential notation which simplifies to study the Fourier series and Fourier transforms, whereas the actually generated and transmitted signal is just the real valued sum of the In-phase and Quadrature component. The signal is separated in two components, the cosine and sine component. The signal power defines beside other factors the positioning accuracy, which should not vary and is kept constant. This constraint not allows for Amplitude Modulation (AM) schemes for the model in (5.1) and thus the symbols equal data bits with an amplitude of 1 (± 1 for data channels and $+1$ for pilot channels). Pilot channels are channels without a navigation data message, which allow receivers for longer integration times and to achieve higher sensitivity. Without usage of data bit removal or prediction techniques, the navigation symbol duration T_{sym} defines the maximum (coherent) integration time T in (s) for GNSS receivers. The model in (5.1) covers the majority of broadcast GNSS signals, whereas others like Alternative Binary Offset Carrier (AltBOC) and Code Shift Keying (CSK) are at least similar [P. Teunissen and Montenbruck, 2017]. Due to the similarity the model can be easily adapted e.g. to represent a BOC modulation scheme or time-multiplexed signals by modifying the code sequence C_{PRN}.

The received signal gathered by the GNSS antenna can be modeled as

$$r(t) \quad = \quad \sum_{i=1}^{N} a_i e^{j\phi_{0;i}} s_i(t - \tau_i) + n_{\text{RF}}(t) \tag{5.2}$$

where s_i is the signal from the i-th visible satellite, a_i is the attenuation factor of the signal power and $n_{\text{RF}}(t)$ is the additive noise component. The propagation time from the i-th satellite to the antenna is expressed as code delay τ_i in (s) and $\phi_{0;i}$ is the carrier phase delay in (rad). The received signal is a superposition on N gathered GNSS signals. For the case that a single signal is considered, a more refined model is given in [P. Teunissen and Montenbruck, 2017, Eq. (14.3)] and in [Misra and Enge, 2010, Eq. (11.2)] as

$$
\begin{aligned}
r_{\mathrm{RF}}(t;\tau,\phi_0,f_d,P_{\mathrm{rcv},c},P_{\mathrm{rcv},s}) = \\
\sqrt{2P_{\mathrm{rcv},c}}D_c(t-\tau)C_{\mathrm{PRN},c}(t-\tau)\cos(2\pi(f_L+f_d)t+\phi_0) \\
+ j\sqrt{2P_{\mathrm{rcv},s}}D_s(t-\tau)C_{\mathrm{PRN},s}(t-\tau)\sin(2\pi(f_L+f_d)t+\phi_0) + n_{\mathrm{RF}}(t) \quad (5.3)
\end{aligned}
$$

where f_L is the signal center frequency in the L-Band in (Hz), f_d is the carrier Doppler shift in (Hz) and P_{rcv} is the received signal power. $n_{\mathrm{RF}}(t)$ is the band-limited Additive White Gaussian Noise (AWGN) having a one-sided Power Spectral Density (PSD) N_0 and a bandwidth determined by the RF chain inside the receiver front-end. The subscript RF is an identifier for the carrier. Before converting the analog signal to a digital signal using an Analog Digital Conversion (ADC), the signal is pre-conditioned. Therefore, the signal passes through bandpass filters to cut out the frequency ranges of interest. The real signal must be sampled with at least the Nyquist frequency or at least half the Nyquist frequency in case of a complex signal, but which is difficult for GNSS frequencies above 1 GHz due to the required high sampling rates. Thus, the carrier RF is mixed down to a more workable IF. The downconverted, digital and band-limited signal in the discrete time domain for a single signal component e.g. the cosine carrier, which is related to the In-phase component of the signal carrying the relevant information (e.g. GPS L1 C/A), can be written without the quadrature component as

$$
\begin{aligned}
r_{\mathrm{IF}}(k;\tau,\phi,f_d,C) &= \sqrt{2C}D(T_s k-\tau)C_{\mathrm{PRN},c}(T_s k-\tau)\cos(2\pi(f_{\mathrm{IF}}+f_d)T_s k+\phi) \\
&\quad + n_{\mathrm{IF}}(k) \quad (5.4)
\end{aligned}
$$

where C is the received signal power P_{rcv} including the the antenna gain and the implementation losses, $k = [0, 1, 2, ...]$ is the sample index with the sample interval T_s in (s) and sampling frequency $f_s = \frac{1}{T_s}$ in (Hz) such that $t = kT_s$. $n_{\mathrm{IF}}(k)$ is the corresponding noise at IF, which is assumed to be white with a power spectral density of N_0. Note that ϕ is the carrier-phase offset in addition to the Doppler shift. The signal parameters of interest are τ, f_d and ϕ, which are estimated by the receiver tracking loops.

5.3 Correlator Model

The receiver internal tracking loops continuously try to align a internally generated replica signal with the incoming GNSS signal. Therefore, the tracking loops take the output from the correlators, the complex valued correlation

value. The correlators correlate the received signal r_{IF} and the internally generated signal $\hat{r}_{\mathrm{IF}}$, whereas the integration time T defines the correlation length in (s). With the assumption that the navigation data bit does not change during the integration interval and without use of the amplitude, the local generated replica at the IF can be written as given in [P. Teunissen and Montenbruck, 2017, Eq. (14.5)] with

$$\hat{r}_{\mathrm{IF}}(k;\hat{\tau},\hat{\phi},\hat{f}_d) = 2C_{\mathrm{PRN}}(T_s k-\hat{\tau})\exp\{j(2\pi(f_{\mathrm{IF}}+\hat{f}_d)T_s k+\hat{\phi})\} \quad (5.5)$$

The correlation process between the true signal r_{IF} and the replica signal $\hat{r}_{\mathrm{IF}}$ can be defined as

$$r_{\mathrm{IF}}(k) = r_{\mathrm{IF}}(k;\tau,\phi,f_d,C) \quad (5.6)$$
$$\hat{r}_{\mathrm{IF}}(k) = \hat{r}_{\mathrm{IF}}(k;\hat{\tau},\hat{\phi},\hat{f}_d) \quad (5.7)$$

with

$$P(\Delta\tau,\Delta f_d,\Delta\phi) = \mathrm{corr}(r_{\mathrm{IF}}(k),\hat{r}_{\mathrm{IF}}(k)) = \sum_{k=1}^{M} r_{\mathrm{IF}}(k)\hat{r}_{\mathrm{IF}}(k) \quad (5.8)$$

and with $\Delta\tau = \tau - \hat{\tau}$, $\Delta f_d = f_d - \hat{f}_d$ and where $\mathrm{corr}(x,y)$ is the correlation function of x and y, M is the number of samples within the integration time $T = MT_s$ and with T_s being the sample interval. The evaluation of the correlation in (5.8) is given in [P. Teunissen and Montenbruck, 2017, Chap. 14.2.3] and leads to the complex valued correlation value, which can be modeled as given in [P. Teunissen and Montenbruck, 2017, Eq. (14.18)] with

$$\begin{aligned} P(\Delta\tau,\Delta f_d,\Delta\phi) &= \sqrt{2TC/N_0}DR(\Delta\tau)\mathrm{sinc}(\Delta f_d T)\exp\{j\Delta\phi\}+\eta \\ &= I + jQ \end{aligned} \quad (5.9)$$

with

$$R(\Delta\tau) = \sum_{k=1}^{M} C_{\mathrm{PRN}}(T_s k-\tau)C_{\mathrm{PRN}}(T_s k-\hat{\tau}) \quad (5.10)$$
$$\mathrm{sinc}(\Delta f_d T) = \frac{\sin(2\pi\Delta f_d T)}{2\pi\Delta f_d T} \quad (5.11)$$

whereas the parameter of interest are modeled as the deviation from the true, given as $\Delta\tau = \tau - \hat{\tau}$, $\Delta f_d = f_d - \hat{f}_d$ and $\Delta\phi = \phi - \hat{\phi}$. $R(\cdot)$ defines the

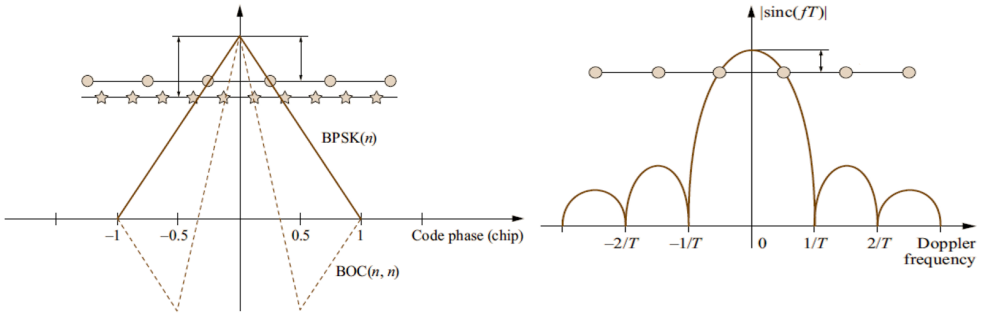

Figure 5.2: Code correlation function (left) and Doppler correlation function (right). Hereby, n defines the chip and subcarrier rate normalized to 1023 MCPS, T the coherent integration time and f the Doppler frequency. The circles and stars indicate correlation points for the acquisition and illustrate, that the correlator spacing need to consider the signal type and influences the detection probability. Figures from [P. Teunissen and Montenbruck, 2017, Fig. 14.6 and 14.7].

correlation function resulting from the PRN code sequence, e.g. a triangle shaped function with the maximum of 1 at $\Delta\tau = 0$ for the BPSK signal of the GPS C/A at L1. The $\text{sinc}(\cdot)$ results from the Doppler deviation of the replica signal to the true, also with it's maximum of 1 at $\Delta f_d = 0$. Note that the width of the sinc-function depends on the integration time T. The code and Doppler correlation function is illustrated in Fig. 5.2. It is assumed that the baseband signal component has a normalized noise component as given in (5.14). The C/N_0 is the carrier-to-noise ratio in (dB-Hz). I and Q represent the post-correlation in-phase and quadrature components which are defined as

$$I = \sqrt{2TC/N_0}DR(\Delta\tau)\text{sinc}(\Delta f_d T)\cos(\Delta\phi) + \eta_I \tag{5.12}$$

$$Q = \sqrt{2TC/N_0}DR(\Delta\tau)\text{sinc}(\Delta f_d T)\sin(\Delta\phi) + \eta_Q \tag{5.13}$$

with the definition of the normalized noise being

$$E[\eta_I^2] = E[\eta_Q^2] = 1 \tag{5.14}$$

whereas $E[x]$ is the expected value of x. The correlation value described by the correlator model in (5.9) is a fundamental value in each GNSS receiver, because from this value all measurements to obtain a PVT solution can be extracted.

5.4 Acquisition

Once a GNSS receiver is switched on, it has no knowledge about its position and current visible satellites (cold start). The receiver starts a signal search and tries to acquire GNSS signals. Therefore, the receiver either selects randomly satellites or selects satellites based on some pre-knowledge, e.g by rough position and almanac (warm start) or ephemeris and recently accurate receiver position and time (hot start). The acquisition stage determines rough synchronization parameters, the code phase $\hat{\tau}$ and Doppler $\hat{f}_d$. These estimates are used to initialize the receiver tracking loops. The search is based on a hypothesis test with the hypothesis

H_0: Signal is not present
H_1: Signal is present.

The test compares the signal power defined as

$$|S|^2 = I^2 + Q^2 = 2TC/N_0 \;\; 2R(\Delta\tau)^2 \text{sinc}(\Delta f_d T)^2 + \eta_{I,Q} \tag{5.15}$$

with the noise

$$\eta_{I,Q} = \eta_I^2 + \eta_Q^2 \tag{5.16}$$

$$E[\eta_{I,Q}] = E[\eta_I^2 + \eta_Q^2] = 2 \tag{5.17}$$

to a defined threshold γ. Therefore, the signal search varies $\hat{\tau}$ and $\hat{f}_d$ until a defined search space (typically a grid in code phase and Doppler direction) has been completely searched through or till a signal was found. Note that in (5.15) the data bit vanished due to the squaring operation which allows a non-coherent integration, but still needs to be accounted to avoid missed detections. Symbol transitions within the integration time can lead to a significant decrease in the amplitude of the correlation result. The longer the integration time the more sensitive is the acquisition unit. But as mentioned before, the maximum coherent integration time is given by the symbol duration or limited resources on the receiver. The integration time can be extended beyond the coherent integration time by non-coherently summing up squared coherent batches such that

$$S_{nc} = \sum_{n=1}^{\nu} |S_n|^2 \tag{5.18}$$

with

$$|S|^2 = I^2 + Q^2 \tag{5.19}$$

where ν is the number of accumulated batches and S is the signal power of (5.9). The total integration time is given with $T_{tot} = T\nu$. Hereby the hypotheses are defined as H_0: $(S_{nc} < \gamma)$ and H_1: $(S_{nc} \geq \gamma)$. The relationship between coherent and non-coherent integration to the obtained Signal-to-Noise Ratio (SNR) is given in [P. Teunissen and Montenbruck, 2017, Eq. (14.31)] with

$$\text{SNR} = \frac{2\nu TC/N_0}{\sqrt{4\nu}} = TC/N_0\sqrt{\nu} \tag{5.20}$$

The SNR is typically expressed in (dB), which refers to the signal power and noise power in a given bandwidth. The SNR can also be expressed as $\text{SNR} = S - N$ with S and N being the signal and noise in (dBm) or (dBW). The C/N_0 defines the carrier-to-noise density usually expressed in (dB-Hz) and refers to the ratio of the carrier power and the noise power per unit bandwidth [Joseph, 2010]. Doubling the coherent integration time doubles the SNR, whereas doubling the number of non-coherent summations results in a gain of $\sqrt{2}$. This is basically caused by the squaring loss, as also the noise is increased with the squaring operation.

This section only briefly discusses the basic principles of an acquisition unit and there exist a variety of methods to efficiently search for signals in space (e.g. Tong, pre-correlation FFT, matched filter structures), methods to detect weak signals and methods to aid the acquisition process by incorporating pre-knowledge such as receiver position, velocity, time, almanac or ephemeris data. More details about acquisition units can be found in [P. Teunissen and Montenbruck, 2017; Misra and Enge, 2010; Borre et al., 2007; Kaplan and Hegarty, 2006; Pany, 2010].

5.5 Tracking

The tracking unit refines the coarse estimates of the acquisition unit and keeps track on the GNSS signals. Hereby each GNSS signal is tracked individually. A generic tracking loop, which can be applied to track the code phase (DLL), Doppler (FLL) and carrier phase (PLL), is shown for the time domain in Fig. 5.3. The variable θ in the figure is a placeholder for the code phase τ, Doppler f_d and carrier phase ϕ.

The correlator block calculates a set of correlation values $P_{I,Q}$ based on (5.8) which can be modeled as in (5.9). The output of the correlation block is a set of typically three correlation values with their in-phase (I) and quadrature (Q) components for an Early, Prompt and Late version of the code $[I_E, Q_E, I_P, Q_P, I_L, Q_L]$. The early and late version is shifted by the correlator spacing, which is a key design parameter for the DLL and commonly chosen

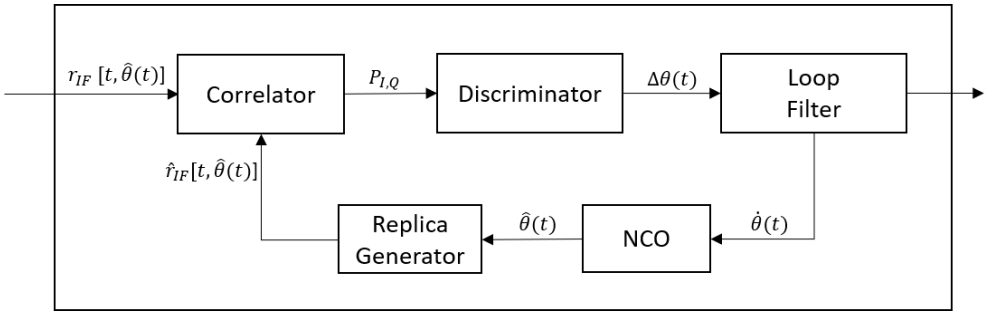

Figure 5.3: Generic structure of a GNSS receiver tracking loop in the time domain. Redrawn and adapted from [P. Teunissen and Montenbruck, 2017, Fig. 14.9].

to be a narrow correlator with e.g. $d = 0.1$ chips. The prompt correlator is placed at $d = 0$ chips. Depending on the tracked signal or for multipath estimation and mitigation techniques, a higher number of correlators might be used. As an example for tracking a Galileo BOC signal additionally, a Very Early and Very Late correlator is placed onto the side lobes of the correlation function in order to properly identify and jump to the main peak, if necessary (bump jumping). The correlator spacing d influences the DLL tracking loop performance and multipath error envelope [P. Teunissen and Montenbruck, 2017, Chap. 14.4.4 and Chap. 15.5, Fig. 15.10].

The discriminators calculate based on the correlation values the alignment error between the internally generated replica $\hat{r}_{\mathrm{IF}}$ and the received signal r_{IF}. This is done for the code phase, Doppler and carrier phase. The simplest definitions of the discriminators for a DLL, FLL and PLL are

$$\begin{aligned} \Delta\tau &= \frac{\alpha_d}{2(2-d)} \frac{I_E^2 + Q_E^2 - I_L^2 - Q_L^2}{I_P^2 + Q_P^2} \\ \Delta f_d &= \frac{(\Delta\phi_k - \Delta\phi_{k-1})}{T} \\ \Delta\phi &= \tan^{-1}\left(\frac{Q_P}{I_P}\right) \end{aligned} \tag{5.21}$$

where $\Delta\tau, \Delta f_d$ and $\Delta\phi$ is the code phase error, Doppler error and carrier phase error, α_d is a modulation scheme dependent factor to achieve unity slope of the resulting discriminator function and k defines the correlation epoch. $\Delta\tau$ is calculated from the imbalance of the early and late correlation value, Δf_d from the carrier phase change from the previous to the current epoch and $\Delta\phi$ is the carrier phase obtained from the complex phasor of the prompt I and Q correlation value. The above shown discriminator functions belong to the simplest formulations and consider the data signal component of GNSS

signals for the DLL and PLL, but there exist several other definitions with different characteristics. The goal of the tracking loop is to steer the tracking error $\Delta\theta$ to $\Delta\theta = 0$, as illustrated in Fig. 5.3.

The S-curve refers to the discriminator function in dependency of the code phase error $\Delta\tau$. The evaluation of the S-curve is illustrated in Fig. 5.4. The shape of the S-curve influences the DLL tracking loop response. The tracking point, the point where the replica signal is aligned with the incoming signal, is shown by zero crossing point. The S-curve is typically linear around the tracking point with a unity slope.

The tracking loop filter gets as input the noisy alignment error information $\Delta\theta$. The loop filters are usually designed to be of first, second or third order and allow to adapt for changes in distance, velocity and accelerations which occur in LOS direction of the tracked GNSS signal. The loop filters are designed to output the rate of change $\dot{\theta}$ to the NCO, as shown in Fig. 5.3.

The NCO acts as an integrator and is responsible to deliver the best estimate $\hat{\theta}$ to the replica signal generator. The estimate of the code phase $\hat{\tau}$ is used for the PRN code generator of the tracked signal whereas the Doppler and carrier phase estimate $\hat{f}_d$ and $\hat{\phi}$ are used to generate the cos/sin carrier waveform of the internal generated replica.

The three tracking loops (DLL, FLL, PLL) depend on each other and thus they can be described as a Multiple Input Multiple Output (MIMO) system. Based on the reason that such systems are difficult to describe and analyze, the individual tracking loops are characterized with the constraint that the others are perfectly aligned, which simplifies the system description to a Single Input Single Output (SISO) system. More details about receiver tracking units can be found in [P. Teunissen and Montenbruck, 2017; Misra and Enge, 2010; Borre et al., 2007; Kaplan and Hegarty, 2006; Pany, 2010].

5.6 Synchronization and Data Demodulation

By synchronization and demodulation of the navigation data message $D(t)$ from (5.9), a receiver can obtain all necessary information for positioning (e.g. satellite ephemeris and atmospheric model parameters). The receiver needs for positioning at least an estimate of the distance to the satellite, the pseudorange. This distance is obtained by measuring the travel-time from the satellite to the receiver multiplied with the speed of light. Therefore, the sent time of the signal needs to be known. Per definition the code phase equals the sent time (transmission epoch) modulo the code period. An estimate of the sent time can be calculated from the code phase of the tracked signal and

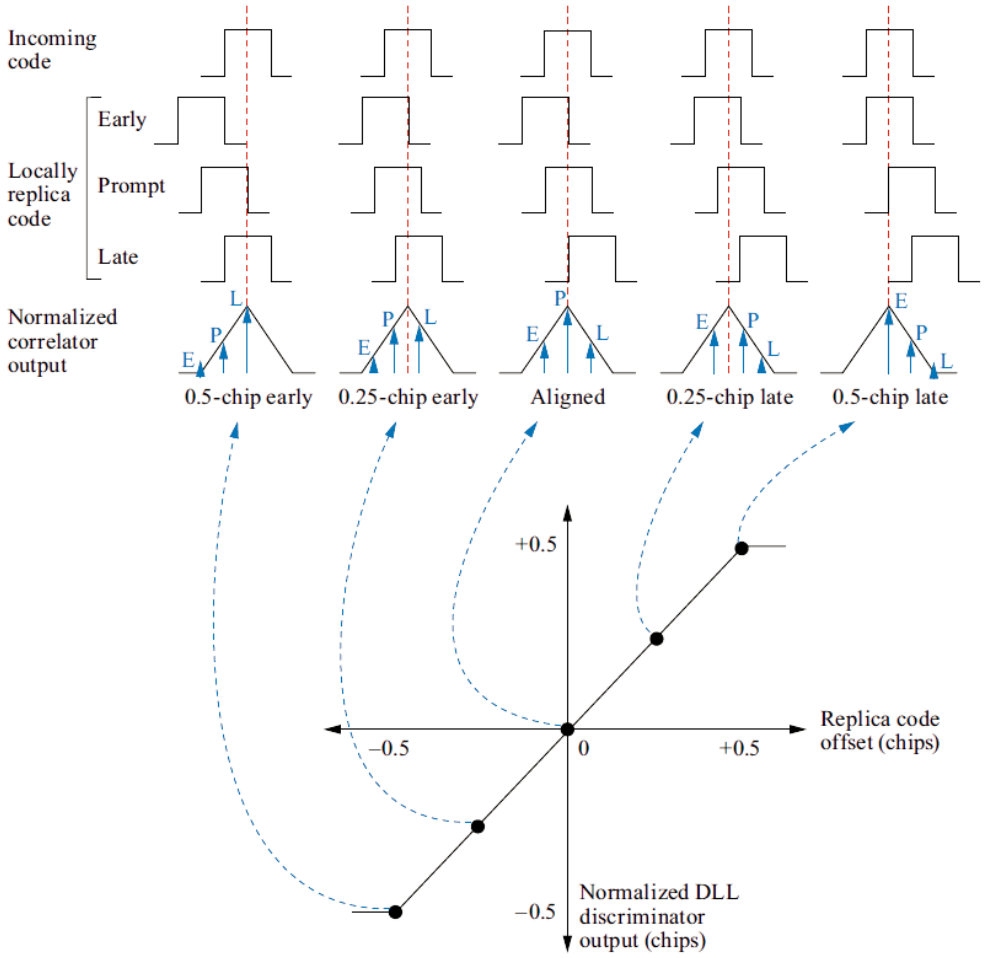

Figure 5.4: Normalized discriminator function (S-curve) of a DLL tracking loop. The upper part of the figure shows the incoming and the early, prompt and late version of the shifted replica signal for correlation and their position on the correlation function. The plot in the lower part of the figure shows the normalized DLL discriminator output. The resulting function is typically linear around the tracking point in the center of the plot. Figure from [P. Teunissen and Montenbruck, 2017, Fig. 4.11].

it's time tag in the navigation message. The DLL continuously steers $\Delta\tau$ to zero and thus the estimated sent time is given as

$$\hat{v}(k) = T_s k - \hat{\tau} \tag{5.22}$$

which follows the true sent time

$$v(k) = T_s k - \tau \tag{5.23}$$

where $t_{rcv} = T_s k$ defines the receiver internal time. The ambiguous code phase equals the difference of the received and sent time modulo the PRN code period (in nominal satellite system time scale). The ambiguity of the code phase can be resolved by the modulated navigation message, which contains a time tag. The data fields in the navigation message describing the time tag define the transmission time of a certain bit/symbol boundary and bit/symbol boundaries typically coincide with PRN code boundaries [P. Teunissen and Montenbruck, 2017, chapter 14.5]. The receiver continuously searches in the data bit stream for a preamble, a defined bit sequence. Once this preamble is found, the receiver can interpret the navigation data bits, extract the sent time and can resolve the ambiguity. There exist also other techniques to resolve the code ambiguity e.g. by resolving it from another tracked signal on a different frequency but from same satellite or performing consistency checks with approximate user coordinates and known satellite ephemeris data [P. Teunissen and Montenbruck, 2017, chapter 14.5]. The most direct way to obtain a data bit can be achieved if a pilot signal is available and phase lock is given. Phase lock means that the carrier phase error $\Delta\phi$ from the discriminator is stable steered towards zero. In such a case the in-phase prompt correlator values $I_{P,k}$ of the data bearing component correspond to the bits or symbols, whereas a positive value is typically assigned to bit '0' and a negative value to bit '1'. Secondly, data bits can be extracted from the prompt correlation values directly, if phase lock of a Costas PLL is achieved on the data signal component. A Costas PLL with the discriminator definition from (5.21) for the phase error is able to deal with data bits and they can be read again from the prompt correlation values $I_{P,k}$. In both cases the preamble also allows to resolve a 180 deg phase ambiguity, which may lead to an inverted bit sequence. In a third case, if the carrier phase cannot be tracked stable by the PLL, the receiver switches to the more robust FLL. But from the FLL the data bits cannot be read directly (no phase lock), but it is possible to detect phase transitions between two epochs as given in [P. Teunissen and Montenbruck, 2017, Eq. (14.61)] using

$$\text{dot}_k = I_k I_{k+1} + Q_k Q_{k+1} \tag{5.24}$$

where the dot-term is positive if the bit sequence remains the same and becomes negative in case of a bit transition. The estimator in (5.24) allows to continue bit estimation for lower $C/N0$, but with the care that a incorrectly detected bit transition flips the complete following bit sequence. The bit error rate can be evaluated analytically, if a stable frequency or phase tracking is assumed. Bit/symbol errors occur because $I_{P,k}$ and $Q_{P,k}$ are nonzero Gaussian random variables. The bit error rate for the PLL is given in [P. Teunissen and Montenbruck, 2017, Eq. (14.62)] as

$$\text{BER}_{\text{PLL}} = \frac{1}{2}\text{erfc}(\sqrt{TC/N_0}) \tag{5.25}$$

and the transition error rate for the FLL is given in [P. Teunissen and Montenbruck, 2017, Eq. (14.63)] as

$$\text{TER}_{\text{FLL}} = \frac{1}{2}\exp(-2TC/N_0) \tag{5.26}$$

In general, the thermal noise contribution does not contribute significantly to the error rates, rather more likely are decoding errors due to occasional blocking of the LOS signal component or fading effects.

More details about signal synchronization and data demodulation can be again found in [P. Teunissen and Montenbruck, 2017; Misra and Enge, 2010; Borre et al., 2007; Kaplan and Hegarty, 2006; Pany, 2010].

5.7 GNSS Measurements

The measurements made by a GNSS receiver are often called observables. As given in [P. Teunissen and Montenbruck, 2017, Chap. (14.6)], primary measurements of the tracking channel are

- the estimated code pseudorange between satellite and receiver
- the estimated Doppler of the received signal
- the estimated carrier phase (carrier pseudorange) of the received signal
- the estimated amplitude (power) of the received signal

These parameters are generated for each tracked signal independently, except for combined tracking of data and pilot signals. The typical output rate of these parameters ranges from 1-20 Hz. The measurements are taken at the same epoch for all tracked channels.

The measured code pseudorange in (m) is given in [P. Teunissen and Montenbruck, 2017, Eq. (14.65)] as

$$p(k) = c\hat{\tau}(k) = c[t_{\mathrm{rx}} - \hat{v}(k)] \tag{5.27}$$

where $t_{\mathrm{rx}} = T_s k$ is the internal receiver time in (s) driven by the sampling rate f_s of the ADC, $\hat{v}(k)$ is the estimated sent time in (s) and c the speed of light in (m/s). The nominal receiver time t_{rx} has an arbitrary offset to the true time, called receiver clock error. This receiver clock error drifts with time according to the quality of the internal clock. The code pseudorange model is given in [P. Teunissen and Montenbruck, 2017, Eq. (14.66)] as

$$p = \rho - c(dt_{\mathrm{rx}} - dt^{\mathrm{sat}}) + I + T + c(d_{\mathrm{rx}} + d^{\mathrm{sat}}) + p_T + \epsilon_{mp} + \epsilon_n \tag{5.28}$$

where ρ defines the geometric distance in (m) between receiver and satellite, dt_{rx} and dt^{sat} are the receiver and satellite clock error in (s), I and T are the ionospheric and tropospheric delay in (m), d_{rx} and d^{sat} are the receiver and satellite hardware delay in (s), p_T covers transient errors of the tracking loop in (m), ϵ_{mp} is the error caused by multipath and ϵ_n is the tracking noise, both in (m). The pseudorange model in (5.28) refers to a single receiver, single satellite, single signal and single frequency. Furthermore, dt^s should account also for relativistic effects and corrections for the antenna phase center are neglected.

The locally generated replica signal as defined in (5.5) has an instantaneous carrier phase of $\hat{\phi}_{NCO}(k)$ defined in (rad) as the argument of the complex exponential [P. Teunissen and Montenbruck, 2017, Chap. (14.6.2)], with

$$\hat{\phi}_{NCO}(k) = 2\pi(f_{\mathrm{IF}} + \hat{f}_d)T_s k + \hat{\phi}(k) \tag{5.29}$$

With this definition the carrier pseudorange measurement in (m) is given in [P. Teunissen and Montenbruck, 2017, Eq. (14.75)] as

$$\varphi(k) = -\lambda \left(\frac{\hat{\phi}_{NCO}(k)}{2\pi} - f_{\mathrm{IF}} T_s k \right) \tag{5.30}$$

where λ defines the carrier wavelength in (m) and is given with $\lambda = c/f_{\mathrm{RF}}$. The corresponding model for the carrier phase in (m) is given in [P. Teunissen and Montenbruck, 2017, Eq. (14.79)] with

$$\varphi = \lambda N + \rho - c(dt_{\mathrm{rx}} - dt^{\mathrm{sat}}) - I + T + c(\delta_{\mathrm{rx}} + \delta^{\mathrm{sat}}) + p_{T'} + \epsilon_{mp'} + \epsilon_{n'} \quad (5.31)$$

where N defines the integer ambiguity of the carrier phase, δ_{rx} and δ^{sat} are the respective frequency dependent hardware delays in (s). The hardware delays are different to the delays in the code pseudorange model due the different frequencies. Note that the sign of the ionospheric delay has changed w.r.t. the code pseudorange model in (5.28). Furthermore, this model neglects antenna phase center corrections and the carrier phase wind-up caused by the orientation difference along the LOS axes of the user and satellite antenna. The carrier phase measurement is in contrast to the code measurement very precise but ambiguous. RTK aims to resolve this unknown integer ambiguity N and enables positioning with sub-centimeter accuracy.

The FLL and PLL are used for carrier tracking, whereas the FLL tracks the carrier frequency and the PLL the carrier phase. Both, the FLL and PLL provide the rate-of-change information of the carrier phase to the carrier NCO, which is used for replica signal generation. The Doppler is defined as the carrier phase change between two consecutive samples, which can be described with $2\pi(f_{IF} + \hat{f}_d)T_s$ and which is a part of the replica signal definition in (5.4). Thus, the Doppler is an internal parameter of the carrier NCO and allows straight-forward to retrieve the Doppler measurement $\hat{f}_d$. The corresponding Doppler model derives from the carrier-phase model via the first time derivative and is defined in (Hz) as

$$f_d = -\frac{1}{\lambda}[\dot{\rho} - c(d\dot{t}_{\mathrm{rx}} - d\dot{t}^{\mathrm{sat}}) + p_{T''} + \epsilon_{mp''} + \epsilon_{n''}] \quad (5.32)$$

For most GNSS applications the atmospheric delay variations and hardware delay variations are neglected, because they vary slowly with time. These variations are only accounted for specific applications where accurate velocity estimates are necessary. The satellite clock drift $d\dot{t}^{\mathrm{sat}}$ is very small, because the satellites are equipped with high grade atomic clocks. The largest contribution to the Doppler is caused by the range rate $\dot{\rho}$ and receiver clock drift $d\dot{t}_{\mathrm{rx}}$.

The signal power of the received signal can be estimated from the in-phase and quadrature component of the prompt correlation value as given in [P. Teunissen and Montenbruck, 2017, Eq. (14.85)] with

$$\widehat{C/N0} = \frac{I_P^2 + Q_P^2 - 2}{2T} \tag{5.33}$$

where T is the integration period. The signal power estimate in (5.33) is valid, if the variance of the noise in the In-Phase and Quadrature channel equals one, as given in (5.14). The signal power estimates are typically very noisy for lower signal strengths and therefore a common approach is to average over longer intervals e.g. 5-10 seconds. It should be noted that transient errors of the tracking loops and misalignments of the replica signal in code and Doppler cause reduction of signal power estimate according to $R(\Delta\tau)$ and $\text{sinc}(\Delta f_d)$.

5.8 Position, Velocity and Time Estimation

The estimation of the user position, velocity and time (PVT) is a central point of a GNSS receiver and is performed in the navigation processor. There exist three different approaches to estimate the user position based on a set of non-linear equations, (1) closed-form solutions, (2) iterative techniques based on linearization and (3) Kalman filtering [Kaplan and Hegarty, 2006]. Formerly, the standard positioning technique was based on LSQ or Weighted Least Squares (WLSQ), whereas the weight depends on the quality of the measurements. Today's GNSS receivers use Kalman filtering techniques for GNSS only solutions and when performing sensor fusion e.g. GNSS+IMU. This chapter discusses the iterative LSQ and WLSQ approach, describes a GNSS only Kalman filtering approach, and briefly mentions a Kalman filter for sensor fusion with the most common combination of GNSS and INS.

5.8.1 Iterative Weighted Least Squares Estimation

The iterative LSQ position and clock error estimation is based on a first order linearization by developing a Taylor series expansion at an approximate user position. Secondary order error sources such as earth rotation compensation, measurement noise, propagation delays and relativistic effects are neglected for the linearization step when building the Jacobi matrix [Kaplan and Hegarty, 2006], but these errors are accounted for when calculating pseudoranges. The iterative LSQ approach describes the estimated (in an idealized case without any error sources the true) user (receiver) position and clock error $\mathbf{x}_{\text{rx}}$ with an approximate component $\hat{\mathbf{x}}_{\text{rx}}$ plus an incremental offset $\boldsymbol{\Delta}\mathbf{x}_{\text{rx}}$, as given by [Kaplan and Hegarty, 2006, Eq. (2.26)] with

$$\mathbf{x}_{\text{rx}} = \hat{\mathbf{x}}_{\text{rx}} + \mathbf{\Delta x}_{\text{rx}} \tag{5.34}$$

where the matrices are defined as

$$\mathbf{x}_{\text{rx}} = \begin{bmatrix} x_{\text{rx}} \\ y_{\text{rx}} \\ z_{\text{rx}} \\ dt_{\text{rx}} \end{bmatrix} \qquad \hat{\mathbf{x}}_{\text{rx}} = \begin{bmatrix} \hat{x}_{\text{rx}} \\ \hat{y}_{\text{rx}} \\ \hat{z}_{\text{rx}} \\ \hat{dt}_{\text{rx}} \end{bmatrix} \qquad \mathbf{\Delta x}_{\text{rx}} = \begin{bmatrix} \Delta x_{\text{rx}} \\ \Delta y_{\text{rx}} \\ \Delta z_{\text{rx}} \\ \Delta dt_{\text{rx}} \end{bmatrix} \qquad \mathbf{r}^{\text{sat},n} = \begin{bmatrix} x^{\text{sat},n} \\ y^{\text{sat},n} \\ z^{\text{sat},n} \end{bmatrix} \tag{5.35}$$

where $\mathbf{r}^{\text{sat},n}$ defines the satellite position of satellite n and dt_{rx} the receiver clock error (time offset to the GNSS system time). The position variables x, y, z are given in meters and the clock error dt_{rx} is given in seconds. The offset of the approximated position and clock error to the estimated position and clock error can be determined directly if $N = 4$, as given in [Kaplan and Hegarty, 2006, Eq. (2.34)], with

$$\mathbf{\Delta x} = \mathbf{H}^{-1}\mathbf{\Delta p} \tag{5.36}$$

where $\mathbf{\Delta x}$ defines the user position and clock error offset to the estimated state, $\mathbf{H}$ defines a matrix characterizing the user-satellite geometry and $\mathbf{\Delta p}$ defines a pseudorange offset matrix with

$$\mathbf{\Delta x} = \begin{bmatrix} \Delta x_{\text{rx}} \\ \Delta y_{\text{rx}} \\ \Delta z_{\text{rx}} \\ -c\Delta dt_{\text{rx}} \end{bmatrix} \qquad \mathbf{H} = \begin{bmatrix} u_x^{\text{sat},1} & u_y^{\text{sat},1} & u_z^{\text{sat},1} & 1 \\ u_x^{\text{sat},2} & u_y^{\text{sat},2} & u_z^{\text{sat},2} & 1 \\ u_x^{\text{sat},3} & u_y^{\text{sat},3} & u_z^{\text{sat},3} & 1 \\ u_x^{\text{sat},n} & u_y^{\text{sat},n} & u_z^{\text{sat},n} & 1 \end{bmatrix} \qquad \mathbf{\Delta p} = \begin{bmatrix} \Delta p_1 \\ \Delta p_2 \\ \vdots \\ \Delta p_n \end{bmatrix} \tag{5.37}$$

where c is the speed of light and $\mathbf{u}^{\text{sat},n} = [u_x^{\text{sat},n}, u_y^{\text{sat},n}, u_z^{\text{sat},n}]$ the unit vector pointing from the approximate user position to the satellite. The unit vector is defined with

$$u_x^{\text{sat},n} = \frac{x^{\text{sat},n} - \hat{x}_{\text{rx}}}{\hat{r}_n} \qquad u_y^{\text{sat},n} = \frac{y^{\text{sat},n} - \hat{y}_{\text{rx}}}{\hat{r}_n} \qquad u_z^{\text{sat},n} = \frac{z^{\text{sat},n} - \hat{z}_{\text{rx}}}{\hat{r}_n} \tag{5.38}$$

$$\hat{r}_n = \sqrt{(x^{\text{sat},n} - \hat{x}_u)^2 + (y^{\text{sat},n} - \hat{y}_u)^2 + (z^{\text{sat},n} - \hat{z}_u)^2} \tag{5.39}$$

The pseudorange offset for satellite n is defined with

$$\Delta p_n = \hat{p}_n - p_n \tag{5.40}$$

where $\hat{p}_n$ defines the approximate pseudorange and p_n the pseudorange measurement as given in (5.27), whereas the pseudorange model is given in (5.28). The approximate pseudorange is calculated with

$$\hat{p}_n = \sqrt{(x^{\text{sat},n} - \hat{x}_{\text{rx}})^2 + (y^{\text{sat},n} - \hat{y}_{\text{rx}})^2 + (z^{\text{sat},n} - \hat{z}_{\text{rx}})^2} + c\hat{d}t_{\text{rx}} \tag{5.41}$$

Typically a GNSS receiver has $N > 4$ satellites in view which lead to an over-determined system and a solution which fits best to the measurements should be found. For that purpose, the principle of LSQ can be used to determine the offset to the approximate position, as given by [Misra and Enge, 2010, Eq. (6.11)] with

$$\mathbf{\Delta x} = (\mathbf{H}^T\mathbf{H})^{-1}\mathbf{H}^T\mathbf{\Delta p} \tag{5.42}$$

This estimate assumes that all pseudorange measurements are of same quality, which is typically not the case. For that purpose, a weighting matrix can be introduced, which rates the quality of each measurement e.g. based on the SNR. The weighting matrix is a diagonal matrix with

$$\mathbf{W} = \begin{bmatrix} w_1 & 0 & 0 & 0 \\ 0 & w_2 & 0 & 0 \\ 0 & 0 & \ddots & \vdots \\ 0 & 0 & \cdots & w_N \end{bmatrix} \tag{5.43}$$

This weight matrix can be used to formulate the WLSQ estimator, as given by [Misra and Enge, 2010, Eq. (6.13)], with

$$\mathbf{\Delta x} = (\mathbf{H}^T\mathbf{W}\mathbf{H})^{-1}\mathbf{H}^T\mathbf{W}\mathbf{\Delta p} \tag{5.44}$$

The iterative estimation process aims to improve the user position with (5.34) as long the improvement drops below a defined threshold. It shall be noted that each iteration lead to (1) a new estimate of the GNSS time, which requires for each satellite a (2) recalculation of the signal transit time, satellite position and corresponding transformations and an update of the (3) geometry matrix $\mathbf{H}$. The convergence is typically very fast and in 2-4 iterations good results can be achieved [Misra and Enge, 2010, Chap. 6.1.1]. The pseudorange residuals for the estimated user position and clock error $\mathbf{x}_{\text{rx}}$ can be obtained by calculating Δp from (5.40) based on the last estimate. The measurement errors (residuals)

$\boldsymbol{\epsilon}_{\text{meas}}$ in LOS direction can be transformed to a position and clock error via the geometry matrix $\mathbf{H}$ with

$$\boldsymbol{\epsilon}_x = \mathbf{H}^{-1}\boldsymbol{\epsilon}_{\text{meas}} \tag{5.45}$$

The velocity and clock drift estimate can be approximated such as done for the position approximation above or can be directly estimated from the Doppler estimates of the receiver tracking loops. The direct estimate of the user velocity and clock drift $\dot{\mathbf{x}}_{\text{rx}}$ is obtained directly if $N = 4$ with

$$\dot{\mathbf{x}}_{\text{rx}} = \mathbf{H}^{-1}\dot{\mathbf{p}}_{\text{rx}} \tag{5.46}$$

With $N > 4$ a LSQ or WLSQ can be used, which is defined as

$$\dot{\mathbf{x}}_{\text{rx}} = (\mathbf{H}^T\mathbf{H})^{-1}\mathbf{H}^T\dot{\mathbf{p}}_{\text{rx}} \tag{5.47}$$

$$\dot{\mathbf{x}}_{\text{rx}} = (\mathbf{H}^T\mathbf{W}\mathbf{H})^{-1}\mathbf{H}^T\mathbf{W}\dot{\mathbf{p}}_{\text{rx}} \tag{5.48}$$

with

$$\dot{\mathbf{x}}_{\text{rx}} = \begin{bmatrix} v_{\text{rx},x} \\ v_{\text{rx},y} \\ v_{\text{rx},z} \\ -cd\dot{t}_{\text{rx}} \end{bmatrix} = \begin{bmatrix} \dot{x}_{\text{rx}} \\ \dot{y}_{\text{rx}} \\ \dot{z}_{\text{rx}} \\ -cd\dot{t}_{\text{rx}} \end{bmatrix} \qquad \dot{\mathbf{p}}_{\text{rx}} = \begin{bmatrix} \dot{p}_{\text{rx},1} \\ \dot{p}_{\text{rx},2} \\ \vdots \\ \dot{p}_{\text{rx},n} \end{bmatrix} \tag{5.49}$$

where $d\dot{t}_{\text{rx}}$ denote the receiver clock drift and $\mathbf{v}_{\text{rx}} = [v_{\text{rx},x}, v_{\text{rx},y}, v_{\text{rx},z}]$ the user velocity. The weight matrix $\mathbf{W}$ has the same definition as in (5.43) but quantifies the quality of the pseudorange rate measurement, e.g. obtained by the FLL /PLL discriminator noise. The pseudorange rate measurement $\dot{p}_n$ of satellite n contains the motion of the satellite $\mathbf{v}^{\text{sat},n}$, the satellite clock drift $d\dot{t}^{\text{sat},n}$ as well as the motion and receiver clock drift of the user $\dot{p}_{\text{rx},n}$. Based on the fact that GNSS satellites use high grade atomic clocks, the satellite clock drift $d\dot{t}^{\text{sat},n}$ can be neglected for all GNSS (neglectable for GPS since the selective availability was disabled) [Misra and Enge, 2010, Chap. (6.2.1)]. The user motion and receiver clock drift $\dot{p}_{\text{rx},n}$ can be measured in LOS direction, as given by [Misra and Enge, 2010, Eq. (6.34)] and above, with

$$\dot{p}_{\text{rx},n} = \dot{p}_n - \mathbf{v}^{\text{sat},n}\mathbf{u}^{\text{sat},n} \tag{5.50}$$

where $\mathbf{u}^{\text{sat},n}$ is the unit vector as defined in (5.38). The pseudorange rate is derived from the Doppler measurement f_d in (Hz) from the receiver tracking loops as defined in (5.32) and above with

$$\dot{p}_n = -f_{d,n}\frac{c}{f_T} \tag{5.51}$$

where f_T is the transmission frequency e.g. L1=1575.42 MHz. The basic equation for (5.51) is given by [Kaplan and Hegarty, 2006, Eq. (2.36)]. This approach assumes that the satellite velocity can be calculated from the orbital model, which is delivered with the satellite ephemeris. The satellite clock drift is also delivered with the ephemeris data, which can be accounted for in (5.51). The user velocity and clock drift is affected by measurement noise and multipath and the computation assumes that the user position and clock error is estimated in advance [Kaplan and Hegarty, 2006, Chap. 2.5].

5.8.2 Kalman Filtering and Sensor Fusion

Apart from LSQ estimation, Kalman Filters (KF) and Extended Kalman Filters (EKF) are used to calculate a filtered navigation solution. The Kalman filter is operated in the PVT domain and assumes linear models and Gaussian distributed measurements. In contrast to the KF, the EKF allows to deal with small non-linearities as it performs an additional linerization step for the calculation of the state covariance matrix and Kalman gain matrix [Wendel, 2007], as indicated by (4.25) and (4.26). The KF and EKF can be used to filter the GNSS only PVT, if no additional sensor is available. For a GNSS only KF two possible implementations exist, (1) the update with a PVT solution e.g. a least-squares or RTK solution or (2) the update with pseudorange and Doppler measurements. The update with pseudorange and Doppler measurements has the benefit, that the state can be updated with less than four measurements. This chapter discusses the required components for the implementation of a PVT KF based on pseudorange and Doppler measurements, and is aligned to the generic description of a KF in chapter 4.2. The state-space representation of a PVT Kalman filter, as defined in (4.7) and (4.8), is

$$\mathbf{x}_k = \mathbf{F}_k\mathbf{x}_{k-1} + \mathbf{Q}_{k-1} \tag{5.52}$$

$$\mathbf{z}_k = \mathbf{H}_k\mathbf{x}_k + \mathbf{R}_k \tag{5.53}$$

with

$$\mathbf{x}_k = \begin{bmatrix}\mathbf{r}_{\mathrm{rx}}\\ \mathbf{v}_{\mathrm{rx}}\\ \mathbf{t}_{\mathrm{rx}}\end{bmatrix} = \begin{bmatrix}x\\ y\\ z\\ v_x\\ v_y\\ v_z\\ dt_{\mathrm{rx}}\\ d\dot{t}_{\mathrm{rx}}\end{bmatrix} \qquad \mathbf{z}_{k,n} = \begin{bmatrix}p_n\\ f_{d,n}\end{bmatrix} \tag{5.54}$$

where $\mathbf{x}_k$ is the estimated user state (PVT) of the current epoch k, $\mathbf{Q}_{k-1}$ the process noise covariance matrix and $\mathbf{R}_k$ the measurement noise covariance matrix. The measurement $\mathbf{z}_{k,n}$ of satellite n consists of the pseudorange measurement p from (5.27) and the Doppler measurement f_d from (5.32). The KF update sequence is given from (4.12) to (4.15) with (4.16) and (4.17) and requires a description of the state propagation (system) matrix $\mathbf{F}_k$ and a description of the measurement (design) matrix $\mathbf{H}_{k,n}$, which are given as

$$\mathbf{F}_k = \begin{bmatrix} 1 & 0 & 0 & T & 0 & 0 & 0 & 0 \\ 0 & 1 & 0 & 0 & T & 0 & 0 & 0 \\ 0 & 0 & 1 & 0 & 0 & T & 0 & 0 \\ 0 & 0 & 0 & 1 & 0 & 0 & 0 & 0 \\ 0 & 0 & 0 & 0 & 1 & 0 & 0 & 0 \\ 0 & 0 & 0 & 0 & 0 & 1 & 0 & 0 \\ 0 & 0 & 0 & 0 & 0 & 0 & 1 & T \\ 0 & 0 & 0 & 0 & 0 & 0 & 0 & 1 \end{bmatrix} \tag{5.55}$$

$$\mathbf{H}_{k,n} = \begin{bmatrix} u_x^{\text{sat},n} & u_y^{\text{sat},n} & u_z^{\text{sat},n} & 0 & 0 & 0 & 1 & 0 \\ 0 & 0 & 0 & u_x^{\text{sat},n} & u_y^{\text{sat},n} & u_z^{\text{sat},n} & 0 & 1 \end{bmatrix} \tag{5.56}$$

where $\mathbf{u}^{\text{sat},n} = [u_x^{\text{sat},n}, u_y^{\text{sat},n}, u_z^{\text{sat},n}]$ is the unit vector as defined in (5.70) pointing to satellite n and T is the update interval (duration of one epoch). In order to calculate the Kalman gain $\mathbf{K}_k$ a description of the process noise $\mathbf{Q}_{k-1}$ and measurement noise $\mathbf{R}_k$ is required. These covariance matrices model the uncertainty in the state propagation model and uncertainty of the measurement given with

$$\mathbf{Q}_{k-1} = \begin{bmatrix} \sigma^2_{\mathbf{Q},x} & 0 & 0 & 0 & 0 & 0 & 0 & 0 \\ 0 & \sigma^2_{\mathbf{Q},y} & 0 & 0 & 0 & 0 & 0 & 0 \\ 0 & 0 & \sigma^2_{\mathbf{Q},z} & 0 & 0 & 0 & 0 & 0 \\ 0 & 0 & 0 & \sigma^2_{\mathbf{Q},vx} & 0 & 0 & 0 & 0 \\ 0 & 0 & 0 & 0 & \sigma^2_{\mathbf{Q},vy} & 0 & 0 & 0 \\ 0 & 0 & 0 & 0 & 0 & \sigma^2_{\mathbf{Q},vz} & 0 & 0 \\ 0 & 0 & 0 & 0 & 0 & 0 & \sigma^2_{\mathbf{Q},clkErr} & 0 \\ 0 & 0 & 0 & 0 & 0 & 0 & 0 & \sigma^2_{\mathbf{Q},clkDft} \end{bmatrix} \tag{5.57}$$

$$\mathbf{R}_k = \begin{bmatrix} \sigma_p^2 & 0 \\ 0 & \sigma_{f_d}^2 \end{bmatrix} \tag{5.58}$$

where exemplary initialization values for $\mathbf{Q}(t_0)$ of the main diagonal components for a commercial-grade C/A code receiver integrated with tactical-grade sensors can be found in [Kaplan and Hegarty, 2006, Chap. 9.2.4.4]

with $\sigma^2_{\mathbf{Q},x,0} = \sigma^2_{\mathbf{Q},y,0} = \sigma^2_{\mathbf{Q},z,0} = 0.01$, $\sigma^2_{\mathbf{Q},vx,0} = \sigma^2_{\mathbf{Q},vy,0} = \sigma^2_{\mathbf{Q},vz,0} = 10^{-5}$, $\sigma^2_{\mathbf{Q},clkErr,0} = 1.1 * 10^{-3}$ and $\sigma^2_{\mathbf{Q},clkDft,0} = 10^{-4}$. It should be noted that the process noise matrix $\mathbf{Q}_{k-1}$ is time dependent and the values above are just an initialization example. The pseudorange and Doppler uncertainty can be an empirical constant, estimated from the discriminator noise or modeled from the $C/N0$. The uncertainty of the state $\mathbf{x}_k$ is described with the covariance matrix $\mathbf{P}_k$, whereas the initial state uncertainty $\mathbf{P}_0$ is given with

$$\mathbf{P}_0 = \begin{bmatrix} \sigma^2_{\mathbf{P},x,0} & 0 & 0 & 0 & 0 & 0 & 0 & 0 \\ 0 & \sigma^2_{\mathbf{P},y,0} & 0 & 0 & 0 & 0 & 0 & 0 \\ 0 & 0 & \sigma^2_{\mathbf{P},z,0} & 0 & 0 & 0 & 0 & 0 \\ 0 & 0 & 0 & \sigma^2_{\mathbf{P},vx,0} & 0 & 0 & 0 & 0 \\ 0 & 0 & 0 & 0 & \sigma^2_{\mathbf{P},vy,0} & 0 & 0 & 0 \\ 0 & 0 & 0 & 0 & 0 & \sigma^2_{\mathbf{P},vz,0} & 0 & 0 \\ 0 & 0 & 0 & 0 & 0 & 0 & \sigma^2_{\mathbf{P},clkErr,0} & 0 \\ 0 & 0 & 0 & 0 & 0 & 0 & 0 & \sigma^2_{\mathbf{P},clkDft,0} \end{bmatrix} \tag{5.59}$$

and need to be defined together with the initial state x_0. It should be noted, that P_k is time dependent and all values will change with time. Just for simplicity only the components on the main diagonal are initialized. An exemplary initialization of the main diagonal components is given in [Kaplan and Hegarty, 2006, Tab. 9.1] with $\sigma^2_{\mathbf{P},x,0} = \sigma^2_{\mathbf{P},y,0} = \sigma^2_{\mathbf{P},z,0} = (20\text{m})^2$, $\sigma^2_{\mathbf{P},vx,0} = \sigma^2_{\mathbf{P},vy,0} = \sigma^2_{\mathbf{P},vz,0} = (10\text{m/s})^2$, $\sigma^2_{\mathbf{P},clkErr,0} = (10^3\text{m})^2$ and $\sigma^2_{\mathbf{P},clkDft,0} = (100\text{m/s})^2$. Typical update rates of the PVT KF are about 1-20 Hz. The GNSS only KF can be extended to consider also accelerations, which requires an extension to 11 states [GPSoft, 2020].

Furthermore, the EKF is nowadays typically used for sensor fusion with an IMU, barometer, magnetometer, odometer or other sensors. The aim of sensor fusion is to find an optimal navigation solution considering all available information, with (ideally) complementary sensors which have uncorrelated error sources. Thus, GNSS is very often combined with an inertial sensor, which measures gyro rates and accelerations, and which is a self-contained system completely independent from external error sources. A GNSS/INS integration with a IMU need also to estimate the attitude e.g. in euler angels with roll ϕ, pitch θ, yaw ψ, accelerometer biases b_a, gyro biases b_g and eventually scale factors s. In such a case the state vector of the KF expands to

$$\mathbf{x_k} = \begin{bmatrix} \begin{bmatrix} \phi & \theta & \psi \end{bmatrix}^{\mathrm{T}} \\ \begin{bmatrix} x & y & z \end{bmatrix}^{\mathrm{T}} \\ \begin{bmatrix} v_x & v_y & v_z \end{bmatrix}^{\mathrm{T}} \\ \begin{bmatrix} t_{clkErr} & t_{clkDft} & \end{bmatrix}^{\mathrm{T}} \\ \begin{bmatrix} b_{a,x} & b_{a,y} & b_{a,z} \end{bmatrix}^{\mathrm{T}} \\ \begin{bmatrix} b_{g,x} & b_{g,y} & b_{g,z} \end{bmatrix}^{\mathrm{T}} \\ \begin{bmatrix} s_x & s_y & s_z \end{bmatrix}^{\mathrm{T}} \end{bmatrix} \tag{5.60}$$

and the corresponding matrices need to be also extended accordingly. Note that a generic description of the KF is given in chapter 4.2 and a generic description of the EKF is given in chapter 4.3. A detailed description of a sensor fusion approach is not part of this work, but [Wendel, 2007] and [Groves, 2013] can be recommended.

5.9 Code/Carrier KF and Vector Tracking

Standard GNSS receivers track the signals individually and there is no coupling between the tracking loops. The signal tracking loop including the code/carrier NCO can be described by a direct-state Kalman filter [Won, Eissfeller, and Pany, 2011]. The measurement update equation for the DLL/PLL/FLL signal tracking loop KF is given in the state-space form in [P. Teunissen and Montenbruck, 2017, Eq. (14.91)] as

$$\hat{\mathbf{x}}_{\mathrm{TL},k} = \mathbf{F}_k \hat{\mathbf{x}}_{\mathrm{TL},k-1} + \mathbf{K}_k \tilde{\mathbf{z}}_{\mathrm{TL},k} \tag{5.61}$$

with

$$\mathbf{x}_{\mathrm{TL},k} = \begin{bmatrix} \tau \\ \phi \\ f_d \\ \dot{f}_d \end{bmatrix} \tag{5.62}$$

where $\mathbf{x}_{\mathrm{TL},k}$ is the state of the tracking loop (subscript TL) at epoch k defined by the code phase τ, carrier phase ϕ, Doppler f_d and Doppler rate $\dot{f}_d$. It should be noted that the estimated Doppler f_d from the updated state vector can be used for the NCO update of the code and carrier tracking loop. The Doppler f_d in (Hz) can be converted to the code rate $\dot{\tau}$ in (chips/s) with a scaling factor $s = f_\tau / f_c$ such that $\dot{\tau} = s f_d$, where f_τ is the chipping rate in (chips/s)

and f_c is the carrier frequency in (Hz) of the signal under consideration. It might be further required to estimate the Ionosphere and rate of change of the Ionosphere to account for differences by the Doppler and code rate. This equation can be set up by the general update equations of a Kalman filter through (4.14) and (4.12), where $\mathbf{x}_{\mathrm{TL},k}$ refers to $\mathbf{m}_{k|k}$. The transition matrix $\mathbf{F}_k$ to propagate the state in time and design (measurement) matrix $\mathbf{H}_k$ to incorporate new measurements are given as

$$\mathbf{F}_k = \begin{bmatrix} 1 & 0 & sT & s\frac{T^2}{2} \\ 0 & 1 & T & \frac{T^2}{2} \\ 0 & 0 & 1 & T \\ 0 & 0 & 0 & 1 \end{bmatrix} \tag{5.63}$$

$$\mathbf{H}_k = \begin{bmatrix} 1 & 0 & 0 & 0 \\ 0 & 1 & 0 & 0 \\ 0 & 0 & 1 & 0 \end{bmatrix} \tag{5.64}$$

where s is the scaling factor from the Doppler to the code rate and T is the integration time. The measurements

$$\tilde{\mathbf{z}}_{\mathrm{TL},k} = \begin{bmatrix} \Delta\tau \\ \Delta\phi \\ \Delta f_d \end{bmatrix} \tag{5.65}$$

are obtained by the discriminator outputs from (5.21), whereas $\tilde{\mathbf{z}}_{\mathrm{TL},k} = (\mathbf{z}_k - \mathbf{H}_k\mathbf{m}_{k|k-1})$ in (4.14) because the discriminators deliver directly the measurement error. The Kalman gain matrix $\mathbf{K}_k = [k_{i,j}]_{4-by-3}$ is computed in the Kalman filters time-varying optimal gain adjustment process as defined in (4.17) or as given in [P. Teunissen and Montenbruck, 2017, Eq. (14.92)].

More advanced receivers make use of the vector tracking concept, which closes the tracking loops via the navigation processor as shown in Fig. 5.5. For vector tracking the navigation processor is typically implemented as a Kalman filter, which is updated by the measurements of the tracking loops. Such a PVT KF is discussed in detail in chapter 5.8.2. Hereby, the tracked state is the PVT solution as given in (5.54). The update of the state is done on a low rate basis e.g. 1 Hz. The required LOS projection from the PVT state to the tracking loop parameters requires knowledge about the ephemeris. The carrier phase-based vector tracking approach is very difficult to realize, because the PVT needs to be accurately known to achieve continuous phase

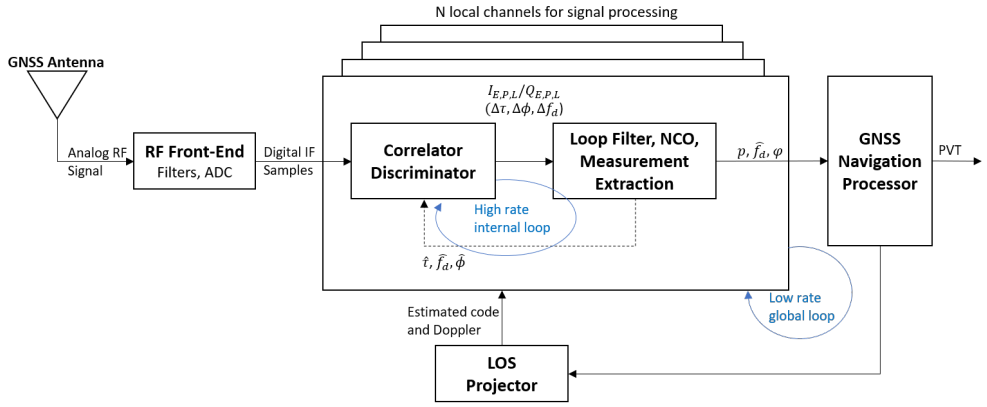

Figure 5.5: Generic structure of a GNSS receiver vector tracking loop. The tracking loops are closed via the navigation processor. Redrawn and adapted from [P. Teunissen and Montenbruck, 2017, Fig. 14.20].

tracking, but can be established as described in [Pany, Falk, et al., 2013]. The classical approach for vector tracking is to implement a DLL/FLL approach with code phase and Doppler only. Therefore, the LOS projection is performed for each satellite n by using the code and Doppler model from (5.28) and (5.32) with

$$\tau_n = \frac{p_n}{c} = \frac{\rho_n}{c} - (dt_{\mathrm{rx}} - dt^{\mathrm{sat},n}) + \frac{I^{\mathrm{sat},n} + T^{\mathrm{sat},n}}{c} + (d_{\mathrm{rx}} + d^{\mathrm{sat},n}) \tag{5.66}$$

and

$$f_{d,n} = -\frac{1}{\lambda}[\dot{\rho}_n - c(d\dot{t}_{\mathrm{rx}} - d\dot{t}^{\mathrm{sat},n})] \tag{5.67}$$

with

$$\rho_n = ||\mathbf{r}^{\mathrm{sat},n} - \mathbf{r}_{\mathrm{rx}}|| \tag{5.68}$$

$$\dot{\rho}_n = -(\mathbf{v}^{\mathrm{sat},n} - \mathbf{v}_{\mathrm{rx}})^{\mathrm{T}}\mathbf{u}^{\mathrm{sat},n} \tag{5.69}$$

$$\mathbf{u}^{\mathrm{sat},n} = \frac{\mathbf{r}^{\mathrm{sat},n} - \mathbf{r}_{\mathrm{rx}}}{||\mathbf{r}^{\mathrm{sat},n} - \mathbf{r}_{\mathrm{rx}}||} \tag{5.70}$$

where ρ_n is the geometric distance between satellite n and the receiver, $\dot{\rho}_n$ is the relative velocity between satellite and receiver and $\mathbf{u}^{\mathrm{sat},n}$ is the unit vector pointing from receiver to the satellite. The replica signal generators will be aligned for each channel based on the projected code phase and Doppler.

This procedure couples the individual tracking loops by the PVT solution. The major benefit of this method is that also very weak signals, e.g. caused by blockage, can be tracked and analyzed [Pany and Eissfeller, 2006]. The major drawback of the method is, that one faulty channel can kick out all tracked

channels because they are coupled together [Lashley and Bevly, 2009]. The method relies also on a recently accurate initial PVT to initialize the Kalman filter. Some descriptions and implementations of current vector tracking receivers are given e.g. in [Vu and Andrle, 2014] and [Ng and Grace Xingxin Gao, 2017].

5.10 Synthetic Multicorrelator

A multi-correlator enlarges the observation space in code phase and Doppler by evaluating a large set of correlation values for distinct offsets. The result is a two-dimensional multi-correlator map, also called Doppler-Delay map, which contains correlation values in code-phase and Doppler direction. This provides new possibilities for signal assessment, monitoring and receiver algorithms, because correlation values at different Doppler offsets are often not utilized. The definition of a single correlation $P_k(\Delta\tau, \Delta f_d, \Delta\phi)$ for epoch k is given by (5.9) and can be evaluated through (5.8). The carrier phase has no influence on the correlation power and the phase error can be retrieved from the maximum correlation value. If the carrier phase is not of further interest it can be set to an arbitrary value e.g. zero or to the phase of the corresponding NCO at same epoch. A multi-correlator map can be produced for the code-phase range offsets $\boldsymbol{\Delta\tau} = [-\Delta\tau_0, \ldots, \Delta\tau_u]$ and Doppler range offsets $\mathbf{\Delta f_d} = [-\Delta f_{d,0}, \ldots, \Delta f_{d,v}]$ by evaluating

$$P_{\mathrm{MC},k;u,v} = \sum_{k=1}^{M} r_{\mathrm{IF}}(k;\tau,\phi,f_d,A)\hat{r}_{\mathrm{IF}}(k;\hat{\tau}+\Delta\tau_u,\hat{f}_d+\Delta f_{d,v},\hat{\phi}=0) \forall u,v \quad (5.71)$$

where the integration time is given with $T = MT_s$ starting from sample epoch k with T_s being the sample period. The evaluation of this massive correlation values is a computational intensive task because the replicas for all correlation points need to be generated and correlated against the high rate sample stream. Thus, real-time performance might not be achieved without having much computational resources on software receivers or massive correlation units on hardware receivers.

There exists a highly efficient synthetic approach in the post-correlation domain using the principle of FFT, which is called Synthetic Multi-Correlator (SMC). The work from [Stöber et al., 2011] provided a prove that this efficient and synthetic approach delivers the same correlation values as a direct multi-correlator. SMCs up to now are used for signal quality monitoring, spoofing detection, as an analysis tool for GNSS receiver and simulator development,

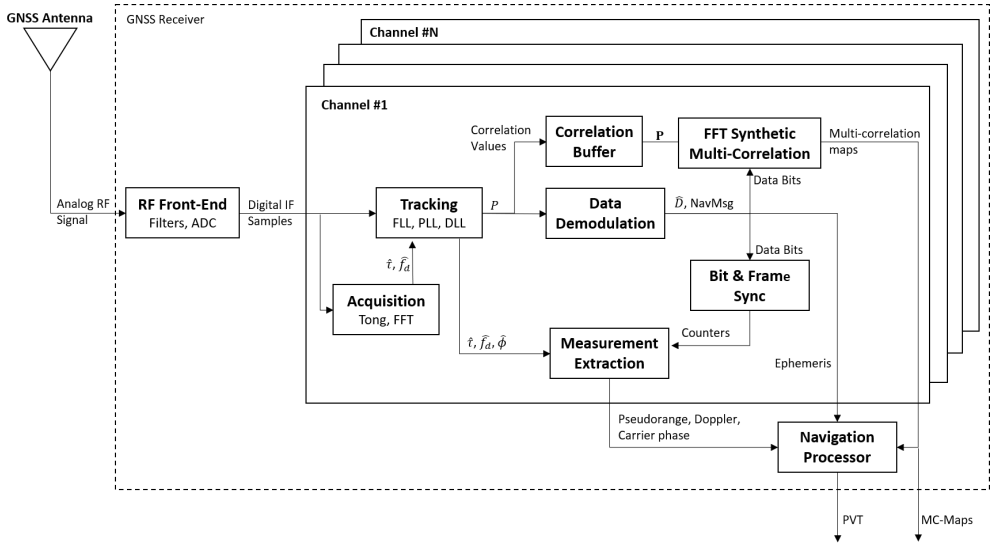

Figure 5.6: Generic architecture of a GNSS receiver with an additional multi-correlator block. Redrawn and adapted from [P. Teunissen and Montenbruck, 2017, Fig. 14.3].

multipath monitoring, bi-static radars, reflectometry systems, teaching purposes and contribute to this work as basis to obtain multi-dimensional probability density functions for a measured signal. The term synthetic is coming from the fact, that no real correlators are placed at the Doppler bins. The evaluation at the Doppler bins is performed using the Fourier transform principle, which shifts a sequence into the frequency domain to obtain its spectral components, hereby the correlation values in the Doppler direction. As shown in Fig. 5.6, the method can be integrated into a typical receiver architecture. In a first step the correlation values $P_l = [P_0, \ldots, P_{L-1}]$ are buffered with respect to time after each integrate-and-dump period. l defines the integrate-and-dump index which can be related to the sample epoch with $k_l = k_0 + lTf_s$, where k_0 refers to the first sample of the first correlation value in the buffer. The number of buffered correlation values depend on the FFT settings, especially on the FFT length. The FFT length is aligned to 2^Λ, where Λ is the FFT order. Without using the zero padding method, the number of buffered correlation values must equal the FFT length of 2^Λ.

The Discrete Fourier Transform (DFT) is the basis for the FFT and is defined as

$$X(m) = \sum_{n=0}^{N-1} x(n) e^{-i2\pi \frac{nm}{N}} \tag{5.72}$$

where $X(m)$ is a Fourier transformed complex value at the m-th frequency bin, N is the discrete Fourier transform length and i the imaginary number.

The FFT is an efficient realization of the DFT. With FFT realizations, like the radix-2 Cooley–Tukey algorithm, the number of operations can be significantly reduced from $O(n^2)$ to $O(n \log n)$. But this fast implementation constrains the DFT length to $N = 2^{\Lambda}$. Using this definition, the synthetic multi-correlation values can be obtained by

$$P_{\mathrm{SMC},k_0;u,m} = \sum_{l=0}^{L-1} P_{\mathrm{MC},k_l;u} \mathrm{e}^{-i2\pi \frac{lm}{L}} \tag{5.73}$$

where $P_{\mathrm{SMC},k_0;u,m}$ is a synthetically generated (SMC) correlation value at sample epoch k_0 with code phase index u (defining the code phase offset) and Doppler bin index m (defining the Doppler offset). Hereby, l defines the index of the correlation value in the correlation buffer and k_l the first sample epoch of the correlation value with index l. A real correlation is still performed for the code-phase bins $P_{\mathrm{MC},k_l;u}$, but the Doppler bins are obtained via the Fourier transform. Due to the FFT properties the Doppler bin is given with $f_{d,m} = \hat{f}_d + \frac{m f_T}{L}$, where $f_T = 1/T$ is the integrate and dump frequency. The evaluation of the correlation values leads to a total integration time of $T_{tot} = LT$. The formulation resembles a extended/long coherent integration time and thus the input correlation values must be free of data bits, which can be established by a prior data bit wipe-off. In order to wipe-off the data bits from the input correlation values, they must be known in advance. This can be achieved in (1) post-processing, when the data bits have been decoded in a prior processing step, (2) in real-time with a reference receiver delivering the data-bits in real-time to the rover, whereas the rover need to be slightly delayed to compensate for the transmission time and in (3) real-time with a prediction of data bits. It shall be noted that the extended integration time narrows the Doppler correlation function as depicted in Fig. 5.2. The upper limit of the total integration time is given either by computational resources or by the receiver clock stability. Fig. 5.7 shows the input data and result of a SMC. The right plot in this figure shows the synthetic multi-correlator map. It can be seen, that the Doppler resolution might be very rough such that only one bin representing clearly the correlation function.

Increasing the FFT length increases the frequency resolution [Oran Brigham, 1990, chapter 9.1], whereas the frequency resolution equals the Doppler resolution. A higher FFT resolution can be achieved synthetically with the method of zero-padding. Hereby, the FFT length is increased and the time domain input values are filled up with zeros. This leads to a larger FFT length N at same signal period, which increases the Doppler resolution (the frequency bins are sinc-interpolated) but also increases the computational load. Fig. 5.8 shows the result of zero padding on the frequency domain values by an increased FFT length of factor $2^3 = 8$. The FFT parameters must

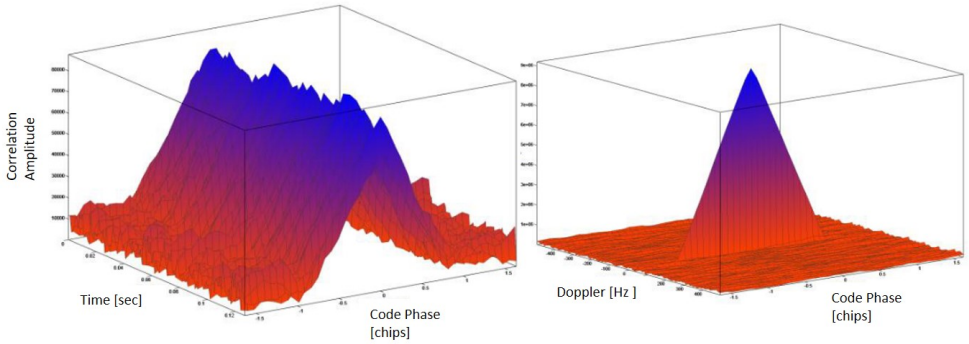

Figure 5.7: Input and result data of a synthetic multi-correlator. The left plot shows the time domain input data with a GPS L1 C/A code signal at C/No=47 dBHz and a coherent integration time of T=1ms. The right plot shows the synthetically generated correlation values using a FFT order of $\Lambda = 7$ which equals to a coherent integration time of $T_{tot} = 128$ ms. Both plots show $|P|$ in the z-Axis [Stöber et al., 2011, Fig. 1 and 2].

be carefully chosen to overcome the effect of leakage, which is basically a limited spectral resolution.

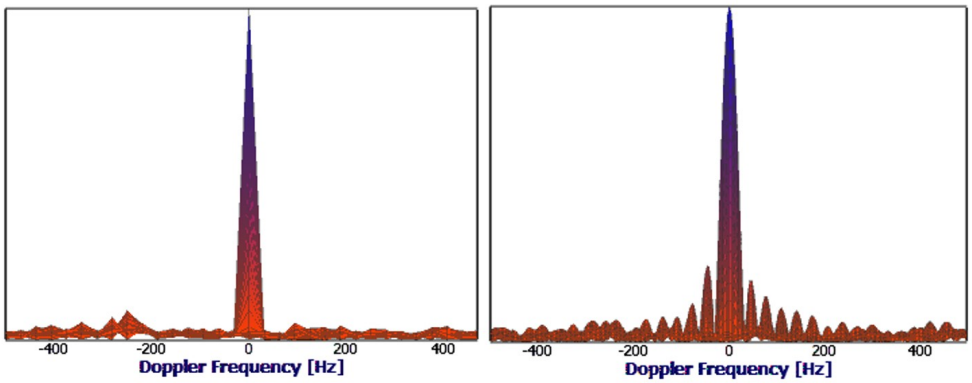

Figure 5.8: GPS L1 C/A signal of satellite PRN 12 with 49.1 dBHz and a total coherent integration time of $T_{tot} = 32$ ms. The left plot uses an FFT order of $\Lambda = 5$ without zero padding. The right plot uses the same input signal with zero padding up to an FFT order of $\Lambda = 8$. It can be clearly seen, that this procedure increases the Doppler resolution. Both plots show $|P|$ in the y-Axis and the sinc behavior of the Doppler is clearly observable in the right plot.

6 Bayesian Direct Position Estimation

The discussion starts with an introduction of the concept of BDPE in chapter 6.1. One important step in the concept of BDPE is the weight update of the Bayesian filter. One novelty of this work is the proposal of an optimal weight update and thus, the integration into the concept of BDPE is discussed in chapter 6.2. Based on the fact that the realization of BDPE includes some assumptions and limitations, related aspects are discussed in chapter 6.3. The discussion includes a major drawback of current BDPE architectures in terms of processing complexity, and therefore a solution to achieve a real-time capable BDPE receiver on top of a conventional receiver is proposed in chapter 6.4.

6.1 Concept of BDPE

The conventional approach to GNSS positioning is a two steps approach with *synchronization* and *trilateration* as shown in Fig. 6.1 [Closas and Gusi-Amigó, 2017]. Hereby, the synchronization step includes the signal acquisition (coarse synchronization) and the signal tracking (fine synchronization). The signal acquisition delivers coarse estimates of the code delay and Doppler, which are handed over to initialize the signal tracking loops. The DLL / FLL / PLL receiver tracking loops synchronize the internally generated replica signals to the received signals in order to deliver refined estimates of the code delay $\hat{\tau}_n$, Doppler $\hat{f}_{d,n}$ and carrier phase $\hat{\phi}_n$ for each tracked signal n. These estimates allow to derive the common observables, the code pseudorange $\hat{p}_n$, the carrier pseudorange $\hat{\varphi}_n$ and the Doppler $\hat{f}_{d,n}$. The decoded ephemeris together with the observables allow in a second step to trilaterate a PVT in the navigation processor. The PVT estimates are shown as $\hat{\mathbf{x}}_{\mathrm{rx}}$ in Fig. 6.1. Some receivers make use of the Vector Tracking (VT) concept as discussed in more detail in chapter 5.9. In this concept the receiver tracking loops are closed via the navigation processor. This is established by a LOS projection of the latest PVT ($\hat{\mathbf{p}}_{\mathrm{rx}}$, $\hat{\mathbf{v}}_{\mathrm{rx}}$ and $\hat{\mathbf{t}}_{\mathrm{rx}}$) in order to estimate the code delay $\hat{\tau}_n$ and Doppler $\hat{f}_{d,n}$ for the next integration periods. This step requires knowledge of the satellite positions and respectively the ephemeris, as depicted in Fig. 6.1. It should be noted, that the projection of the carrier phase is very difficult to realize due to the short wavelength of the given carrier frequency, as it requires a very

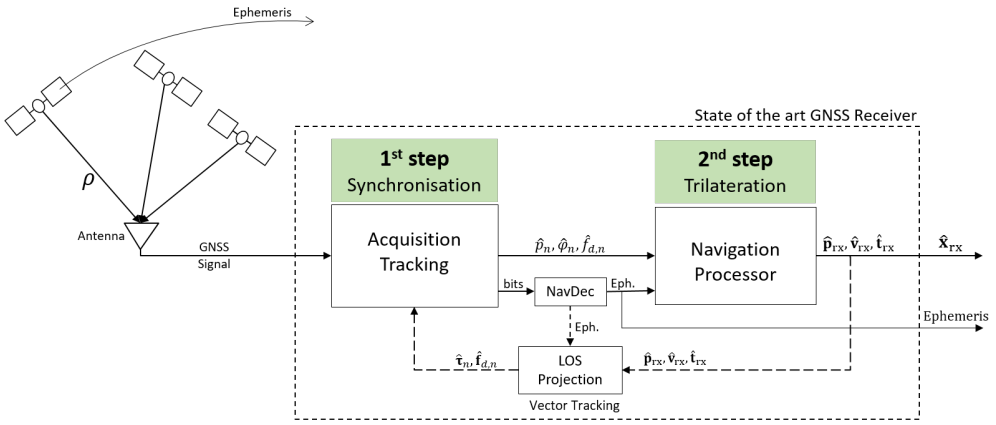

Figure 6.1: Principle of a state of the art GNSS receiver with a two steps positioning approach, synchronization of the replica signals to the received signals and trilateration of the position.

precise knowledge of the PVT, satellite positions, atmospheric effects as well as other minor contributions to avoid induced cycle slips. A typical approach is to let the carrier phase run freely without an alignment at the PVT loop update step. Such a setup is also considered in this work. It should be noted, that the LOS projection in Fig. 6.1 accounts also for atmospheric effects, if they are known.

For a more detailed understanding lets repeat the received complex basedband signal as given in [Closas and Gusi-Amigó, 2017, Eq. (1)] with

$$r(t) \quad = \quad \sum_{n=1}^{N} a_n s_n(t-\tau_n)\exp\{j2\pi f_{d,n}t + j\phi_n\} + n(t) \tag{6.1}$$

which is the continuous time equivalent model to (5.4), but with intermediate frequency $f_{\mathrm{IF}} = 0$, and where N is the number of received LOS signals, a_n is the complex amplitude, $s(t)$ is the transmitted navigation signal including the spreading code, possibly navigation data message and secondary code, t is the time, τ_n is the time delay, $f_{d,n}$ is the Doppler deviation, ϕ_n is the carrier phase, j is the imaginary number, the subscript n is the signal index and $n(t)$ is the noise component. The received signal can be modeled in dependency of the receiver state $\mathbf{x}_{\mathrm{rx}} = [x, y, z, v_x, v_y, v_z, dt_{\mathrm{rx}}, d\dot{t}_{\mathrm{rx}}]^{\mathrm{T}}$ with x, y, z as the user position and v_x, v_y, v_z as the user velocity, both in the Earth Centered Earth Fixed (ECEF) coordinate frame and dt_{rx}, $d\dot{t}_{\mathrm{rx}}$ as the user clock error and clock drift such that

$$r(\mathbf{x}_{\mathrm{rx}}, t) = \mathbf{q}(\mathbf{x}_{\mathrm{rx}}, t)^{\mathrm{T}}\mathbf{a} + n(t) \tag{6.2}$$

with

$$\mathbf{q}(\mathbf{x}_{\mathrm{rx}}, t) = \begin{bmatrix} s_1(t-\tau_1(\mathbf{x}_{\mathrm{rx}}))\exp\{j2\pi f_{d,1}(\mathbf{x}_{\mathrm{rx}})t + j\phi_1(\mathbf{x}_{\mathrm{rx}})\} \\ \vdots \\ s_n(t-\tau_n(\mathbf{x}_{\mathrm{rx}}))\exp\{j2\pi f_{d,n}(\mathbf{x}_{\mathrm{rx}})t + j\phi_n(\mathbf{x}_{\mathrm{rx}})\} \end{bmatrix} \tag{6.3}$$

and where $\mathbf{a} = [a_1, \ldots, a_n]^{\mathrm{T}}$ is a vector containing the amplitudes of the signals. Each receiver channel maximizes the Cross Ambiguity Function (CAF) to get estimates of the code delay $\hat{\tau}_n$ and Doppler $\hat{f}_{d,n}$. It should be noted, that the maximization of the CAF is fulfilled by a receiver channel in a FLL/DLL tracking loop setup, which computes the Maximum Likelyhood Estimator (MLE) as given in [Closas and Gusi-Amigó, 2017, Eq. (2)] with

$$\Lambda_n(\tau_n, f_{d,n}, N_c, N_{nc}) = \frac{1}{N_{nc}} \sum_{k=0}^{N_{nc}-1} \left| \int_{kT_{\mathrm{PRN}}N_c}^{(k+1)T_{\mathrm{PRN}}N_c} r(t)s_n(t-\tau_n)\exp\{-j2\pi f_{d,n}t\}dt \right|^2 \tag{6.4}$$

with

$$(\hat{\tau}_n, \hat{f}_{d,n}) = \underset{\tau_n, f_{d,n}}{\operatorname{argmax}}\{\Lambda_n(\tau_n, f_{d,n}, N_c, N_{nc})\} \tag{6.5}$$

where $\Lambda(\cdot)$ delivers the correlation result for the given code delay τ_n and Doppler $f_{d,n}$ when using N_c non-coherently summed correlation batches with a coherent integration time of $N_c T_{\mathrm{PRN}}$ seconds, where T_{PRN} is the duration of the PRN code sequence. It should be noted, that (6.4) includes an absolute value operation to deliver the amplitude independent of the resulting relative carrier phase, which makes the definition of the carrier phase in the replica signal obsolete. The pseudorange is given with $p_n = c\tau_n$ with c as the speed of light. The pseudorange measurements have a non-linear relationship with the user position $\mathbf{p}_{\mathrm{rx}} = [x, y, z]^{\mathrm{T}}$ and can be modeled as

$$p_n = \rho_n(\mathbf{p}_{\mathrm{rx}}) - c(dt_{\mathrm{rx}} - dt_n^{\mathrm{sat}}) + I_n + T_n + c(d_{\mathrm{rx}} + d_n^{\mathrm{sat}}) + \epsilon_n \tag{6.6}$$

where ρ defines the geometric distance in (m) between the user and the satellite, dt_{rx} and dt_n^{sat} are the receiver and satellite clock error in (s), I and T are the ionospheric and tropospheric delay in (m), d_{rx} and d_n^{sat} are the receiver and satellite hardware delay in (s) and ϵ_n accounts all occurring unmodeled errors. Note that (5.28) is a more detailed equivalent in terms of error sources. The relationship between the Doppler, the user and the satellite motion can be modeled with

$$f_{d,n} = -(\mathbf{v}_n^{\text{sat}} - \mathbf{v}_{\text{rx}})^{\text{T}} \mathbf{u}_n \frac{f_c}{c} \tag{6.7}$$

where $\mathbf{v}_{\text{rx}} = [v_x, v_y, v_z]^{\text{T}}$ and $\mathbf{v}_n^{\text{sat}} = [v_{x,n}, v_{y,n}, v_{z,n}]^{\text{T}}$ are the velocity vectors of the user and the satellite in (m/s), f_c is the carrier frequency in (Hz) and c is the speed of light (m/s). The direction vector pointing from the user antenna to satellite n is defined as $\mathbf{u}_n = (\mathbf{p}_n^{\text{sat}} - \mathbf{p}_{\text{rx}})/(|\mathbf{p}_n^{\text{sat}} - \mathbf{p}_{\text{rx}}|)$, whereas $\mathbf{p}_n^{\text{sat}}$ is the satellite position vector.

The full PVT solution obtained from the navigation processor is the current user state $\mathbf{x}_{\text{rx}} = [\mathbf{p}_{\text{rx}}^{\text{T}}, \mathbf{v}_{\text{rx}}^{\text{T}}, \mathbf{t}_{\text{rx}}^{\text{T}}]^{\text{T}}$, whereas the time consists of the receiver clock error and receiver clock drift and is given with $\mathbf{t}_{\text{rx}}^{\text{T}} = [dt_{\text{rx}}, d\dot{t}_{\text{rx}}]^{\text{T}}$.

From (6.6) and (6.7) it can be seen that $\boldsymbol{\tau} \triangleq \boldsymbol{\tau}(\mathbf{x}_{\text{rx}})$ and $\mathbf{f}_d \triangleq \mathbf{f}_d(\mathbf{x}_{\text{rx}})$, which allows to setup a function for the joint correlation function $\Psi(\cdot)$, which is the non-coherent sum over all satellite signals for a distinct receiver state $\mathbf{x}_{\text{rx}}$, defined as

$$\Psi(\mathbf{x}_{\text{rx}}, N_c, N_{nc}) = \sum_{n=1}^{N} \Lambda_n(\tau_n(\mathbf{x}_{\text{rx}}), f_{d,n}(\mathbf{x}_{\text{rx}}), N_c, N_{nc}) \tag{6.8}$$

and which is the principle of DPE. The MLE for DPE maximizes the cost function in (6.8) as

$$\hat{\mathbf{x}}_{\text{rx}} = \underset{\mathbf{x}_{\text{rx}}}{\text{argmax}} \{\Psi(\mathbf{x}_{\text{rx}}, N_c, N_{nc})\} \tag{6.9}$$

which is the maximization of the joint correlation function by varying the receiver PVT state $\mathbf{x}_{\text{rx}}$. In contrast to the classical two stage estimation approach, DPE is a reverse single step estimation approach which aims to estimate the PVT directly from the received signal samples [Closas, Fernández-Prades, and Fernández–Rubio, 2007].

BDPE applies Bayesian estimation principles on top of DPE, as also discussed in [Closas, Fernández-Prades, Bernal, et al., 2008]. According to the discussion in chapter 4, different type of Bayesian filters exist. The main difference to the MLE is, that Bayesian filters deliver a filtered estimate over time and allows to include side information e.g. from an IMU or probabilistic maps. The following equations are relevant for non-parametric Bayes filters, as this work focuses on the optimal weight update function for a grid-based and a particle filter. Bayes filters rely on two steps *prediction* and *update* and require

therefore a propagation and update model. Let's briefly summarize the most relevant equations for BDPE. The propagation of the state from $\mathbf{x}_{\mathrm{rx},k-1}$ to $\mathbf{x}_{\mathrm{rx},k}$ is given with

$$\mathbf{x}_{\mathrm{rx},k} = \mathbf{f}_k(\mathbf{x}_{\mathrm{rx},k-1}, \mathbf{v}_{k-1}) \tag{6.10}$$

where $\mathbf{f}_k(\cdot)$ is a possibly non-linear function and $\mathbf{v}_{k-1}$ models the process noise. The measurement model, which relates the state $\mathbf{x}_{\mathrm{rx},k}$ to the measurements $\mathbf{z}_k$ is given with

$$\mathbf{z}_k = \mathbf{h}_k(\mathbf{x}_{\mathrm{rx},k}, \mathbf{n}_k) \tag{6.11}$$

where $\mathbf{n}_k$ defines the measurement noise. The simplest BDPE propagation model for (6.10) is a linear model as given in (5.52) with

$$\mathbf{x}_{\mathrm{rx},k} = \mathbf{F}_k \mathbf{x}_{\mathrm{rx},k-1} + \mathbf{Q}_{k-1} \tag{6.12}$$

which considers a constant velocity and constant clock drift for the interval $T = N_c N_{nc} T_{\mathrm{PRN}}$ seconds when using the same definition for $\mathbf{F}_k$ and $\mathbf{Q}_{k-1}$ as given in (5.55) and (5.57). For some other state propagation models and for the inclusion of other sensors into the propagation model the reader is referred to [Closas, Fernández-Prades, Bernal, et al., 2008]. The BDPE measurement model for (6.11) is given in (6.2) with

$$\mathbf{z}_k = \mathbf{q}(\mathbf{x}_{\mathrm{rx},k})^{\mathrm{T}} \mathbf{a} + n_k \tag{6.13}$$

The prediction and measurement update step using (6.12) and (6.13) is performed according to the Chapman-Kolmogorov equation in (4.3) and the Bayes rule in (4.4). The aim of Bayesian filters is to estimate the true posterior PDF $p(\mathbf{x}_{\mathrm{rx},k}|\mathbf{z}_{1:k})$, which can be represented in the case of a particle filter as given in (4.35) as

$$p(\mathbf{x}_{\mathrm{rx},k}|\mathbf{z}_{1:k}) \approx \sum_{i=1}^{N_s} w_k^i \delta(\mathbf{x}_{\mathrm{rx},k} - \mathbf{x}_{\mathrm{rx},k}^i) \tag{6.14}$$

Hereby, a set of N_s samples and corresponding weights w_k^i are used to reconstruct the posterior PDF. The update step of a sequential Bootstrap particle filter, which updates the weights w_k^i with the new measurements, is defined in (4.39) with

$$w_k^i \propto w_{k-1}^i p(\mathbf{z}_k|\mathbf{x}_{\mathrm{rx},k}^i) \tag{6.15}$$

In order to extract the PVT state from the signal samples the step of signal correlation is inevitable, because the GNSS signal needs to be recovered from the noise. From the known BDPE related literature in [Closas, Fernández-Prades, Bernal, et al., 2008] and [Closas, 2009] it is assumed that the weight update is based on the assumption that

$$p(\mathbf{z}_k|\mathbf{x}^i_{\mathrm{rx},k}) := \alpha^{-1}\Psi(\mathbf{x}^i_{\mathrm{rx},k}, N_c, N_{nc}) \tag{6.16}$$

with

$$\alpha = \int \Psi(\mathbf{x}_{\mathrm{rx}}, N_c, N_{nc}) d\mathbf{x}_{\mathrm{rx}} \tag{6.17}$$

whereas α is a normalization factor in order to interpret the joint correlation function as a PDF. It should be noted, that this normalization step is obsolete if the weights in (6.15) are normalized after the weight update such that

$$\sum_{i=1}^{N_s} w^i_k = 1 \tag{6.18}$$

After the weight update the number of effective particles is measured with (4.41) and a resampling step is triggered if a defined threshold is exceeded. The assumption in (6.16) let operate the particle filter (or grid-based filter) on the joint correlation function, which resembles a 8-dimensional direct PVT tracking.

The PVT state and accuracy estimate is based on the updated and normalized weights. The posteriori belief is the best PVT estimate of the current state and is generated as a weighted mean with

$$\hat{\mathbf{x}}_{\mathrm{rx},k} = \sum_{i=1}^{N_s} w^i_k \mathbf{x}^i_{\mathrm{rx},k} \tag{6.19}$$

If the particle density is high and the resolution small, the particle with the highest weight can be optionally be used as the best estimate such that

$$\hat{\mathbf{x}}_{\mathrm{rx},k} = \sum_{i=1}^{N_s} \delta(\arg\max_{i\in[1,N_s]}(w^i_k) - w^i_k)\mathbf{x}^i_{\mathrm{rx},k} \tag{6.20}$$

where $\delta(\cdot)$ refers to the Dirac operator. The expected gain in the SNR of DPE is significant and depends on the number of used GNSS signals. The formulation is given in [Closas and Gusi-Amigó, 2017] with

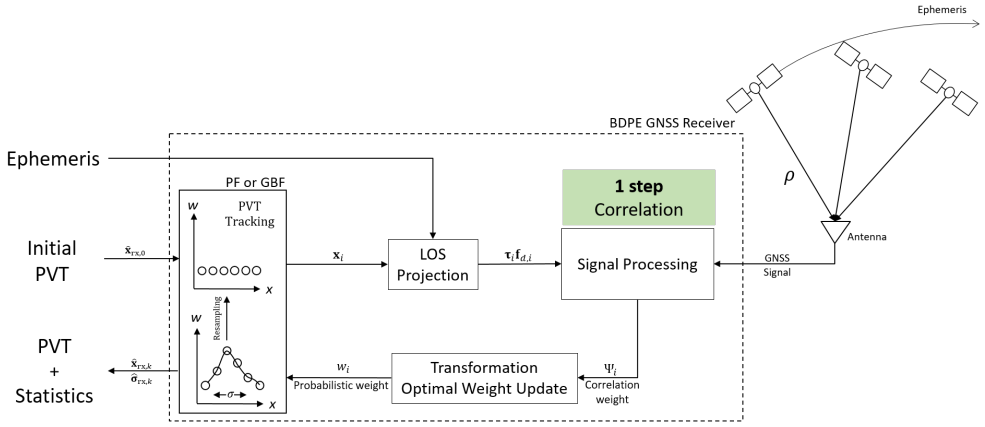

Figure 6.2: Principle of a BDPE GNSS receiver with a single step position estimation approach.

$$G_{dB} > 10 \log_{10}(N) \tag{6.21}$$

where N is the number of GNSS signals and G_{dB} is the expected gain compared to classical tracking techniques. It is impressive, that with 3 GNSS systems, 3 frequencies and 10 satellites (of each system) in view a gain in the SNR of about 19.5 dB could be achieved for same integration periods, which makes the method superior in sensitivity compared to classical approaches.

In contrast to the common two steps positioning approach, BDPE is an inverse single step estimation method, which is depicted in Fig. 6.2. As indicated in the figure, a BDPE receiver requires as input (1) the GNSS signal samples, a (2) rough initial PVT and the (3) ephemeris data. Hereby, the initial PVT $\hat{\mathbf{x}}_{\mathrm{rx},0}$ is required to initialize the PF or GBF, as indicated by the PF/GBF block in Fig. 6.2. The upper plot in the block indicates an initial distribution of the particles, symbolically shown by the weights plotted over one dimension, whereas the true BDPE filter has an 8-dimensional state space. The update step in a BDPE receiver evaluates the new weight for each particle. Therefore, each particle state $\mathbf{x}_i$ is projected into the LOS code delay $\boldsymbol{\tau}_i$ and Doppler $\mathbf{f}_{d,i}$ for each satellite. Thus, $\boldsymbol{\tau}_i$ and $\mathbf{f}_{d,i}$ are vectors. The correlation step is performed for all satellite signals N for all particles or grid-nodes i. The output of the correlation step is a scalar non-coherent joint correlation weight ψ_i. Two options exist now for the filter update, the (1) direct use of the joint correlation weight such that $w_i = \psi_i$, or (2) a prior transformation to a true probabilistic weight such that $w_i = Q(\psi_i)$, where $Q(\cdot)$ should denote a transformation function. The updated weights, as indicated by the lower plot in the left block in Fig. 6.2, allow the PF or GBF to estimate the current state $\hat{\mathbf{x}}_{\mathrm{rx},k}$ and variance $\hat{\boldsymbol{\sigma}}_{\mathrm{rx},k}$. The resampling step of the Bayes filter is indicated by the arrow pointing from the lower plot to the upper plot and by the equalized weights w_i.

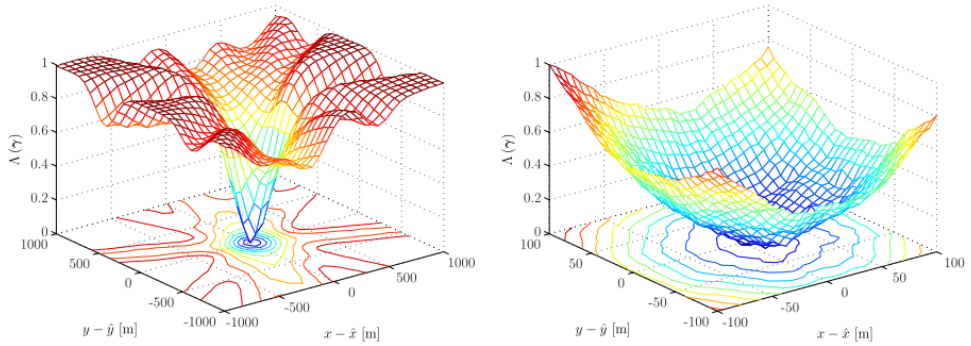

(a) Single Antenna receiver

(b) Single Antenna receiver (zoom)

Figure 6.3: MLE cost function for DPE from [Closas, 2009, Fig. 4.6]. It should be noted, that the cost function $\gamma(\cdot)$ in this figure relates to a normalized inverse version of $\psi(\cdot)$ in (6.8). The function is evaluated for $\gamma \triangleq [x, y]^{\mathrm{T}}$, where $x - \hat{x}$ and $y - \hat{y}$ refers to the position offset in the ECEF coordinate frame.

The cost function for the MLE of DPE is shown in Fig. 6.3. The figure shows a normalized inverse version of $\psi(\cdot)$ in (6.8) spanned over the xy-plane in the ECEF frame. A BDPE receiver aims to track the peak of the joint correlation function and therefore a particle filter or grid-based filter need to cover the peak properly in order to get reasonable estimates of the receiver state.

6.2 The Weight Update

The weight update as given in (6.16) with

$$p(\mathbf{z}_k|\mathbf{x}^i_{\mathrm{rx},k}) := \alpha^{-1}\Psi(\mathbf{x}^i_{\mathrm{rx},k}, N_c, N_{nc}) \tag{6.22}$$

and with

$$\alpha = \int \Psi(\mathbf{x}_{\mathrm{rx}}, N_c, N_{nc}) d\mathbf{x}_{\mathrm{rx}} \tag{6.23}$$

interprets the joint correlation function $\Psi(\cdot)$ as a PDF. This assumption is a working principle and simplifies the realization of a BDPE receiver, but comes along with drawbacks. Three major problems arise with the definition in (6.22)

(1) the joint correlation function does by far not reflect the true PVT accuracy of some meters

(2) the dependency of the PVT accuracy on the signal strengths is not reflected properly
(3) the approach is not a valid mathematical description

The extension of the joint correlation function is visible in both plots in Fig. 6.3 for GPS L1 C/A signals, which results from the non-coherent sum of the correlation functions of all tracked signals projected into the PVT domain. Both plots are spanned over the xy-plane of the ECEF frame, whereas plot (b) is a zoomed version of plot (a). This figure clearly underlines statement (1), as the expected standard deviation of the peak is in the magnitude of several tens of meters. Evidence of statement (2) is given inherently by the extension (width) of the correlation function, which solely depends on the signal type, respectively the code rate, the subcarrier frequency and modulation scheme, but not on the signal strength. In order to get proper variance estimates, a measurement model with a dependency on the signal strength is required. Nevertheless, direct tracking of the joint correlation function in the PVT domain using a particle filter is possible and was shown in [Dampf, Witternigg, et al., 2017] and [Witternigg et al., 2017].

One novelty of this work is the development of an optimal weight update function for BDPE, which also properly reflects the measurement accuracy based on the signal strength. The optimal weight update can be derived from the probabilistic description of the signal samples and is given with

$$p(\mathbf{z}_k|\mathbf{x}^i_{\mathrm{rx},k}) = \frac{1}{(2\pi)^L}\exp\{-L\}N\sqrt{\frac{\pi}{2L}}\prod_{n=1}^{N}\exp\left\{\frac{|P_n(\tau_n, f_{d,n})|^2}{4}\right\}I_0\left(\frac{|P_n(\tau_n, f_{d,n})|^2}{4}\right) \tag{6.24}$$

where L defines the correlation length in samples, N the number of signals, $P_n(\tau_n, f_{d,n})$ is the correlation value at code delay τ_n and Doppler $f_{d,n}$, which depend on $\mathbf{x}^i_{\mathrm{rx},k}$ according to the LOS projection, and I_0 refers to the Bessel function of the first kind and order zero. Hereby, the measurement $p(\mathbf{z}_k|\mathbf{x}^i_{\mathrm{rx},k})$ represents a multi-dimensional PDF, which depends on the state $\mathbf{x}^i_{\mathrm{rx},k}$. It should be noted, that the equation builds the product of PDFs of multiple signals. The PDF of a single signal is a 2D joint PDF which delivers a probabilistic description of the measurement in the code phase and Doppler domain, whereas the variance of the PDF represents the measurement accuracy of the signal. This definition accounts for problem (1) and (2), because it reflects the true measurement accuracy in dependency of the signal strength as it depends on the correlation value $P_n(\cdot)$. The development of the optimal weight update equation with a discussion on the measurement accuracy, numerical constrains and efficient realizations is discussed in detail in chapter 7.

The proposed BDPE implementation directly tracks the 8-dimensional PVT state by using as input multi-dimensional probability density functions. Fig.

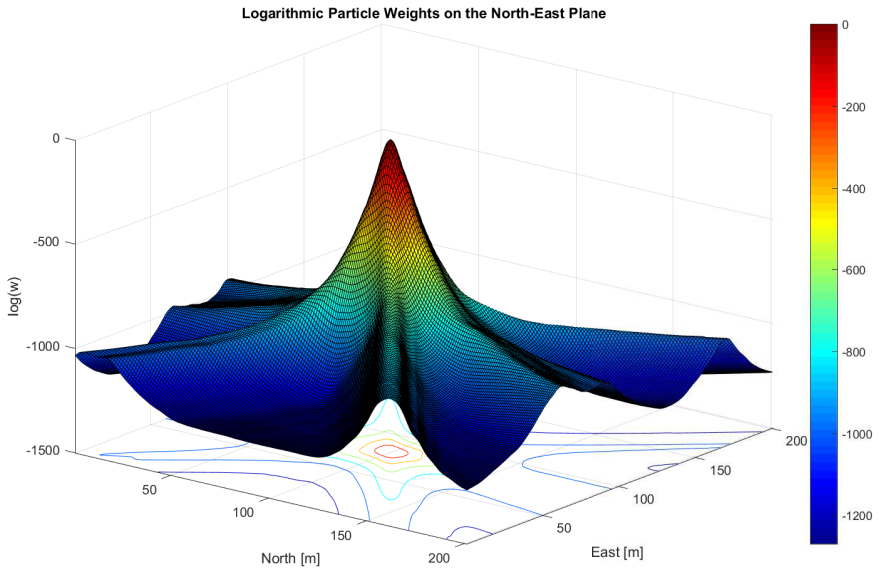

Figure 6.4: The plot shows the normalized logarithmic particle weights $\widetilde{w}_k^i$ from (B.14), assuming a uniform distribution from the previous epoch, i.e., $\widetilde{w}_{k-1}^i = 0$ and using the optimal particle weight update from (B.13). The particles are equidistantly distributed over a grid in the north-east plane. The lines through the plot correspond to the weighted correlation function in the position domain and thus refer to a GNSS signal. In a proper case (correct user velocity, clock error and drift), the lines overlap at a distinct point in the position domain, which is in this case the northeast plane. The resulting peak represents the probability of the 2D position. Note that the plotted weights are normalized and in the logarithmic scale, thus the peak has the maximum value of 0. The coherent integration time for this plot was set to $T_{coh} = 2$ ms. The processed data refers to open sky. It was recorded at latitude LAT = 47.06446263 deg, longitude LON = 15.40777110 deg on the rooftop of Reininghausstraße 13a, Graz, Austria [Dampf, Frankl, and Pany, 2018, Fig. 2].

6.4 shows an ideal tracking state, where all used GNSS signals overlap in a distinct PVT. The figure shows the joint probability density function for a 2-dimensional grid, where the weights of the equidistant grid nodes are spanned of the north-east plane of a local coordinate frame. Thus, this figure shows the joint probability function of the horizontal position. In the horizontal local coordinate frame each GNSS signal looks like a wall. In an ideal tracking case as shown in Fig. 6.4, the GNSS signals overlap at the true PVT, which brings the significant sensitivity gain in DPE. In other words, DPE allows to accumulate signal energy from different signals in the PVT domain. It shall be noted, that in this example the intersection of the north-east plane is made at the true PVT and thus the correlation in the PVT domain results in a clear unimodal maximum.

Fig. 6.5 shows an suboptimal case with an improper aligned receiver clock

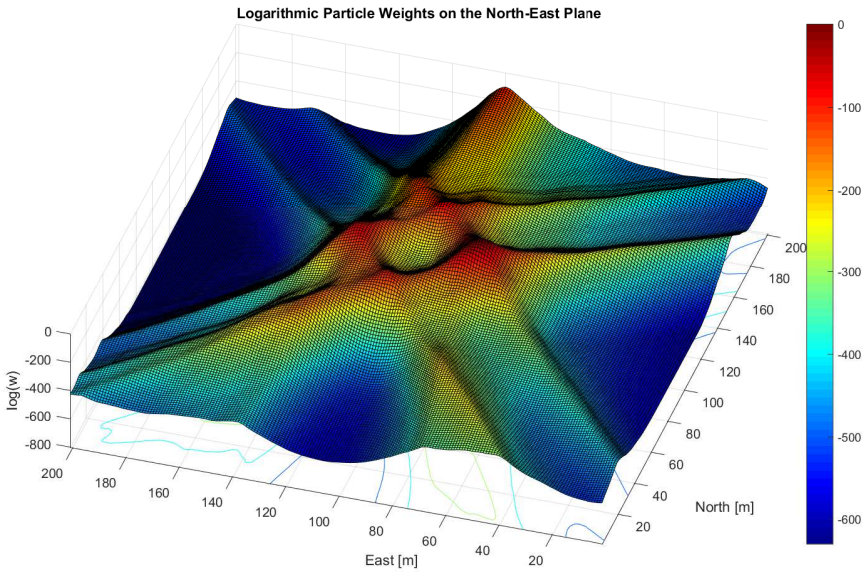

Figure 6.5: This plot depicts a case when the clock error is improperly aligned. The GNSS signals do not overlap at a distinct position in the north-east plane. The plot shows the normalized logarithmic particle weights $\widetilde{w}_k^i$ from Equation (B.14), assuming a uniform distribution from the previous epoch, i.e., $\widetilde{w}_{k-1}^i = 0$ and using the optimal particle weight from Equation (B.13). The particles are equidistantly distributed over a grid. The lines through the plot correspond to the weighted correlation function in the position domain and thus refer to a distinct GNSS signal. The lines look very broad even after the weight update, which comes from the logarithmic scale given by $\log(w_k^i)$. The coherent integration time for this plot was set to $T_{coh} = 2$ ms. The processed data refers to open sky. It was recorded at LAT = 47.06446263 deg, LON = 15.40777110 deg on the rooftop of Reininghausstraße 13a, Graz, Austria [Dampf, Frankl, and Pany, 2018, Fig. 3].

error. In such a case the GNSS signals do not perfectly overlap and a offset between the signals become visible, because the PDF of a single signal is very sharp. In such a situation the gain of DPE is partially or completely lost. I shall be noted, that for this case a optimum still exists at the true clock error, but it should illustrate cases when signals do not perfectly overlap. This can be the case, if all processed signals do not intersect at a distinct PVT e.g. if large atmospheric effects are not modeled or just multipath signals are present. Nevertheless, with the Bayesian estimator, which calculates the PVT with a weighted mean, a proper state estimate can be performed, unless the signals drop below the noise floor. The work in [Dampf, Frankl, and Pany, 2018] and chapter 7 outline the optimal way to perform the weight update and how to prevent from losing the gain of DPE.

6.3 Discussion on BDPE Aspects

This chapter discusses different aspects which need to be considered for a BDPE receiver. The discussion covers the initialization of a BDPE receiver, the LOS projection, the impact of atmospheric effects and possible support of augmentation systems, the phase coherency, the benefit of multiple systems and frequencies, the impact of the type of navigation signal as well as problems with the high computational complexity.

6.3.1 Initialization

As visible in Fig. 6.2, BDPE requires an initial position and knowledge about the ephemeris. As also proposed in [Closas and Gusi-Amigó, 2017], a BDPE receiver can be operated on top of a conventional GNSS receiver. Once the ephemeris have been decoded and an initial PVT is available, the receiver can switch to BDPE tracking.

If such an architecture is not used, the initial PVT and ephemeris need to be available from external sources. The ephemeris data (e.g. ultra-rapid orbits) can be easily obtained via the Internet. Since the emerging technology paradigms such as the Internet of Things (IOT) or smart cities, a Internet connection can be assumed to be available nearly everywhere, especially in urban areas and in numerous devices [GSA, 2017]. The initial position can be obtained for example by using a LTE position or a position entered by the user. The initial velocity can be assumed to be zero for low dynamic scenarios, but for higher dynamics, e.g. aircraft or rockets, an approximate initial velocity might be needed. The initial time can also be retrieved from the LTE network or Internet using the Network Time Protocol (NTP) or Precission Time Protocol (PTP). Furthermore, the time could also be obtained in Europe from the DCF77 long-wave time signal. It is important, that the initial uncertainty of the PF or GBF must cover the true PVT, otherwise no convergence can be expected.

The initial PVT is given with

$$\mathbf{x}_{\mathrm{rx},k=0} = \begin{bmatrix} \mathbf{r}_{\mathrm{rx},0} \\ \mathbf{v}_{\mathrm{rx},0} \\ \mathbf{t}_{\mathrm{rx},0} \end{bmatrix} = \begin{bmatrix} [x_0, y_0, z_0]^{\mathrm{T}} \\ [v_{x,0}, v_{y,0}, v_{z,0}]^{\mathrm{T}} \\ [dt_{\mathrm{rx},0}, d\dot{t}_{\mathrm{rx},0}]^{\mathrm{T}} \end{bmatrix} \tag{6.25}$$

and is used to initialize the particle states of a particle filter, whereas the PVT uncertainty is described by the probability distribution of the particles. Under the assumption that the initial distribution is Gaussian, the particles can be initialized with

$$p(\mathbf{x}_{\mathrm{rx},k=0}) = \mathcal{N}(\mathbf{x}_{\mathrm{rx},k=0}, \mathbf{P}_{k=0}) \tag{6.26}$$

where $\mathbf{P}_{k=0}$ is the covariance matrix for the initial state uncertainty. Typically, in GNSS the vertical position accuracy is less accurate as the horizontal due to the geometry of the satellites. The simplest way to account for this fact is to perform the initialization in a local coordinate frame e.g. North East Down (NED) and shift it to the working ECEF frame, which is not explicitly shown here. Once an initial set of particles is drawn with (6.26), the particle filter is initialized.

6.3.2 LOS Projection

The aim of the BDPE receiver is to track the peak of the joint correlation function as shown in Fig. 6.3. Therefore, the replica signal alignment for the correlation process must be modeled accurately, such that the individual signals overlap in the PVT domain. The extended LOS projection model for multiple systems for the code pseudorange is given with

$$p_n = \rho_n(\mathbf{p}_{\mathrm{rx}}) - c(dt_{\mathrm{rx}} - dt_n^{\mathrm{sat}}) + I_n + T_n + c(d_{\mathrm{rx}} + d_n^{\mathrm{sat}}) + cd_{\mathrm{sys}} + \epsilon_n \tag{6.27}$$

and needs to be as accurate as possible, because the code phase for the replica signal alignment is contained in the pseudorange p_n. The pseudorange model contains

- the geometric range $\rho_n = ||\mathbf{p}_n^{\mathrm{sat}} - \mathbf{p}_{\mathrm{rx}}||$, which depends on the accuracy of the satellite position $\mathbf{p}_n^{\mathrm{sat}}$ from the ephemeris. Thus, the projection error could be reduced when using precise ephemeris.
- the satellite clock error dt_n^{sat}, which is known from the ephemeris. It should be noted, that the receiver clock error dt_{rx} is part of the receiver state, which is to be estimated.
- the ionospheric delay I_n, which can be calculated using the Klobuchar model and which parameters are part of the ephemeris. Beside the standard Klobuchar model there exist several possibilities to get more accurate estimates for the ionospheric delay, (1) use more accurate models like NeQuick, (2) use correction data from SBASs like WAAS or EGNOS, (3) use PPP correction data, (4) use a differential approach like DGNSS or RTK, or (5) use a dual frequency approach.
- the tropospheric delay T_n, which can be modeled with assumptions on the vertical profile of the troposphere, which consists on a hydrostatic and wet component delay. Several models exist which can be grouped in

geodetic or navigation-oriented models, whereas some models require surface meteorological data.
- the frequency dependent receiver hardware delay d_{rx}, which is induced by the receiver hardware. The receiver hardware delay is typically constant and can be estimated in a time synchronized simulator setup or with differential methods, if the delay of the reference is known.
- the frequency dependent satellite hardware delay d_n^{sat}, which is known from the ephemeris data.
- the system offset d_{sys}, which defines the time offset between the different GNSSs. The system offset might be retrieved from the ephemeris or needs to be estimated.

The LOS projection does not account for any other errors indicated by ϵ_n, like multipath or scintillation effects. A inaccurate projection model results in residual errors which cause relative offsets of the correlation functions in the PVT domain, which might lead to a reduction of the gain of DPE and difficulties in tracking a possibly distorted peak.

6.3.3 Atmospheric Effects

Atmospheric effects occur during propagation of the signal from sky to earth. During the propagation the signal passes the ionosphere I and troposphere T, as modeled in (6.27). Hereby, the ionized atmosphere delays the code and advances the carrier phase, whereas the total electron content and signal travel distance through this layer defines the magnitude of the delay. The ionospheric delay on the code is typically in the magnitude of 2-10 m and the tropospheric delay on the code and carrier is in the magnitude of about 2.3-2.5 m, if the satellite is in zenith [Misra and Enge, 2010, Tab. 5.4]. Both effects are relevant to DPE, because the correlation functions and PDFs need to overlap in the PVT domain such that all available signal energy of the tracked GNSS signals accumulate in a distinct point, as illustrated by Fig. 6.4 and Fig. 6.5. Otherwise, the maximum possible signal to noise ratio cannot be exploited, which leads to a reduced sensitivity. This can be critical with high code rate signals, which have a very narrow correlation function and PDFs due to the improved ranging performance, e.g. for GPS L5 or Galileo E5AltBOC. The effect of non-overlapping signals in the PVT domain for unmodeled ionospheric errors is similar to an artificial delay in the receiver clock error. Both effects cause delays on each pseudorange, but it should be made clear, that the delays for the artificial clock error is the same for all pseudoranges, whereas the atmospheric delays are different for all pseudoranges. Thus, the resulting effect in the PVT domain of unmodeled atmospheric delays is expected to be similar as a delay in the clock error as shown in Fig. 6.5. If atmospheric models are properly applied, the tension reduces and the gain

could be recovered, which is illustrated in Fig. 6.4. Without modeling of the atmospheric delays, a reduced gain of DPE is expected, whereas higher code rate signals are affected stronger.

6.3.4 Augmentation Systems

Augmentation systems improve the GNSS position by delivering supplemental data. Beside plausibility information on GNSS signals and accurate correction data for satellite clocks and orbits, a significant part of the position improvement is resulting from accurate information about the ionospheric layer. The availability of correction data from an SBAS or GBAS system allows to model the ionospheric delays more precisely and reduce the UERE. DPE relies on a reasonable accurate pseudorange model to be able to accumulate the correlation functions or PDFs for a distinct PVT. The more accurate the pseudorange model, the better is the overlay of the correlation functions or PDFs and the higher is the estimated accuracy and sensitivity. Thus, augmentation systems allow to model the ionospheric delay I in (6.27) more accurately. But augmentation systems have in context of DPE only a small beneficial impact, because it is expected that the dominant part of the sensitivity gain of DPE can also be achieved without correction data from augmentation systems.

6.3.5 Phase Coherency

The herein presented approach for DPE and BDPE is based on a non-coherent sum of correlation functions, which is shown by the absolute value operation in (6.4) with

$$\Lambda_n(\tau_n, f_{d,n}, N_c, N_{nc}) = \frac{1}{N_{nc}} \sum_{k=0}^{N_{nc}-1} \left| \overbrace{\int_{kT_{\mathrm{PRN}}N_c}^{(k+1)T_{\mathrm{PRN}}N_c} r(t)\, \underbrace{s_n(t-\tau_n)\exp\{-j2\pi f_{d,n}t\}}_{\text{replica signal}}\, dt}^{\text{complex correlation value } P_n} \right|^2 \tag{6.28}$$

If the absolute value of the complex correlation value P_n is build, the resulting phase of the correlation value vanishes and the summation becomes non-coherent. Based on the fact that only a non-coherent summation is considered for DPE, the phase in the exponential of the replica signal is obsolete. This applies also for the introduced optimal weight update, which is also based on absolute correlation values as given in (6.24) with

$$p(\mathbf{z}_k|\mathbf{x}^i_{\mathrm{rx},k}) = \frac{1}{(2\pi)^L}\exp\{-L\}N\sqrt{\frac{\pi}{2L}}\prod_{n=1}^{N}\exp\left\{\frac{\overbrace{|P_n(\tau_n, f_{d,n})|}^{\text{absolute of } P_n}^2}{4}\right\} I_0\left(\frac{\overbrace{|P_n(\tau_n, f_{d,n})|}^{\text{absolute of } P_n}^2}{4}\right) \tag{6.29}$$

This aspect simplifies the BDPE setup significantly, because phase coherency must not be achieved. Thus, the LOS projection needs to be just accurate in the meter to decimeter level, depending on the extension of the used correlation functions, respectively the used GNSS signal types, or the extension of the PDFs. Nevertheless, a phase coherent approach would be a very interesting research area. The phase coherent approach would require a precise knowledge of the atmospheric delays in order to converge (similar to PPP) as well as a highly resoluted PVT space to be able to resolve the carrier phase ambiguity. The starting point for a phase coherent approach would be the probabilistic function in (7.2).

6.3.6 Multi-System and Multi-Frequency

Using multiple GNSS systems for positioning brings the benefit of a higher number of available satellites, which improves with classical positioning techniques the availability and accuracy of the PVT. DPE adds an additional benefit, the method improves also the sensitivity with an increasing number of satellites and signals. The gain is coming from the fact, that DPE is tracking all signals at once. This approach allows to accumulate the signal energy from all available signals, whereas classical tracking methods rely on the signal energy of a single signal. The improvement in sensitivity is significant and the major benefit of DPE. The sensitivity gain of DPE is given in equation (6.21). But the full gain of DPE can only be exploited with a good parameter modeling or parameter estimation, and becomes visible, if all estimated or modeled parameters fit to the true parameters. When calculating a PVT with multiple systems and multiple frequencies, some additional parameters need to be accounted for. For DPE, the system time offset is an important parameter. Each GNSS system works in its individual time frame, which is the GPS Time (GPST), GLONASS Time (GLONASST), Galileo System Time (GST) and Beidou Time (BDT). The GNSS system times are referenced to Coordinated Universal Time (UTC), also known as Greenwich Mean Time (GMT) or International Atomic Time (TAI). The offset between UTC and TAI is defined as $T_{UTC} = T_{TAI} + T_{LeapSeconds}$. The time specifications of the systems, as defined in [ESA, 2018], are given with:

- GPST is synchronized to UTC(USNO) at 1 ms level, but typically kept within 25 ns (about 7.5 m)

- GLONASST is synchronized to UTC(SU)+3h at 1 ms level (about 300 m)
- GST is synchronized to TAI at 50 ns level (about 15 m)
- BDT is synchronized to UTC at 100 ns level (about 30 m)

These system offsets are crucial for Multi-GNSS DPE, because the auto-correlation functions or PDFs of the measurements need to overlap in order to exploit the full gain of DPE. It needs to be considered, that the auto-correlation function of a BPSK(1) has an extension of about +/- 300 m and a BPSK(10) of about +/- 30 m, and the PDFs of the signal measurements might be more narrow. In general, the system offsets need to be significantly smaller than the width of the auto-correlation functions or extension of the expected PDFs, such that the correlation functions or PDFs overlap in the PVT domain in order to exploit the gain. The system offsets can be estimated with DPE by adding another dimension, but which further increases the computational complexity, or need to be supplied by externals means. Based on the fact, that the drift of the system-offsets is very small due to very high-quality clocks, the offsets can be queried e.g. via the Internet and applied in the DPE receiver. The system offset d_{sys} needs to be accounted in (6.27), but is not explicitly written in the equation as this work considers just a single system (GPS).

Frequency dependent delays arise in the satellite, in the transmission channel and in the receiver. The frequency dependent instrumental delays caused by the satellite and receiver hardware are neglectable small for DPE, but they are transmitted for each satellite in the navigation message and can be calibrated for any GNSS receiver. The frequency dependent delays in the transmission channel allows to estimate the ionospheric delays, whereas the ionospheric delays are typically modeled in a single frequency receiver (e.g. using the Klobuchar model). Estimating the ionospheric delays with a multi-frequency DPE approach is possible, but increases the dimensionality of the estimation problem, as an estimate for each satellite is required. It is expected, that the ionospheric models are sufficient accurate for DPE, especially when considering inaccuracies of in the pseudorange model, as it is proposed in chapter 7.1.

6.3.7 Impact of the Navigation Signal

The type and parameters of a navigation signal have an impact on the auto-correlation function and thus also on DPE. Higher code-rates lead to a sharper (narrow) auto-correlation function, which allows conventional tracking methods to track the navigation signal more precisely [Misra and Enge, 2010, Chap. 3.3 and 10.6]. The impact is the same for DPE, because the sharp auto-correlation function leads to a narrow PDF in LOS direction. This effect can be translated to the PVT domain, resulting in a smaller variance of the estimated PVT. The variance of the PDF of the PVT depends also on the modulation

type, as for example a BOC(1,1) results in a sharper auto-correlation peak compared to a BPSK(1). One important aspect of different modulation types is, that they inherently can cause multi-modal PDFs, which is e.g. the case for an BOC(1,1). The three autocorrelation peaks of the BOC(1,1) leading to a multi-modal PDF. But due to an exponential weighting, as visible in (6.29), the side lobes may only be visible with logarithmic plots. Furthermore, the variance of the PDF of the PVT also depends on the received signal strength (signal amplitude). An increase in the signal amplitude behaves the same way as increasing the integration time, both result in a higher correlation value. This effect is shown in Fig. 7.1 and thus the transmission power of the satellites impacts the DPE estimate. The navigation message on data signals need to be accounted for long integration periods, which can be done by (1) building the non-coherent sum of short coherent batches or by (2) performing a prior navigation data bit wipeoff. In this aspect, this is not required for data free pilot signals.

6.3.8 Computational Complexity

The major drawback of DPE and BDPE is the computational complexity, as it

(1) requires to solve an 8-dimensional optimization problem and it
(2) requires a computational complex signal correlation step for each tracked signal for each optimization step in (1).

When considering a minimalistic GBF with just $N_{s,d=1} = 3$ nodes for each dimension to reconstruct the PDF of the PVT for $d = 8$ dimensions, which uses for the evaluation just $N = 8$ signals, the number of

$$N_{\text{corrs}} = N_{s,d=1}^{d} N = 52488 \tag{6.30}$$

correlators are required. A classical receiver would just require for the same example about $N_{\text{corrs}} = 48$ correlators (when consider an Early-Prompt-Late correlator for the In-phase and Quadrature channel). This simple example gives a order of magnitude of the processing complexity, whereas even a higher number of grid nodes or particles is required to properly represent the PDF. It could easily be seen, that achieving a real-time capable BDPE receiver, which performs a continuous tracking (no snapshot processing) is a very difficult task.

The work in [Peretic and Grace X Gao, 2020a] proposes to split up the 8-dimensional state into 2x4-dimensions by tracking the position and clock error (4 states) and velocity and clock drift (4 states) separately. The goal of

the separation is a reduction in computational complexity. This reduces the grid size from $N^8_{s,d=1}$ to $2N^4_{s,d=1}$, where $N_{s,d=1}$ is the number of grid nodes per dimension. This leads to a reduction in complexity of $N^8_{s,d=1} - 2N^4_{s,d=1}$. This is a significant reduction, but it needs to be considered, that both search spaces are inherently coupled and the full gain of DPE can only be exploit if both, the position and velocity search spaces are at their maxima's.

The realization of a real-time capable BDPE receiver is a challenging task which might require a tradeoff between the used algorithms, the targeted positioning performance and available computational resources. One novelty of this work is the proposed real-time capable BDPE architecture as discussed in the next chapter 6.4.

6.4 Proposed BDPE Receiver Architecture

In order to realize a real-time capable BDPE receiver or grid-based analysis tool which is independent from external information, two problems need to be solved,

(1) a significant reduction of the processesing complexity and
(2) to stay independent on external information.

In order to solve these problems, a maximum reuse of existing and high-efficient GNSS signal processing elements of an existing software receiver is targeted and the BDPE receiver is setup on top of a conventional GNSS receiver. This allows to solve both problems, because high-efficient methods together with enabling assumptions allow to reduce the processing complexity and the basis of a conventional receiver allows to stay independent, because DPE/BDPE can be initialized with a conventional PVT solution and can reuse the decoded ephemeris for the LOS projection. Therefore, it is proposed to use three enabling key elements to achieve a integrated real-time BDPE receiver,

(1) a vector tracking setup as discussed in chapter 5.9
(2) the usage of synthetically generated multi-correlation values (Doppler-Delay maps) as discussed in chapter 5.10
(3) and the assumption that interpolated correlation values are sufficiently accurate for DPE/BDPE when using a non-coherent approach

Hereby, the vector tracking concept is used for the LOS projection, which is required for DPE to align the receiver internal replica signals for the correlation process. Furthermore, the FFT based synthetic multi-correlator is applied to a time series of common correlation values to obtain very efficiently a Doppler-Delay map for each integration period. The proposed receiver architecture is shown in Fig. 6.6.

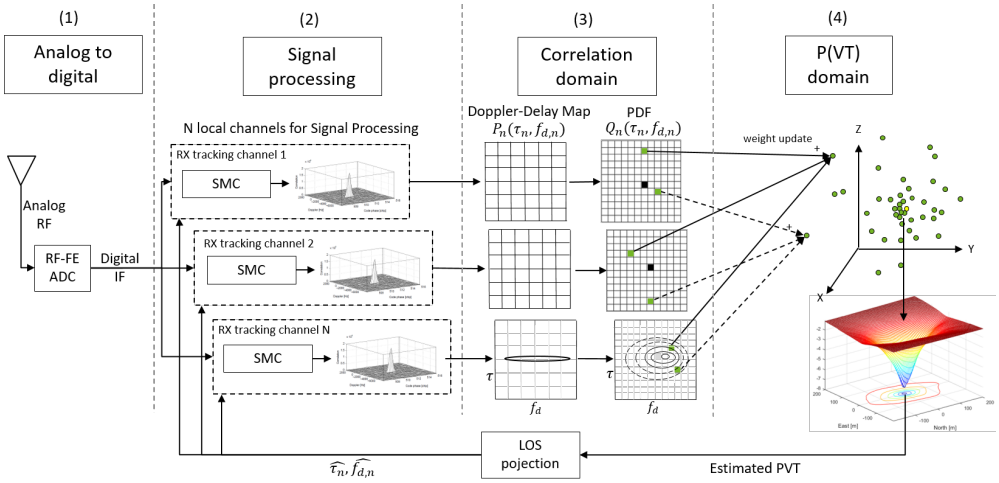

Figure 6.6: BDPE processing scheme as implemented in the SX3 software based GNSS receiver; (**1**) refers to the analogue to digital conversion, the first stage of the receiver; (**2**) refers to the GNSS signal processing, which produces massive number of correlation values using synthetical FFT based correlation methods for each tracked channel. The correlation values are converted to 2D joint PDFs in (**3**), which are further used to update the particle weights of a particle filter as shown in (**4**). For the grid-based analysis tool the particles in (**4**) are distributed over a equidistant grid and can be interpreted as grid nodes. Adapted from [Dampf, Lichtenberger, and Pany, 2019, Fig. 1].

The first block (1) refers to the RF front-end which does the signal conditioning of the analogue signal and the ADC. The digital I/Q-samples are the input to the signal processing block (2), which uses a channelized structure for signal acquisition, tracking and producing massive correlation values with the SMC. The second block consists of common FLL/PLL/DLL tracking loops, which are steered by the vector tracking feedback loop. Each tracking channel consists of a list of correlators with defined code offsets (not only Early-Prompt-Late correlators). The replica signals are generated and correlated against the incoming signal for each integration period. Each channel stores (buffers) a series of short coherently integrated correlation values (e.g. 1 ms) for all code offsets. The SMC removes the data bits and performs a complex FFT on the buffered series of complex valued correlation values to obtain the frequency domain (Doppler domain). This resembles a long coherent integration time and the output of the SMC is a non-coherently integrated Doppler-Delay map for each integration interval. The Doppler-Delay maps for each tracked signal are delivered to the third block (3), which shows the measured data in the correlation domain. One novelty of this work is the conversion of the Doppler-Delay maps into 2D joint PDFs, which deliver a probabilistic description of the measurements. The PDFs are used as measurement input for the fourth block (4), which shows the navigation processor. The measurement update from block (3) to (4) assumes that interpolated

data from the Doppler-Delay map or the PDF is sufficient. The navigation processor uses a Bayesian filter (grid or particle filter) to estimate the PVT directly from the correlation values. It should be noted, that the generation of the correlation values in the Doppler-Delay map is an intermediate step to achieve a high processing efficiency. In the literature BDPE is referred to a PVT estimate directly from the signal samples, but which implicitly requires the signal correlation step and which is explicitly shown in Fig. 6.6. Thus, the interpretation of the filter update directly from the signal samples and directly from the correlation values is the same, as the correlation values represent the state of the signal samples for a given code-phase and Doppler. The Bayes filter in the navigation processor in block (4) estimates the PVT, which is feedback via the vector tracking loop to the signal processor. The LOS projection uses the best estimate of the PVT and the ephemeris to obtain the signal synchronization parameters code delay $\hat{\tau}_n$ and Doppler $\hat{f}_{d,n}$ for the next correlation epoch for each signal n.

The correlation values of the Doppler-Delay map are obtained with the SMC, which applies the FFT on a time series of complex correlation values as discussed in chapter 5.10 and as given in (5.73) with

$$P_{\mathrm{SMC},k_0;u,m} = \sum_{l=0}^{L-1} P_{\mathrm{MC},k_l;u} \mathrm{e}^{-i2\pi \frac{lm}{L}} \tag{6.31}$$

where $P_{\mathrm{SMC},k_0;u,m}$ is a synthetically generated correlation value at sample epoch k_0 with code phase index u (defining the code phase offset) and Doppler bin index m (defining the Doppler offset). Hereby, l defines the index of the correlation value in the correlation buffer and k_l the first sample epoch of the correlation value with index l. Thus, $P_{\mathrm{MC},k_l;u}$ denotes the real correlation value at k_l in the time series of correlation values with the code offset index u. The resulting correlation values of the SMC can be represented in a matrix notation as $\mathbf{P}_{\mathrm{SMC}}$. This formulation delivers a discrete grid of complex correlation values in dependency of the code delay and Doppler. The major benefit of this FFT based approach is, that it is possible to generate massive correlation values for many signals very efficiently, in parallel and in real-time. The correlation values in (6.31) acts as input for the optimal weight update as given in (6.24) with

$$p(\mathbf{z}_k|\mathbf{x}^i_{\mathrm{rx},k}) = \underbrace{\frac{1}{(2\pi)^L} \exp\{-L\} N \sqrt{\frac{\pi}{2L}}}_{\text{const.}} \prod_{n=1}^{N} \underbrace{\exp\left\{\frac{|P_n(\tau_n, f_{d,n})|^2}{4}\right\} I_0\left(\frac{|P_n(\tau_n, f_{d,n})|^2}{4}\right)}_{Q_n(\tau_n, \omega_n)} \tag{6.32}$$

with

$$P_n(\tau_n, f_{d,n}) = f(\mathbf{P}_{\mathrm{SMC},n}, \tau_n, f_{d,n}) \tag{6.33}$$

where $f(\cdot)$ is a defined interpolation method used to interpolate τ_n and $f_{d,n}$ from the grid $\mathbf{P}_{\text{SMC}}$. As mentioned earlier, it is possible to update the Bayes filter with Doppler-Delay maps or with PDFs. In both cases, a bilinear interpolation is sufficient for $f(\cdot)$, if the resolution of $\mathbf{P}_{\text{SMC},n}$ for the code delay and Doppler is fine enough to deliver a reasonable accurate representation of the code and Doppler correlation function and PDF in (3) for the requested particles in (4) of Fig. 6.6. Based on the fact that the used software receiver is limited in the resolution of the correlator spacing by the sample period and the Doppler resolution is defined by the FFT settings of the SMC, a upsampling interpolation is required because the calculated PDF has a very narrow extension compared to the correlation function. It should be noted, that the true code correlation function has a rounded peak due to the band limitation of the RF front-end and the true Doppler correlation function has a rounded peak due to the sinc-shaped Doppler correlation function. Both could not be properly reconstructed with linear interpolation methods, which would lead to a sharp peaked triangle for the code and Doppler correlation function. According to the Nyquist-Shannon sampling theorem or respectively Whittaker-Shannon interpolation formula (sinc-interpolation) given with

$$x(t) = \sum_{-\infty}^{\infty} x[n]\text{sinc}\left(\frac{t - nT}{T}\right) \tag{6.34}$$

both, the code and Doppler correlation function can be optimally reconstructed. Hereby, $x(t)$ is the continuous interpolation result, $x[n]$ is the discrete input sequence and in this case the discrete complex correlation values from $P_{\text{SMC},n}$, T is the sample interval and $\text{sinc}(\cdot)$ denotes the normalized sinc function. In this work and as shown in Fig. 6.7 a 2D sinc-interpolation is used for $f(\cdot)$ in (6.33) to interpolate the Doppler-Delay map from the SMC. It should be noted that the sinc-interpolation is computationally expensive compared to a linear interpolation, thus a two-staged approach with a single prior sinc-upsampling step and later bilinear interpolation might be beneficial with a large number of particles or grid-nodes.

The proper interpolated correlation values allow to calculate the unnormalized PDF $Q_n(\tau_n, \omega_n)$ as an intermediate step for each signal n with

$$Q_n(\tau_n, \omega_n) = \exp\left\{\frac{|P_n(\tau_n, f_{d,n})|^2}{4}\right\} I_0\left(\frac{|P_n(\tau_n, f_{d,n})|^2}{4}\right) \tag{6.35}$$

This allows to calculate the PDF $p(\mathbf{z}_k|\mathbf{x}^i_{\text{rx},k})$ in (6.32) in a parallelized way and store the matrix $\mathbf{Q}_n$ as an intermediate result. This conversion step from correlation values of a Doppler-Delay map to 2D joint PDFs is depicted in Fig. 6.7 for a single GPS C/A code signal. The first row shows the Doppler-Delay

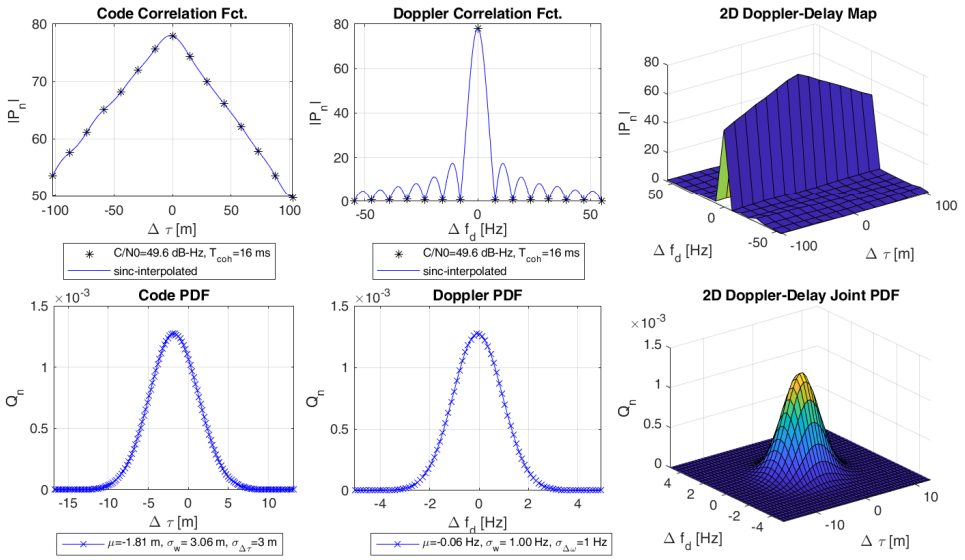

Figure 6.7: This figure shows in the first row the correlation result of the SMC for a single GPS C/A signal. The first row shows from left to right the triangular-shaped code correlation function, the sinc-shaped Doppler correlation function and the 2D Doppler-Delay map as output from the SMC. The black stars show the correlation values and the blue line is the sinc-interpolation result. The second row shows from left to right the corresponding PDFs, the marginalized PDF of the measurement in the code domain, the marginalized PDF of the measurement in the Doppler domain and the 2D Doppler-Delay joint PDF. The blue stars indicate the sinc-upsampled support points for the calculation of the PDF. The maps are centered at the last navigation solution.

map from the SMC. The code and Doppler correlation function are selected to contain the maximum correlation value (peak) of the Doppler-Delay map. The blue line shows the sinc-interpolated correlation values. The second row shows the normalized PDF $\mathbf{Q}_n$, whereas the code and Doppler PDF are the marginalization of the 2D joint PDF. It should be noted, that the measurement in the code and Doppler domain in $\mathbf{Q}_n$ has a very narrow extension compared to the code and Doppler correlation function, which is the main reason for the sinc-interpolation step. The 2D joint PDF in Fig. 6.7 shows the normalized probabilistic measurement of a single satellite, which is the input for the measurement update step of a particle or grid-based filter.

The attached Bayes filter framework of the navigation processor, as depicted in Fig. 6.8, allows beside GNSS measurements also measurements from other sensors. A very common approach in GNSS is the sensor fusion with an IMU, whereas the measurements of the IMU can be incorporated at the propagation step of the filter, which requires an adaption of the dynamic model and which is depicted by the red block in the figure. As the Bayes filter is operated in

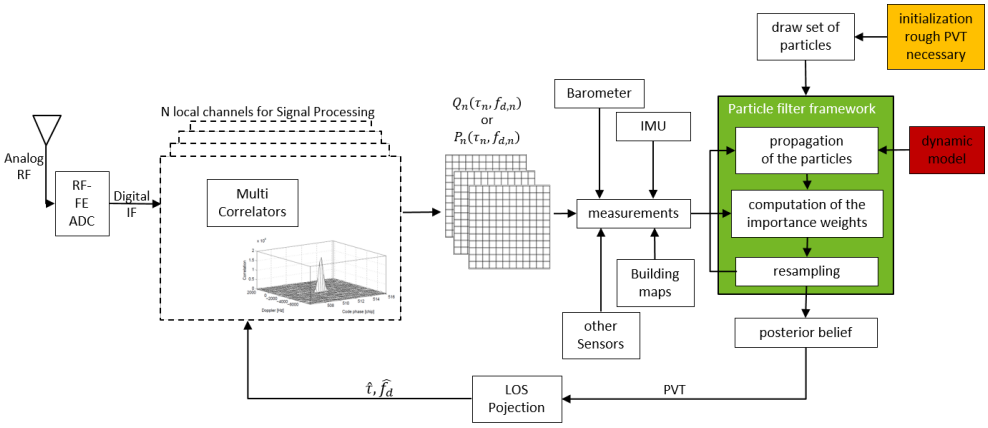

Figure 6.8: BDPE filter framework for a particle filter which is initialized with a set of particles. The filter executes three steps, propagating the particles in time, update the particle weight by incorporating a new set of measurements and resampling in case of high degeneracy. The posterior belief can be estimated from the resampled particle cloud. For the grid-based analysis tool the propagation and resampling step is obsolete, the grid nodes remain equidistantly distributed and the center of the grid is aligned to a reference solution.

the PVT domain, it is easily possible to incorporate data from probabilistic maps, which might contain a likelihood of the user position (e.g. a car is most likely located on a road). The grid-based or particle filter is initialized with an approximate PVT and corresponding uncertainty, which is depicted by the yellow block in the figure. In case of a grid-based filter, the grid-nodes are equidistantly distributed over a defined 8-dimensional PVT grid. It is convenient to align the position and velocity grid with the ECEF or navigation frame, as it allows an intuitive interpretation of the results. For the particle filter, the particles can be distributed according a defined distribution, whereas the implementation supports a Gaussian and a uniform initial distribution. As shown by the green block in Fig. 6.8, a particle filter executes iteratively three major steps, the state propagation, the measurement update and the resampling step.

6.5 Impact of Signal Degradation on DPE

The quality of the estimated PVT relies on the quality of the measured signal, but all received signals have been degraded during the transmission from the satellite to the receiver. A brief summary of error sources and how they impact DPE are given in the paragraphs below.

Multipath is caused by reflective environmental conditions, whereas strong multipath can be typically observed e.g. in urban canyons or beside buildings.

Multipath impacts on DPE as it deforms the correlation function and thus the PDF in the correlation domain. An example of the correlation function and thereof resulting PDF in the correlation domain is shown in Fig. 6.7. Based on the fact that the PDF in the PVT domain relies on the PDF in the correlation domain (as shown by the arrows between step (3) and (4) in Fig. 6.6), the resulting PDF in the PVT domain, as for example shown in Fig. 6.4, is also affected. The multipath will bias the resulting PVT estimate, but have less impact compared to classical tracking methods. The reason for the reduced impact on BDPE is the exponential weighting, whereas classical methods have a linear dependency on the correlation amplitude. The linear dependency is resulting from the S-cure, which describes the DLL discriminator function in dependency of the code phase error, as shown in Fig. 5.4. Multipath can be constructive and destructive, depending on the offset of the carrier phase. If the carrier phases are shifted by 180 deg to each other, the multipath is destructive. Multipath simulations and real-world data are discussed for the correlation domain in chapter 8.3 and real-world results are discussed for the PVT domain in chapter 8.7.1.

Signal Blockage occurs typically in forests or indoors. In case of signal blockage, the received signal is significantly weakened, diffracted and comes along with multipath. The signals are mostly that weak that classical tracking methods will have a loss of lock. In such situations DPE can fully exploit the additional tracking gain as given in (6.21). But the correlation function is significantly deformed which can lead to multi-modal PDFs in the correlation and PVT domain. Such scenarios are analyzed in chapter 8.7.1 and 8.7.2.

Interference and Jamming reduces the quality or completely denies the PVT estimate of a GNSS receiver and can be separated into intentional and unintentional interference. Unintentional interference sources are resulting from strong transmitted signals close to the GNSS frequency bands or from defect transmission hardware. Intentional interference aims to degrade the PVT estimate of the user under attack. Jamming litters the GNSS frequency bands in order to reduce the SNR until selected or all GNSS signals cannot be tracked anymore, which results in a bad positioning performance or complete denial of a PVT solution. Jamming can be separated in narrowband or wideband jamming. A narrowband jammer uses just a Continuous Wave (CW) signal on a distinct frequency, whereas wideband jammers typically use a chirping CW over a selected frequency range or noise with a selected bandwidth. Jamming is much more likely in contrast to spoofing, because jammers can be easily built and ordered in the Internet, whereas spoofing is much more complex and requires more technical expertise. Different methods exist to counter-fight interference sources on receiver side such as adaptive notch filtering [Kang, Kim, and Park, 2014], [Chien, 2015] or nulling antennas [McMichael et al., 2016].

Spoofing is intentional interference in order to deny, degrade or mislead the PVT of a user. Spoofing is closely related to matched spectrum jamming, which transmits a signal with a valid PRN and same modulation parameters as the true GNSS signals, but without navigation data or a valid PVT. If the PVT should be decepted, the spoofer need to generate authentic GNSS signals with a valid and consistent code, Doppler, PVT and navigation data message. State-of-the-art receivers may detect a spoofing scenario by observing the signal parameters, e.g. consistent C/No, changing Automatic Gain Control (AGC) values, or by identifying unexpected or incorrect navigation data bits. It is expected, that DPE is more resilient to spoofing compared to classical tracking methods, because the replica signal generation is coupled with the navigation solution and thus they may also rely on unaffected GNSS signals, similar to vector tracking. A spoofing attack with a valid PVT will become visible with DPE by observing a second maxima in the PVT domain. If the PVT of the spoofer is close to the PVT of the true PVT, the correlation functions and PDFs become deformed (like in a multipath case), if the PVT of the spoofer has a significant PVT offset to the true PVT, the PVTs can clearly be separated from each other and a spoofing attack could be easily detected with DPE, as it would be the case for a multi-correlator receiver. Bayesian filters are also used for multiple-target tracking, which can also be applied for tracking the spoofing signals or PVTs. Thus, BDPE in general allows to separate multiple PVTs in the PVT domain, as long as they are distinguishable from each other. Some upcoming GNSS signals are planned to carry an authentication code in order to be able to authenticate/separate correct and manipulated navigation signals. Spoofing is today mainly present in military warfare, but research is ongoing on how to protect critical infrastructure from such events. A comprehensive report on the worldwide spoofing activity is given in [C4ADS, 2019].

6.6 Previous and Parallel related work on DPE and BDPE

DPE was introduced in [Closas, Fernández-Prades, and Fernández–Rubio, 2007], [Closas, 2009] by formulating the problem and it shows how a DPE receiver estimates the PVT in a single step directly from the signal samples [Closas, Fernández-Prades, Bernal, et al., 2008]. As DPE allows for a significant increase in tracking sensitivity, this method was investigated in different GNSS related topics like GNSS signal acquisition performance in [Axelrad et al., 2011], [He and Petovello, 2014], [Esteves, Mohamed, and Ries, 2014], improved positioning accuracy when fusing DPE with visual information in [Ng and Grace Xingxin Gao, 2016a] or improving the robustness of position and time estimation during jamming and meaconing attacks in [Ng, Member,

et al., 2012], [Ng and Grace Xingxin Gao, 2016b]. The first real-time capable implementation of BDPE into a commercial software-based GNSS receiver was shown in [Dampf, Witternigg, et al., 2017] and [Witternigg et al., 2017], even if suboptimal but computational efficient algorithms and limitations in number of tracked GNSS signals have been made as a tradeoff to achieve real-time performance [Dampf, Frankl, and Pany, 2018]. Two difficulties arise with BDPE, the (1) receiver architecture of estimating the PVT directly from the signal samples deviates significantly from common receiver architectures, and (2) a particle or grid-based filter for BDPE requires a probabilistic description of the measurements. Beside this work solutions to these problems are given in [Dampf, Frankl, and Pany, 2018], which discusses a BDPE integration into a standard software receiver architecture using a vector tracking loop and a synthetic multi-correlator, shows how to perform the measurement update directly from correlation values instead of signal samples, shows how to convert the correlation values into a probabilistic description of the measurement in the range domain, shows how to achieve an optimal and stable weight update and shows a derivation of the optimal particle weight update for multiple GNSS signals. In order to increase the stability for BDPE using the optimal weight update, the mathematical framework was extended from measurements in the range domain to the Doppler domain in [Dampf and Pany, 2018]. The Stanford University is also developing a DPE receiver, whereas techniques and algorithms have been published in [Peretic and Grace X Gao, 2020a] and results have been analyzed in [Peretic and Grace X Gao, 2020b]. Investigations regarding direct time estimation with multiple spatial distributed antennas are dicussed in [Garcia-Molina and Fernandez-Rubio, 2020]. This work compares the achieved results to the results presented in [Axelrad et al., 2011], [Closas and Gusi-Amigó, 2017], [Peretic and Grace X Gao, 2020a] and [Peretic and Grace X Gao, 2020b]. All work on DPE aim to improve the PVT estimate, especially in challenging signal environments. The sources of signal degradation and impact on DPE is discussed in the next chapter.

7 Optimal Weight Update

In this BDPE approach one of the most crucial steps is to perform an optimal particle weight update directly from correlation values. This step is indicated in Fig. 6.6 by the transition from the third to the fourth block and in Fig. 6.8 with *computation of the importance weights*. Within this work two papers have been published, which derive an optimal and numerically stable particle weight update function in [Dampf, Frankl, and Pany, 2018] and extends the mathematical framework from the code phase to the Doppler in [Dampf and Pany, 2018]. The weight update equations in the latter publication allow for an optimal and stable particle weight update directly from the FFT based correlation values, which depend on code phase and Doppler.

7.1 Development of the Optimal Weight Update based on Code Phase and Doppler

This work derives the mathematical framework for the optimal weight update used in Bayesian filters. Equation (4.39) is repeated in (7.1) and shows the particle filter weight update for a Bootstrap filter.

$$w_k^i \propto w_{k-1}^i p(\mathbf{z}_k|\mathbf{x}_k^i) \tag{7.1}$$

In order to implement a Bootstrap filter, a probabilistic model of $p(\mathbf{z}_k|\mathbf{x}_k^i)$ with dependency of the prior state must be available. The state vector $\mathbf{x}_k^i$ is given in (5.54). The measurements $\mathbf{z}_k$ at current epoch k refer to a vector containing the raw GNSS samples. In order to update the particle weight, BDPE directly maps the PVT at the particles to the raw signal samples, which contains a superposition of all GNSS signals. Thus, a probabilistic description of the samples dependent on multiple GNSS signals must be available [Dampf, Frankl, and Pany, 2018]. Such a probabilistic model is given in [Pany, 2010, Eq. (5.9)] for a single GNSS signal with

$$p(\mathbf{s}|A,\tau,\omega,\phi) = \frac{1}{(2\pi)^L}\exp\left\{-\frac{1}{2}\sum_{\mu=1}^{L}|s_\mu - \underbrace{Ac(t_\mu-\tau)\exp\{i\omega t_\mu - i\phi\}}_{\text{Signal Model}}|^2\right\} \tag{7.2}$$

where the vector $\mathbf{s} \in \mathbb{C}^L$ contains all signal samples $s_\mu, \mu \in \{1,...,L\}$, which depend on the signal model parameters, the real valued signal amplitude $A \in \mathbb{R}^+$, the time delay $\tau \in \mathbb{R}$, the Doppler frequency $\omega \in \mathbb{R}$, the carrier phase $\phi \in [0, 2\pi[$ and i the imaginary number. The term $c(t_\mu - \tau) \in [-1, 1]$ refers to the modulated PRN code and the term $\exp\{i\omega t_\mu - i\phi\}$ to the signal carrier. The parameter $t_\mu \in \mathbb{R}$ defines the time at sample index μ and depends on the sampling frequency $f_s \in \mathbb{R}$ such as $t_\mu = \mu/f_s$. The probability distribution $p(\mathbf{z}_k|\mathbf{x}_k^i)$ in the weight update equation (7.1) can be related to the sample distribution in (7.2), where $\mathbf{z}_k$ equals the measured sample vector such as $\mathbf{s} = \mathbf{z}_k$, where $t_{\mu=1}$ corresponds to the time of the first sample in epoch k and $t_{\mu=L}$ to the time of the last sample in epoch k. The parameters A, τ, ω, ϕ for a single replica can directly be related to the PVT state $\mathbf{x}_k$, respectively, to the state of each PVT particle [Dampf, Frankl, and Pany, 2018]. The state $\mathbf{x}_k$ is given in (5.54), where the three-dimensional position and velocity is given in the ECEF reference frame.

The replica signal code phase τ_n and Doppler ω_n for a single signal of satellite n are related to $\mathbf{x}_k$ using (5.66) and (5.67) with $\omega_n = 2\pi f_{d,n}$. The equations need knowledge about the satellite position and velocity and thus the ephemeris data must be known. In a simplified simulation without atmospheric effects the terms for the troposphere and the ionosphere can be neglected. Additionally, in a synchronized simulator-receiver setup the terms for the clock corrections can be neglected. In such a setup, the correlation functions will perfectly overlap in the PVT domain. Furthermore it should be noted, that neglected hardware delays are expected to have no significant impact because (1) it is expected that there are no relative satellite hardware delays in a simulator setup if not explicitly simulated, and (2) the minor receiver hardware delay will move, without any further impact, into the clock error estimate.

Basically, the goal of the derivation is to retrieve a formulation for an optimal particle weight in dependence of an arbitrary number of used GNSS signals dependent on the code phase τ and Doppler ω only. This is necessary, because just a non-coherent DPE approach is targeted as a first realization. It should be noted, that a phase-coherent DPE approach is very difficult to achieve and can be considered as a follow-on investigation. In principle it is possible to relate the probabilistic model also on the signal amplitude and carrier phase, but the dimensionality and thus the complexity of the problem increases significantly.

Under the assumption that the carrier phase is uniformly distributed over 0 and 2π, it can be integrated out or in other words marginalized, as shown in [Pany, 2010], to

$$\begin{aligned} p(\mathbf{s}|A,\tau,\omega) &= \frac{1}{(2\pi)^L}\int_{\phi=0}^{2\pi}\exp\left\{-\frac{1}{2}\sum_{\mu=1}^{L}|s_\mu - Ac(t_\mu-\tau)\exp\{i\omega t_\mu - i\phi\}|^2\right\}d\phi \\ &= \frac{1}{(2\pi)^L}\exp\left\{-\frac{1}{2}\sum_{\mu=1}^{L}|s_\mu|^2\right\}\exp\left\{-\frac{LA^2}{2}\right\}I_0(A|P(\tau,\omega)|\sqrt{L}) \end{aligned} \tag{7.3}$$

with the definition of the correlator value $P_n(\tau,\omega)$ as

$$P_n(\tau,\omega) = \frac{1}{\sqrt{L}}\sum_{\mu=1}^{L}\bar{s}_\mu c_n(t_\mu-\tau)\exp\{-i\omega t_\mu\} \tag{7.4}$$

The correlation value $P_n(\tau,\omega)$ is taken from the multi-correlation maps as shown in Fig. 6.6 and I_0 refers to the Bessel function of the first kind and order zero [Dampf, Frankl, and Pany, 2018]. The stepwise integration procedure to obtain (7.3) from (7.2) is given in Appendix A and a similar equation for joint detection of weak GNSS signals can be found in [He and Petovello, 2014].

The next step is to integrate out the signal amplitude A and extend the signal model to multiple GNSS signals. The mathematical derivation to achieve a probabilistic description with dependency on multiple GNSS signals and on Doppler-delay maps is shown in detail in Appendix B. The result of the derivation in Appendix B is given by (7.5) with

$$p(\mathbf{s}|\boldsymbol{\tau},\boldsymbol{\omega}) = \frac{1}{(2\pi)^L}\exp\{-L\}N\sqrt{\frac{\pi}{2L}}\prod_{n=1}^{N}\exp\left\{\frac{|P_n(\tau_n,\omega_n)|^2}{4}\right\}I_0\left(\frac{|P_n(\tau_n,\omega_n)|^2}{4}\right) \tag{7.5}$$

With this equation a numerical problem exist and it cannot be solved directly with a computer due to a limited precision, especially with long integration times which lead to high correlation values P. This problem can be solved by doing the weight update in the logarithmic scale. The problem is discussed in detail and solved in Appendix B, whereas the stable plain weight update sequence for multiple GNSS signals N is given with

$$\widetilde{w}_{k-1}^{i} = \log(w_{k-1}^{i}) \tag{7.6}$$

$$\widetilde{w}_{k}^{i} = \widetilde{w}_{k-1}^{i} + \sum_{n=1}^{N} \left(\frac{|P_n(\tau_n, \omega_n)|^2}{2} - \log\left(\sqrt{2\pi \frac{|P_n(\tau_n, \omega_n)|^2}{4}} \right) \right) \tag{7.7}$$

$$\overline{w}_{k}^{i} = \widetilde{w}_{k}^{i} - \max(\widetilde{w}_{k}^{i}) \tag{7.8}$$

$$w_{k}^{i} = \exp(\overline{w}_{k}^{i}) \tag{7.9}$$

$$w_{k}^{i} = \frac{w_{k}^{i}}{\sum_{i=1}^{N_s} w_{k}^{i}} \tag{7.10}$$

The result of this plain weight update sequence is shown in Fig. 7.1 with a constant signal strength and different coherent integration times T_{coh}. It can be seen, that the resulting probability distribution function in the lower plot is not Gaussian distributed. It is more similar to a Laplace distribution (without proof), which is briefly discussed in chapter 8.2 and illustrated in Fig. 8.2. The shape and extension of the PDF depends on the received signal strength, on the signal type (higher bandwidth signals have a sharper correlation function which results in a smaller variance of the PDF), integration time and environmental conditions (e.g. multipath). A detailed discussion on the resulting PDF is published by the article in [Dampf, Frankl, and Pany, 2018] and in chapter 8. Tiny PDFs can be problematic with Bayesian filters, because the recursive estimation of the PDF can be suboptimal if the peak is located between grid nodes of a grid-based filter or cannot be covered well by particles of a particle filter.

Furthermore the extension of the PDF does not represent the true accuracy, because the model in (7.7) does not account for a UERE such as atmospheric effects (ionosphere, troposphere) or environmental effects (multipath, fading), which can lead to an instable or suboptimal behavior of a Bayesian filter. To account for these uncertainties in the raging accuracy, Gaussian nuisance parameters for the code phase and Doppler are introduced. The nuisance parameters model the measurement noise as Gaussian distributions. The mathematical formulation is given in detail in Appendix C and was published in [Dampf and Pany, 2018]. The resulting weight update for a Bayesian filter including the nuisance parameters is given with

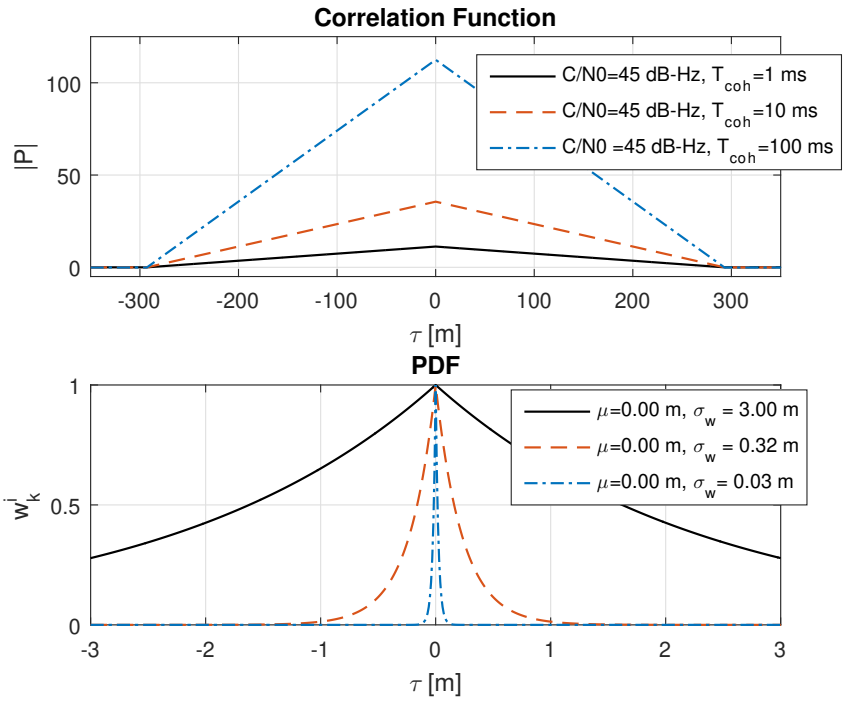

Figure 7.1: The plot is based on a MATLAB [The MathWorks Inc., 2019] simulation. The upper plot shows the correlation function from (7.4) for different coherent integration times for a $C/N0 = 45$ dB-Hz. The simulated signal was generated without noise (i.e., the C/No merely defines the correlation amplitude). The lower plot shows the corresponding probability function after one weight update from (7.9), for one signal $N = 1$ and assuming a uniform distribution from the previous epoch, i.e., $\widetilde{w}_{k-1}^{i} = 0$ from (7.7). The statistics in the lower plot refer to the weighted mean μ and weighted standard deviation σ_w [Dampf and Pany, 2018, Fig. 4].

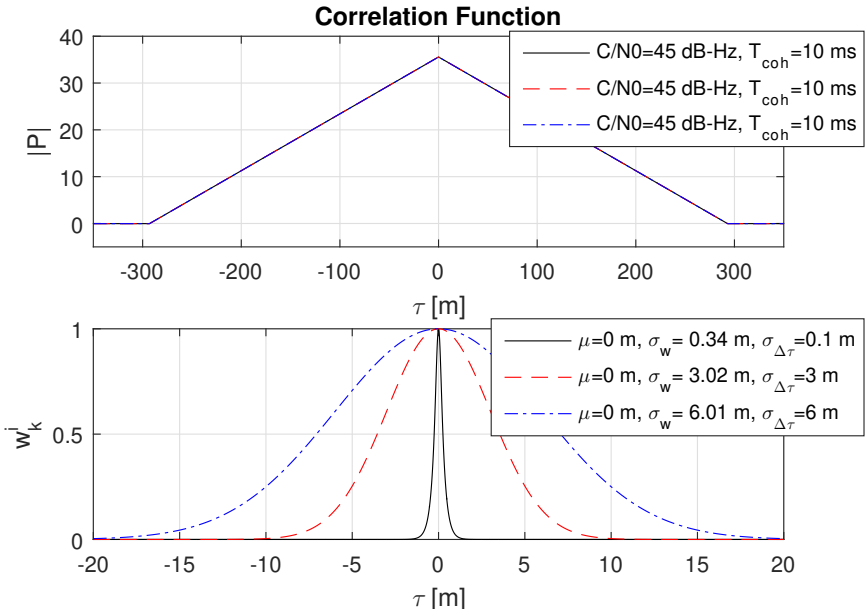

Figure 7.2: Impact of different code delay bias standard devications $\sigma_{\Delta\tau}$ on the weights w_k^i for a coherent integration time $T_{coh} = 10$ ms. It can be seen that σ_w approaches the theoretical limits for $\sigma_{\Delta\tau} = 3$ and $\sigma_{\Delta\tau} = 6$ [Dampf, Frankl, and Pany, 2018, Fig. 7].

$$\begin{aligned}\tilde{w}_k^i \;=\; & \tilde{w}_{k-1}^i + \sum_{n=1}^{N}\left[\log\left(\frac{p(\Delta\tau_1)p(\Delta\omega_1)}{\sqrt{2\pi\frac{|P_n(\tau_n+\Delta\tau_1,\omega_n+\Delta\omega_1)|^2}{4}}}\right) + \frac{|P_n(\tau_n+\Delta\tau_1,\omega_n+\Delta\omega_1)|^2}{2}\right. \\ & + \log\left(\sum_{k=1}^{K}\sum_{j=1}^{J}\exp\left\{\frac{|P_n(\tau_n+\Delta\tau_k,\omega_n+\Delta\omega_j)|^2}{2} - \frac{|P_n(\tau_n+\Delta\tau_1,\omega_n+\Delta\omega_1)|^2}{2}\right\}\right. \\ & \left.\left.\frac{p(\Delta\tau_k)p(\Delta\omega_j)}{p(\Delta\tau_1)p(\Delta\omega_1)}\;\frac{|P_n(\tau_n+\Delta\tau_1,\omega_n+\Delta\omega_1)|}{|P_n(\tau_n+\Delta\tau_k,\omega_n+\Delta\omega_j))|}\right)\right]\end{aligned} \tag{7.11}$$

and is used instead of (7.7), whereas $p(\Delta\tau)$ and $p(\Delta\omega)$ describe the uncertainty for the code phase and Doppler as a Gaussian with zero mean, as shown in (C.1) and (C.3). The effect is visualized in Fig. 7.2 for a constant coherent integration time $T_{coh} = 10$ ms. The increased estimated weighted standard deviation $\sigma_{\Delta\tau}$ due to the convolution with zero mean Gaussian with given $\sigma_{\Delta\tau}$ is clearly visible in the lower plot. Hereby, $\sigma_{\Delta\tau}$ defines the minimum variance of the PDF of the signal which can be interpreted as the maximum ranging accuracy. The proposed approach allows to cover an unmodeled UERE and to stabilize a Bayesian filter, which takes this PDF as measurement input.

The nuisance parameters (measurement noise) are applied to the measurement in the code and Doppler domain. As a result, a two-dimensional map

similar to a Doppler-Delay correlation map is obtained, which shows the joint PDF in Fig. 7.3. The left plots correspond to the plain weight update using (7.7) and the right plots correspond to the update with nuisance parameters from (7.11). The nuisance parameters define a lower limit for the variance of the measurement, which is visible by the increased extension of the peak.

The calculation of the particle weights based on the proposed logarithmic weight update sequence with (7.11) is computationally expensive, especially if the convolution with the gaussian nuisance parameters is performed in the time domain. Therefore, a computationally efficient approach in the frequency domain is proposed in chapter 7.2.

7.2 Performance Optimized Generation of Logarithmic PDFs

The performance optimized generation of a PDF was published in [Dampf, Lichtenberger, and Pany, 2019] and is also discussed here to give a complete overview of the implemented algorithm. In order to describe a more efficient algorithm, equation (7.11) and (7.7) are rewritten to

$$\begin{aligned} Q_n(\tau_n,\omega_n) &= \log\left(\frac{p(\Delta\tau_1)p(\Delta\omega_1)}{\sqrt{2\pi\frac{|P_n(\tau_n+\Delta\tau_1,\omega_n+\Delta\omega_1)|^2}{4}}}\right)+\frac{|P_n(\tau_n+\Delta\tau_1,\omega_n+\Delta\omega_1)|^2}{2} \\ &\quad+\log\left(\sum_{k=1}^{K}\sum_{j=1}^{J}\exp\left\{\frac{|P_n(\tau_n+\Delta\tau_k,\omega_n+\Delta\omega_j)|^2}{2}-\frac{|P_n(\tau_n+\Delta\tau_1,\omega_n+\Delta\omega_1)|^2}{2}\right\}\right. \\ &\quad\left.\frac{p(\Delta\tau_k)p(\Delta\omega_j)}{p(\Delta\tau_1)p(\Delta\omega_1)}\,\frac{|P_n(\tau_n+\Delta\tau_1,\omega_n+\Delta\omega_1)|}{|P_n(\tau_n+\Delta\tau_k,\omega_n+\Delta\omega_j))|}\right) \qquad (7.12) \\ \widetilde{w}_k^i &= \widetilde{w}_{k-1}^i+\sum_{n=1}^{N}Q_n(\tau_n,\omega_n) \qquad (7.13) \end{aligned}$$

where (7.12,A) corresponds to the first line of (7.12), (7.12,B) corresponds to the exponential term in the second line of (7.12) and (7.12,C) corresponds to the of summation term of the second and third line of (7.12). Hereby the Gaussian nuisance parameters are described with $p(\Delta\tau) \sim \mathcal{N}(\mu_\tau,\sigma_\tau^2)$ and $p(\Delta\omega) \sim \mathcal{N}(\mu_\omega,\sigma_\omega^2)$, both centered at mean $\mu_\tau = 0$ m, $\mu_\omega = 0$ Hz and with a user defined standard deviation σ_τ and σ_ω. The multi-correlator maps produced by the receiver are centered at state x_k which was used for generating the correlation values, thus $\Delta\tau$ and $\Delta\omega$ are code phase and Doppler offsets to x_k. $\Delta\tau_1$ and $\Delta\omega_1$ from (7.12) correspond to the maximum correlation value of the multi-correlator grid found with $\underset{\Delta\tau_1,\Delta\omega_1}{\text{argmax}}\, P_n(\tau+\Delta\tau),\omega+\Delta\omega)$.

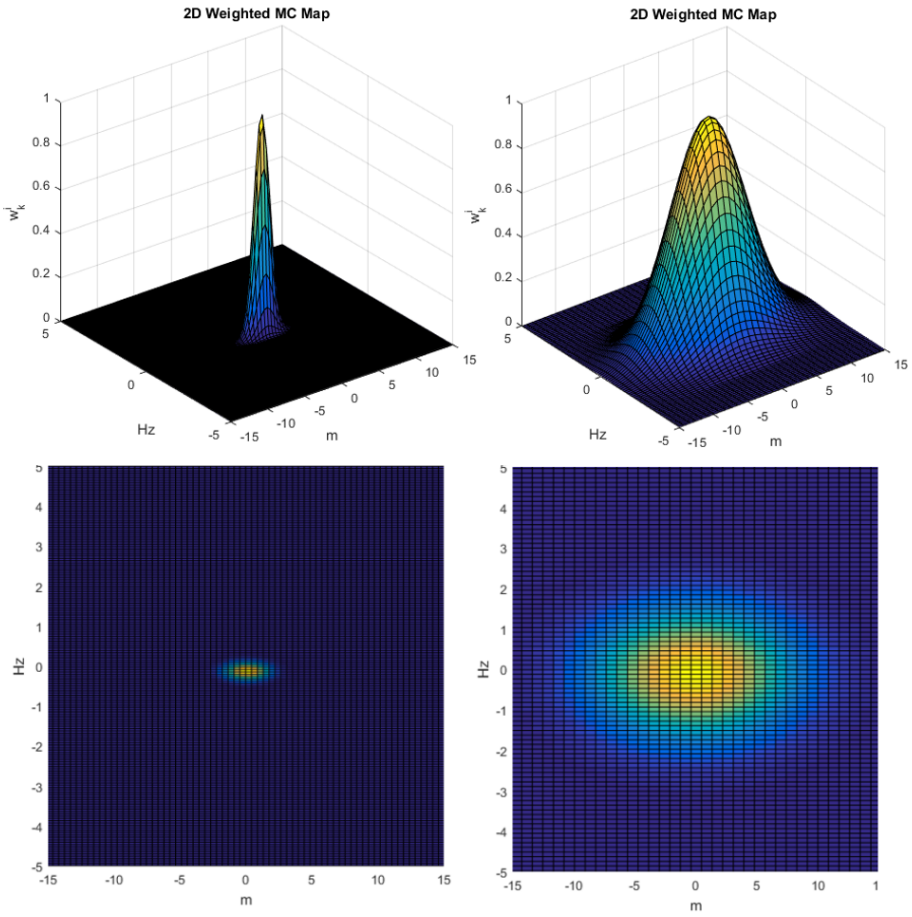

Figure 7.3: These plots show the joint probability density function for the range and Doppler based on a coherent integration time of $T_{coh} = 103$ ms. The values are normalized to 1. The left plot shows the joint PDF from the plain weight update and the right plot shows the joint PDF including the introduced nuisance parameters from (7.11) with $\sigma_{\Delta\tau} = 5$ m and $\sigma_{\Delta\omega} = 1$ Hz [Dampf and Pany, 2018, Fig. 8 and 9].

Hereby, (7.13) is the core step of the weight update in the logarithmic scale and can be separated into three parts: (1) The history $\widetilde{w}^i_{k-1}$ refers to the weight of the previous epoch and for epoch-wise analysis the variable is set to $\widetilde{w}^i_{k-1} = 0$. (2) is the sum of all GNSS signals which contribute to the weight $\widetilde{w}^i_k$ and (3) describe a logarithmic PDF map $Q_n(\tau_n, \omega_n)$ for signal n. Herby, $Q_n(\tau_n, \omega_n)$ from (7.12) can be generated for each satellite individually and is based on the multi-correlator values $P_n(\tau_n, \omega_n)$ and the nuisance parameters σ_τ and σ_ω. For a real-time particle filter based BDPE receiver it is crucial to efficiently calculate $Q_n(\tau_n, \omega_n)$ from (7.12). A grid of multi-correlator values $P_n(\tau_n, \omega_n)$ is produced in the software receiver by applying FFT on a time series of correlator values at defined correlator (code phase) offsets. The FFT transforms this timely sequenced correlation values from the time domain into the frequency domain and the correlation values become dependent on the Doppler.

In more detail, the software receiver produces a discrete two-dimensional multi-correlator map $P_{n,i,j}(\tau_{n,i,j}, \omega_{n,i,j})$ in code phase (index i) and Doppler direction (index j). This chapter describes the processing steps to obtain efficiently a discrete logarithmic probability density function $Q_{n,k,l}(\tau_{n,k,l}, \omega_{n,k,l})$ for each signal n. The algorithm is optimized for the CPU and uses for parallelization the Open Multi-Processing (OpenMP) [OpenMP ARB, 2020] and for vectorization the Intel® Integrated Performance Primitives (IPP) [Intel Corporation, 2020], which allow to utilize the principle of Single Instruction Multiple Data (SIMD). Based on the fact, that all arithmetic operations need to be applied on a two-dimensional grid, the data is interpreted as an image in order to make use of the highly optimized IPP Image Processing toolset. It is beneficial, that $Q_{n,k,l}(\tau_{n,k,l}, \omega_{n,k,l})$ can be calculated independent for each signal n, which can be easily parallelized and the processing is done in parallel on different threads. Fig. 7.4 shows the three major processing steps, which are up-sampling, exponential weighting and convolution with the nuisance parameters.

7.2.1 Up-Sampling

The number of code phase bins i depend on the extension of the map in code phase direction, which is defined by the number of correlators (typically 7 correlators $i = 1, \ldots, 7$ for the optimized approach with a correlator spacing of $\Delta d = c/f_s = 14.9$ m at $f_s = 20$ MHz, where c is the speed of light). The number of Doppler bins j depend on the number of timely sequenced correlator values which are used for the synthetically generated multi-correlator map. The Doppler resolution is given with $\Delta f_d = \frac{1}{T_{coh}\Lambda}$, $T_{coh} = 1$ ms and where Λ denotes the FFT length. The first step in the up-sampling procedure cuts a reasonable range in code phase and Doppler direction from the center

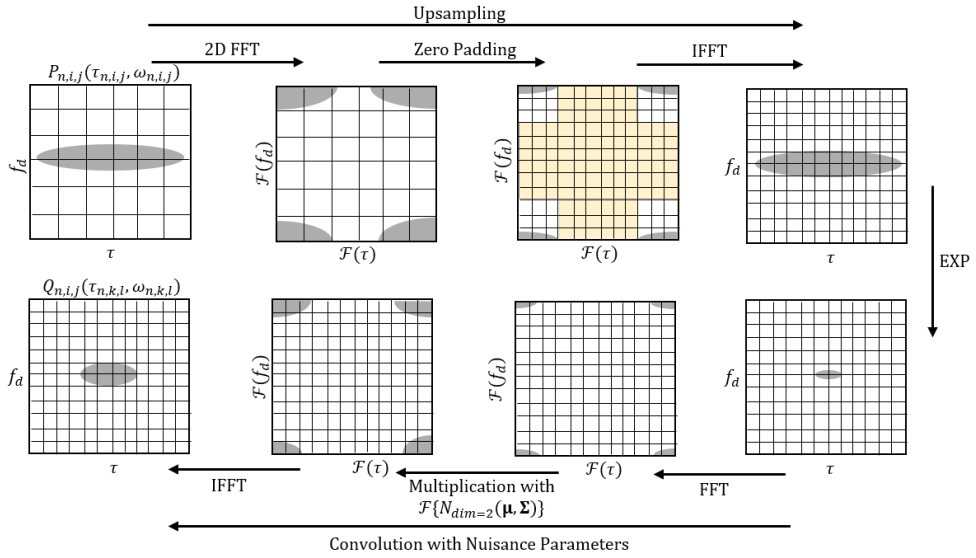

Figure 7.4: Processing chain when calculating the logarithmic probability density function $Q_{n,k,l}(\tau_{n,k,l}, \omega_{n,k,l})$ from multi-correlator maps $P_{n,i,j}(\tau_{n,i,j}, \omega_{n,i,j})$. The first row shows the FFT based up-sampling procedure, the last column to the right refers to the exponential weighting and the second row corresponds to the convolution with the nuisance parameters $\mathcal{F}\{\mathcal{N}_{\text{dim}=2}(\boldsymbol{\mu}, \boldsymbol{\Sigma})\}$ [Dampf, Lichtenberger, and Pany, 2019, Fig. 2].

of the map (e.g. $i = 1, \ldots, 7$ and $j = 64 - 3, \ldots, 64 + 4$, leading to a quadratic map with 7x7 bins) and shifts the cut multi-correlator map into the frequency domain using the DFT. All IPP Fourier transform operations cause a cross-flip on the quadrants, which is indicated by the second map in Fig. 7.4. The second step applies the method of zero-padding. The inverse Fourier transform on a rectangle in the frequency domain leads to a 2D sinus cardinalis function in the time domain. Thus, the zero-padding operation (rectangular extension) equals a sinc-interpolation in the time domain, which is used to interpolate the multi-correlator values. The sinc-interpolation is used because the analog RF signal samples pass through a bandpass filter in the receiver front-end. Based on the fact that a bandpass filter is a rectangular window in the frequency domain and a sinus cardinalis in the time domain [Oran Brigham, 1990, Example 4.6], a sinc-interpolation up-sampling algorithm was chosen. The insertion of zeros is shown by the yellow area in Fig. 7.4. The new (up-sampled) number of bins is calculated by the number of inserted zeros, such that $(k = i + \#\text{zeros})$ and $(l = j + \#\text{zeros})$. Herby it is considered that the new number of bins are $k, l \in 2^x$ with x being the order of the FFT and Inverse Fast Fourier Transform (IFFT). This allows to use the much more efficient FFT/IFFT instead of the DFT/Inverse Discrete Fourier Transform (IDFT). The used up-sampled grid size can be defined by the user and was chosen to be 512x512 bins.

7.2.2 Exponential and Convolution

The exponential function (7.12,B) is applied on the up-sampled multi-correlator map. The resolution after up-sampling must be fine enough, such that a significant number of grid nodes cover the extension and shape of the resulting function after applying the exponential, as shown by the lower right plot in in Fig. 7.4. The utilization of the nuisance parameters to cover unmodeled UEREs is done by convolution with a 2-dim (multivariate) normal distribution $\mathcal{N}_{\text{dim}=2}(\boldsymbol{\mu}, \boldsymbol{\Sigma})$, where $\boldsymbol{\mu} = [\mu_\tau = 0, \mu_\omega = 0]$ is a vector of length 2 containing the zero mean and $\boldsymbol{\Sigma}_{2x2} = \begin{bmatrix} \sigma_\tau & 0 \\ 0 & \sigma_\omega \end{bmatrix}$ is the covariance matrix. Hereby, μ must be a zero vector, otherwise an offset would be introduced during the convolution. The convolution in the time domain equals a multiplication in the frequency domain. This Fourier transform property is utilized to perform an efficient convolution with the nuisance parameters, whereas this convolution step is indicated with (7.12,C). Therefore, a discrete grid of the multivariate probability distribution is generated with the up-sampling size of e.g. 512x512 bins, shifted to the frequency domain and is buffered for each multiplication step. Thus, $\mathcal{F}\{\mathcal{N}_{\text{dim}=2}(\boldsymbol{\mu}, \boldsymbol{\Sigma})\}$ needs only be generated once, as long the nuisance parameters σ_τ and σ_ω do not change. The convolution with the nuisance parameters equals in image processing a Gaussian blur filter. After the IFFT, some scaling is applied, which refers to (7.12,A). The result of this process is $Q_{n,k,l}(\tau_{n,k,l}, \omega_{n,k,l})$, which is referred to as logarithmic probability density function.

7.2.3 Computational Performance

The performance has been evaluated on an Intel® Core i7-6700HQ quad core CPU (8 threads) with up to 3.5 GHz integrated in a notebook from the year 2015. The software was compiled with an Intel® compiler using the Intel® Parallel Studio XE Professional 2018 to support optimal parallelization with OpenMP [OpenMP ARB, 2020] and vectorization with the IPP [Intel Corporation, 2020]. The software was compiled for release without linked debug information and with highest compiler optimization level O3. Based on the fact, that writing files to the hard drive is a very time-consuming task, all log output and file dumps have been disabled. The achieved processing times for different settings are plotted in Fig. 7.5 and listed in Tab. 7.1. The analysis focuses on the generation time of the upsampled map $Q_{n,k,l}(\tau_{n,k,l}, \omega_{n,k,l})$ with Single Threading (ST) only, whereas the processing time of the weight update for the particles or grid-nodes is focused on ST and Multi Threading (MT). Thus, the left plot in Fig. 7.5 shows the upsampling time for a single signal, whereas this time scales linearly with the number of processed signals, if only ST is used. The right plot in Fig. 7.5 shows the processing time for the

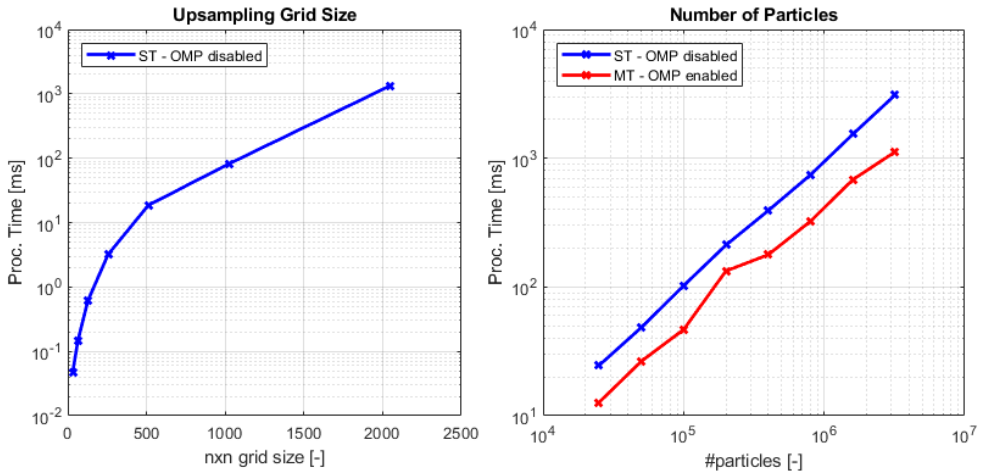

Figure 7.5: These plots show the processing time of the upsampling process in dependence of the grid size (left) and the processing time to update a given number of particles or grid nodes (right). The left plot has a linear scale for the grid size on the x-axis and a logarithmic scale for the processing time on the y-axis. The right plot uses a logarithmic scale for both, the number of particles on the x-axis and the processing time on the y-axis. The plotted values are listed in Tab. 7.1.

particle or grid node weight update step. Based on the fact, that the number of particles is significantly larger than the available CPU cores, a meaningful performance gain with MT is expected, whereas the red-line in the right plot of Fig. 7.5 shows the MT results. It can be seen, that the MT case is almost parallel to the ST case, but with an offset. This offset equals a constant reduction in processing time with same number of particles or grid nodes. The theoretical gain, when neglecting the overhead for parallelization, which can be achieved with a quad-core CPU and hyper-threading technology, is given with a factor of 8, but only a factor of 2 was achieved with the current architecture.

The generation of $Q_{n,k,l}(\tau_{n,k,l}, \omega_{n,k,l})$ with 512x512 bins out of $P_{n,i,j}(\tau_{n,i,j}, \omega_{n,i,j})$ with 7x7 bins took in average 18 ms. When fully utilize the quad-core CPU, theoretically 8 maps can be generated in parallel also in 18 ms plus a minor parallelization overhead. The processing of the particle filter needs for 25000 particles in average 12 ms with MT, whereas the expected ideal parallelization gain was not achieved. Beside the time for signal correlation, these times are the major drivers when targeting a real-time BDPE receiver or a real-time capable analysis tool. It is assumed, that the required processing time will significantly decrease when using the latest CPU technology, a higher number of cores and when further improve the architecture for parallelization. It can be concluded, that a real-time BDPE receiver or PDF analysis tool based on logarithmic probability density functions from (7.12) can be realized with latest CPU performances and when choosing appropriate settings.

Table 7.1: This table lists the achieved upsampling time in dependence of the grid size in the left part of the table and the processing time to perform the weight update on a given number of particles/grid nodes in the right part of the table. Vectorization with the IPP is applied for the ST and MT case and MT is implemented with the use of OpenMP. The processing times are averaged with 100 maps (epochs), values with (*) are averaged with 25 maps (epochs) and k refers to thousand. The listed values are plotted in Fig. 7.5.

Grid Size [-]	**time ST [ms]**	**Particles [-]**	**time ST [ms]**	**time MT [ms]**
32x32	0.047	25k	24.543	12.681*
64x64	0.146	50k	48.413*	26.461*
128x128	0.613	100k	102.324*	46.650*
256x256	3.194	200k	211.342*	133.052*
512x512	18.605	400k	391.917*	177.999*
1024x1024	81.967	800k	743.717*	324.110*
2048x2048	1337.054*	1600k	1536.220*	681.975*
		3200k	3099.332*	1121.322*

8 Analysis of the Probability Density Function

This chapter starts with a discussion on the processing setup for the analysis tool and estimation of statistical parameters. The presented results show a (joint) Probability Density Function (PDF) and correspond to the correlation domain or PVT domain. The correlation domain results focus on the pseudorange PDF in LOS direction (1-D) and the PVT domain results focus on the local north-east plane (2-D). In order to understand the behavior of PDFs in general, the discussion is continued with the product of Gaussian and non-Gaussian PDFs in a 1-D and 2-D domain. Thereafter, an analysis of the pseudorange PDF in LOS direction based on simulations and real-world data is presented. Once the simplified one-dimensional behavior is understood, 2-D joint PDFs in the PVT domain are discussed in context of the satellite constellation geometry and impact of nuisance parameters. This chapter is concluded with a comparison of the derived PDF to existing publications and a comprehensive analysis of real-world data in challenging environments. A large part this chapter has been published in [Dampf, Frankl, and Pany, 2018], [Dampf and Pany, 2018] and [Dampf, Lichtenberger, and Pany, 2019].

8.1 Processing Setup and Statistics

The analysis is done with three different processing setups, (1) simulations are performed with MATLAB [The MathWorks Inc., 2019] to illustrate the behavior of the PDFs, (2) simulations are performed with a GNSS simulator and the SX3 [IFEN GmbH, 2019b] GNSS software receiver and (3) real-world data has been recorded and post-processed with the SX3 only. Hereby, the SX3 is configured to process the data with the implemented BDPE navigation module as discussed in chapter 6.

The 2D analysis is based on a grid-based filter as discussed in chapter 4.5, but with some assumptions. The analysis is performed with the SX3 software receiver and the implemented BDPE navigation module. Hereby, the grid-based filter was parametrized such that the particles are distributed over an equidistant grid centered at a reference position. The analysis focuses on the unfiltered PDF of the state estimate and thus the weight is evaluated for each

epoch without considering any history. Thus, the weight from the previous epoch $w^i_{k-1|k-1}$ in (4.32) is obsolete, which makes also the state propagation in (4.30) obsolete. The grid-based analysis tool evaluates the weight from (4.33) based on the weight update sequence (7.6) to (7.10) and with (7.11) instead of (7.7). In order to generate high resolute PDFs, only 2 dimensions are analyzed in the PVT domain. The presented data will focus on the position domain in north-east direction, but results are also shown for the velocity in north-east and clock error/clock drift. An analysis of a subspace (e.g. 1-dimensional or 2-dimensional) still requires knowledge of all PVT states, thus the remaining dimensions need to be tracked in parallel. Therefore, the BDPE module can be aided or fully aligned to a reference PVT from a SPP (least squares code-based position solution) [Tian et al., 2013] or Low Visibility Positioning (LVP) (vector tracking Kalman filtered position solution) [Pany and Eissfeller, 2006], [Won, Eissfeller, and Pany, 2011] solution. The aiding concept and processing setup is shown in Fig. 8.1. Hereby, the implementation supports a full PVT aiding or any combination of position, velocity and time. The word aiding was chosen for the case when the module is operated in the BDPE tracking mode and any subspace of the PVT is aided by a reference, but it should be noted that for the grid-based analysis a full alignment to the reference PVT is done. The analysis is based on the following steps,

1. calculate the reference PVT,
2. align the center of the grid to the reference PVT,
3. update the weights (generate the PDF of the state estimate),
4. calculate the statistics of the PDF,
5. dump the results to a file,
6. and plot the results with MATLAB.

The scenario and the processing options for the analysis with the GNSS simulator are listed Tab. 8.1, whereas a simple static scenario with GPS L1 C/A signals and equal received power level for all signals is considered.

Table 8.1: List of parameters used for the GNSS simulator and receiver

Scenario	Static Open Sky
Rcv. Power Level	50 dBHz (all satellites)
System	GPS
Frequency Band	L1
Signal	C/A Code
Ionosphere	disabled
Troposphere	disabled
User Position ECEF $[x, y, z]$	[4171691.176, 872119.610, 4730006.239] m
User Velocity ECEF $[v_x, v_y, v_z]$	[0.0, 0.0, 0.0] m/s
Sample Rate f_s	20.64 MHz

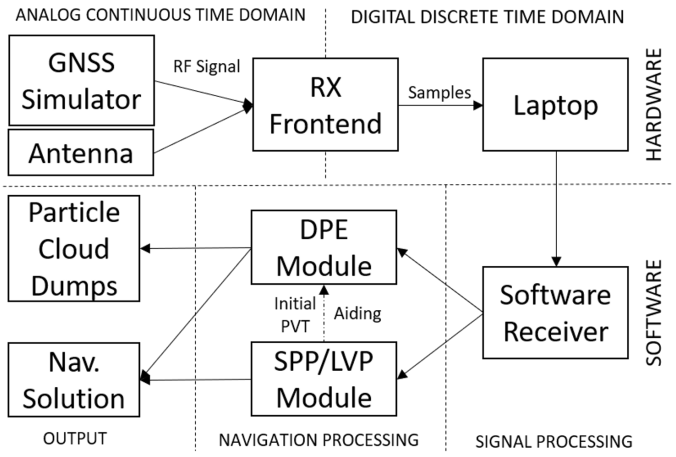

Figure 8.1: The schema shows the aided/aligned BDPE receiver setup for high-resolution analysis of the PDF for a 1-dimensional or 2-dimensional subspace, which is used for the simulations with the GNSS simulator and for the real-world setup [Dampf, Lichtenberger, and Pany, 2019, Fig. 3].

The SX3 and BDPE module processing settings to generate the correlation functions and PDFs in the PVT domain are listed in Tab. 8.2. Hereby, the generation of the correlation function in the PVT domain is performed with the large grid and the generation of the PDFs in the PVT domain is performed with the small grid settings. The different grid sizes are necessary, because the extension of the PDF is in order of 10 meters, whereas the correlation function in the PVT domain (for GPS L1 C/A) is in order of 300 meters.

Table 8.2: List of parameters used for generation of the PDFs (small grid) and the correlation function (large grid) in the PVT domain.

	Small Grid	**Large Grid**
Coherent Integration Time T_{coh}	16 ms	16 ms
Number of correlators	15	61
Nuisance Param. Code $\sigma_{\Delta\tau}$	3 m	-
Nuisance Param. Doppler $\sigma_{\Delta\omega}$	1 Hz	-
Position Grid Size	40x40 m or 50x50 m	1000x1000m
Position Grid Resolution	0.2 m	5 m
Doppler Grid Size	2x2 m/s	-
Doppler Grid Resolution	0.01 m/s	-
Time Grid Size	10 m and 1 m/s	-
Time Grid Resolution	0.1 m and 0.01 m/s	-

Regarding the presented statistics, all mean and variance estimates in this work are based on a Gaussian distribution assumption and use the equations

for the weighted mean and weighted variance

$$\mathbf{m} = \sum_{i=1}^{N} w_k^i \mathbf{x}_k^i \tag{8.1}$$

$$\sigma^2 = \frac{\sum_{i=1}^{N} w_k^i (\mathbf{x}_k^i - \mathbf{m})^2}{\sum_{i=1}^{N} w_k^i} \tag{8.2}$$

where $\mathbf{m}$ is the weighted mean vector based on the weight w_k^i from (7.10) and the particle 8-dim state $\mathbf{x}_k^i$ for epoch k. For completeness, the weighed variance vector σ^2 is normalized with $\sum_{i=1}^{N} w_k^i$, which is in principal not necessary because the weights are already normalized in (7.10).

8.2 Product of Probability Density Functions

The aim of this section is to get an understanding of Gaussian and Non-Gaussian products for the 1-dimensional (correlation domain) and 2-dimensional (PVT domain) case. The section shows, how Gaussians behave and interact when building the product with another Gaussian or non-Gaussian. At the particle weight update, the product of distributions corresponding to each satellite is built, which is visible in (7.13). Note that (7.13) shows a sum because the update is performed in the logarithmic scale. The PDF of a measurement in the code domain looks similar to a Laplace distribution with the plain weight update and with an infinite sampling bandwidth. This can be seen when comparing the shape of the Laplace distribution (c) in Fig. 8.2 to the infinite bandwidth measurement in Fig. 7.1. Furthermore, the PDF of a measurement in the code domain becomes Gaussian like distributed, if the nuisance parameters are applied (convolution with a Gaussian), and becomes non-Gaussian in challenging signal environments. Fig. 8.3 shows in the first two plots (upper row) the normalized result of a product between two biased Gaussians. A bias in the mean can be caused by unmodeled UEREs (ionosphere, troposphere, multipath or other errors). It should be noted, that the offset between the Gaussians does not lead to multi-modality, because the product of two Gaussian PDFs result in another Gaussian with different mean and variance [Smith III, 2011, Chap. Product of Two Gaussian PDFs]. It needs to be distinguished between a multiplication of random variables and the multiplication of (their) Probability Density Functions (PDFs). The product of two Gaussian PDFs lead to another Gaussian, but which is not a PDF. A Gaussian PDF can be obtained with an additional normalization step, which is illustrated in Fig. 8.4. The third plot (lower left) in Fig. 8.3 illustrates the product between two Gaussians with different variance, which results in

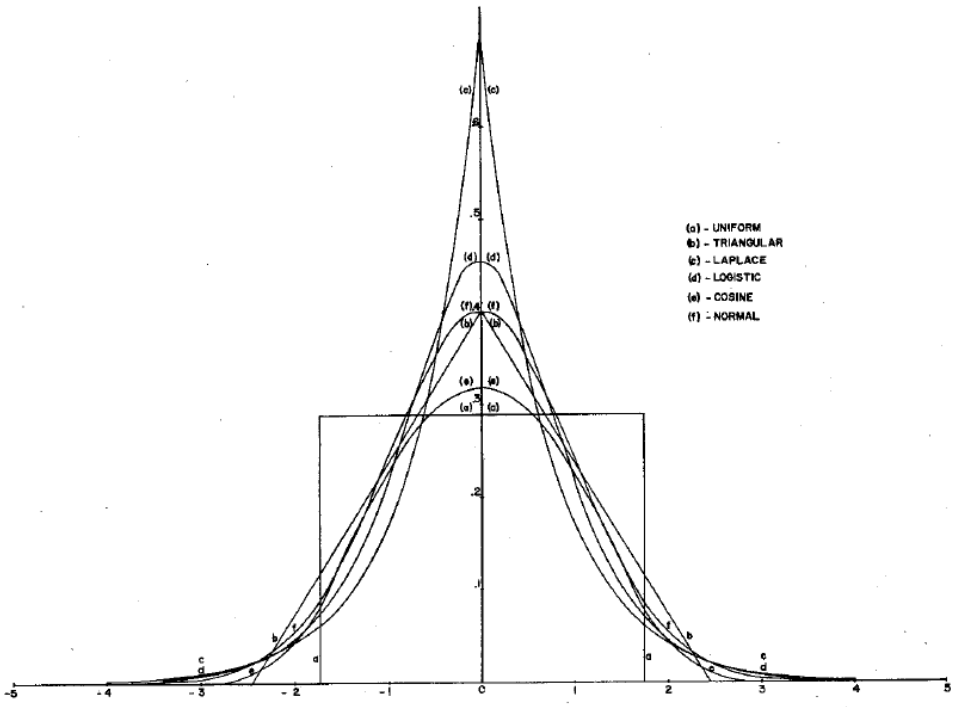

Figure 8.2: This plot illustrates different PDFs, where (a) is a uniform distribution, (b) a triangular distribution, (c) a Laplace distribution, (d) a logistic distribution, (e) a cosine distribution and (f) a normal distribution [Kotz, Kozubowski, and Podgórski, 2001, Fig. 2.1].

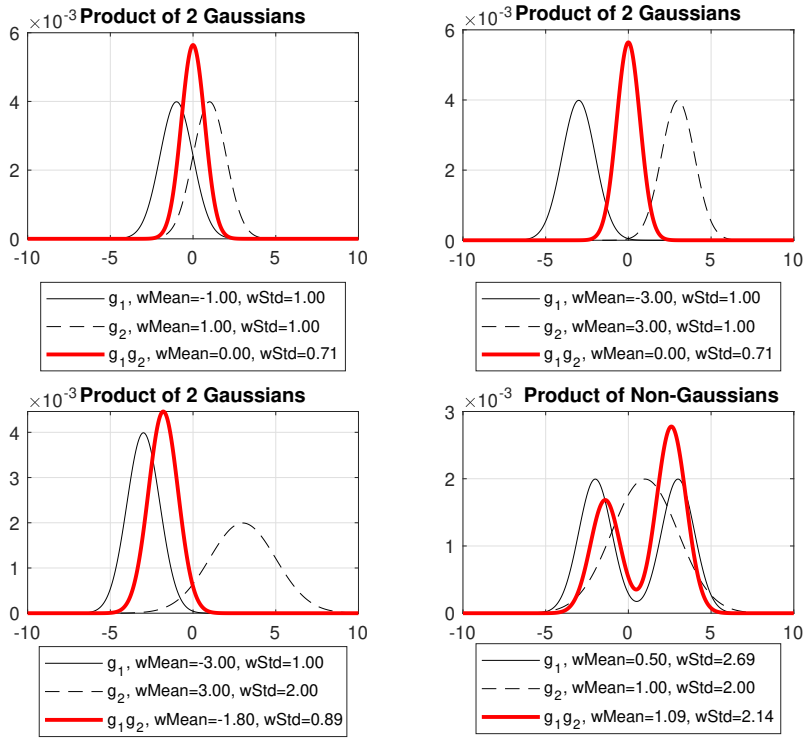

Figure 8.3: These plots illustrate how Gaussian and Non-Gaussian distributions behave when building their products. All presented results have been normalized to $\sum w_k^i = 1$ in order to obtain a PDF. The first three plots show the result of the product of two Gaussians and third plot the result of a Gaussian with a multi-modal PDF.

another Gaussian located closer to the Gaussian with smaller variance. This is very interesting and refer to a weighting of the quality of the measurements, whereas good signals with a small variance have a stronger contribution to the resulting PDF. The fourth plot (lower right) shows the product between a Gaussian and a non-Gaussian multi-modal PDF, which results in another non-Gaussian multi-modal PDF. This means, that in case of just a single non-Gaussian or multi-modal distributed measurement, the result in the PVT domain must become also non-Gaussian or multi-modal.

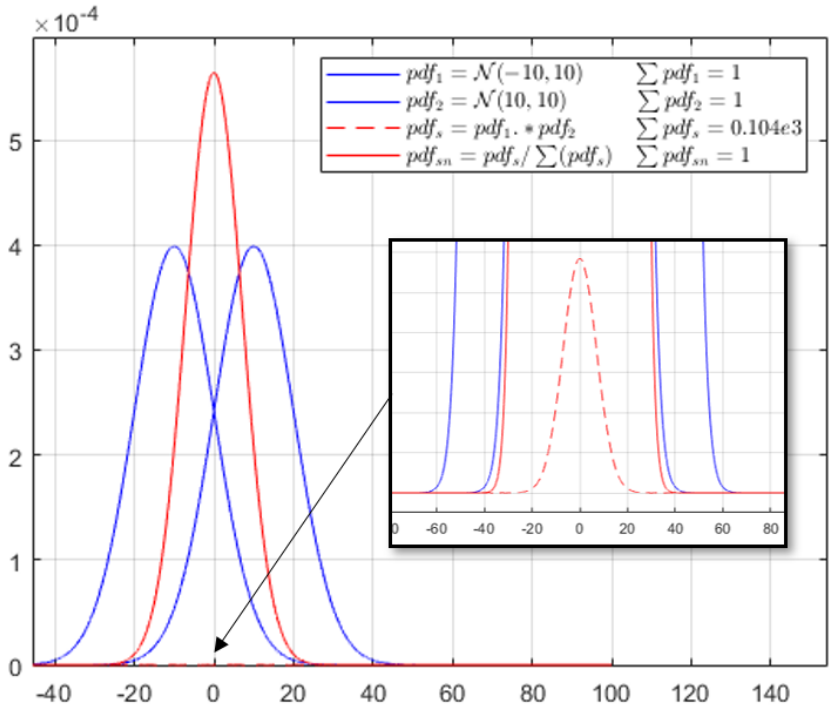

Figure 8.4: This plot proves that the product of 2 Gaussian PDFs is a Gaussian, but not a PDF, as shown by the dashed red line. This is just because the integral over the new Gaussian does not sum up to 1. But after normalization of the resulting Gaussian, a Gaussian PDF can be obtained, which is shown by the continuous red line.

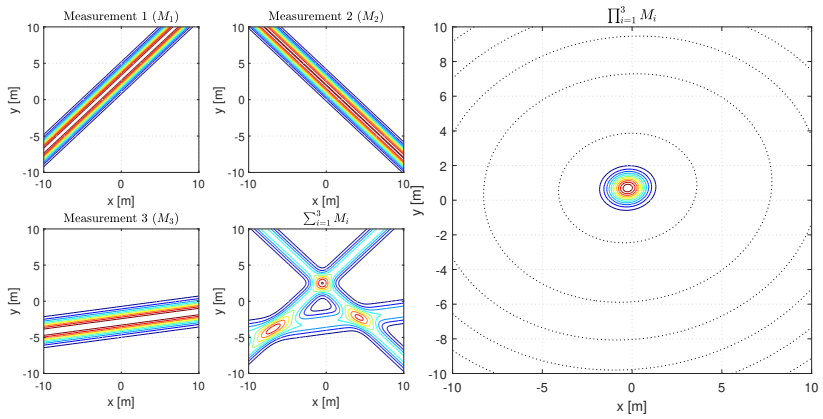

Figure 8.5: This figure illustrates on a 2-dimensioanl plane that the product of biased Gaussian measurements along a straight line (M1, M2, and M3) lead to another biased Gaussian, as shown by the right plot. These biases result from unmodeled UEREs. The Gaussians are placed along a straight constant amplitude line, which should come close to a real measurement of a single satellite [Dampf, Lichtenberger, and Pany, 2019, Fig. 15].

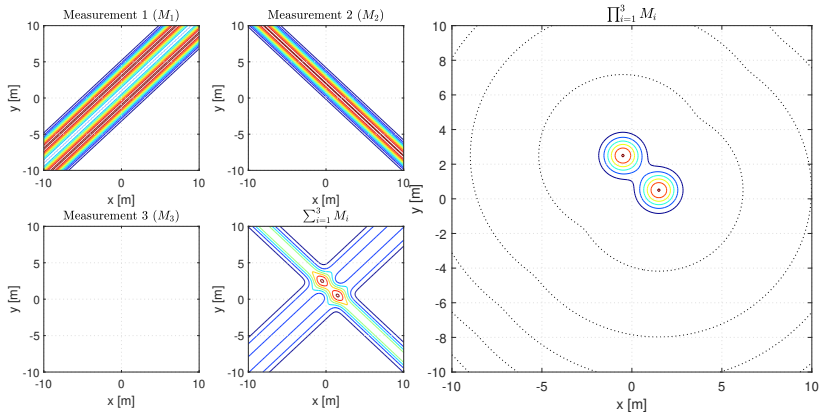

Figure 8.6: This figure illustrates that multi-modalities in the 2-dimensional plane (right plot in the figure) can only result from multi-modal measurements as depicted by M_1. Note that measurement M_3 is not used for this illustration [Dampf, Lichtenberger, and Pany, 2019, Fig. 16].

In general, biases result from unmodeled UEREs, if any PVT or modeling parameter in (5.28) or (5.32) is misaligned with the true. Multi-modality appears only if the measurement itself is multi-modal, which can be the case in challenging environments. These two cases are illustrated in Fig. 8.5 and Fig. 8.6 for a 2-dimensional case. Both figures illustrate the measurements M_n as a Gaussian in the local plane. The middle lower plot in each figure shows the

sum of the measurements just for completeness, whereas the result obtained by (7.13) is the product of the measurements illustrated by the large plot to the right. The results of the 1-dimensioanl case from Fig. 8.3 are applicable to the 2-dimensional case. Hereby, the plot in Fig. 8.5 shows that the product of three Gaussian measurements M_1, M_2 and M_3 results in a joint Gaussian PDF. Fig. 8.6 illustrates the second case, where the product of a non-Gaussian multi-modal measurement M_1 with a Gaussian M_2 result in another multi-modal PDF. These principles are applicable for the multi-dimensional case, but it should be noted that measurements are noisy and not Gaussian distributed, which leads to a similar but not same behavior with real measurements.

8.3 Understanding the Pseudorange Probability Density Function

The content of this chapter was published in [Dampf, Frankl, and Pany, 2018]. The previous chapter 7 presented the optimal weight update sequence for DPE when using a Bayes filter, whereas the sequence is given by (7.6) to (7.10) and the problem with the resulting narrow probability function is shown in Fig. 7.1. In (7.11), a possible solution is proposed to overcome the presented issues. In order to understand the behavior of the proposed weight update function, an analysis is performed for (7.11) within this chapter for a single signal $N = 1$ and assuming a uniform distribution from the previous epoch, i.e., $\widetilde{w}_{k-1}^{i} = 0$. All simulations have been performed completely with MATLAB [The MathWorks Inc., 2019], except the real-world scenarios, which take as input the correlation values from the GNSS software receiver. The MATLAB simulation performs a correlation with a simulated GNSS signal. In order to see clearly the impact of the different parameters, the simulated signal was generated without noise. All following plots show the correlation values $|P|$ from (7.4) and the resulting weight w_k^i from Equation (7.9) when using (7.11) as weight update function. For visualization purposes (7.9) is plotted instead of (7.10). This is because of the normalized amplitude to 1, which makes a comparison easier to visualize. The derived equations do not consider any present multipath signal, thus there is no estimation of multipath parameters nor a handling or mitigation of multipath.

The next subsections analyze the impact on the resulting probability function for

- different signal strengths,
- different code delay bias variances,
- constructive and destructive multipath,
- short, medium and far multipath,

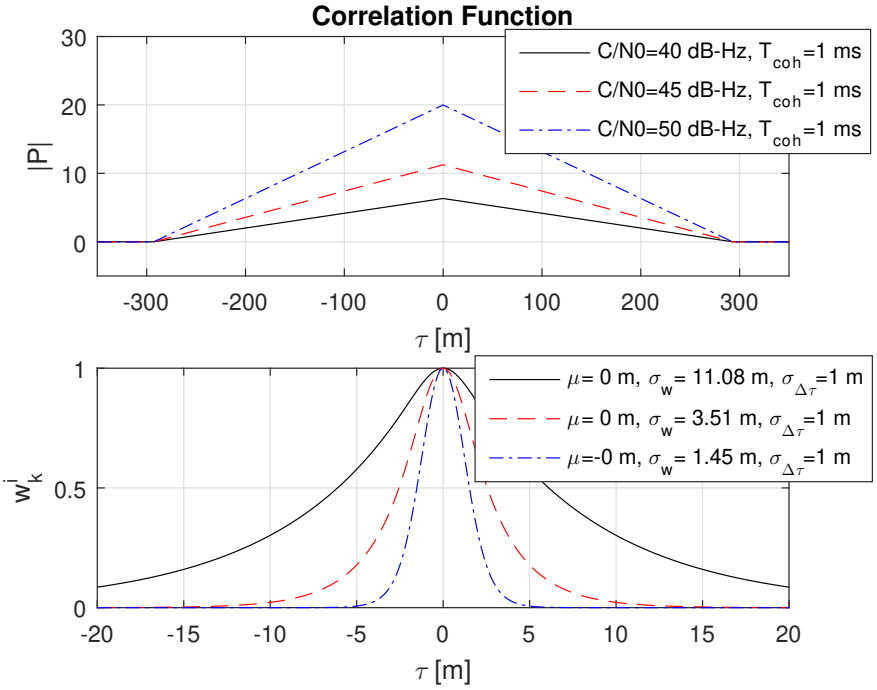

Figure 8.7: Impact of different GNSS signal amplitudes on the correlation values $|P|$ and resulting probability function for a constant coherent integration time T_{coh} and constant code delay bias standard deviation $\sigma_{\Delta\tau}$. Higher signal strengths result in a smaller weighted standard deviation σ_w of the probability function [Dampf, Frankl, and Pany, 2018, Fig. 5].

- different multipath amplitudes,
- two significant real-world scenarios under open-sky and urban conditions.

8.3.1 Impact of Different Signal Strengths

Basically, a higher GNSS signal amplitude increases the correlation value from (7.4) and thus influences (7.11). From this, it is expected that changes in amplitude do not shift the mean of the resulting probability function but influence the variance. This is obvious, because a stronger received GNSS signal must result in a more accurate estimate, which is shown in Fig. 8.7.

8.3.2 Impact of Different Code Delay Bias Variances

Basically, the expected measurement accuracy σ_w strongly depends on the amplitude of the correlation value $|P|$ and thus on the coherent integration

time T_{coh} and the navigation signal strength. However, with the introduction of a theoretical lower limit of the measurement accuracy in (C.5) defined by $\sigma_{\Delta\tau}$, the estimated accuracy σ_w must approach the lower limit $\sigma_{\Delta\tau}$ with an increasing correlation value $|P|$. This behavior is shown in three consecutive plots in Fig. 8.8–8.10 with an increasing coherent integration time $T_{coh} = [1, 10, 100]$ ms. From this series, it is clearly visible that σ_w also approaches a very small $\sigma_{\Delta\tau} = 0.1$ m in the case of a long coherent integration time $T_{coh} = 100$ ms.

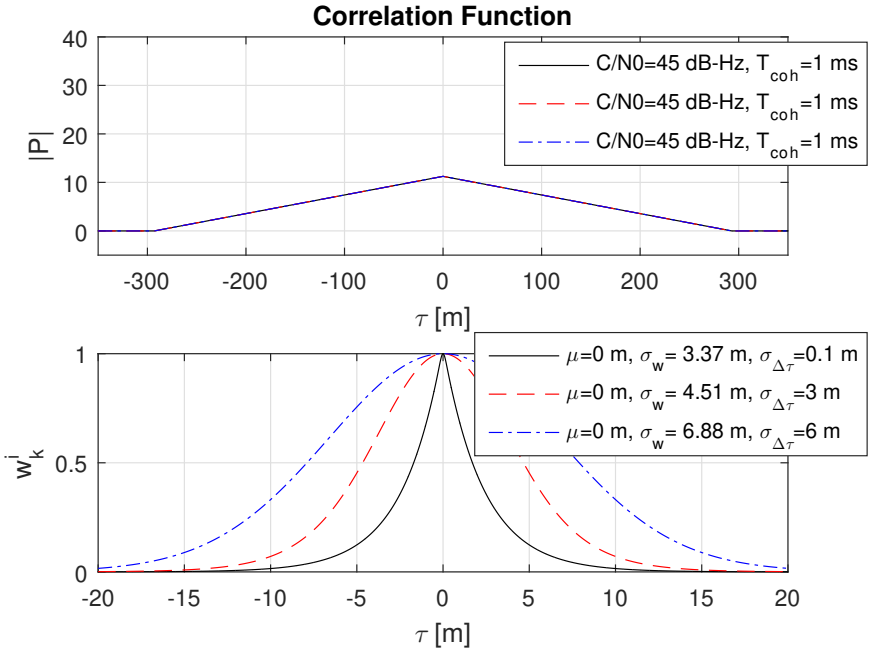

Figure 8.8: Impact of different code delay bias standard deviations $\sigma_{\Delta\tau}$ on the weights w_k^i for a coherent integration time $T_{coh} = 1$ ms. For the given conditions, only the weighted standard deviation σ_w for $\sigma_{\Delta\tau} = 6$ m seems to approach the theoretical lower limit of $\sigma_{\Delta\tau}$. In particular, $\sigma_{\Delta\tau} = 0.1$ m cannot be reached due to the influence of the low correlation time T_{coh} at given $C/N0$ [Dampf, Frankl, and Pany, 2018, Fig. 6].

The magnitude of $\sigma_{\Delta\tau}$ should cover residual user range errors (coming from orbit, satellite clock, multipath or ionospheric errors), which can be in the range of several meters.

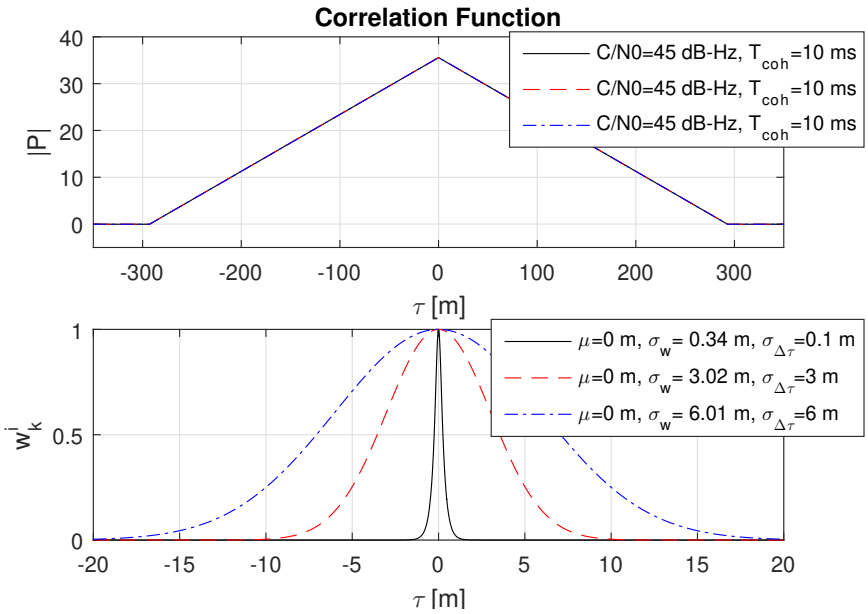

Figure 8.9: Impact of different code delay bias standard deviations $\sigma_{\Delta\tau}$ on the weights w_k^i for a coherent integration time $T_{coh} = 10$ ms. It can be seen that σ_w approaches the theoretical limits for $\sigma_{\Delta\tau} = 3$ m and $\sigma_{\Delta\tau} = 6$ m [Dampf, Frankl, and Pany, 2018, Fig. 7].

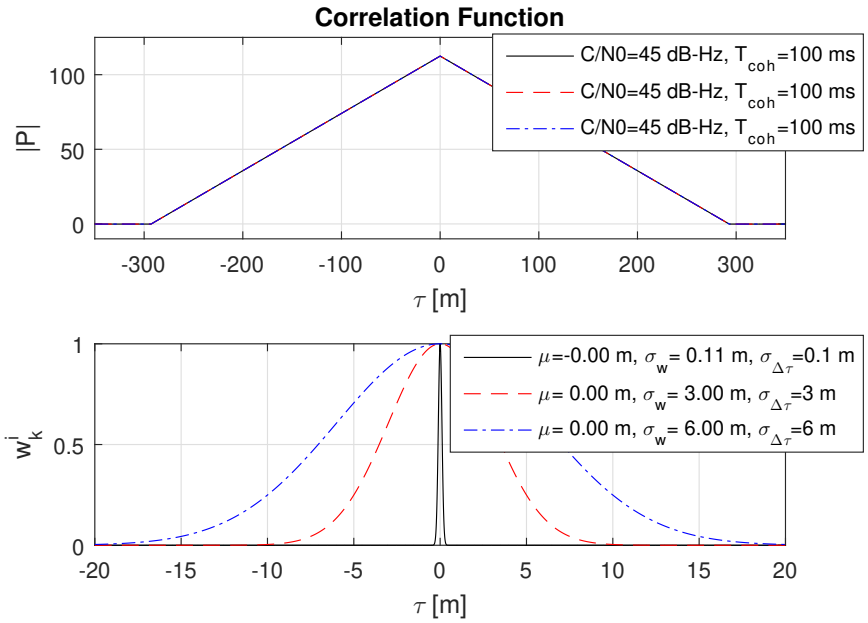

Figure 8.10: Impact of different code delay bias standard deviations $\sigma_{\Delta\tau}$ on the weights w_k^i for a coherent integration time $T_{coh} = 100$ ms. It can be seen that σ_w now approaches the theoretical limits for all $\sigma_{\Delta\tau}$. Note also the significantly changed amplitude on $|P|$ [Dampf, Frankl, and Pany, 2018, Fig. 8].

8.3.3 Impact of Constructive and Destructive Multipath

The influence of constructive and destructive multipath is shown for a realistic case with a multipath amplitude of $\alpha_{MP} = 0.5$ with respect to the LOS signal and a multipath offset of $\Delta\tau_{MP} = 50$ m in Fig. 8.11. As similar to the conventional Delay-Lock-Loop (DLL) in a GNSS receiver and thereof resulting pseudorange measurement, the weighted mean μ of the probability function also becomes biased. It can be seen that the resulting bias in μ is in the opposite direction for the constructive and destructive case. Furthermore, the destructive multipath reduces the amplitude of the correlation value $|P|$, which increases the weighted standard deviation σ_w, while the constructive multipath acts in the opposite direction and may also reduce the variance in distinct cases as visible in Fig. 8.12 for the black line. Furthermore, it can be seen that constructive and destructive multipath changes the resulting probability function in a different way, even if the multipath parameters $\Delta\tau_{MP}$ and α_{MP} are exactly the same.

8.3.4 Impact of Short, Medium and Far Multipath

The impact on short, medium and far multipath on the probability function is shown on a strong multipath case $\alpha_{MP} = 0.9$. Basically, it is expected that such a strong multipath seldomly occurs in typical real-world scenarios, but it was chosen to clearly visualize the impact of an increasing multipath offset. It can be seen in Fig. 8.12 that an increase in $\Delta\tau_{MP}$ directly increases σ_w.

An interesting effect is the short constructive multipath case with an $\Delta\tau_{MP} = 3$ m. In this case, the weighted standard deviation σ_w is underestimated and shows a smaller variance than the LOS signal. This can be dangerous because this leads to a biased and at the same time more accurate measurement, compared to the truth. Considering the present multipath and incorporating it into the models for the weighting may prevent such an underestimation.

8.3.5 Impact of Different Multipath Amplitudes

It is expected that an increase of the multipath amplitude α_{MP} further shifts the mean and increases the variance. This case is outlined in Fig. 8.13. Naturally, in the case that the multipath signal is as strong as the LOS signal, the resulting probability function automatically covers the whole uncertainty range with a mean exactly between the two signals. This case is shown with the dash-dotted blue line in Fig. 8.13.

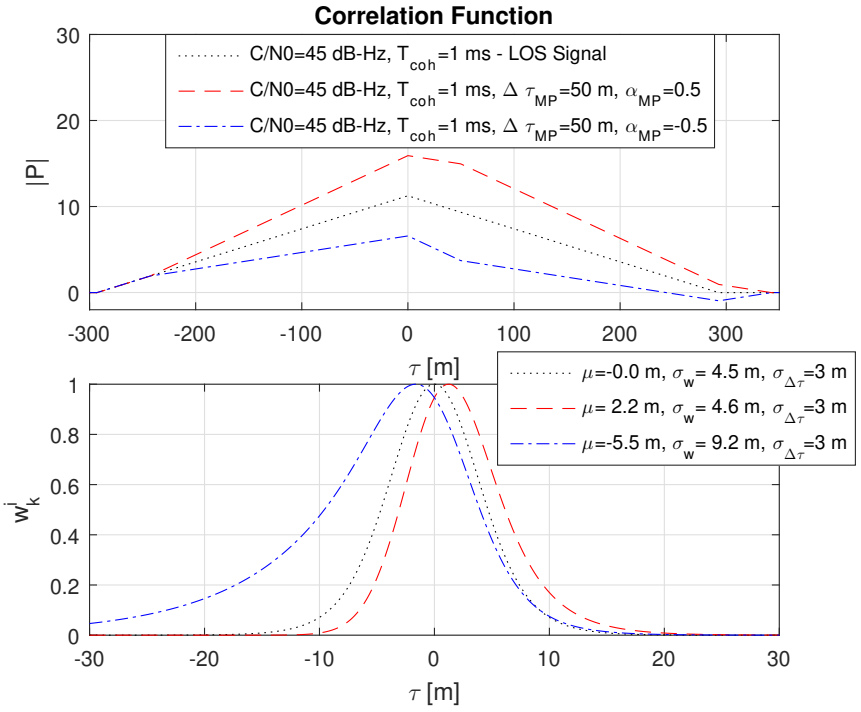

Figure 8.11: Influence of constructive and destructive multipath on the probability function with a relative multipath offset of $\Delta\tau_{MP} = 50$ m and an amplitude of $\alpha_{MP} = 0.5$ with respect to the line-of-sight signal. The black dotted line refers to the LOS signal. It can be seen that the multipath variants shift the weighted mean μ in the opposite direction and that the destructive multipath significantly increases σ_w due to the lower amplitude in $|P|$ [Dampf, Frankl, and Pany, 2018, Fig. 9].

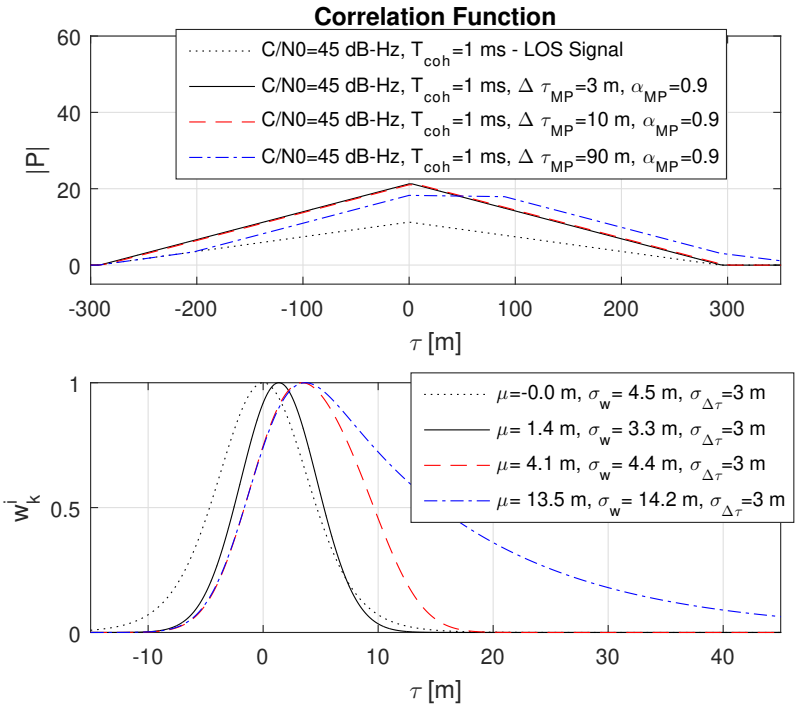

Figure 8.12: Impact of different multipath offsets $\Delta\tau_{MP}$ on the probability function. For a better visualization, a strong relative multipath to the LOS signal with $\alpha_{MP} = 0.9$ is chosen. It can be seen that higher offsets increase the weighted mean μ but do not necessarily increase the weighted standard deviation σ_w. The dotted black line refers to the LOS signal [Dampf, Frankl, and Pany, 2018, Fig. 10].

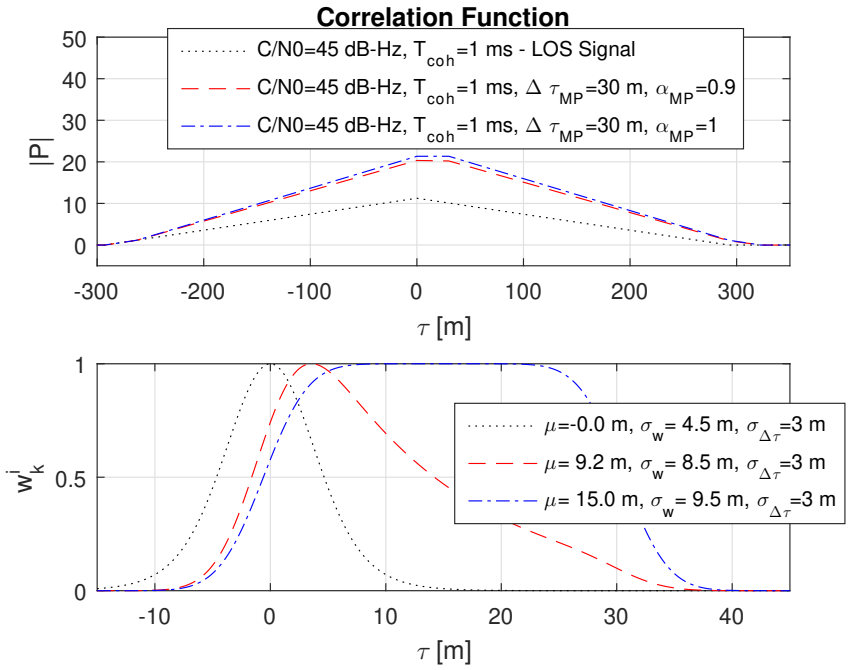

Figure 8.13: An increase of the multipath amplitude α_{MP} shifts the weighted mean μ and increases the weighted standard deviation σ_w. The probability function naturally covers the uncertainty also in the case of $\alpha_{MP} = 1$, when the multipath signal is as strong as the LOS signal. The dotted black line refers to the LOS signal [Dampf, Frankl, and Pany, 2018, Fig. 11].

8.3.6 Real-World Open Sky and Urban Scenario

The real-world tests evaluate the probability function with realistic data for the code pseudorange. Therefore, two scenarios have been selected: (1) an open sky case on a rooftop antenna in order to see the probability function under ideal conditions and (2) an urban case, where multipath is present and a significant shift and deformation on the probability function should be present.

The data was recorded in Graz, Austria and post-processed with the SX3 software receiver [IFEN GmbH, 2019b]. The receiver was configured to dump the multi-correlator maps to files, which contain the correlation values $|P|$ and which are related to the latest PVT. The multi-correlator maps contain correlation values for a range of code phases τ and Dopplers f_d, as indicated by the left grids in (3) of Fig. 6.6. For all real-world tests, the red crosses in the upper plots of Fig. 8.15 to Fig. 8.18 correspond to the correlation values along the Doppler bin which contains the correlation maxima. In order to obtain a high-resolution probability function, the correlation values (red crosses) have been interpolated with sinc function (black line).

It is of major importance that the input correlation values $|P|$ are of correct amplitude, because it basically drives the shape of the probability function and variance estimate. In order to obtain the same amplitude for $|P|$ as in (7.4), all amplitude scaling elements have been verified in the receiver. The GNSS signal samples $\bar{s}_\mu$ in (7.4) have been recorded with a quantization of 2 bits in the Analog Digital Conversion (ADC) stage. The two bits refer to the value range $[-3 \; -1 \; 1 \; 3]$ and thus the RMS of the recorded samples differs from that in (7.4) because the Automatic Gain Control (AGC) within the receiver front-end steers the amplitude of the GNSS signal in a way to optimally use the available quantization range. The RMS value of the samples $\bar{s}_\mu$ can be measured by the receiver. In this experiment, the RMS for the GPS L1 band was measured with $\beta_{s_\mu,RMS} = 1.71$, as also shown in Fig. 8.14. Due to computational efficiency, the replica signal used for the correlation was generated with an amplitude of 8, thus it is simply $\beta_{rep} = 8$. Based on this, the correlation values can be obtained after applying the scaling factors as

$$|P(\tau,\omega)| = |P_{MC,map}(\tau,\omega)| \; (\beta_{s_\mu,RMS} \; \beta_{rep})^{-1} \tag{8.3}$$

where $|P_{MC,map}(\tau,\omega)|$ refers to the correlation value from the multi-correlator map of the software receiver.

For both scenarios, open sky and urban, the code delay bias standard deviation was set to $\sigma_{\Delta\tau}$ = 3 m and has been evaluated at three epochs. The open sky case is shown in Fig. 8.15 and refers to good open sky conditions of GPS L1 C/A satellite PRN 12. The probability functions for all epochs show a slight bias of $\mu \approx -1$ m with respect to the feed back PVT. The weighted standard

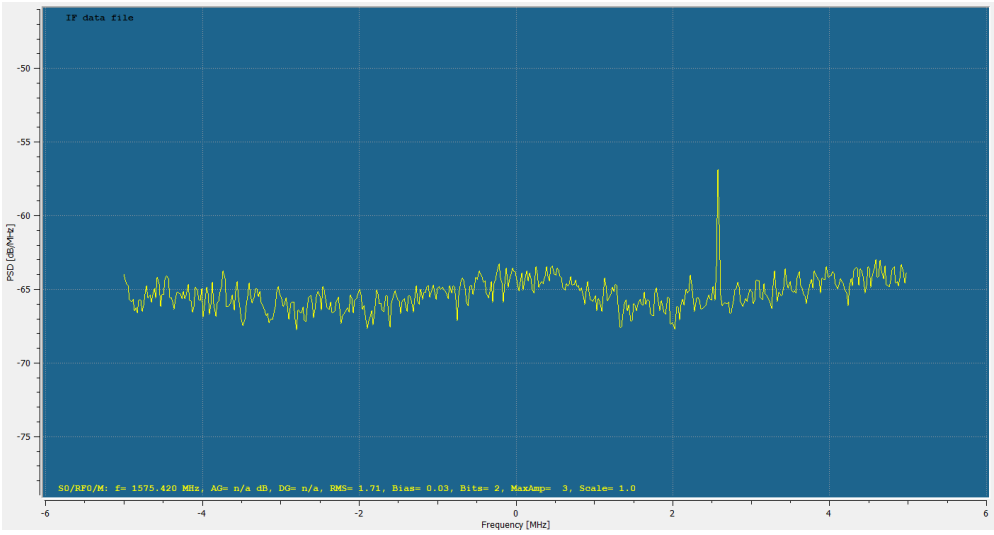

Figure 8.14: Frequency spectrum of the GPS L1 band with a Root Mean Square (RMS) of the samples evaluating to $\beta_{s_\mu,RMS} = 1.71$. At frequency offset of approximately 2.5 MHz a CW interference peak is present. The dataset was recorded with a measurement van during a measurement campaign. Based on the CW interference being present during the complete measurement run, it is assumed that it was caused by one of the active on-board measurement instruments or radio connections. Additionally, it is assumed that the present CW interference does not influence the measurement because it is significantly outside the main lobe of the analyzed GPS L1 C/A signal [Dampf, Frankl, and Pany, 2018, Fig. 12].

deviation σ_w nearly approaches the theoretical lower limit of $\sigma_{\Delta\tau} = 3$ m. No other significant effects are visible.

The urban scenario was recorded during a test drive through Graz. The data has been post-processed and analyzed with the software receiver. An urban environment with significant deformation on the correlation function was selected and analyzed with MATLAB. The analysis focuses on the GPS L1 C/A satellites PRN 27, PRN 21 and PRN 18, as respectively shown in Fig. 8.16, 8.17 and 8.18. A overview of the analyzed scenario is given in Fig. 8.19, which shows the three analyzed positions (red dots) and the satellite constellation. Satellite PRN 27 in Fig. 8.16 and satellite PRN 18 in Fig. 8.17 show a significant variation in amplitude of the correlation values $|P|$, basically due to shadowing and multipath effects. Satellite PRN 21 in Fig. 8.17 is less affected by the environment, because the signal amplitude remains nearly constant and no other significant effects are visible. Nearly all of the probability functions face a significant bias in μ and increased weighted standard deviation σ_w compared to a standard open sky signal. Especially the weighted standard deviation of PRN 18 at third column in Fig. 8.18 shows a significant increase due to the lowered correlation amplitude. Furthermore, the correlation function as well as the probability function of satellite PRN 27 in Fig. 8.16, position at time W/S 1901/317840.4 (middle row) seem to be significantly affected by multipath, which is assumed due to the flattened peak in the correlation function and the resulting deformation of the probability function.

For clarification and as noted briefly above, all presented real-world scenarios show the resulting probability function with respect to the latest PVT estimate, not to a high accurate absolute reference. It should be considered that the latest PVT estimate might be already biased and thus the herein presented offset μ might not show the true bias. Dedicated analysis is planned for future studies using in one case a GNSS simulator and in another case a surveyed static reference position together with precise orbits. Nevertheless, the presented figures give an impression of the effects occurring (deformations and shifts) on the probability function. This is clearly visible when comparing the open sky case to the urban scenario, even if the biases cannot be quantified with absolute values.

8.4 Impact of the Constellation Geometry on the Probability Density Function

This analysis has been performed with a full constellation multi-frequency GNSS simulator [IFEN GmbH, 2019a] and it focuses on the dependency of the PDF on the satellite constellation geometry, whereas further dependencies are given by the signal type and strength, and the number of accumulated signals.

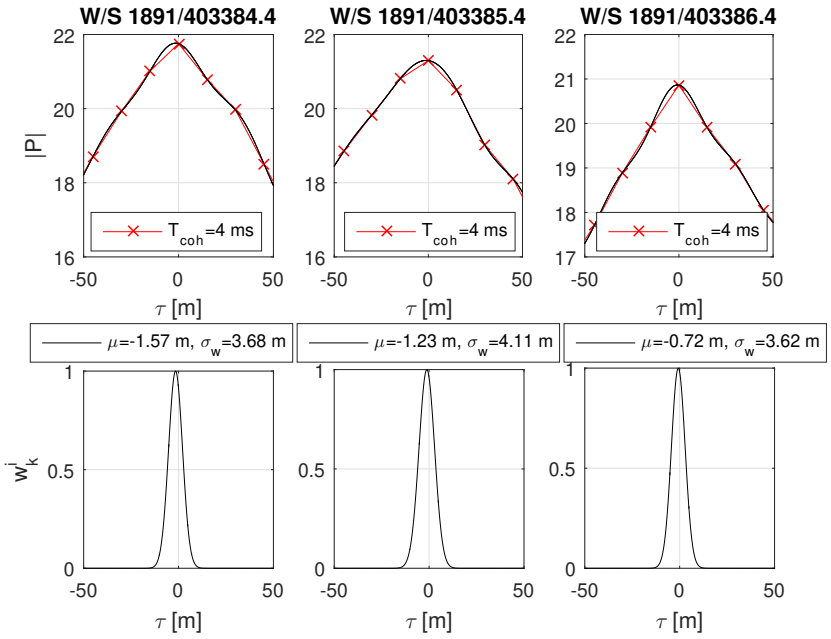

Figure 8.15: Real-world open sky scenario of satellite GPS L1 C/A PRN number 12. The plots show from left to right three epochs referring to GPS Week/Second W/S. The weighted standard deviations σ_w approach the theoretical lower limit of $\sigma_{\Delta\tau} = 3$ m for this ideal case. The dataset was recorded on the roof at LAT = 47.06446263 deg, LON = 15.40777110 deg at the Reininghausstraße 13a, Graz, Austria. The red crosses in the upper plots show the correlation values at code offset τ. The black line in the upper plot shows the sinc interpolated correlation values, which are used to obtain the weights w_k^i shown in the lower plots [Dampf, Frankl, and Pany, 2018, Fig. 13].

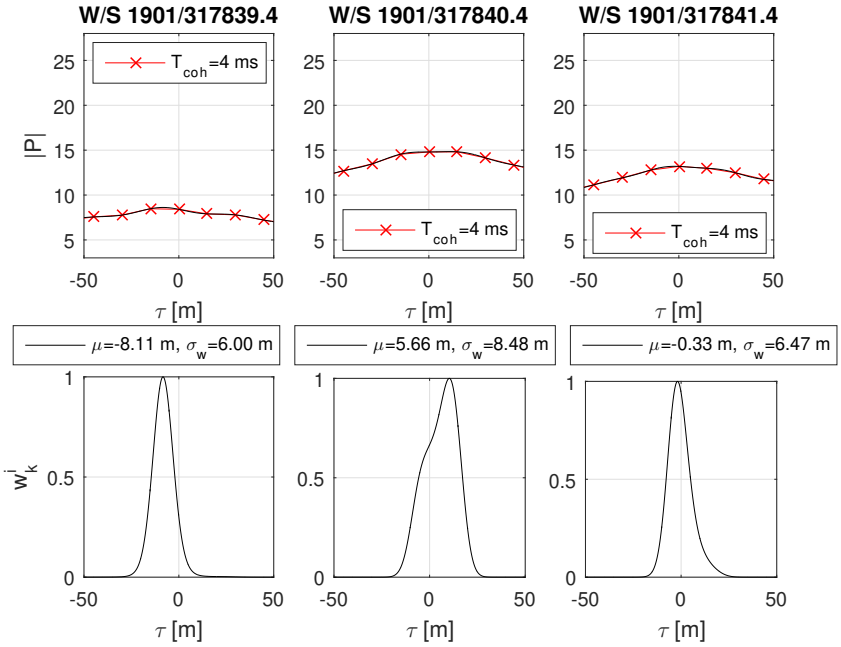

Figure 8.16: Real-world urban scenario of satellite GPS L1 C/A PRN 27. The plots show from left to right three epochs at different places in a urban environment, referring to the red dots from left to right in Fig. 8.19. It is expected that the correlation values $|P|$ vary significantly due to shadowing and multipath. The weighted mean is shifted for all positions and both the correlation and probability function of the second point (middle row) seem to be significantly affected by multipath. The red crosses in the upper plots show the correlation values at code offset τ. The black line in the upper plot shows the sinc interpolated correlation values, which are used to obtain the weights w_k^i shown in the lower plots [Dampf, Frankl, and Pany, 2018, Fig. 14].

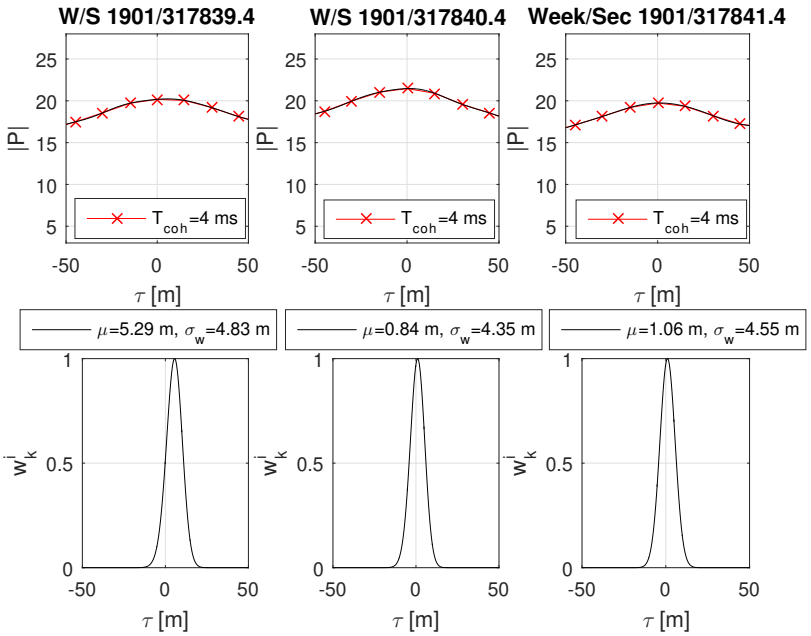

Figure 8.17: Real-world urban scenario of satellite GPS L1 C/A PRN 21. The plot content is analogical to Fig. 8.16. For this satellite, it is assumed that the signal is less affected by the environment because there are fewer variations of the signal amplitude. Only in the case of the first position is the probability function biased [Dampf, Frankl, and Pany, 2018, Fig. 15].

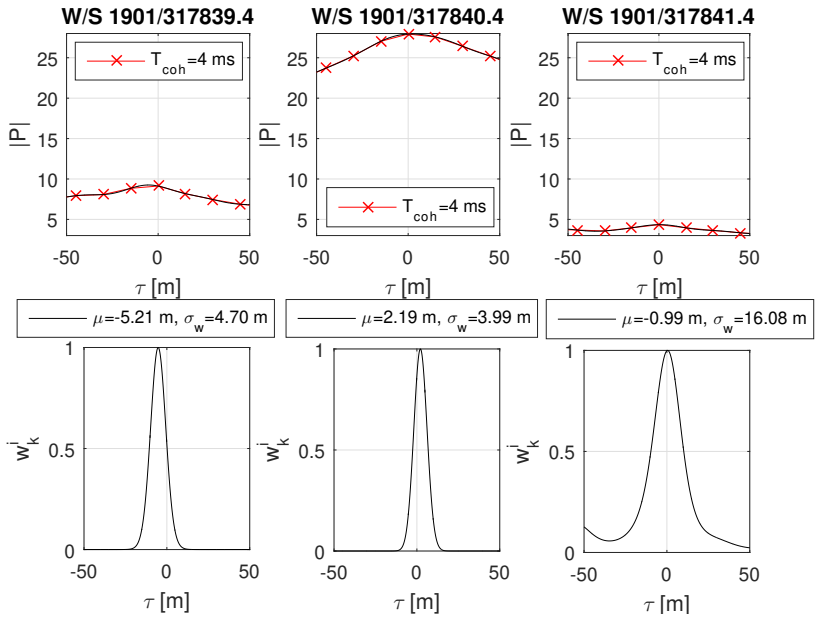

Figure 8.18: Real-world urban scenario of satellite GPS L1 C/A PRN 18. The plot content is analogical to Fig. 8.16. This satellite signal is significantly affected by the environment. From the azimuth of satellite PRN 18 and the location of the buildings as shown in Fig. 8.19, it can be assumed that the GNSS signal is blocked at the first and last positions, which fits to the amplitude of the correlation values. Interestingly, in the case of the third position, the significantly small correlation value leads to an increase in variance estimate [Dampf, Frankl, and Pany, 2018, Fig. 16].

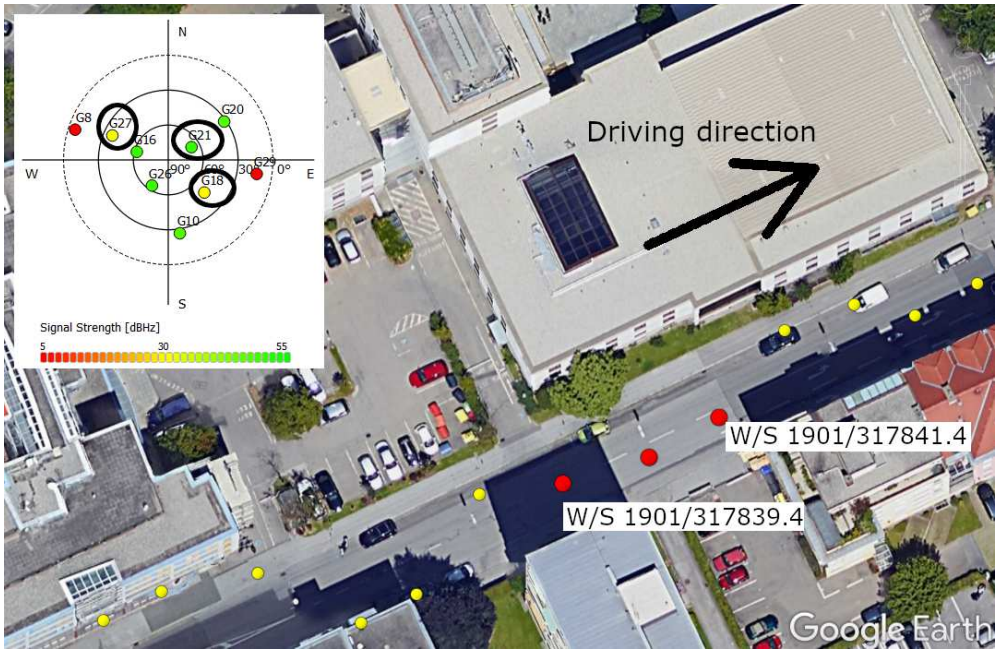

Figure 8.19: Environment for the urban scenario with three red measurement points. The driving direction was to the east, thus the red measurement points refer from left to the right column in Fig. 8.16, 8.17 and 8.18. The upper left plot shows the satellite constellation. The three analyzed satellites PRN 27, PRN 21 and PRN 18 are marked with a black circle. The measurement was taken in the Steyrergasse in Graz, Austria. The point at W/S 1901/317839.4 refers to LAT = 47.06430622 deg, LON = 15.45391867 deg. Map image © 2017 Google, Landsat/Copernicus [Dampf, Frankl, and Pany, 2018, Fig. 17].

A more detailed analysis is given in [Dampf, Lichtenberger, and Pany, 2019]. The baseline is to generate signals free of any atmospheric and environmental effects and analyze undisturbed signals in the PVT domain. The simulation setup parameters are listed in Tab. 8.1. For the analysis a two-dimensional grid (grid nodes equal particles) can be aligned with the ECEF or local East North Up (ENU) coordinate frame. For visualization mostly, the north-east axes of the local frame is used throughout this work, but in some cases e.g. when comparing to other publications, the plots are aligned to the XY-axes of the ECEF frame. All presented simulation results in this section correspond to the satellite constellation given by the top right sky plot in Fig. 8.22. The presented PDFs are based on the weights w_k^i from (7.10) and using (7.11) for the update. The plots are shown in the north-east offset of the BDPE solution to the reference. The reference is at position north=0 m and east=0 m and can be a SPP or LVP solution. An absolute high accurate GNSS-INS reference solution is not available. Based on the fact, that the SPP and LVP solution is accurate to approximately 1-3 m depending on the environmental conditions, also the mean of the PDF varies in that magnitude.

The PDF on the north-east plane in the local coordinate frame of a single satellite is shown in Fig. 8.20. The evaluated satellite PRN is located in the north-west. The plot shows the probability of the user position, which is with a single satellite the range sphere expressed as a probabilistic function projected onto the local north-east frame. The result look like a straight wall orthogonal to the azimuth of the satellite and is Gaussian like distributed in LOS direction. This plot is made under the assumption that all other states (height, velocity, clock error and drift) are well aligned.

In case of two satellites with nearly 90 deg offset in the azimuth the probability of the user position in the local north-east plane becomes circular. This is depicted in Fig. 8.21. The circular like shape is resulting from the intersection of two Gaussian-like distributions projected onto the north-east plane. The circles represent the likelihood of the 2-dimensional user position, whereas the maximum likelihood is located at the peak of the joint PDF. The result in this figure is closely related to the geometry and thus to the Geometric Dilution of Precision (GDOP), but with the difference that the underlaying probability distribution of a single measurement is non-Gaussian. The shape of the PDF is related to the covariance of the PVT and the size is related to the GDOP.

In case of a glancing intersection of two satellites, the probability of the user position becomes strongly elliptical. This is depicted in the upper left plot of Fig. 8.22. Hereby the used satellites PRN 13 and 2 have an azimuth closely of about 180 deg to each other, which allows according to the GDOP a good estimation of the position in LOS direction of the satellites but result in a bad position estimate orthogonal to the LOS. Respectively the probability of the

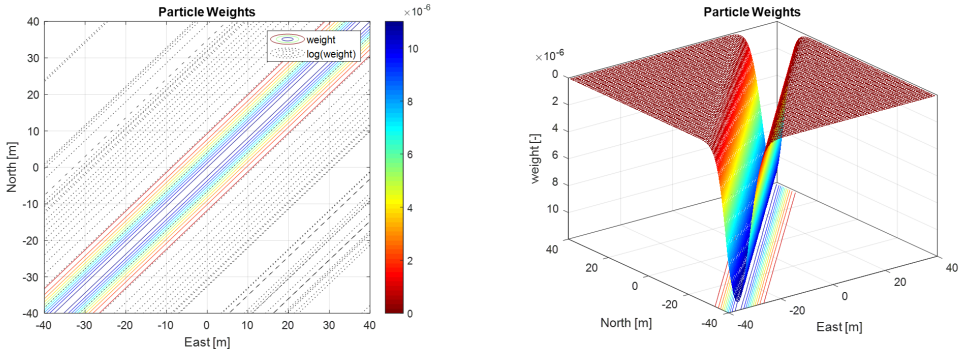

Figure 8.20: Particle weights plotted in the local north-east frame for a single signal of PRN 13 (az=313.3 deg, el=21.0 deg) in the sky plot of Fig. 8.22. The spherical satellite range projected onto the north-east plane appears within the relatively small area (40 x 40 m) as a straight line. Therefore, the particle weights result in a straight wall-like shape orthogonal to the azimuth of the satellite but with a Gaussian-like shape in direction of the azimuth. Thus, the measurement of a single satellite is not Gaussian distributed on a 2-dimensioaonl plane [Dampf, Lichtenberger, and Pany, 2019, Fig. 7].

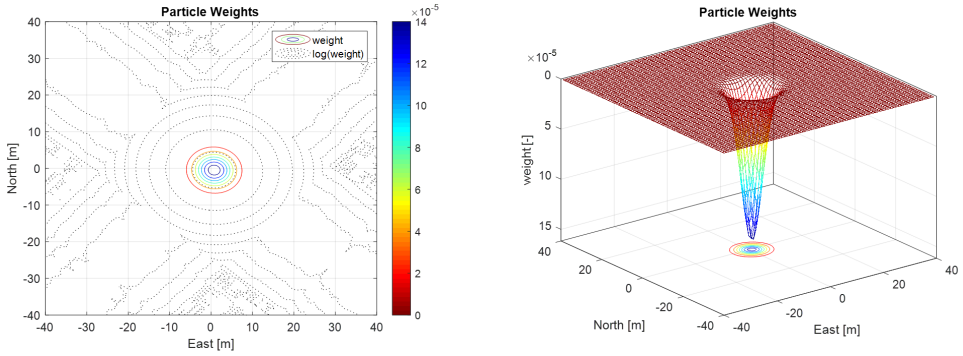

Figure 8.21: Particle weights plotted in the local north-east frame for 2 signals. The map contains Sat PRN 3 (az=39.9 deg, el=15.6 deg) and PRN 13 (az=313.3 deg, el=21.0 deg) which intersect at the center point. The corresponding sky plot is shown in Fig. 8.22. Note that the black dotted lines show the logarithmic weights, which should make the background structure of the PDF more visible [Dampf, Lichtenberger, and Pany, 2019, Fig. 4].

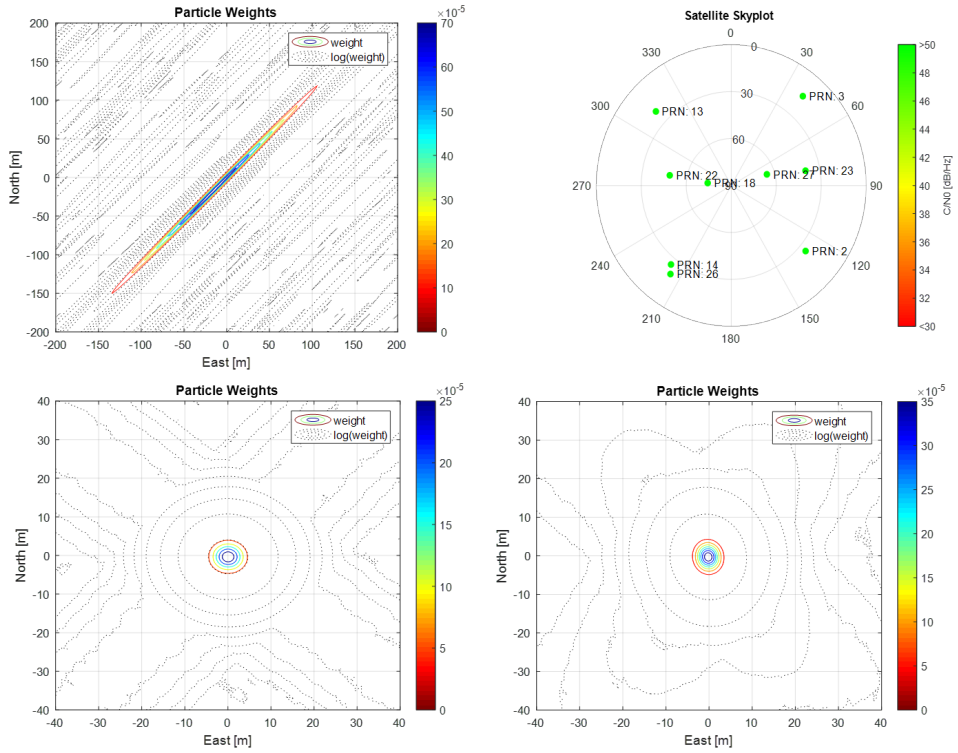

Figure 8.22: The upper left plot shows the probability of the user position in case of a glancing intersection of PRN 13 and PRN 2. The upper right plot shows the sky plot of the simulation. The lower left plot shows 4 satellite signals with PRN 13, 3, 2, 14. The lower right plot shows the probability of the user position based on 8 signals, all except PRN 26. Note that the black dotted lines show the logarithmic weights, which should make the background structure of the PDF more visible [Dampf, Lichtenberger, and Pany, 2019, Fig. 8, 9, and 6].

user position becomes highly elliptical. If the number of signals increases, the probability of the user position becomes circular in case of ideal conditions. This is depicted by 4 signals in the lower left and by 8 signals in the lower right plot of Fig. 8.22. It can be shown, that the number of satellites impacts the estimated accuracy, which can be seen if the lower right plot of Fig. 8.22 (8 signals) is compared to the left plot of Figure 8.21. It can be stated, that the variance decreases with increasing number of satellites, which is in accordance with the GDOP.

The variance of the PDF depends also on the signal strength, whereas a lower signal strength results in a higher variance. This can be seen by equation (7.11), because the correlation value $P(\tau, \omega)$ directly depends on the signal strength. Furthermore, the PDF depends on the signal type. It is known that GNSS signals with a higher bandwidth result in a higher ranging performance and thus having a sharper correlation function [Ávila-Rodríguez, 2008, Chap.

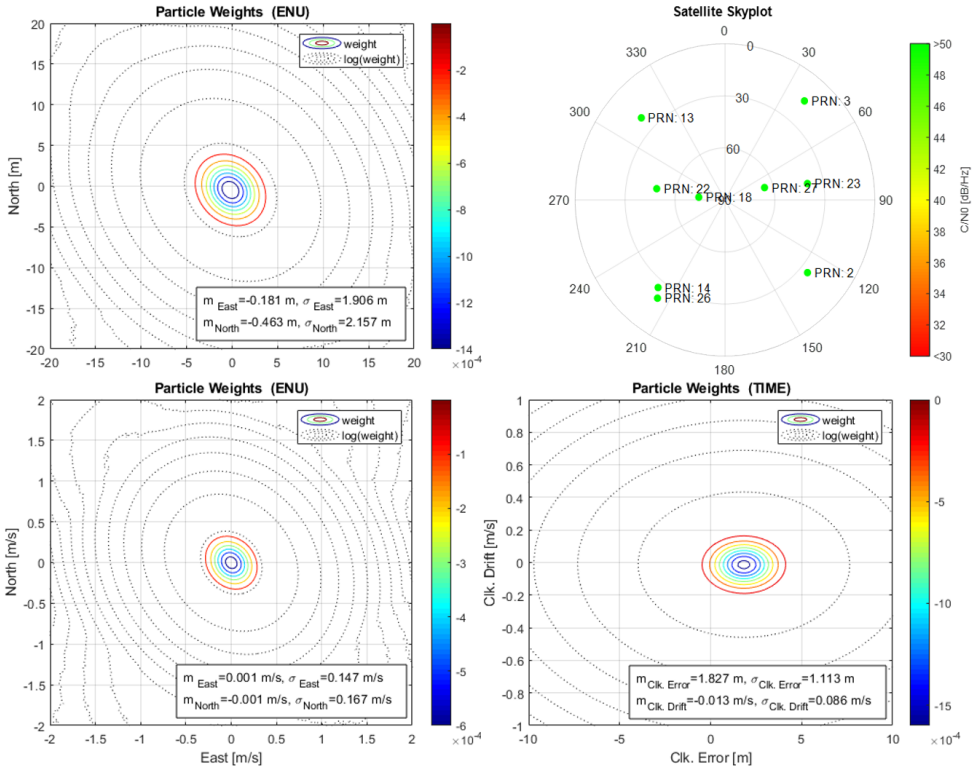

Figure 8.23: These plots show the 2D PDF for the position, velocity and time (from left to right). The position and time is plotted on the north-east plane, whereas the time shows the clock error and clock drift. The plot contains all 9 satellites from the sky plot.

4.8.4], [Misra and Enge, 2010, Chap. 3.3 and 10.6]. This reduces the variance of the PDF, which is reasonable because higher bandwidth signals have a higher ranging accuracy. The shape of the PDF also depends on the environmental conditions. For example, multipath can change the shape significantly. Furthermore, Fig. 8.23 shows for completeness the PDFs for the position, velocity and time.

8.5 Impact of Nuisance Parameters

The impact of nuisance parameters is shown with an open sky scenario on a rooftop antenna without any environmental disturbances. These results have been published in [Dampf, Lichtenberger, and Pany, 2019]. The aim of this discussion is to show on real data the benefit of convoluting with Gaussian nuisance parameters. The herein presented plots show the PDF of the 2-dimensional position in the local navigation frame. The PDF depends on nine visible satellites. To achieve a proper visualization of the effect, a long

coherent integration time of $T_{coh} = 128$ ms is used together with an artificially introduced delay error $\Delta\epsilon$ in the pseudorange model from (5.66) with

$$\tau_n = \frac{p_n}{c} = \frac{\rho_n}{c} - (dt_{\mathrm{rx}} - dt^{\mathrm{sat},n}) + \frac{I^{\mathrm{sat},n} + T^{\mathrm{sat},n}}{c} + (d_{\mathrm{rx}} + d^{\mathrm{sat},n}) + \Delta\epsilon \quad (8.4)$$

The artificial error $\Delta\epsilon$ is a range error which is applied on all satellites. The long integration time leads to a very narrow PDF, as shown in Fig. 7.1 with the plain weight update and in Fig. 8.8, 8.9 and 8.10 with nuisance parameters. This has the benefit, that a typical range error of about 8 meters (e.g. strong ionospheric effects or multipath) on all satellites leads to a clearly visible biased and multi-modal PDF. This effect is outlined in Fig. 8.24. The left plot corresponds to the unmodified position result $\Delta\epsilon = 0$. The maximum has only a slight offset which can arise from the SPP reference position or slight deviations from the applied atmospheric models (standard Klobuchar for the ionosphere). The middle and right plot apply an artificial delay error of $\Delta\epsilon$. It can be clearly seen, that the tensions grow and the PDF degenerates with an increasing $\Delta\epsilon$. Two problems arise in such cases: In case of sudden biases (e.g. caused when driving through urban canyons) the particles of a particle filter might not cover the new state and the tracking of the PVT might be lost. Secondly, the tendency to multi-modal distributions can be represented by a particle filter, but the particle density around the true PDF is reduced because the particles are spread over a larger space, which can lead to a non-optimal performance especially with a higher dimensionality. It is of crucial importance, that the full 8-dimensional PVT state is covered by the particle cloud or grid. If just one state is not covered properly, the correlation used for all other dimensions also breaks away.

It is expected that an increase of the Gaussian nuisance parameter for the code $\sigma_{\Delta\tau}$ helps to recover back to a unimodal distribution and less biased PDF. This effect is shown in Fig. 8.25, whereas the plots from left to right clearly underline this statement. It can also be seen, that the mean of the PDF becomes closer the true position at the center of the plot, which can be explained such that neighbor maxima have more influence because of the convolution, which basically equals a Gaussian averaging. It is expected that the resulting PDF stabilizes a particle filter used for BDPE in case of unmodeled UEREs and with multi-modal measurements in challenging environments. Evidence, that the proposed procedure should give Appendix E, which shows a time series of several epochs of the discussed approach.

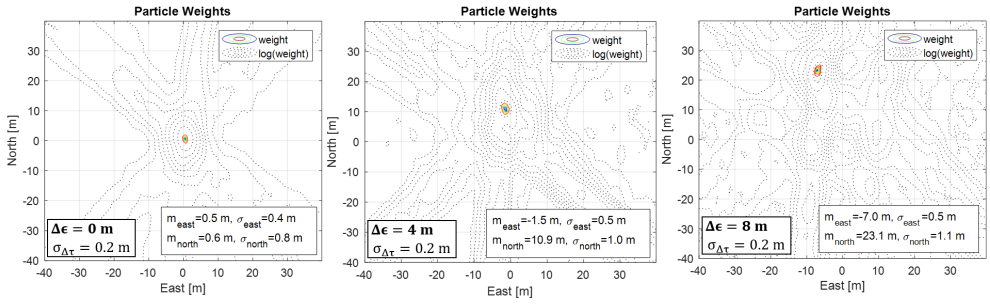

Figure 8.24: These plots are generated from a rooftop antenna setup with a coherent integration time of $T_{coh} = 128$ ms, with a $\sigma_{\Delta\tau} = 0.2$ m and an increasing artificial delay error of $\Delta\epsilon = [0, 4, 8]$ m. The long integration time and small $\sigma_{\Delta\tau}$ leads to a very tiny PDF, as visible in the left plot. The introduced delay error $\Delta\epsilon$ increases the tension until a significant bias and multi-modal distribution with many local maxima appears, as visible in the right plot [Dampf, Lichtenberger, and Pany, 2019, Fig. 13].

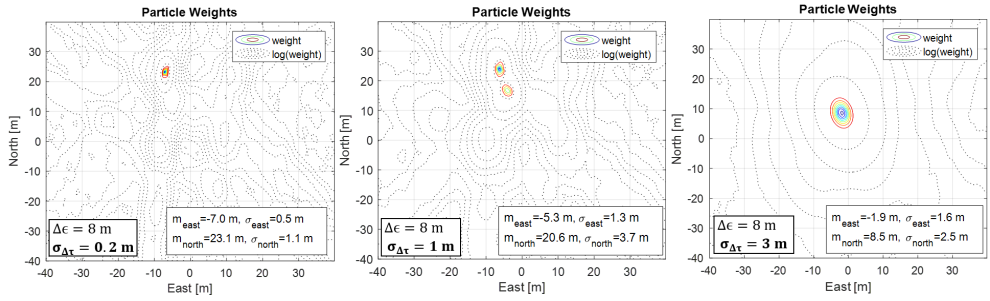

Figure 8.25: These plots are generated from a rooftop antenna setup with a coherent integration time of $T_{coh} = 128$ ms and an artificial delay error of $\Delta\epsilon = 8$ m. From the left to the right plot the code nuisance parameter was increased such that $\sigma_{\Delta\tau} = [0.2, 1, 3]$ m. This reduces the number of local maxima until a clear unimodal distribution appears again. The resulting PDF in the right plot faces a more accurate position with a reasonable std. dev., while the left improper parametrized plot must be interpreted with caution, as the result would be a very deviated position with a low standard deviation [Dampf, Lichtenberger, and Pany, 2019, Fig. 14].

8.6 Link to Other Publications

In the last years some DPE related results have been published in different papers. This chapter aims to modify the weight update in such a way, to make the results comparable to the results published in two different independent papers. All previous related work on DPE, including the two reference papers, estimate the PVT based on the correlation function in the PVT domain. Hereby, the correlation function in the PVT domain is built by a non-coherent sum of the correlation functions of the individual signal measurements. This is also possible with the herein presented approach by slightly modifying the equations such that they deliver a non-coherent sum of the correlation function of N signals. Therefore, equation (7.6) to (7.10) are rewritten to

$$\widetilde{v}_k^i = \sum_{n=1}^{N} |P_n(\tau_n, \omega_n)| \tag{8.5}$$

$$v_k^i = \frac{\widetilde{v}_k^i}{\max(\widetilde{v}_k^i)} \tag{8.6}$$

where v_k^i contains the normalized non-coherent sum of the correlation functions. Hereby, v_k^i is the weight update equivalent to w_k^i from (7.10), but was renamed to avoid a misinterpretation of the content. Hereby, (8.5) and (8.6) do not have to perform an exponential weighting, which can cause numerical issues, and thus (7.6), (7.8) and (7.9) are obsolete and are neglected for (8.5) and (8.6). Furthermore, just a single epoch is considered and thus an equivalent to w_{k-1}^i from (7.13) is not written in (8.5). The work from [Axelrad et al., 2011] presents an approach of a high sensitivity acquisition algorithm based on a collective detection of GNSS signals in the position domain, which equals $\widetilde{v}_k^i$ from (8.5), but may have another weighting or scaling. The result in [Axelrad et al., 2011] is compared to the results obtained in this work in Fig. 8.27. The work from [Closas and Gusi-Amigó, 2017] discusses DPE and uses (8.5) and (8.6) for the weight update. The result in [Closas and Gusi-Amigó, 2017] is compared to the result obtained in this work in Fig. 8.26. The plot is qualitatively the same, but slight differences appear due to a different satellite constellation and simulated signal parameters. The plots in Fig. 8.28 are results of this work and have been obtained with the scaling as given by (A), (B) and (C). All three plots are based on the same input parameters $P_n(\tau_n, \omega_n)$.

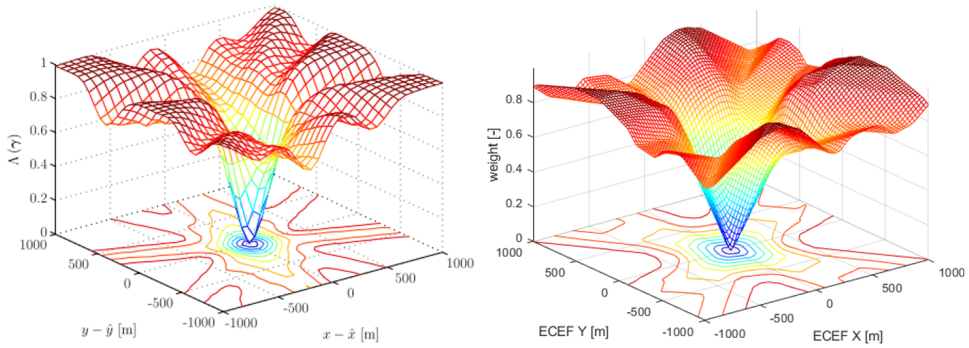

Figure 8.26: The left plot shows the result obtained in [Closas, 2009, Fig. 4.6] and the right plot shows the results obtained in this work with scaling (B) and as discussed in Fig. 8.28.

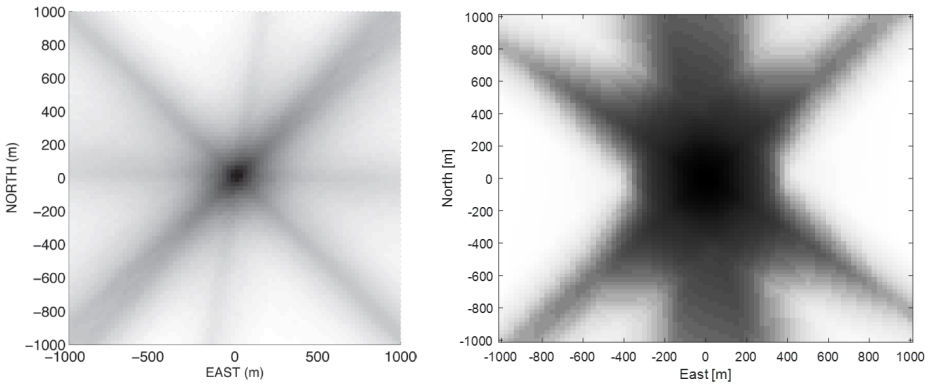

Figure 8.27: The left plot shows the result obtained in [Axelrad et al., 2011, Fig. 8] and the right plot shows the results obtained in this work with scaling (A) and as discussed in Fig. 8.28.

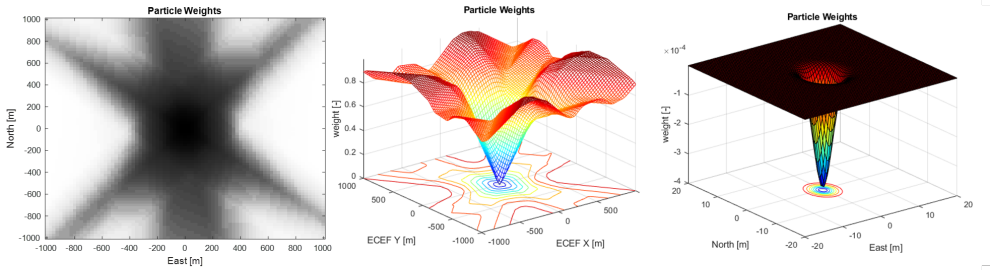

(A) $v_k^i = \frac{\tilde{v}_k^i}{\max(\tilde{v}_k^i)}$ (B) $v_k^i = -\frac{\tilde{v}_k^i}{\max(\tilde{v}_k^i)} + 1$ (C) $v_k^i = -\frac{w_k^i}{\sum_{i=1}^N w_k^i}$

Figure 8.28: These plots link the generated results to other publications. The plots have been generated with a simulated scenario using the settings from Tab. 8.1 with the constellation given in Fig. 8.22. The receiver uses a coherent integration time of $T_{coh} = 128$ ms for generating $P_n(\tau_n, \omega_n)$ and a $\sigma_{\Delta\tau} = 3$ m and $\sigma_{\Delta\omega} = 1$ Hz for generating $Q_n(\tau_n, \omega_n)$. The first and second plot show v_k^i, which is $\tilde{v}_k^i$ from (8.5) and scaled as given by (A) and (B). The first plot is an equivalent to [Axelrad et al., 2011, Fig. 8] and is plotted in the local frame on a north-east plane with an extension of 1000 m, but looks slightly different (black center) due to the different simulation and processing settings. The plot was generated with a logarithmic greyscale and shows clearly the crossing black lines which correspond to the correlation function of each accumulated signal. The second plot shows an equivalent to [Closas, 2009, Fig. 4.6] and [Closas and Gusi-Amigó, 2017, Fig. 2 and 3] plotted in the ECEF frame on the XY plane also with an extension of 1000 m. The third plot shows v_k^i, which refers to w_k^i from (7.10), which is scaled as given in (C) and which is a PDF plotted in the local coordinate frame with an extension of 40 m [Dampf, Lichtenberger, and Pany, 2019, Fig. 11].

8.7 Real-World Results of the PDF Analysis

The results show a 2-dimensional probability density function of the user position for different signal conditions and purely based on GNSS signals. The recording and post-processing parameters are listed in Tab. 8.3. The aim of the real-world data analysis is to analyze the shape and extension of the probability density function of the user position and to proof that strongly non-Gaussian and multi-modal PDFs can appear under real signal conditions, which justify Bayesian estimation techniques as they are able to deal with non-Gaussian measurements.

Table 8.3: List of parameters used for the real-world data analysis

Scenario	Urban Environment / Indoor
Antenna	Geodetic 3G+C
Sample Rate f_s	20.64 MHz (real)
Quantization	2 bit
Frequency Band	L1
Signal	C/A Code
Coherent Itegration Time T_{coh}	16 ms
Number of correlators	15 / 61
Nuisance Param. Code $\sigma_{\Delta\tau}$	3 m
Nuisance Param. Doppler $\sigma_{\Delta\omega}$	1 Hz

Therefore, the analysis focuses on an urban environment and an indoor dataset. Furthermore, detailed time series of the herein analyzed scenarios can be found in Appendix D.

8.7.1 Urban Environment

The urban environment dataset is based on a measurement drive with a car through the city Graz. The scenario contains open sky, sub-urban, urban, bridges and tunnels, whereas the focus in this work is on an urban canyon with multipath and a bridge underpass with significant shadowing. Fig. 8.29 shows the environmental conditions of the analyzed two scenarios, whereas the yellow trajectory is the reference trajectory of the Kalman filtered PVT solution, to which the PDFs are related. The result of one evaluated epoch is presented with three plots, as shown in e.g. in Fig. 8.30. The first plot in the row shows the result as presented in [Closas and Gusi-Amigó, 2017], but shifted into the local north-east plane, and which is based on (8.6). This should give an impression of how the sum of the correlation values behave in the 2-dimensional position domain under the given environmental conditions. The

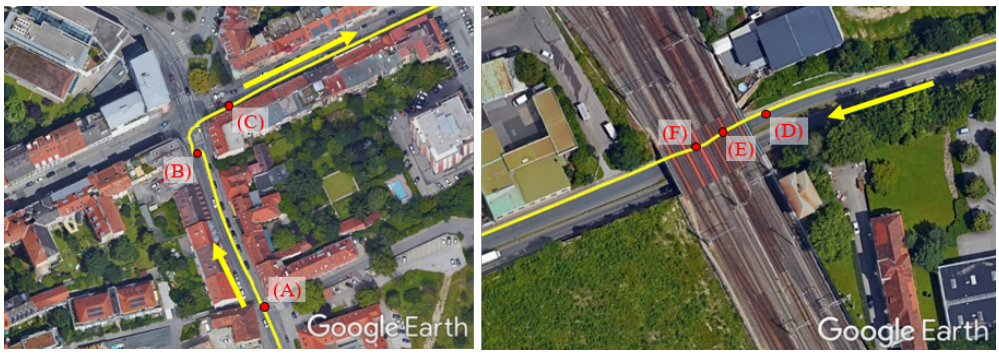

Figure 8.29: The left plot shows an urban canyon with buildings up to 6 floors at the corner Steyrergasse-Münzgrabenstrasse, Graz, Austria and the right plots shows an underpass of a railway bridge at the Peter-Tunner Gasse, Graz, Austria. The yellow reference trajectory corresponds to a Kalman filtered vector tracking solution. The left plot shows an area of significant multipath short before the cross-roads when driving from the south to the north-east. The right plot refers to a short signal blockage when passing under the bridge from the east to the west. The PDF have been analyzed at position (A), (B), (C), (D), (E) and (F) [Dampf, Lichtenberger, and Pany, 2019, Fig. 17].

second plot shows in contrast to that the resulting PDF from (7.10), whereas the black dotted lines show the logarithmic weight from (7.10) in order to visualize also the structure of the joint PDF of values with lower magnitudes. Furthermore, a sky plot is shown in the third plot, which shows the satellite constellation and the signal strength of the current epoch. The satellites are identified in the plot with their PRN number and are shown according to their azimuth and elevation, with respect to the current position. The signal strength is given in (dB/Hz), whereas good signal conditions above 50 dB/Hz are shown in green and bad signal conditions below 34 dB/Hz are shown in red. But it should be noted, that the C/No might not be fully up to date at the shown epoch, because the C/No estimation process in the receiver need time due to an averaging. This causes, that the C/No is not updated immediately, for example at the presented bridge underpass.

Fig. 8.30, 8.31 and 8.32 show the results in the urban canyon at the positions (A), (B) and (C) in Fig. 8.29. Position (A) was selected at a crossroad to have a good visibility as reference for the resulting PDF, which is shown in the middle plot of Fig. 8.30. Position (B) was selected at a point where significant multipath is present. The present multipath causes a shift of about 3 m of the Kalman filtered vector tracking solution at a static position short before the crossroad. The resulting PDF in the middle plot of Fig. 8.31 shows a significant increase of the variance compared to the quasi open sky conditions at the crossroad of Fig. 8.30. Very interesting is, that the probability of the user location is significantly deformed to the south-west, same direction to which the reference solution was shifted. It is assumed, that the area in the

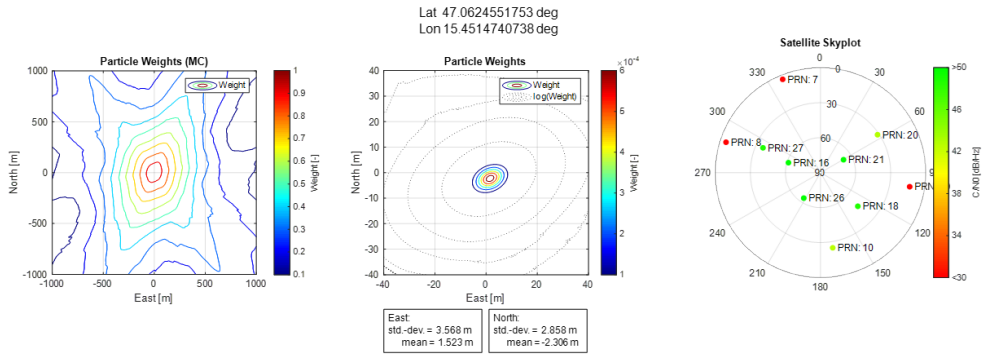

Figure 8.30: Urban Canyon: These plots correspond to position (A) in Fig. 8.29. The left plot shows the weights based on (8.6) and the center plot shows the weights from (7.10). The position is at a crossroad and thus the signals are not obstructed which lead to a small std. dev. of 3 m [Dampf, Lichtenberger, and Pany, 2019, Fig. 18].

south-west with an increased probability of the user position is caused by the present multipath from satellite PRN 21. Thus, multipath deforms and biases the PDF, which is consistent with the work published in [Dampf, Frankl, and Pany, 2018]. The example in Fig. 8.32 is also representative, as the PDF has as small extension to the south and north-east, which can be explained by the satellite constellation. The constellation shows strong (good) signals from south and north-east, but weak (bad) signals from north-west and south-east, which is consistent with the simulation in chapter 8.4. A good signal reduces the variance in the direction of the LOS to the satellite and in case of the herein 2-dim result in direction of the azimuth, which is assumed to lead to the given shape of the PDF.

Fig. 8.33, 8.34 and 8.35 show a bridge underpass and Fig. 8.33 is again the quasi open sky reference. Under the bridge the signals become significantly weakened, which leads to a significant increase in the extension of the PDF compared to the urban canyon multipath scenario. This is visible by the reported std. dev. in Fig. 8.34 and 8.35. It is very interesting, that the PDFs still show a clear maximum, whereas position (F) shows already a second maxima at the edge of the analyzed space.

8.7.2 Indoor

The indoor dataset analyzes entering a massive concrete made building with 3 floors. The building and reference trajectory are shown in Fig. 8.36. The measurement started in urban sky conditions and as reference trajectory the Kalman filtered vector tracking solution was used. As shown in the left plot, the reference trajectory was available until entering the passage, approximately at position (H). Thereafter, no PVT solution was available with vector tracking,

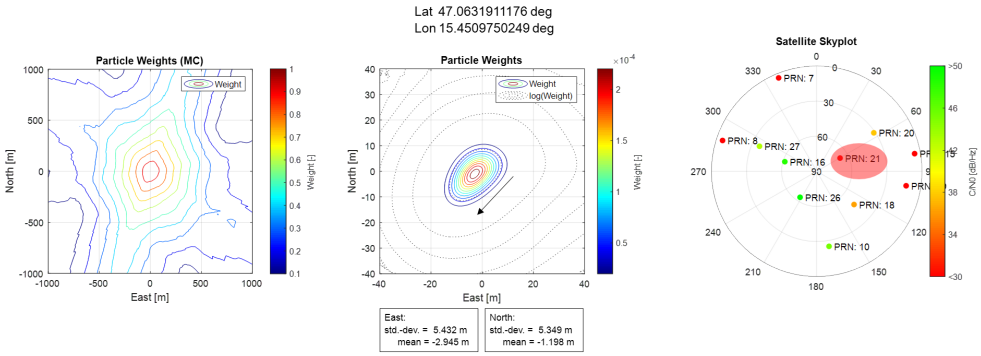

Figure 8.31: Urban Canyon: These plots correspond to position (B) in Fig. 8.29. The position is in an urban canyon waiting to enter the crossroad. The Kalman filtered vector tracking position moved approx. 3 m to the left while being at a static position, which indicates that significant multipath is present. The PDF from the middle plot shows a non-Gaussian deformation to the south-west, indicated by the arrow, and a higher std. dev. of approx. 5.4 m, which is assumed to be caused by the present multipath. The skyplot shows that some satellites are obstructed significantly [Dampf, Lichtenberger, and Pany, 2019, Fig. 19].

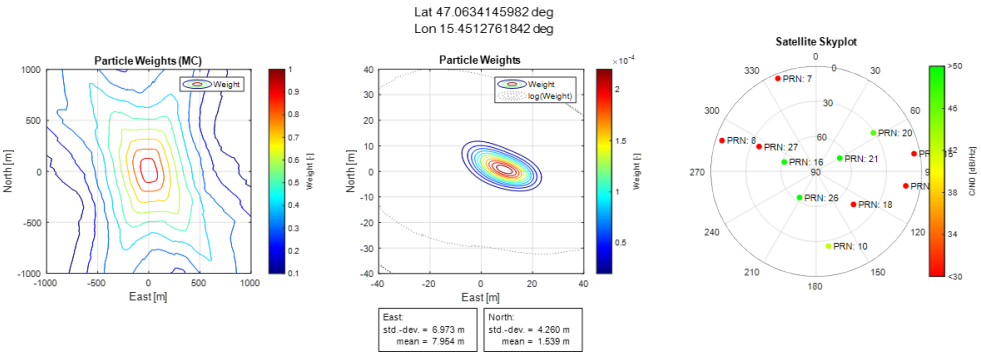

Figure 8.32: Urban Canyon: These plots correspond to position (C) in Fig. 8.29. The position is in an urban area where the satellites PRN 10, 26, 16, 21 and 20 deliver a recently good estimate, and thus it is assumed the PDF in the middle plot has lower extension to the south and north-east. The suboptimal constellation also leads to an increased std. dev. of 4.2 to 6.9 m [Dampf, Lichtenberger, and Pany, 2019, Fig. 20].

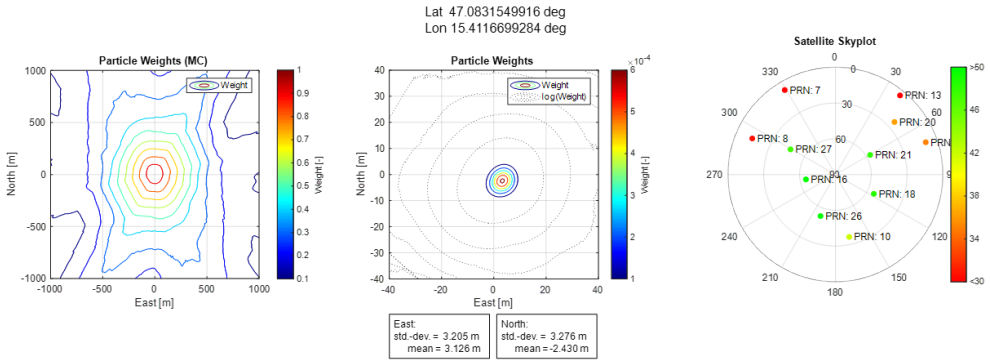

Figure 8.33: Bridge: These plots correspond to position (D) in Fig. 8.29. The position is short before passing the bridge. The signals are not obstructed as indicated in the sky plot which leads to the usual open sky std. dev. of about 3 m [Dampf, Lichtenberger, and Pany, 2019, Fig. 21].

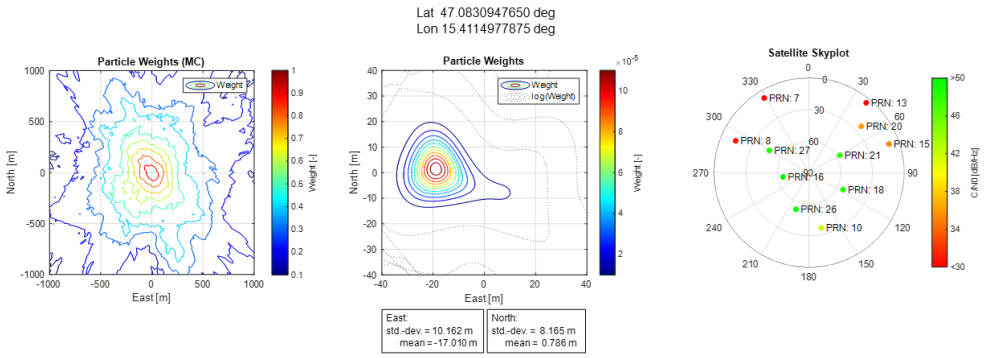

Figure 8.34: Bridge: These plots correspond to position (E) in Fig. 8.29. The position is located shortly after entering below the railway bridge which causes significantly obstructed signals. The signal strength estimation period averages over several seconds, thus the sky plot does not show the reduced C/No for the short underpass. The PDF shows a significant bias together with an increased extension up to 10 m std. dev. [Dampf, Lichtenberger, and Pany, 2019, Fig. 22].

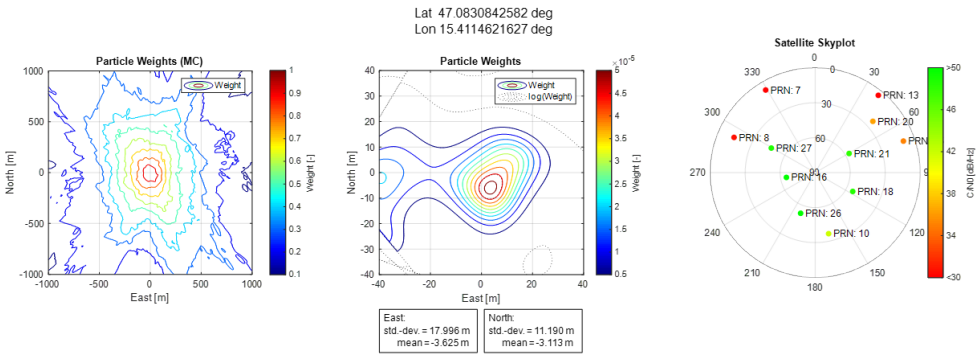

Figure 8.35: Bridge: These plots correspond to position (F) in Fig. 8.29. The position is fully under the bridge and it is expected that only signals from low elevation satellites or extremely weakened signals from LOS satellites are gathered by the antenna. The C/No in the sky plot is still not updated due to an averaged signal strength estimate. The PDF is multi-modal with a strong peak in the vicinity of the reference position and a weak peak at an offset of 30 m to the east. Due to bad signal conditions the std. dev. increases up to 18 m [Dampf, Lichtenberger, and Pany, 2019, Fig. 23].

but it was possible to propagate the receiver time and constrain the position and velocity to the last estimates and to calculate PDFs for the position domain. Position (I) is therefore not located on the yellow trajectory and shows the approximate indoor position for Fig. 8.39. Hereby, the first position (G) and corresponding Fig. 8.37 is the reference PDF generated at quasi open sky conditions before entering the building. Fig. 8.38 and 8.39 show as expected an increased extension of the PDF. Very interesting is, that the PDF of the 2D position in (I) becomes multi-modal, whereas most indoor positions showed a clear unimodal distribution. For the multi-modal case it is assumed, that at least one measurement was multi-modal, which lead to the multi-modal PDF in the position domain. The reported standard deviation increased up to about 13 m, which is still impressive, as it is by far magnitudes lower than the extension of the reported SPP solution shown by the yellow dots in the right plot of Fig. 8.36 (as long a SPP solution was available). The presented results underline the gain of DPE in weak signal conditions and show that the PDF in challenging GNSS signal scenarios can become strongly non-Gaussian distributed or multi-modal. The state-of-the-art GNSS position estimation techniques assume Gaussian distributed measurements, which is not the case in difficult signal conditions. Thus, it is expected that Bayes filters with the capability to account for non-Gaussian distributions and multi-modalities, such as grid-based or particle filters, perform better in such conditions.

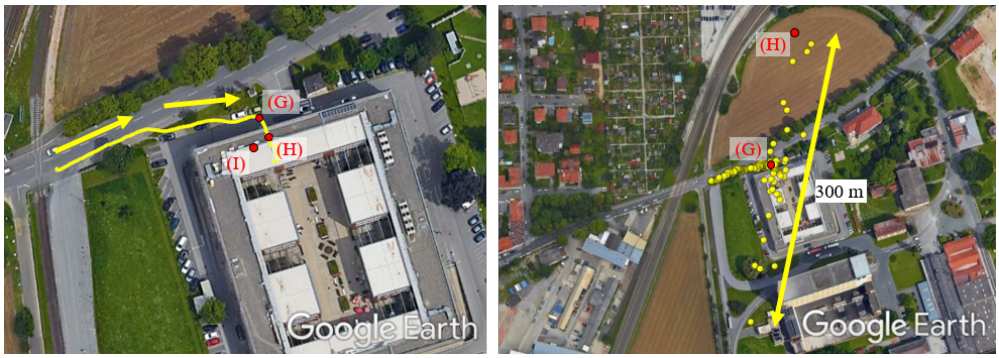

Figure 8.36: The indoor dataset was recorded at the Reininghausstraße 13, Graz, Austria. The processing setup for the left plot is the same as in Tab. 8.3 and shows a Kalman filtered vector tracking solution. The right plot shows an unfiltered SPP solution with a large error up to 150 m. Based on the fact that the vector tracking solution in the left plot does not follow the true trajectory, position (I) is placed at the approximate true position. For (G) and (H) a SPP solution is available, which is referenced in the right plot [Dampf, Lichtenberger, and Pany, 2019, Fig. 24].

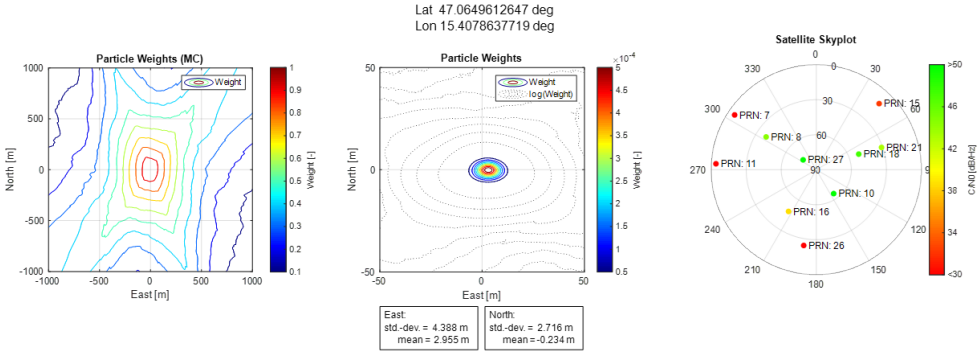

Figure 8.37: Indoor: These plots correspond to position (G) in Fig. 8.36. The position is short before entering the building which leads to the typical std. dev. of about 3 m [Dampf, Lichtenberger, and Pany, 2019, Fig. 25].

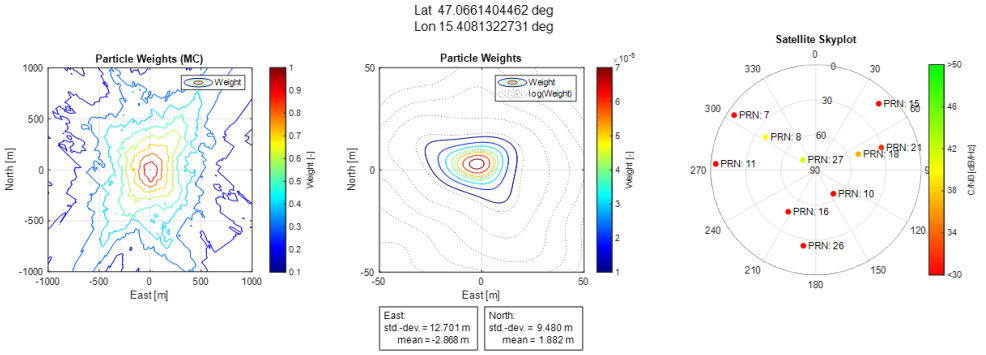

Figure 8.38: Indoor: These plots correspond to position (H) in Fig. 8.36. The position is short after entering the passage of the building. The skyplot shows already a reduced visibility of the signals. The PDF shows a significant non-Gaussian deformation of the probability of the user position with an increased std. dev. of up to 12 m in east-west direction [Dampf, Lichtenberger, and Pany, 2019, Fig. 26].

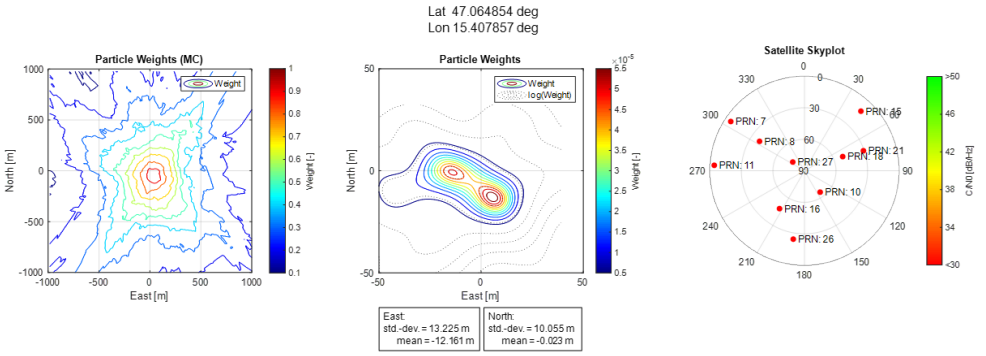

Figure 8.39: Indoor: These plots correspond to position (I) in Fig. 8.36. The position is inside the building where no direct LOS visibility to any satellite is given. Most epochs inside the building still show unimodal distributions, but some epochs such as this one, shows a multi-modal distribution. This can be interpreted such that two likelihood maxima exist for the user position. The weighted mean from the statistics is placed near the left maxima, which is at least plausible, because position (I) is located in the north-west with respect to the reference position [Dampf, Lichtenberger, and Pany, 2019, Fig. 27].

9 Summary, Conclusions and Outlook

The work presents a concept of a real-time capable BDPE receiver analysis tool to generate a PDF in the PVT domain. The introduction in chapter 1 delivers an overview of the current and future GNSS market segments as well as state-of-the-art and emerging positioning techniques. The current state of all global and regional satellite navigation systems is summarized in chapter 2. It is discussed in chapter 3, how the concept of BDPE can be placed in context of existing GNSS positioning techniques. Many state-of-the-art GNSS receivers as well as BDPE rely on Bayesian filtering techniques. It was shown that BDPE deal with non-Gaussian multi-modal measurements as well as with non-linear state propagations. Thus, the principles of Bayes filters with focus on a grid-based filter and a particle filter are introduced in chapter 4. The fundamentals of a GNSS receiver are discussed in chapter 5 and all steps till the required input to the proposed BDPE approach, the synthetically generated multi-correlator values, are explained in detail. The theory of the particle and grid-based filter is linked to the concept of BDPE in chapter 6, which describes the proposed receiver architecture for a real-time capable software based BDPE GNSS receiver. A major part of this work is given in chapter 7, which derives the mathematical framework for the optimal weight update for Bayes filter, which rely on a probabilistic description of the GNSS measurements. Bayes filter for DPE need such a probabilistic description of the measurements, which are based on the samples or the correlation values. Furthermore, the chapter discusses limited precision effects of numerical operations when solving the equations on a computer, and discusses the introduction of nuisance parameters, which are used to cover unmodeled UEREs in the range and Doppler model to stabilize BDPE solutions. Furthermore, a performance optimized method is presented to perform all required calculations in real-time. An analysis of the resulting PDF in the PVT domain is presented in chapter 8. The analysis uses an aligned grid to a PVT reference to generate the PDF of a 2-dimensional subspace (2D-position, 2D-velocity or 2D-time) with a high resolution, in order to analyze and understand the size, shape and deformation in different conditions. This knowledge helps to establish an ideal parametrization of a grid-based or particle filter, because this PDF is the fundamental measurement for a particle or grid-based filter. Hereby, the chapter discusses in general the product of PDFs, the impact of different signal and processing parameters, the impact of multipath, the impact of the satellite constellation geometry, and the impact of the proposed

nuisance parameters to the PDF. Furthermore, the produced results are linked to other publications. The results in chapter 8.7 apply the proposed methods to real-world scenarios. The analysis focuses on challenging scenarios for GNSS when driving through an urban canyon with significant present multipath, underpassing a bridge and going indoors. It is known that Bayesian methods, which do not assume underlying Gaussian distributions for the measurements and a linear state propagation, exploit their benefits with non-Gaussian measurements and a non-linear propagation. The results clearly demonstrate, that the probability distribution of the user position, velocity and time can become non-Gaussian in challenging environments. Moreover, strong deformations and multi-modalities are possible. It was also clearly shown, that even in the most severe situations the PDF showed a clear maximum in the north-east position domain. Furthermore, the generated PDF of the user position is compared to an SPP solution, which underlines the sensitivity gain of DPE. This gain is resulting from the non-coherent sum of correlation values over multiple GNSS signals and can be seen in the presented indoor scenario.

This work extends the current research on DPE by delivering the mathematical framework and proposes a computational efficient way to update a Bayesian particle filter or grid-based filter in an optimal way with a probabilistic description of the GNSS measurements. This allows in contrast to state-of-the-art methods to calculate not only the PVT, it also delivers a PDF of the user PVT. The proposed method takes as input correlation values, the same as state-of-the-art receivers use. The proposed method differs from the state-of-the-art receivers, as it estimates the PVT collectively on all available GNSS signals. Most current receivers perform a single channel tracking to obtain the range and Doppler measurement. The PVT estimate is performed based on this measurements with a LSQ, WLSQ or KF approach, as explained in chapter 5.8. More advanced GNSS receivers use vector tracking, a method which closes the signal tracking loops via the navigation solution. This method is already close to DPE and is a collective signal tracking method, but still estimates the Doppler and range on a single channel basis. In contrast, DPE/BDPE directly estimates the PVT recursively and collectively based on the signal samples or correlation values. When comparing these methods, vector tracking delivers a sensitivity gain compared to single channel tracking methods, whereas the performance improvement from vector tracking is contingent on the number of available satellites and their geometry [Lashley and Bevly, 2009]. The sensitivity gain of DPE in (6.21) from [Closas and Gusi-Amigó, 2017] also depends on the number of available GNSS signals, whereas the impact of the satellite geometry on the PDF is visualized in chapter 8. Summarized, both methods vector tracking and DPE/BDPE deliver a sensitivity gain compared to the single channel tracking methods. The benefit of BDPE compared to vector tracking is, that the method delivers a PDF of the PVT and can deal with non-Gaussian multi-modal measurements and a non-linear propagation,

but with the drawback of a much higher computational complexity.

9.1 Lessons Learned

The first idea of the approach was to build the non-coherent sum of the correlation values in the PVT domain, same as done in [Closas, 2009] or [Axelrad et al., 2011], and put on top the Bayesian filter. This actually worked straight forward and was presented in [Dampf, Witternigg, et al., 2017] and [Witternigg et al., 2017]. But this approach was suboptimal, because it re-interpreted the non-coherent sum of the correlation values in the PVT domain as a PDF and an empirical amplitude scaling has been applied between consecutive epochs in order to stabilize the filter. An optimal BDPE receiver requires to update the Bayesian grid-based or particle filter with a probabilistic description of the measurement. Since such a description did not exist for correlation values, this work investigated to derive the mathematical framework to convert correlation values into a probabilistic description of the measurement. The effort to obtain such a description, which can also be evaluated in real-time, was strongly underestimated. The derivation of the mathematical framework required to solve very complex integrals and required to extend existing single signal models to multiple signals based on empirical mathematical schemas, as discussed in chapter 7 and derived in Appendix A and Appendix B. Once the equations have been derived it turned out, that the weight update cannot performed on a computer because of the limited precision of mathematical operations. Thus, all equations have been shifted to the logarithmic scale and a stable weight update sequence was defined, as discussed also in Appendix B. After evaluation of that equations it turned out, that the PDF of the pseudorange and Doppler measurement became very narrow for strong signals, broadband signals and long integration times. It was found, that these narrow PDFs does not represent the true range and Doppler accuracy accordingly and caused problems at the alignment in the PVT domain, as they need to overlap to exploit the gain of DPE. Hereby, UEREs caused the narrow PDFs to jump between consecutive epochs, which can lead to loss of lock of the tracked PVT solution in case of a particle filter or grid-based filter, because the PDF needs to be covered properly and with a reasonable resolution. Thus, the concept of nuisance parameters was introduced to prevent this behavior, which is discussed in Appendix C. Hereby, Gaussian nuisance parameters are used to describe unmodeled UEREs in order to deliver a reasonable variance of the PDF of a GNSS signal measurement. Evaluating the derived equations is computationally demanding, as it requires a convolution of the PDF with a Gaussian for 2-dimensions, code phase and Doppler. In order to achieve real-time performance, an algorithm is proposed in chapter 7.2. The implementation in the software based GNSS receiver considers the capabilities of

the used CPU and uses vectorization by using the Intel IPPs [Intel Corporation, 2020]. Furthermore, the tracking of the 8-dimensional PVT state is not trivial, because it requires a large number of particles or fine grid to achieve a good coverage of the tracked PVT state. Additionally, all Bayesian filter parameters such as the process noise and dynamic model need to be chosen carefully in order to achieve a stable convergence of the filter. Summarized, many aspects which have not been addressed in advance, but which needed to be investigated and which lead to the underestimated effort to achieve an optimal and real-time capable BDPE receiver. Nevertheless, the presented results are worldwide unique and outstanding, as it is possible to calculate and analyze the probability of the user position, velocity and time in real-time, proof that BDPE performs better compared to a SPP solution and deliver the fundamental mathematical as well as processing framework for a real-time BDPE receiver.

9.2 Possible Future Investigations

Three aspects are very interesting to be investigated in future.

The first proposed investigation to continue is the realization of BDPE with the herein proposed optimal probabilistic weight update. Therefore, the weight update needs to be used by the particle or grid-based filter. To achieve a stable tracking behavior of the PVT, the Bayes filter needs to be well parametrized such that the PDF of the PVT is well covered by the grid or particle cloud. This should be achievable in a first step for defined user dynamics and environmental conditions. Once this is achieved, a sensitivity comparison between BDPE, vector tracking and a standard SPP navigation solution would be of high interest in order to proof, that the theoretical promises can be achieved in real conditions.

The second aspect is the problem and complexity of a Bayesian filter with a high dimensionality. A reduction of the dimensionality simplifies the problem and is possible for slow moving users. If the user can be assumed to be static or slow moving, the velocity states can be neglected, which reduces the dimensionality from 8 to 5 estimated states. Hereby, the velocity error expressed in a Doppler frequency must be significantly smaller than $\frac{1}{T_{coh}}$, according to the sinc-behavior of the Doppler correlation function, in order to keep the correlation loss low. The zero crossing points of the correlation function, for example $T_{coh} = 10$ ms and a wavelength $\lambda = 0.19$ m for the L1-band is at $f_d = \frac{1}{T_{coh}} = 100$ Hz, which equals a velocity of $v = f_d\lambda = 19$ m/s. In order to stay in the main lobe of the sinc, the absolute velocity error should not exceed e.g. $\frac{f_d}{2} = 9.5$ m/s $= 34.2$ km/h, which is sufficient for many applications such as pedestrians or construction machinery.

The third proposed research aspect is the comparison of an adaptable grid-based filter to a particle filter. Hereby, the grid-based filter can be propagated from one epoch to the next, same as the particle filter does. Hereby, the extension of the grid can be adapted according to the variance of the PDF of the covered state, and the resolution can be adapted as a tradeoff between processing complexity and resolution of the PDF. It is expected, that the grid-based filter is stable in challenging multipath environments, even if the nuisance parameters do not cover the multipath error completely. In such a case, the PDF of the PVT start jumping and the particles of a particle filter might not cover the new state properly, whereas a grid-based filter would still deliver reasonable estimates as long the new state is covered by the grid.

9.3 Outlook of GNSS and DPE Receivers

The current trend of GNSS receivers depends on the type of receiver. Mass-market low-cost receivers, which are used in mobile phones and in the automotive industry start to incorporate a second frequency in order to facilitate precise positioning techniques such as RTK and PPP. This should enable location-based services which require a more accurate PVT or should fulfill the absolute position requirements in self-driving cars. Today's professional GNSS receivers, as e.g. used in for surveying, can perfectly compensate for atmospheric errors, but still struggle with multipath, especially at construction sites. In the last years some advanced methods emerged, which promise a significant step forward in compensating the impact of multipath. These methods are based on forming a synthetic antenna gain pattern or known as beamforming techniques, either by use of antenna arrays or synthetically with a single antenna and known antenna motion. Based on the fact that the hardware complexity of antenna arrays is very high and that the motion of a single antenna is nowadays already precisely known in GNSS-INS receivers, it is expected that synthetic aperture antenna processing algorithms based on a single antenna and known motion, as proposed in [Pany, Falk, et al., 2013], will be implemented in near future in commercial GNSS receivers. Latest publications show, that synthetic aperture processing algorithms have already been implemented on mass-market Acorn RISC Machines (ARM) chipsets e.g. in a mobile phone [Faragher, 2018], which supports the expectation of this trend.

Mass-market as well as professional receivers are implemented in Application-Specific Integrated Circuits (ASICs) or Field Programmable Gate Arrays (FPGAs) to fulfill dominating requirements on power consumption and size. If more complex positioning algorithms need to be solved, e.g. sensor fusion with an IMU or calculating a precise position with RTK or PPP, typically ARM CPUs are used in addition to fulfill this task. The low power consumption of

an ARM processor causes to have only a Reduced Instruction Set Computer (RISC) architecture available, which also have very limited computational and memory resources. Thus, GNSS receivers are tailored and specifically designed for a set of applications. When thinking on DPE in GNSS receivers, two problems arise, (1) the architecture of current GNSS receivers do not support the required architecture by DPE and (2) the computational complexity of DPE is, at the moment, too high to be implemented on state-of-the-art receivers. Thus, it is expected that DPE or BDPE receivers will not be implemented in mass-market receivers soon. But it is expected, that first implementations with a reduced complexity, as briefly discussed in chapter 9.2, focusing only on the position and time estimate or as proposed in [Peretic and Grace X Gao, 2020a] to split up the position/time and velocity/time drift estimation process, will be realized soon.

Appendix

Appendix A

This section shows the integration step of the carrier phase ϕ on the sample distribution for a single GNSS signal. The result of integrating out ϕ can also be found in [Pany, 2010], but a detailed stepwise approach is also shown here for completeness. The proof in Appendix A was supported by Katrin Frankl. The sample distribution of a discrete GNSS signal is given with

$$p(\mathbf{s}|A,\tau,\omega,\phi) = \frac{1}{(2\pi)^L}\exp\left\{-\frac{1}{2}\sum_{\mu=1}^{L}|s_\mu - Ac(t_\mu-\tau)\exp\{i\omega t_\mu - i\phi\}|^2\right\} \quad \text{(A.1)}$$

where $\mathbf{s} \in \mathbb{C}^L$ contains all signal samples $s_\mu, \mu \in 1,...,L$. The time at a sample μ is given by $t_\mu = \frac{\mu}{f_s}$, where f_s is the sampling frequency. The probability $p(\cdot)$ basically depends on the replica signal parameters amplitude $A \in \mathbb{R}^+$, code delay $\tau \in \mathbb{R}$, Doppler $\omega \in \mathbb{R}$ and uniform distributed carrier phase $\phi \in [0,...,2\pi[$. Let also define $c_{\mu,\tau} = c(t_\mu - \tau)$ and i be the imaginary number. The sample distribution for a single signal in dependence of $[A,\tau,\omega]$ is achieved by integrating out the carrier phase ϕ such as

$$p(\mathbf{s}|A,\tau,\omega) = \frac{1}{2\pi}\int_{\phi=0}^{2\pi}\frac{1}{(2\pi)^L}\exp\left\{\underbrace{-\frac{1}{2}\sum_{\mu=1}^{L}|s_\mu - Ac_{\mu,\tau}\exp\{i\omega t_\mu - i\phi\}|^2}_{R}\right\}d\phi \quad \text{(A.2)}$$

With the definition of the absolute $|z| = \sqrt{z\bar{z}}$ and complex conjugation $\overline{y+z} = \bar{y}+\bar{z}$ as well as $\overline{yz} = \bar{y}\bar{z}$, the term R from (A.2) can be expanded to

$$
\begin{aligned}
R &= -\frac{1}{2}\sum_{\mu=1}^{L}\Big[s_\mu\overline{s_\mu} \\
&\quad -s_\mu\overline{Ac_{\mu,\tau}\exp\{i\omega t_\mu - i\phi\}} - \overline{s_\mu}Ac_{\mu,\tau}\exp\{i\omega t_\mu - i\phi\} \qquad \text{(A.3)} \\
&\quad +Ac_{\mu,\tau}\exp\{i\omega t_\mu - i\phi\}\overline{Ac_{\mu,\tau}\exp\{i\omega t_\mu - i\phi\}}\Big] \\
&= -\frac{1}{2}\sum_{\mu=1}^{L}\Big[|s_\mu|^2 \qquad \text{(A.4)} \\
&\quad -2\Re(\overline{s_\mu}Ac_{\mu,\tau}\exp\{i\omega t_\mu - i\phi\}) \qquad \text{(A.5)} \\
&\quad +A^2|c_{\mu,\tau}|^2\Big] \qquad \text{(A.6)}
\end{aligned}
$$

where $\Re(\cdot)$ and $\Im(\cdot)$ defines the real and imaginary part. To obtain (A.5) the following mathematical relationship

$$
\begin{aligned}
s\bar{z} + \bar{s}z &= (x+iy)\overline{(u+iv)} + \overline{(x+iy)}(u+iv) \\
&= (x+iy)(u-iv) + (x-iy)(u+iv) \qquad \text{(A.7)} \\
&= 2xu + 2yv \\
&= 2\Re(\bar{s}z)
\end{aligned}
$$

where $s = (x+iy)$ and $z = (u+iv)$ are complex valued numbers, was used. For (A.6) it was considered, that $|\exp\{i\omega t_\mu - i\phi\}|^2 = 1$, because of $|e^{iz}| = 1, z \in \mathbb{C}$. With (A.4) to (A.6) equation (A.2) can be rewritten to be

$$
\begin{aligned}
p(\mathbf{s}|A,\tau,\omega) &= \frac{1}{2\pi}\int_{\phi=0}^{2\pi}\frac{1}{(2\pi)^L}\exp\Big\{-\frac{1}{2}\sum_{\mu=1}^{L}|s_\mu|^2 \qquad \text{(A.8)} \\
&\quad -\frac{A^2}{2}\sum_{\mu=1}^{L}|c_{\mu,\tau}|^2 \qquad \text{(A.9)} \\
&\quad +A\sum_{\mu=1}^{L}\Re(\overline{s_\mu}c_{\mu,\tau}\exp\{i\omega t_\mu - i\phi\})\Big\}d\phi \qquad \text{(A.10)}
\end{aligned}
$$

From that restructuring it can be seen, that ϕ only depends on (A.10) and the equation can be rewritten to

$$
\begin{aligned}
p(\mathbf{s}|A,\tau,\omega) &= \frac{1}{(2\pi)^L}\exp\left\{-\frac{1}{2}\sum_{\mu=1}^{L}|s_\mu|^2\right\} \\
&\quad \exp\left\{-\frac{A^2}{2}\sum_{\mu=1}^{L}|c_{\mu,\tau}|^2\right\} \\
&\quad \underbrace{\frac{1}{2\pi}\int_{\phi=0}^{2\pi}\exp\left\{A\sum_{\mu=1}^{L}\Re(\overline{s_\mu}c_{\mu,\tau}\exp\{i\omega t_\mu - i\phi\})\right\}d\phi}_{m}
\end{aligned}
\tag{A.11}
$$

The basic idea from (A.11) is to bring the integral in a form of a known solution, therefore let define m to be the integral term of (A.11) with

$$
m = \frac{1}{2\pi}\int_{\phi=0}^{2\pi}\exp\left\{A\sum_{\mu=1}^{L}\Re(\overline{s_\mu}c_{\mu,\tau}\exp\{i\omega t_\mu - i\phi\})\right\}d\phi \tag{A.12}
$$

which can be expanded with the schema of $\Re(\bar{s}z) = \frac{1}{2}(\bar{s}z + s\bar{z})$ to

$$
\begin{aligned}
m &= \frac{1}{2\pi}\int_{\phi=0}^{2\pi}\exp\Big\{\frac{A}{2}\exp\{-i\phi\}\sum_{\mu=1}^{L}\bar{s}c_{\mu,\tau}\exp\{i\omega t_\mu\} \\
&\quad + \frac{A}{2}\overline{\exp\{-i\phi\}}\sum_{\mu=1}^{L}s\overline{c_{\mu,\tau}\exp\{i\omega t_\mu\}}\Big\}d\phi
\end{aligned}
\tag{A.13}
$$

Inserting in (A.13) the definition of the correlation value

$$
\overline{P(\tau,\omega)} = \frac{1}{\sqrt{L}}\sum_{\mu=1}^{L}\bar{s}c_{\mu,\tau}\exp\{i\omega t_\mu\} \tag{A.14}
$$

from (5.11) in [Pany, 2010] leads to

$$
m = \frac{1}{2\pi}\int_{\phi=0}^{2\pi}\exp\Big\{\underbrace{\frac{A}{2}\exp\{-i\phi\}\sqrt{L}\overline{P_{\tau,\omega}} + \frac{A}{2}\overline{\exp\{-i\phi\}}\sqrt{L}P_{\tau,\omega}}_{n}\Big\}d\phi \tag{A.15}
$$

With the following auxiliary calculation, n from (A.15) can be expressed with trigonometric functions. Let therefore redefine $a =: \frac{A}{2}\sqrt{L}$ and $P_{\tau,\omega} =: u + vi$ and reformulate n by

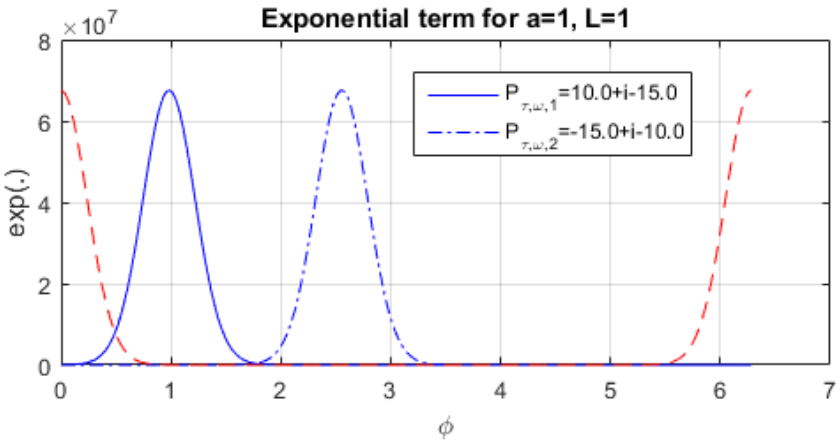

Figure A.1: This figure illustrates the exponential term from (A.17) with an arbitrary amplitude A and length L for two representative correlation values $P_{\tau,\omega,1}$ and $P_{\tau,\omega,2}$. The complex valued correlation values are shifted in phase by $\frac{\pi}{2}$ and are shown in blue. The red line illustrates the result, when shifting the maximum for each example to $\phi = 0$.

$$\begin{aligned} n &= \frac{A}{2}\exp\{-i\phi\}\sqrt{L}\overline{P_{\tau,\omega}} + \frac{A}{2}\overline{\exp\{-i\phi\}}\sqrt{L}P_{\tau,\omega} \\ &= a\exp\{-i\phi\}(u - vi) + a\overline{\exp\{-i\phi\}}(u + vi) \\ &= a[\cos(\phi) - i\sin(\phi)](u - vi) + a[\cos(\phi) + i\sin(\phi)](u + vi) \\ &= 2au\cos(\phi) - 2av\sin(\phi) \\ &= a\sqrt{L}\Re(P_{\tau,\omega})\cos(\phi) - a\sqrt{L}\Im(P_{\tau,\omega})\sin(\phi) \end{aligned} \tag{A.16}$$

With (A.16), equation (A.15) can be rewritten to be

$$m = \frac{1}{2\pi}\int_{\phi=0}^{2\pi} \exp\left\{A\sqrt{L}\Re(P_{\tau,\omega})\cos(\phi) - A\sqrt{L}\Im(P_{\tau,\omega})\sin(\phi)\right\}d\phi \tag{A.17}$$

Basically the exponential term in (A.17) is periodically from o to 2π, which is illustrated by Fig. A.1, and thus shifting the maxima by a an abitrary value ϕ does not change the result of the integral. It is shown in the next steps, that a shift of the maxima to $\phi = 0$ simplifies the the exponential term and thus also the analytical evaluation of the integral. The maxima of the exponential term in (A.17) can be found by

$$\frac{d}{d\phi}\exp\left\{A\sqrt{L}\Re(P_{\tau,\omega})\cos(\phi)-A\sqrt{L}\Im(P_{\tau,\omega})\sin(\phi)\right\} \stackrel{!}{=} 0 \quad \text{(A.18)}$$

$$\exp\left\{A\sqrt{L}\Re(P_{\tau,\omega})\cos(\phi)-A\sqrt{L}\Im(P_{\tau,\omega})\sin(\phi)\right\}$$
$$\left[A\sqrt{L}\Re(P_{\tau,\omega})(-\sin(\phi))-A\sqrt{L}\Im(P_{\tau,\omega})\cos(\phi)\right] \stackrel{!}{=} 0 \quad \text{(A.19)}$$

$$\Leftrightarrow$$

$$-A\sqrt{L}\Re(P_{\tau,\omega})\sin(\phi) = A\sqrt{L}\Im(P_{\tau,\omega})\cos(\phi) \quad \text{(A.20)}$$

$$\tan(\phi) = \frac{\sin(\phi)}{\cos(\phi)} = -\frac{\Im(P_{\tau,\omega})}{\Re(P_{\tau,\omega})} \quad \text{(A.21)}$$

$$\phi = \arctan\left(-\frac{\Im(P_{\tau,\omega})}{\Re(P_{\tau,\omega})}\right) \quad \text{(A.22)}$$

With (A.22) the phase in (A.17) can be shifted to zero by

$$m = \frac{1}{2\pi}\int_{\phi=0}^{2\pi}\exp\left\{A\sqrt{L}\Re(P_{\tau,\omega})\cos\left(\phi+\arctan\left(-\frac{\Im(P_{\tau,\omega})}{\Re(P_{\tau,\omega})}\right)\right)\right.$$
$$\left.-A\sqrt{L}\Im(P_{\tau,\omega})\sin\left(\phi+\arctan\left(-\frac{\Im(P_{\tau,\omega})}{\Re(P_{\tau,\omega})}\right)\right)\right\}d\phi \quad \text{(A.23)}$$

With the addition theorems

$$\cos(\alpha+\beta)=\cos(\alpha)\cos(\beta)-\sin(\alpha)\sin(\beta)$$
$$\sin(\alpha+\beta)=\sin(\alpha)\cos(\beta)+\cos(\alpha)\sin(\beta)$$

equation (A.23) can be rewritten to

$$m = \frac{1}{2\pi}\int_{\phi=0}^{2\pi}\exp\left\{A\sqrt{L}\Re(P_{\tau,\omega})\left[\cos(\phi)\cos\left(\arctan\left(-\frac{\Im(P_{\tau,\omega})}{\Re(P_{\tau,\omega})}\right)\right)\right.\right.$$
$$\left.-\sin(\phi)\sin\left(\arctan\left(-\frac{\Im(P_{\tau,\omega})}{\Re(P_{\tau,\omega})}\right)\right)\right]$$
$$-A\sqrt{L}\Im(P_{\tau,\omega})\left[\sin(\phi)\cos\left(\arctan\left(-\frac{\Im(P_{\tau,\omega})}{\Re(P_{\tau,\omega})}\right)\right)\right.$$
$$\left.\left.+\cos(\phi)\sin\left(\arctan\left(-\frac{\Im(P_{\tau,\omega})}{\Re(P_{\tau,\omega})}\right)\right)\right]\right\}d\phi \quad \text{(A.24)}$$

and with the definition of

$$\cos(\arctan(x)) = \frac{1}{\sqrt{1+x^2}}$$
$$\sin(\arctan(x)) = \frac{x}{\sqrt{1+x^2}}$$

equation (A.24) can be rewritten to

$$\begin{aligned} m &= \frac{1}{2\pi}\int_{\phi=0}^{2\pi} \exp\left\{ A\sqrt{L}\Re(P_{\tau,\omega}) \left[\cos(\phi)\frac{1}{\sqrt{1+\frac{\Im(P_{\tau,\omega})^2}{\Re(P_{\tau,\omega})^2}}} - \sin(\phi)\frac{-\frac{\Im(P_{\tau,\omega})}{\Re(P_{\tau,\omega})}}{\sqrt{1+\frac{\Im(P_{\tau,\omega})^2}{\Re(P_{\tau,\omega})^2}}} \right] \right. \\ &\quad \left. -A\sqrt{L}\Im(P_{\tau,\omega}) \left[\sin(\phi)\frac{1}{\sqrt{1+\frac{\Im(P_{\tau,\omega})^2}{\Re(P_{\tau,\omega})^2}}} + \cos(\phi)\frac{-\frac{\Im(P_{\tau,\omega})}{\Re(P_{\tau,\omega})}}{\sqrt{1+\frac{\Im(P_{\tau,\omega})^2}{\Re(P_{\tau,\omega})^2}}} \right] \right\} d\phi \quad \text{(A.25)} \\ &= \frac{1}{2\pi}\int_{\phi=0}^{2\pi} \exp\left\{ A\sqrt{L}\cos(\phi) \left[\underbrace{\frac{\Re(P_{\tau,\omega})}{\sqrt{1+\frac{\Im(P_{\tau,\omega})^2}{\Re(P_{\tau,\omega})^2}}} + \frac{\Im(P_{\tau,\omega})^2}{\Re(P_{\tau,\omega})\sqrt{1+\frac{\Im(P_{\tau,\omega})^2}{\Re(P_{\tau,\omega})^2}}}}_{o} \right] \right\} d\phi \end{aligned}$$

In a side calculation the term o in (A.25) can be simplified to

$$\begin{aligned} o &= \frac{\Re(P_{\tau,\omega})}{\sqrt{1+\frac{\Im(P_{\tau,\omega})^2}{\Re(P_{\tau,\omega})^2}}} + \frac{\Im(P_{\tau,\omega})^2}{\Re(P_{\tau,\omega})\sqrt{1+\frac{\Im(P_{\tau,\omega})^2}{\Re(P_{\tau,\omega})^2}}} \\ &= \frac{\Re(P_{\tau,\omega})^2 + \Im(P_{\tau,\omega})^2}{\Re(P_{\tau,\omega})\sqrt{1+\frac{\Im(P_{\tau,\omega})^2}{\Re(P_{\tau,\omega})^2}}} \\ &= \frac{\left(\Re(P_{\tau,\omega})^2 + \Im(P_{\tau,\omega})^2\right)\sqrt{1+\frac{\Im(P_{\tau,\omega})^2}{\Re(P_{\tau,\omega})^2}}}{\Re(P_{\tau,\omega})\left(1+\frac{\Im(P_{\tau,\omega})^2}{\Re(P_{\tau,\omega})^2}\right)} \\ &= \Re(P_{\tau,\omega})\sqrt{1+\frac{\Im(P_{\tau,\omega})^2}{\Re(P_{\tau,\omega})^2}} \\ &= \sqrt{\Re(P_{\tau,\omega})^2 + \Im(P_{\tau,\omega})^2} = ||P_{\tau,\omega}|| \quad \text{(A.26)} \end{aligned}$$

which further simplifies (A.25) to be

$$m = \frac{1}{2\pi}\int_{\phi=0}^{2\pi}\exp\left\{A||P_{\tau,\omega}||\sqrt{L}\cos(\phi)\right\}d\phi \tag{A.27}$$

The definition of the modified Bessel function of the first kind is given with

$$I_n = \frac{1}{\pi}\int_{\phi=0}^{\pi}\exp\left\{x\cos(\theta)\right\}\cos(n\theta)d\theta \tag{A.28}$$

whereas the modified Bessel function of the first kind and order $n = 0$ is given as

$$I_0 = \frac{1}{\pi}\int_{\phi=0}^{\pi}\exp\left\{x\cos(\theta)\right\}d\theta \tag{A.29}$$

which is of same integral type as (A.27) and thus the integral can be solved to be

$$m = I_0\left(A||P_{\tau,\omega}||\sqrt{L}\right) \tag{A.30}$$

When inserting now m in (A.11) and knowing that the absolute squared sum of the binary PRN code is $\sum_{\mu=1}^{L}|c_{\mu,\tau}|^2 = L$, the sample distribution for a single signal in dependence of $[A, \tau, \omega]$ can be obtained to be

$$p(\mathbf{s}|A,\tau,\omega) = \frac{1}{(2\pi)^L}\exp\left\{-\frac{1}{2}\sum_{\mu=1}^{L}|s_\mu|^2 - \frac{LA^2}{2}\right\}I_0\left(A||P(\tau,\omega)||\sqrt{L}\right) \tag{A.31}$$

Appendix B

This appendix shows the extension of the probabilistic model to multiple GNSS signals and how to obtain a numerically stable weight update in the logarithmic scale. This part of the work was published in [Dampf, Frankl, and Pany, 2018]. In a first step (A.1) is extended to two signals with the aim to find a mathematical rule to extend it to multiple signals. The extended model for two signals is defined as

$$\begin{aligned}
\mathbf{q_8} &= [A_1, \tau_1, \omega_1, \phi_1, A_2, \tau_2, \omega_2, \phi_2] \\
p(\mathbf{s}|\mathbf{q_8}) &= \tfrac{1}{(2\pi)^L} \exp\left\{ \underbrace{-\frac{1}{2}\sum_{\mu=1}^{L} \left| s_\mu - \left[\overbrace{A_1 c_1(t_\mu - \tau_1)\exp\{i\omega_1 t_\mu - i\phi_1\}}^{r_1} + \overbrace{A_2 c_2(t_\mu - \tau_2)\exp\{i\omega_2 t_\mu - i\phi_2\}}^{r_2} \right] \right|^2}_{m} \right\}
\end{aligned} \tag{B.1}$$

With the definition of $|z| = \sqrt{z\bar{z}}$, $|z|^2 = z\bar{z}$ and the definition of the replica signals r_1 and r_2, m can be expanded to

$$\begin{aligned}
m &= -\frac{1}{2}\sum_{\mu=1}^{L} \left(s_\mu \overline{s_\mu} - s_\mu \overline{[r_1 + r_2]} - \overline{s_\mu}[r_1 + r_2] + [r_1 + r_2]\overline{[r_1 + r_2]} \right) \\
&= -\frac{1}{2}\sum_{\mu=1}^{L} \left(s_\mu \overline{s_\mu} - s_\mu \overline{r_1} - s_\mu \overline{r_2} - \overline{s_\mu} r_1 - \overline{s_\mu} r_2 + r_1\overline{r_1} + r_2\overline{r_1} + r_1\overline{r_2} + r_2\overline{r_2} \right) \\
&= -\frac{1}{2}\sum_{\mu=1}^{L} \Big(|s_\mu|^2 + |r_1|^2 - 2Re(\overline{s_\mu} r_1) + \overbrace{|r_2|^2 - 2Re(\overline{s_\mu} r_2) + \underbrace{2Re(\overline{r_1} r_2)}_{\text{xcorr} \approx 0}}^{\text{new terms due to 2nd signal}} \Big)
\end{aligned} \tag{B.2}$$

With $|r_n|^2 = A_n^2 |c_n(t_\mu - \tau_n)|^2$ and neglecting the cross-correlation term xcorr leads to

$$\begin{aligned}
m = -\tfrac{1}{2}\textstyle\sum_{\mu=1}^{L} \Big(& |s_\mu|^2 + A_1^2 |c_1(t_\mu - \tau_1)|^2 - 2Re(\overline{s_\mu} A_1 c_1(t_\mu - \tau_1)\exp\{i\omega_1 t_\mu - i\phi_1\}) \\
& + A_2^2 |c_2(t_\mu - \tau_2)|^2 - 2Re(\overline{s_\mu} A_2 c_2(t_\mu - \tau_2)\exp\{i\omega_2 t_\mu - i\phi_2\}) \Big)
\end{aligned} \tag{B.3}$$

Inserting (B.3) in (B.1), consider that the sum of the squared PRN code leads to $\sum_{\mu=1}^{L} |c(t_\mu - \tau_2)|^2 = L$ and realigning the terms to integrate out ϕ_1 and ϕ_2 leads to

$$
\begin{aligned}
\mathbf{q_6} &= [A_1, \tau_1, \omega_1, A_2, \tau_2, \omega_2] \\
p(\mathbf{s}|\mathbf{q_6}) &= \frac{1}{(2\pi)^L} \exp\left\{-\frac{1}{2}\sum_{\mu=1}^{L}\left|s_\mu\right|^2\right\} \\
&\quad \frac{1}{(2\pi)}\int_{\phi_1=0}^{2\pi} \exp\left\{-\frac{LA_1^2}{2}\right\} \exp\left\{A_1 \sum_{\mu=1}^{L} Re(\overline{s_\mu} c_1(t_\mu - \tau_1) \exp\{i\omega_1 t_\mu - i\phi_1\}\right\} d\phi_1 \\
&\quad \frac{1}{(2\pi)}\int_{\phi_2=0}^{2\pi} \exp\left\{-\frac{LA_2^2}{2}\right\} \exp\left\{A_2 \sum_{\mu=1}^{L} Re(\overline{s_\mu} c_2(t_\mu - \tau_2) \exp\{i\omega_2 t_\mu - i\phi_2\}\right\} d\phi_2 \\
&= \frac{1}{(2\pi)^L} \exp\left\{-\frac{1}{2}\sum_{\mu=1}^{L}\left|s_\mu\right|^2\right\} \\
&\quad \exp\left\{-\frac{LA_1^2}{2}\right\} I_0(A_1|P_1(\tau_1,\omega_1)_1|\sqrt{L}) \\
&\quad \exp\left\{-\frac{LA_2^2}{2}\right\} I_0(A_2|P_2(\tau_2,\omega_2)_2|\sqrt{L})
\end{aligned}
\tag{B.4}
$$

It can be shown in (B.4) that the extension to multiple GNSS signals follows the same structure as shown in (A.2) for a single GNSS signal, if the (quasi) orthogonal cross correlation terms are neglected as shown in (B.2).

Solving an integral of type $\int_0^\infty \exp\{-\frac{x^2}{c}\} I_0(xp)dx$ was performed with the help of Wolfram Mathematica [Wolfram Research Inc., 2018] which was used to integrate out the amplitude as

$$
\begin{aligned}
p(\mathbf{s}|\tau_1,\omega_1,\tau_2,\omega_2) &= \frac{1}{(2\pi)^L}\exp\left\{-\frac{1}{2}\sum_{\mu=1}^{L}|s_\mu|^2\right\} \\
&\quad \int_{A_1=0}^{\infty}\exp\left\{-\frac{LA_1^2}{2}\right\} I_0(A_1|P_1(\tau_1,\omega_1)_1|\sqrt{L})dA_1 \\
&\quad \int_{A_2=0}^{\infty}\exp\left\{-\frac{LA_2^2}{2}\right\} I_0(A_2|P_2(\tau_2,\omega_2)_2|\sqrt{L})dA_2 \\
&= \frac{1}{(2\pi)^L}\exp\left\{-\frac{1}{2}\sum_{\mu=1}^{L}|s_\mu|^2\right\} \\
&\quad \sqrt{\frac{\pi}{2L}}\exp\left\{\frac{|P_1(\tau_1,\omega_1)|^2}{4}\right\} I_0\left(\frac{|P_1(\tau_1,\omega_1)|^2}{4}\right) \qquad \text{(B.5)} \\
&\quad \sqrt{\frac{\pi}{2L}}\exp\left\{\frac{|P_2(\tau_2,\omega_2)|^2}{4}\right\} I_0\left(\frac{|P_2(\tau_2,\omega_2)|^2}{4}\right)
\end{aligned}
$$

With the assumption of using Gaussian distributed complex valued samples s_μ whose real and imaginary parts are each of variance one and zero mean, the sum over the absolute squared samples approximates to $L \approx \frac{1}{2}\sum_{\mu=1}^{L}|s_\mu|^2$. This approximation can be made if the GNSS signal amplitude is significantly smaller than the noise. This is generally the case for GNSS signals when considering receivers operated on the earths ground [Misra and Enge, 2010]. With this approximation, (B.5) can be rewritten for N GNSS signals as

$$
p(\mathbf{s}|\boldsymbol{\tau},\boldsymbol{\omega}) = \frac{1}{(2\pi)^L}\exp\{-L\}N\sqrt{\frac{\pi}{2L}}\prod_{n=1}^{N}\exp\left\{\frac{|P_n(\tau_n,\omega_n)|^2}{4}\right\} I_0\left(\frac{|P_n(\tau_n,\omega_n)|^2}{4}\right) \qquad \text{(B.6)}
$$

Equation (B.6) defines the probability function $p(\mathbf{z}_k|\mathbf{x}_k^i)$ for an arbitrary number N GNSS signals in order to obtain w_k^i in (4.39). Note that the code-phase and Doppler values changed from a scalar to vectors $\boldsymbol{\tau} \in \mathbb{R}^N$ and $\boldsymbol{\omega} \in \mathbb{R}^N$. However, with this equation, the weight cannot be evaluated directly due to finite precision effects when solving the equation on a computer. In particular, the terms $\exp\left\{\frac{|P_n(\tau_n,\omega_n)|^2}{4}\right\}$ and $I_0\left(\frac{|P_n(\tau_n,\omega_n)|^2}{4}\right)$ use a typically 'large' correlation value P, which causes a numerical problem. The common maximum value that can be stored on 64-bit platforms is a double precision floating-point value (not considering dedicated floating point libraries). The maximum value is limited to 1.7E $\pm$ 308 (15 digits) [Microsoft Cooperation, 2018]. Considering the term $\exp\left\{\frac{|P_n(\tau_n,\omega_n)|^2}{4}\right\}$ in Equation (B.6), the numerical limits are approximately reached for a correlation value $P_n(\tau_n,\omega_n) > 53.28$. A solution to overcome the effect of limited digital precision is proposed in the

next chapter.

Logarithmic Weight Update

When performing the particle weight update, the numerical values can be too large to be evaluated by a computer. The numerical issues at the weight update when evaluating (B.6) can be solved by shifting the equations to the logarithmic scale and performing an additional normalization step. As a first step, let

$$I_\alpha(z) \approx \frac{e^z}{\sqrt{2\pi z}}\Big(1 - \frac{4\alpha^2 - 1}{8z} + \frac{(4\alpha^2 - 1)(4\alpha^2 - 9)}{2!(8z)^2} + ...\Big) \tag{B.7}$$

be an approximation of the Bessel function of first kind, where only the first term is used to approximate the function with order zero, resulting in

$$I_0(z) \approx \frac{e^z}{\sqrt{2\pi z}} \tag{B.8}$$

With (B.8), (B.6) can be rewritten to

$$p(\mathbf{s}|\boldsymbol{\tau}, \boldsymbol{\omega}) \approx \underbrace{\frac{1}{(2\pi)^L} \exp\{-L\} N \sqrt{\frac{\pi}{2L}}}_{H_{const}} \prod_{n=1}^{N} \left(\frac{\exp\left\{ \frac{|P_n(\tau_n, \omega_n)|^2}{2} \right\}}{\sqrt{2\pi \frac{|P_n(\tau_n, \omega_n)|^2}{4}}} \right) \tag{B.9}$$

Based on the reason that a later introduced normalization step is performed in (B.14), the constant term H_{const} can be neglected. With that, the weight update from (4.39) can be expressed as

$$w_k^i \propto w_{k-1}^i \prod_{n=1}^{N} \left(\frac{\exp\left\{ \frac{|P_n(\tau_n, \omega_n)|^2}{2} \right\}}{\sqrt{2\pi \frac{|P_n(\tau_n, \omega_n)|^2}{4}}} \right) \tag{B.10}$$

Let define $\widetilde{w}_k^i = \log(w_k^i)$ and $\widetilde{w}_{k-1}^i = \log(w_{k-1}^i)$. Then, the update can be written in logarithmic scale as

$$\widetilde{w}_k^i \propto \widetilde{w}_{k-1}^i + \sum_{n=1}^{N} \left(\frac{|P_n(\tau_n, \omega_n)|^2}{2} - \log\left(\sqrt{2\pi \frac{|P_n(\tau_n, \omega_n)|^2}{4}} \right) \right) \tag{B.11}$$

The weight update from (4.39) can now be done in five steps from equation (B.12) to (B.16) using

$$\widetilde{w}_{k-1}^{i} = \log(w_{k-1}^{i}) \tag{B.12}$$

$$\widetilde{w}_{k}^{i} = \widetilde{w}_{k-1}^{i} + \sum_{n=1}^{N} \left(\frac{|P_n(\tau_n, \omega_n)|^2}{2} - \log\left(\sqrt{2\pi \frac{|P_n(\tau_n, \omega_n)|^2}{4}} \right) \right) \tag{B.13}$$

$$\overline{w}_{k}^{i} = \widetilde{w}_{k}^{i} - \max(\widetilde{w}_{k}^{i}) \tag{B.14}$$

$$w_{k}^{i} = \exp(\overline{w}_{k}^{i}) \tag{B.15}$$

$$w_{k}^{i} = \frac{w_{k}^{i}}{\sum_{i=1}^{N_s} w_{k}^{i}} \tag{B.16}$$

This series of equations allows for performing the weight update within numerical boundaries (e.g., double precision) and can be used to implement the optimal particle weight update for any Bayesian filter working with GNSS correlation values.

Appendix C

This appendix shows the introduction of Gaussian nuisance parameters for the code delay and Doppler. The derivation of the code delay was published in [Dampf, Frankl, and Pany, 2018]. The herein presented extended derivation for the code phase and Doppler was published in [Dampf and Pany, 2018]. For the 2-dimensional introduction of a Gaussian nuisance parameter for the code delay $\delta\tau$ and Doppler $\delta\omega$ let define

$$\begin{aligned} \Delta\tau &\sim N(0, \sigma^2_{\Delta\tau}) && \text{(C.1)} \\ p(\Delta\tau) &= \frac{1}{\sqrt{2\pi}\sigma_{\Delta\tau}} \exp\left\{-\frac{1}{2}\frac{\Delta\tau^2}{\sigma^2_{\Delta\tau}}\right\} && \text{(C.2)} \end{aligned}$$

and

$$\begin{aligned} \Delta\omega &\sim N(0, \sigma^2_{\Delta\omega}) && \text{(C.3)} \\ p(\Delta\omega) &= \frac{1}{\sqrt{2\pi}\sigma_{\Delta\omega}} \exp\left\{-\frac{1}{2}\frac{\Delta\omega^2}{\sigma^2_{\Delta\omega}}\right\} && \text{(C.4)} \end{aligned}$$

With these definitions the probability function can be modified to include the code delay uncertainty with

$$p(\mathbf{s}|\tau,\omega) = \int_{\Delta\tau=-\infty}^{\infty} p(\Delta\tau)p(\mathbf{s}|\tau+\Delta\tau,\omega)d\Delta\tau \qquad \text{(C.5)}$$

and both, code delay and Doppler uncertainty by

$$p(\mathbf{s}|\tau,\omega) = \int_{\Delta\tau=-\infty}^{\infty}\int_{\Delta\omega=-\infty}^{\infty} p(\Delta\tau)p(\Delta\omega)p(\mathbf{s}|\tau+\Delta\tau,\omega+\Delta\omega)d\Delta\tau d\Delta\omega \qquad \text{(C.6)}$$

The discrete form of (C.6) can be written as

$$p(\mathbf{s}|\tau,\omega) \approx \sum_{k=1}^{K}\sum_{j=1}^{J} p(\Delta\tau_k)p(\Delta\omega_j)p(\mathbf{s}|\tau+\Delta\tau_k,\omega+\Delta\omega_j) \qquad \text{(C.7)}$$

where k denote the index in code phase direction and j the index in Doppler direction. The extension of (C.7) to two GNSS signals can be written as

$$q_4 = [\tau_1, \omega_1, \tau_2, \omega_2] \tag{C.8}$$

$$\begin{aligned} p(\mathbf{s}|q_4) &= \frac{1}{(2\pi)^L} \exp\left\{-\frac{1}{2}\sum_{\mu=1}^{L}|s_\mu|^2\right\} \\ &\sum_{k=1}^{K}\sum_{j=1}^{J} p(\Delta\tau_k)p(\Delta\omega_j)\sqrt{\frac{\pi}{2L}}\exp\left\{\frac{|P_1(\tau_1+\Delta\tau_k,\omega_1+\Delta\omega_j)|^2}{4}\right\} I_0\left(\frac{|P_1(\tau_1+\Delta\tau_k,\omega_1+\Delta\omega_j)|^2}{4}\right) \\ &\sum_{k=1}^{K}\sum_{j=1}^{J} p(\Delta\tau_k)p(\Delta\omega_j)\sqrt{\frac{\pi}{2L}}\exp\left\{\frac{|P_2(\tau_2+\Delta\tau_k,\omega_2+\Delta\omega_j)|^2}{4}\right\} I_0\left(\frac{|P_2(\tau_2+\Delta\tau_k,\omega_2+\Delta\omega_j)|^2}{4}\right) \end{aligned} \tag{C.9}$$

which can be generalized to multiple GNSS signals N and simplified to the weight update equation

$$w_k^i \propto w_{k-1}^i \prod_{n=1}^{N}\left\{\sum_{k=1}^{K}\sum_{j=1}^{J}\underbrace{p(\Delta\tau_k)p(\Delta\omega_j)\frac{\exp\left\{\frac{|P_n(\tau_n+\Delta\tau_k,\omega_n+\Delta\omega_j)|^2}{2}\right\}}{\sqrt{2\pi\frac{|P_n(\tau_n+\Delta\tau_k,\omega_n+\Delta\omega_j)|^2}{4}}}}_{c_{k,j}}\right\} \tag{C.10}$$

In order to obtain again a logarithmic weight update procedure, let define

$$a_{k,j} = \frac{p(\Delta\tau_k)p(\Delta\omega_j)}{\sqrt{2\pi\frac{|P_n(\tau_n+\Delta\tau_k,\omega_n+\Delta\omega_j)|^2}{4}}} \tag{C.11}$$

$$b_{k,j} = \frac{|P_n(\tau_n+\Delta\tau_k,\omega_n+\Delta\omega_j)|^2}{2} \tag{C.12}$$

The existing logarithmic weight update procedure can be reformulated for a two-dimensional case accounting for a code phase and Doppler nuisance parameter as

$$\sum_{k=1}^{2}\sum_{j=1}^{2} c_{k,j} = a_{1,1}e^{b_{1,1}} + ... + a_{2,2}e^{b_{2,2}} = a_{1,1}e^{b_{1,1}}\left(1 + ... + e^{b_{2,2}-b_{1,1}}\frac{a_{2,2}}{a_{1,1}}\right) \tag{C.13}$$

where $a_{1,1}$ and $b_{1,1}$ define the maximum of the two dimensional grid. The equation can further be generalized for multiple grid points to

$$\sum_{k=1}^{K}\sum_{j=1}^{J} c_{k,j} = a_{1,1}e^{b_{1,1}}\left(1 + \sum_{k=2}^{K}\sum_{j=2}^{J}\underbrace{e^{b_{k,j}-b_{1,1}}}_{<1 \text{ if } b_{1,1,\max}}\frac{a_{k,j}}{a_{1,1}}\right) \tag{C.14}$$

which leads to the following stable update

$$\log\left(\sum_{k=1}^{K}\sum_{j=1}^{J} c_{k,j}\right) = \log(a_{1,1}) + b_{1,1} + \log\left(1 + \sum_{k=2}^{K}\sum_{j=2}^{J} e^{b_{k,j}-b_{1,1}}\frac{a_{k,j}}{a_{1,1}}\right) \tag{C.15}$$

With the formulation of (C.15) the weight update can be rewritten as

$$\begin{aligned}\widetilde{w}_k^i &= \widetilde{w}_{k-1}^i + \sum_{n=1}^{N}\left[\log\left(\frac{p(\Delta\tau_1)p(\Delta\omega_1)}{\sqrt{2\pi\frac{|P_n(\tau_n+\Delta\tau_1,\omega_n+\Delta\omega_1)|^2}{4}}}\right) + \frac{|P_n(\tau_n+\Delta\tau_1,\omega_n+\Delta\omega_1)|^2}{2}\right. \\ &\quad + \log\left(\sum_{k=1}^{K}\sum_{j=1}^{J}\exp\left\{\frac{|P_n(\tau_n+\Delta\tau_k,\omega_n+\Delta\omega_j)|^2}{2} - \frac{|P_n(\tau_n+\Delta\tau_1,\omega_n+\Delta\omega_1)|^2}{2}\right\}\right. \\ &\quad \left.\left.\frac{p(\Delta\tau_k)p(\Delta\omega_j)}{p(\Delta\tau_1)p(\Delta\omega_1)}\ \frac{|P_n(\tau_n+\Delta\tau_1,\omega_n+\Delta\omega_1)|}{|P_n(\tau_n+\Delta\tau_k,\omega_n+\Delta\omega_j))|}\right)\right] \end{aligned} \tag{C.16}$$

whereas $\Delta\tau_1$ and $\Delta\omega_1$ are the offsets to the maximum correlation value of the 2-dimensional discrete grid.

Appendix D

This appendix shows time series of the urban environment, bridge underpass and indoor environment. All plots have been generated with the settings given in Tab. 8.2. Two plots are shown for each epoch, the sum of correlation values and the PDF, both in the local ENU coordinate system. Details of how the plots are generated can be found in chapter 8.6. The plots are generated with 4 Hz and cover a time span of 7 seconds, resulting in 28 epochs where each page covers 1 second.

Urban Environment

The urban environment scenario was recorded in the Steyrergasse, Graz, Austria. The trajectory is shown in the figure below.

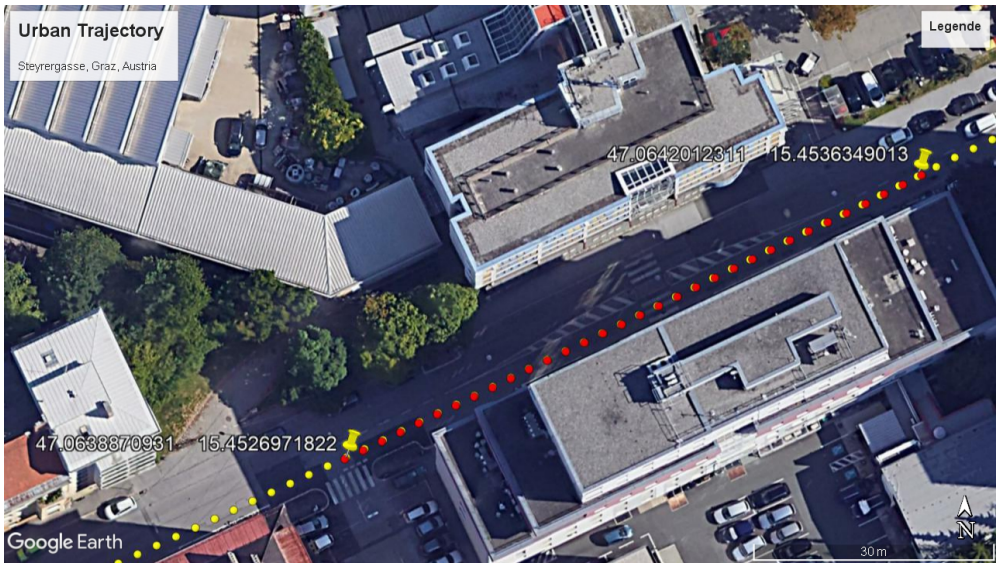

Figure D.1: Urban trajecotry corresponding to the time series in the Steyrergasse, Graz, Austria. The red positions of the trajectory refer to the PDFs of Fig. D.2 to D.8

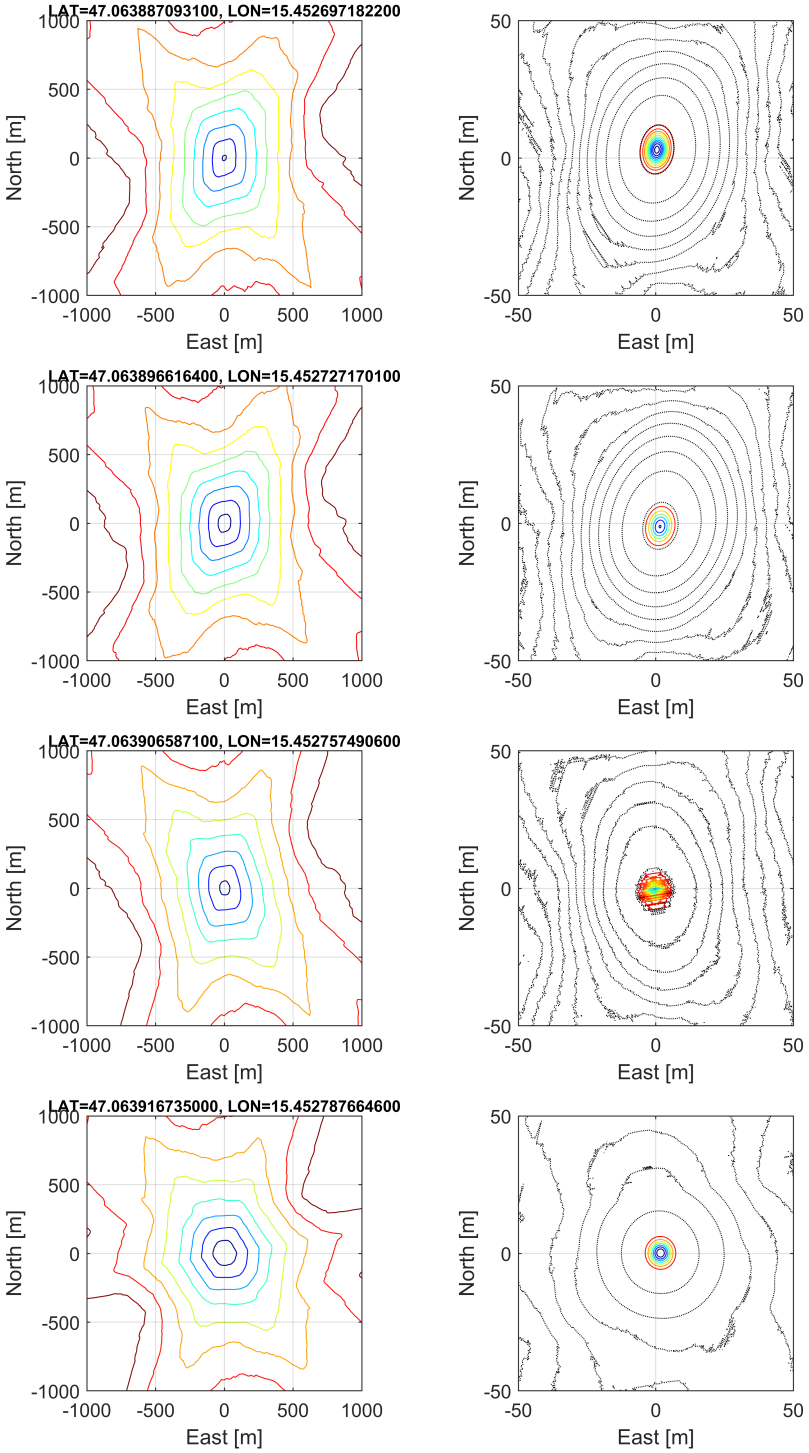

Figure D.2: PDF time series of the urban trajectory - Part 1

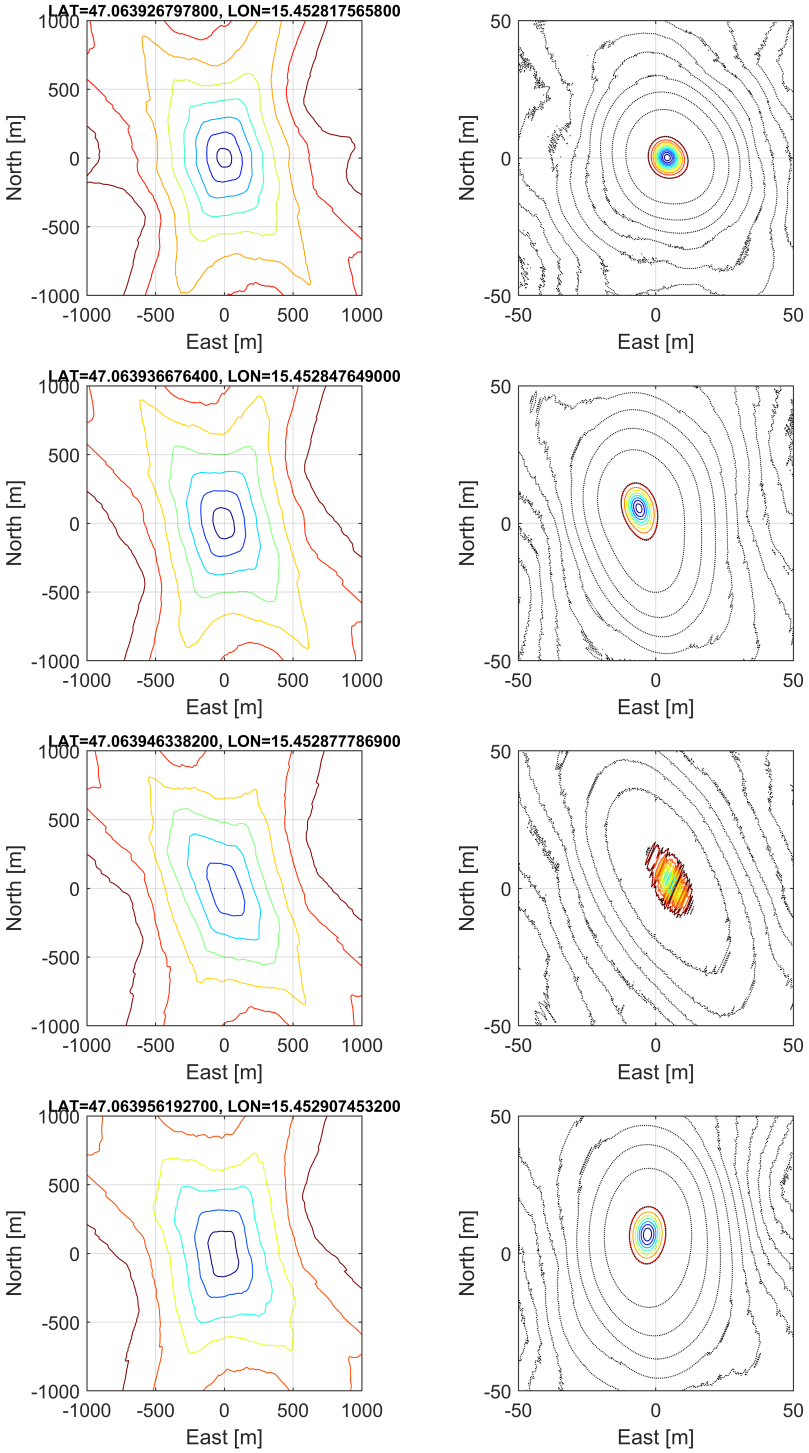

Figure D.3: PDF time series of the urban trajectory - Part 2

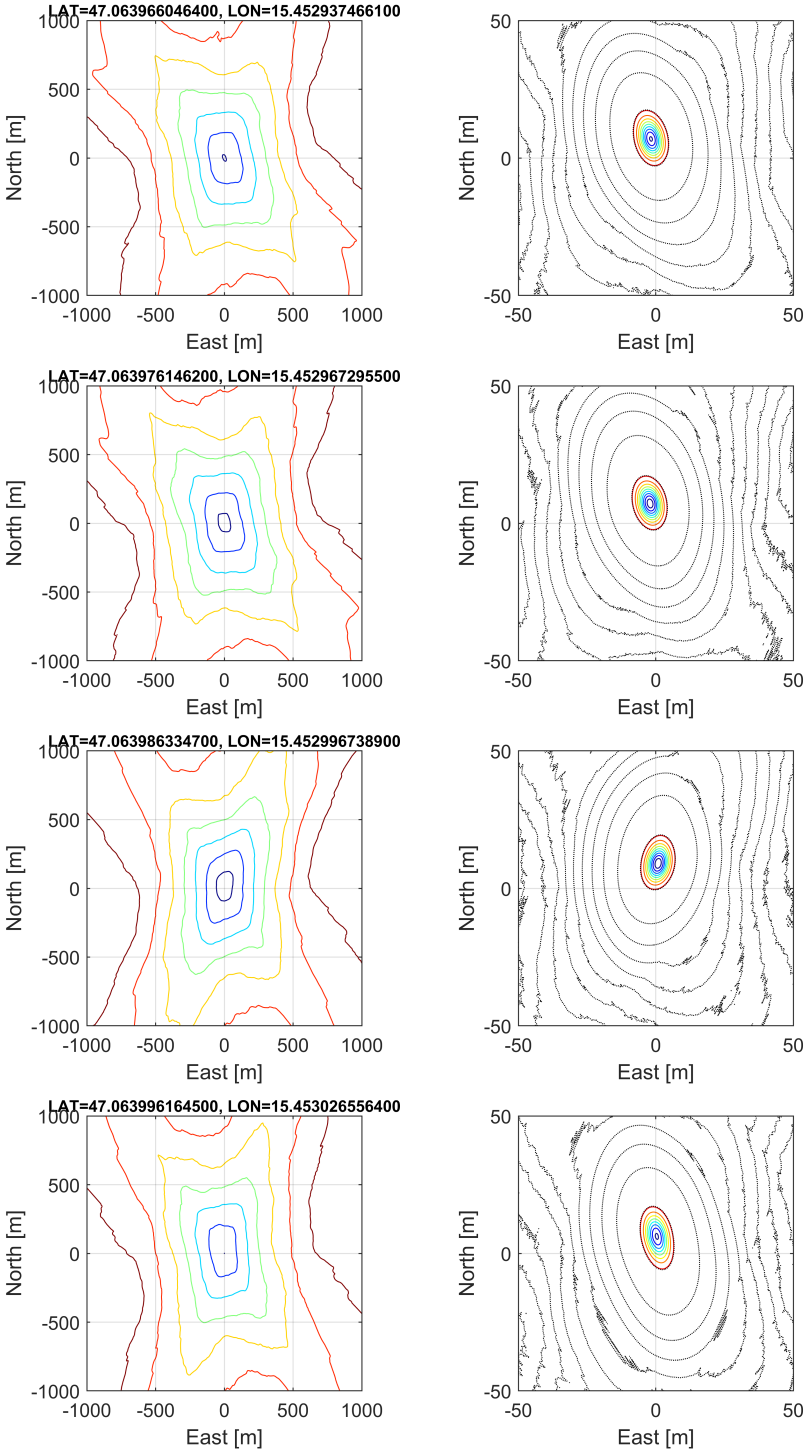

Figure D.4: PDF time series of the urban trajectory - Part 3

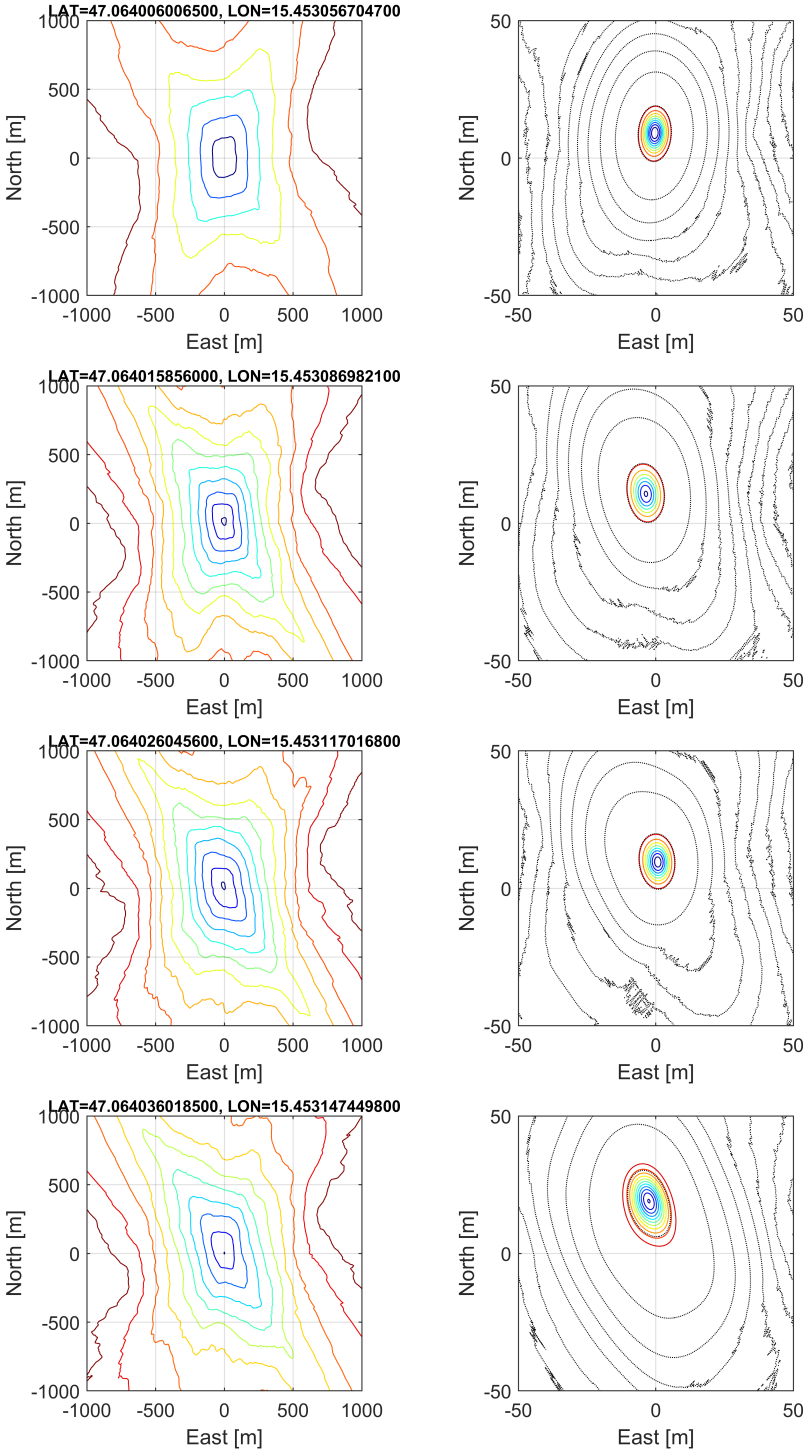

Figure D.5: PDF time series of the urban trajectory - Part 4

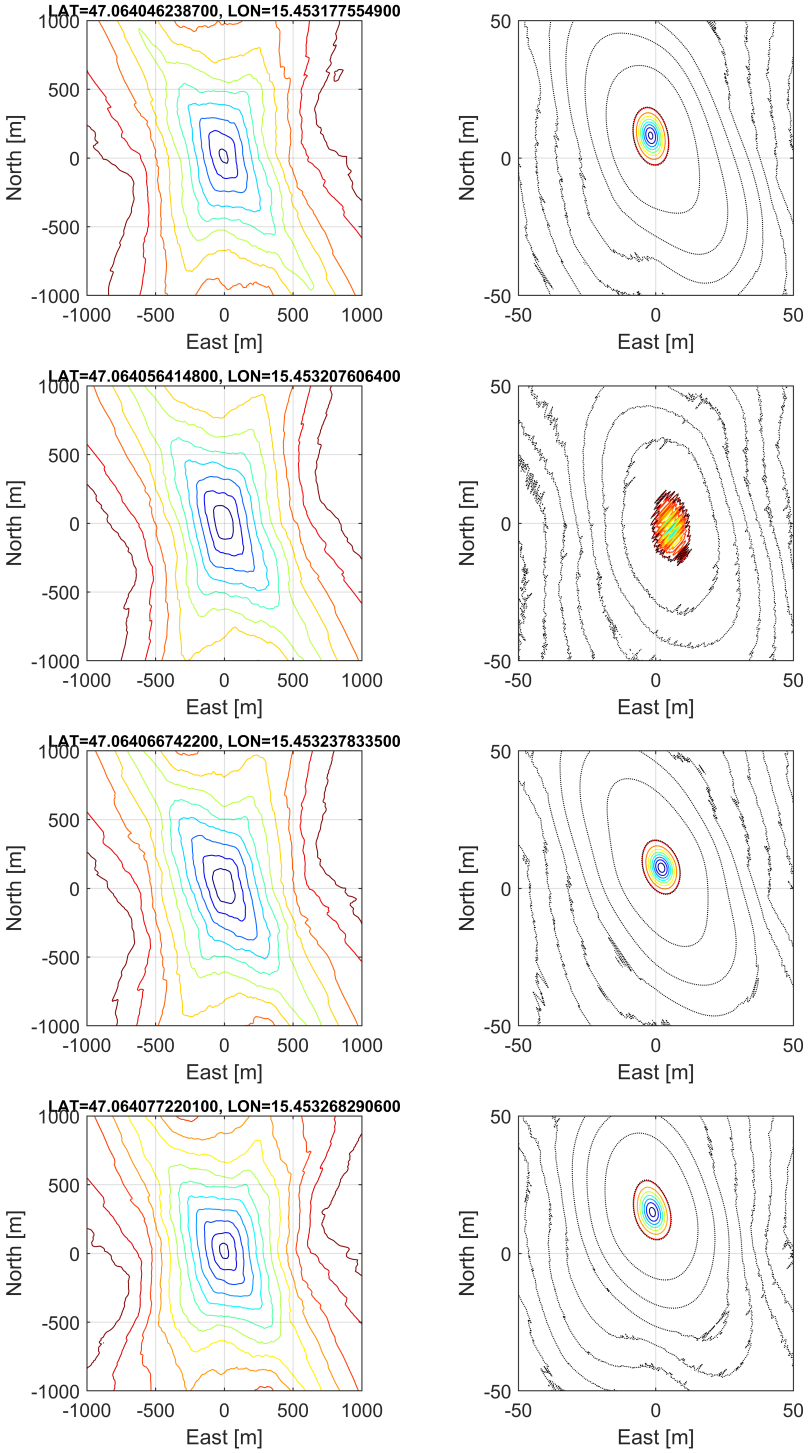

Figure D.6: PDF time series of the urban trajectory - Part 5

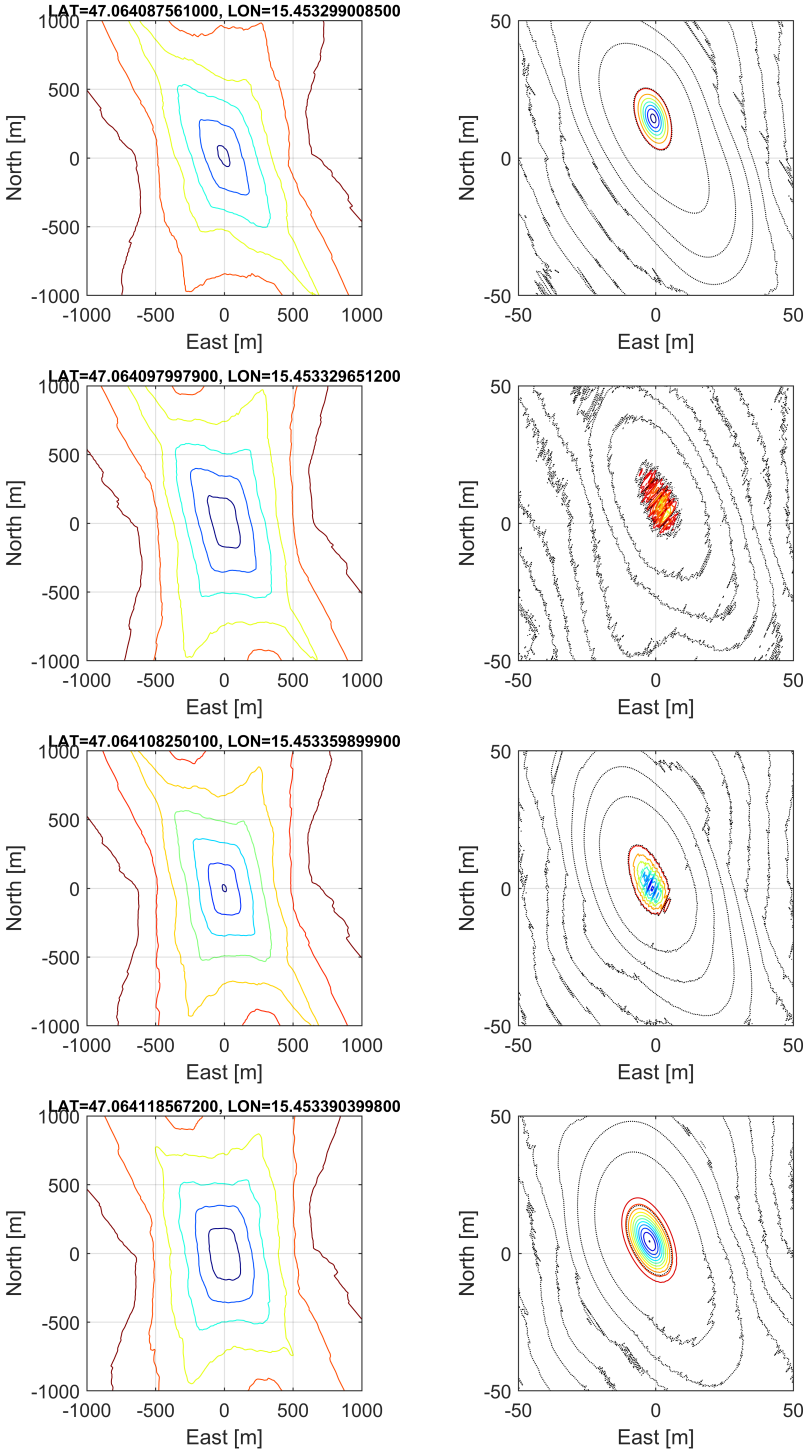

Figure D.7: PDF time series of the urban trajectory - Part 6

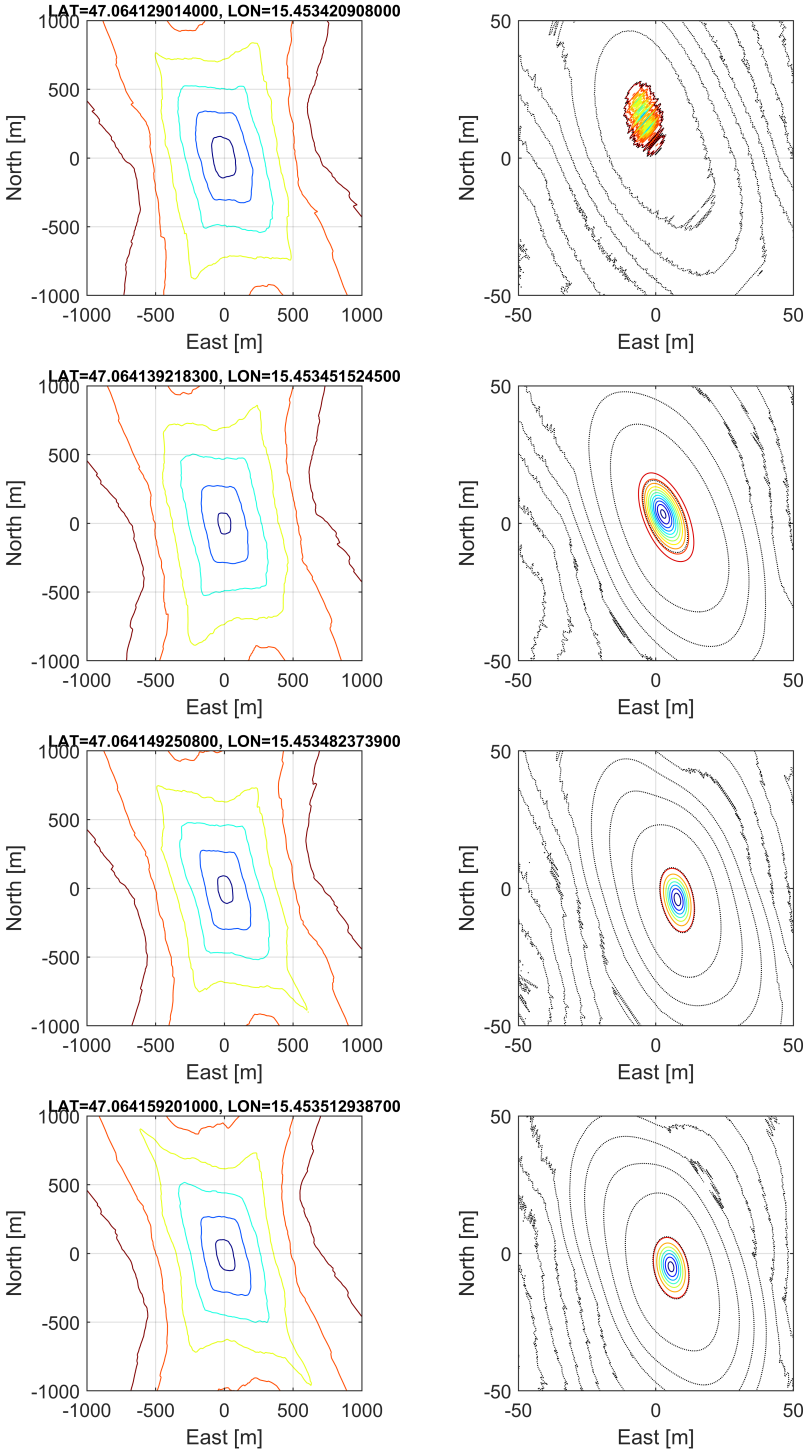

Figure D.8: PDF time series of the urban trajectory - Part 7

Bridge Underpass

The bridge underpass was recorded in the Peter-Tunner-Gasse, Graz, Austria. The trajectory is shown in the figure below.

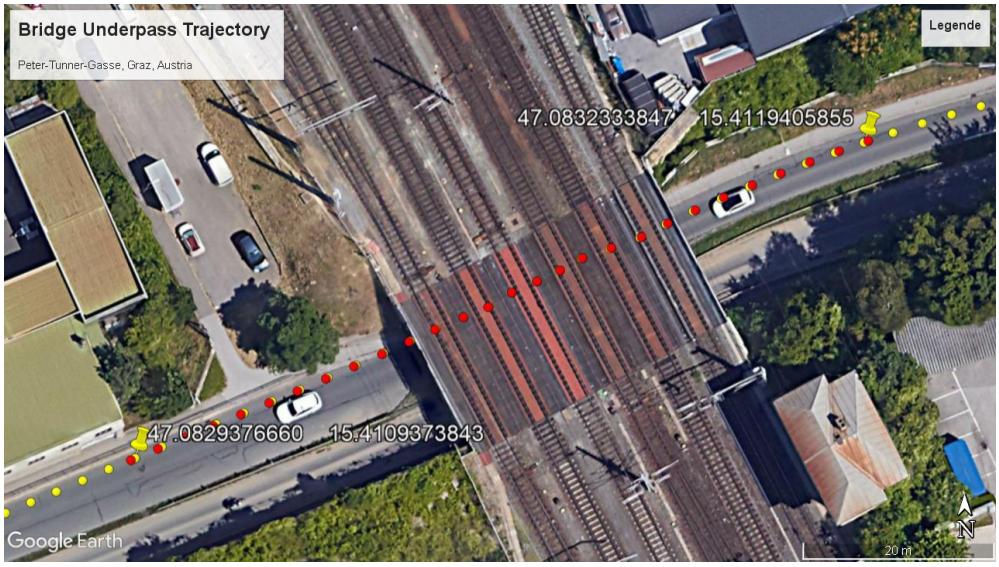

Figure D.9: Bridge underpass trajecotry corresponding to the time series in the Peter-Tunner-Gasse, Graz, Austria. The red positions of the trajectory refer to the PDFs of Fig. D.10 to D.16

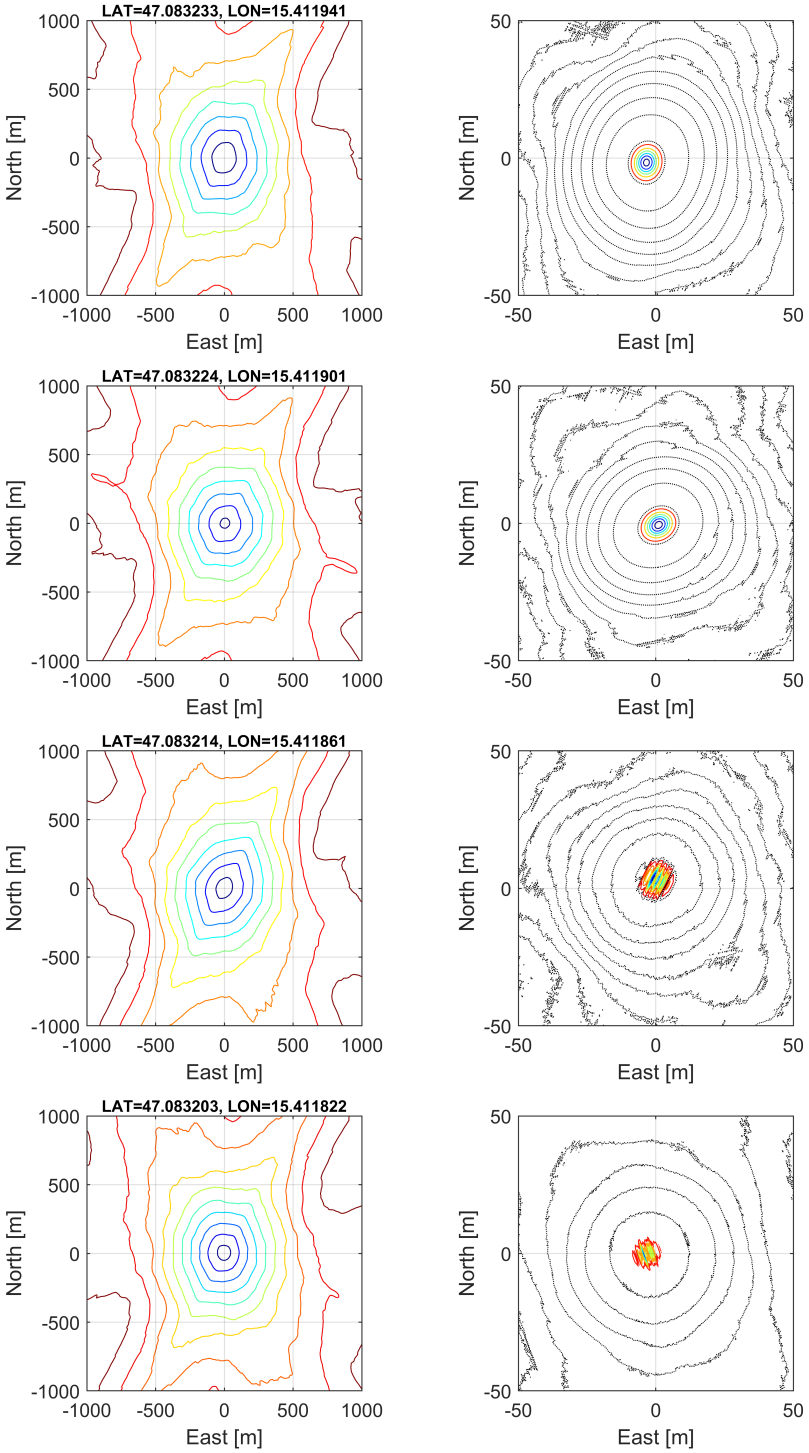

Figure D.10: PDF time series of the bridge underpass - Part 1

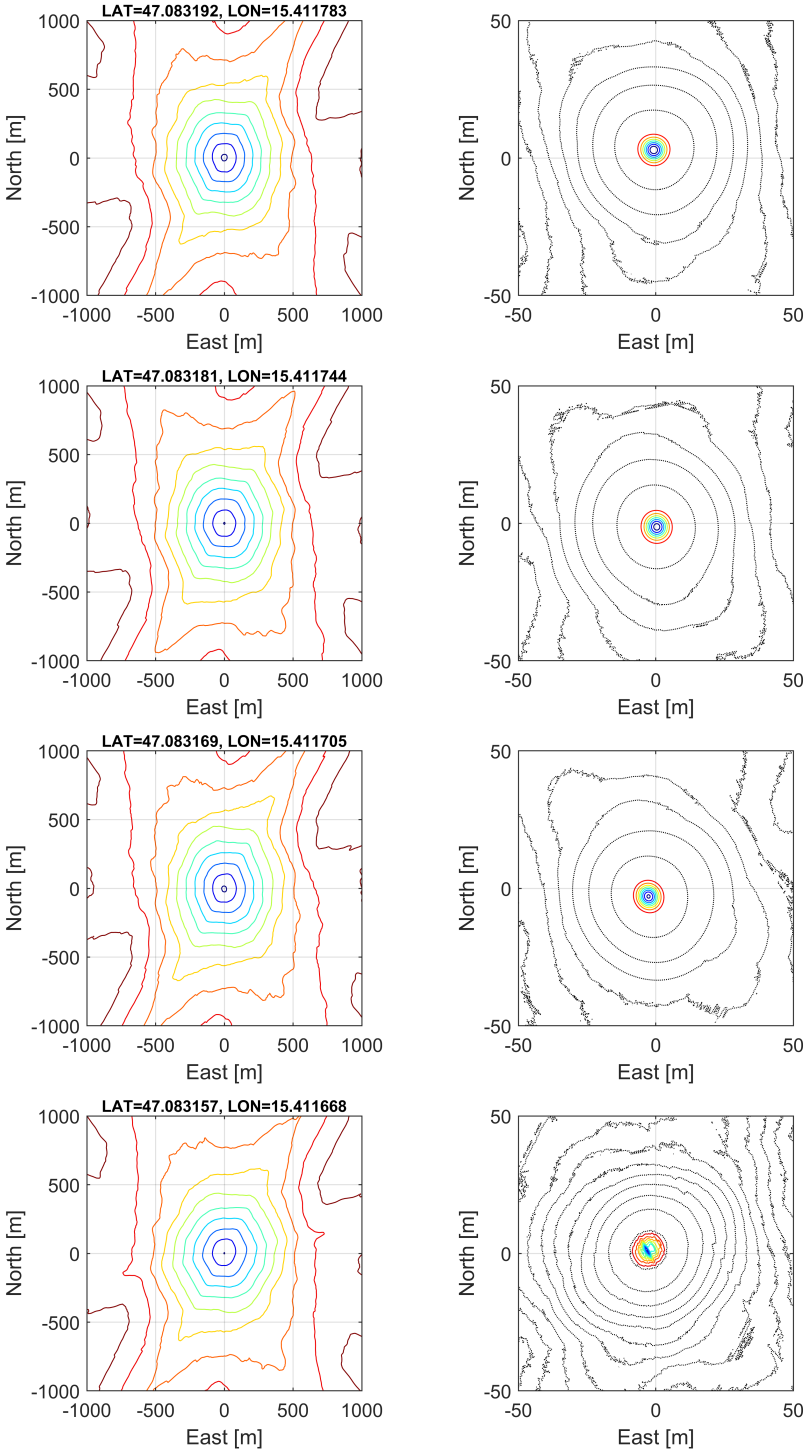

Figure D.11: PDF time series of the bridge underpass - Part 2

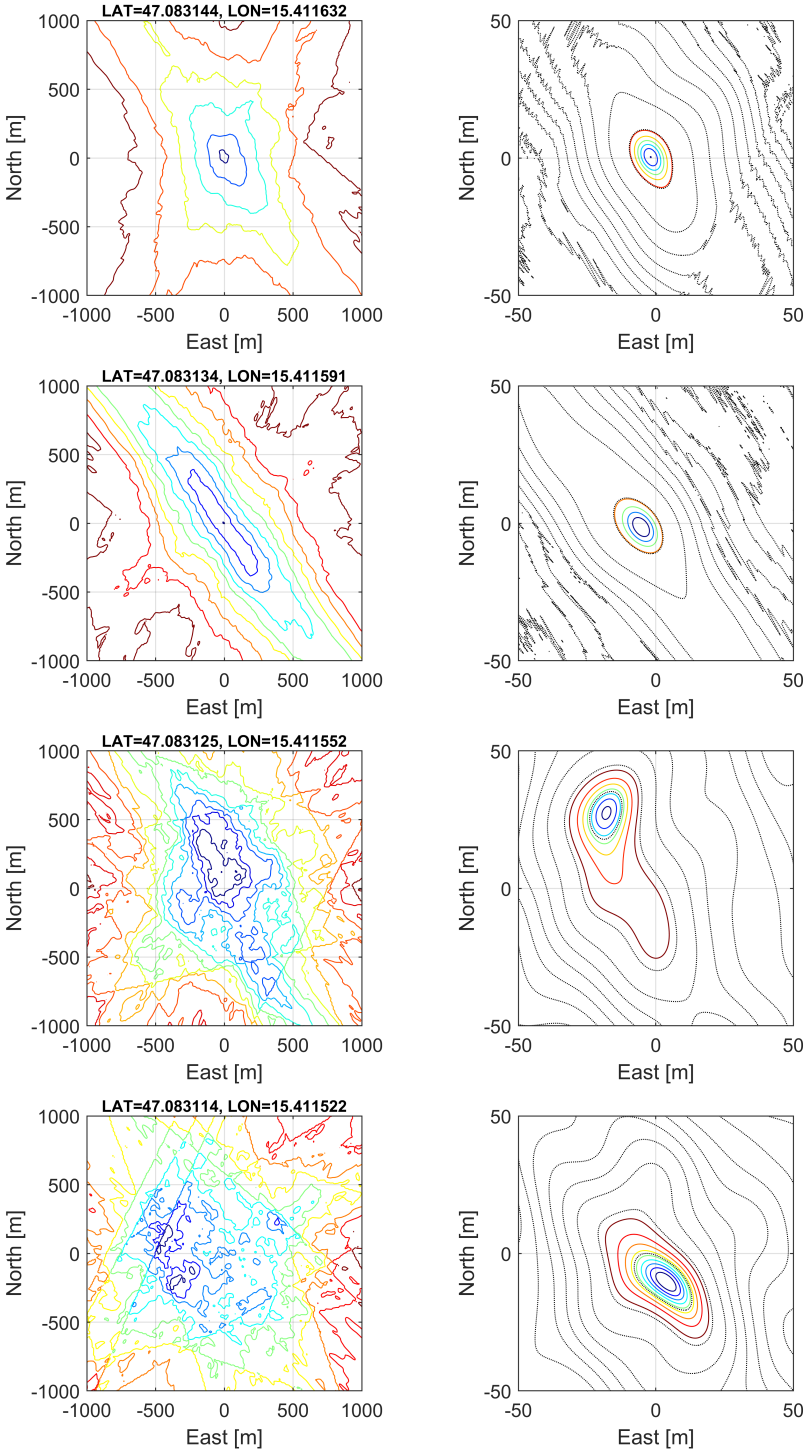

Figure D.12: PDF time series of the bridge underpass - Part 3

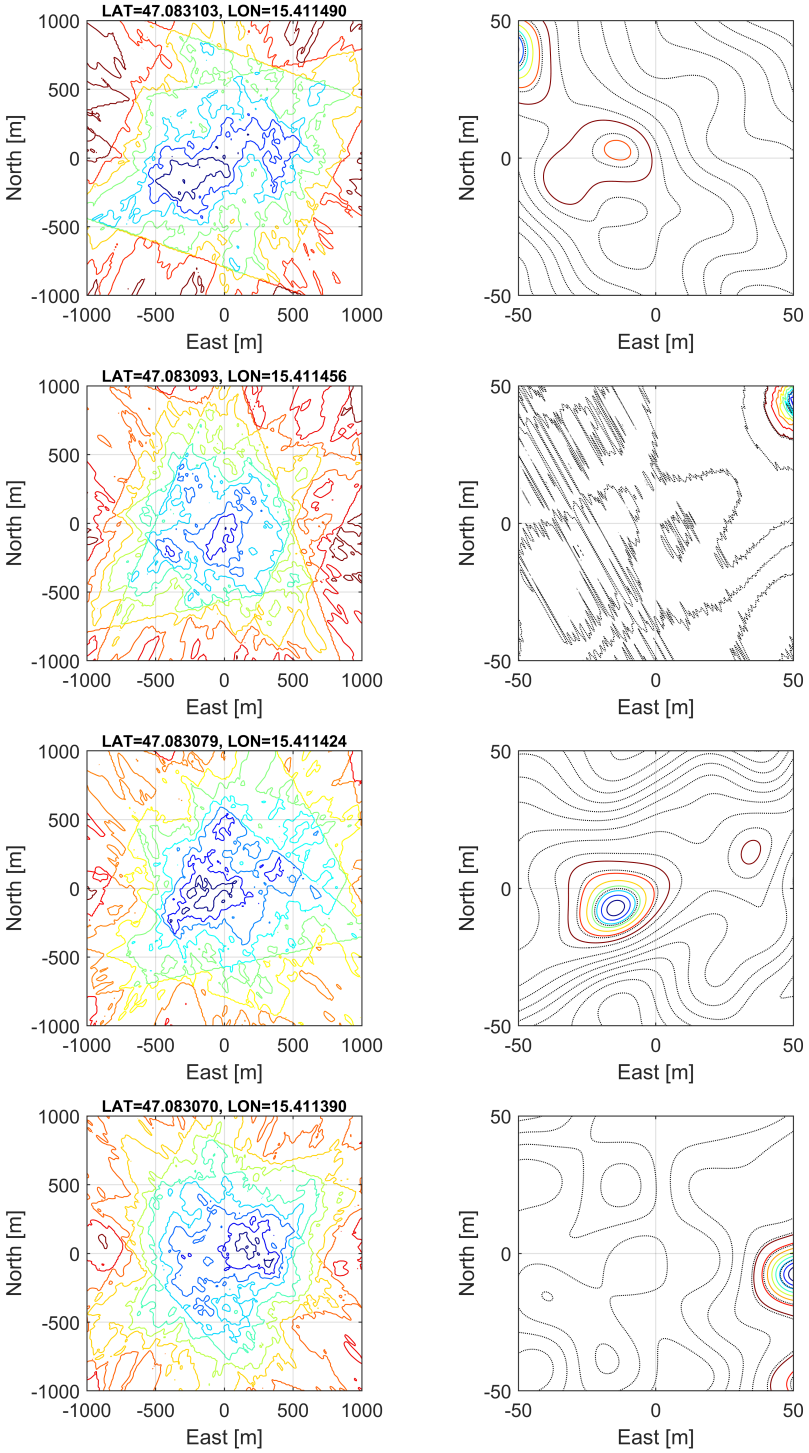

Figure D.13: PDF time series of the bridge underpass - Part 4

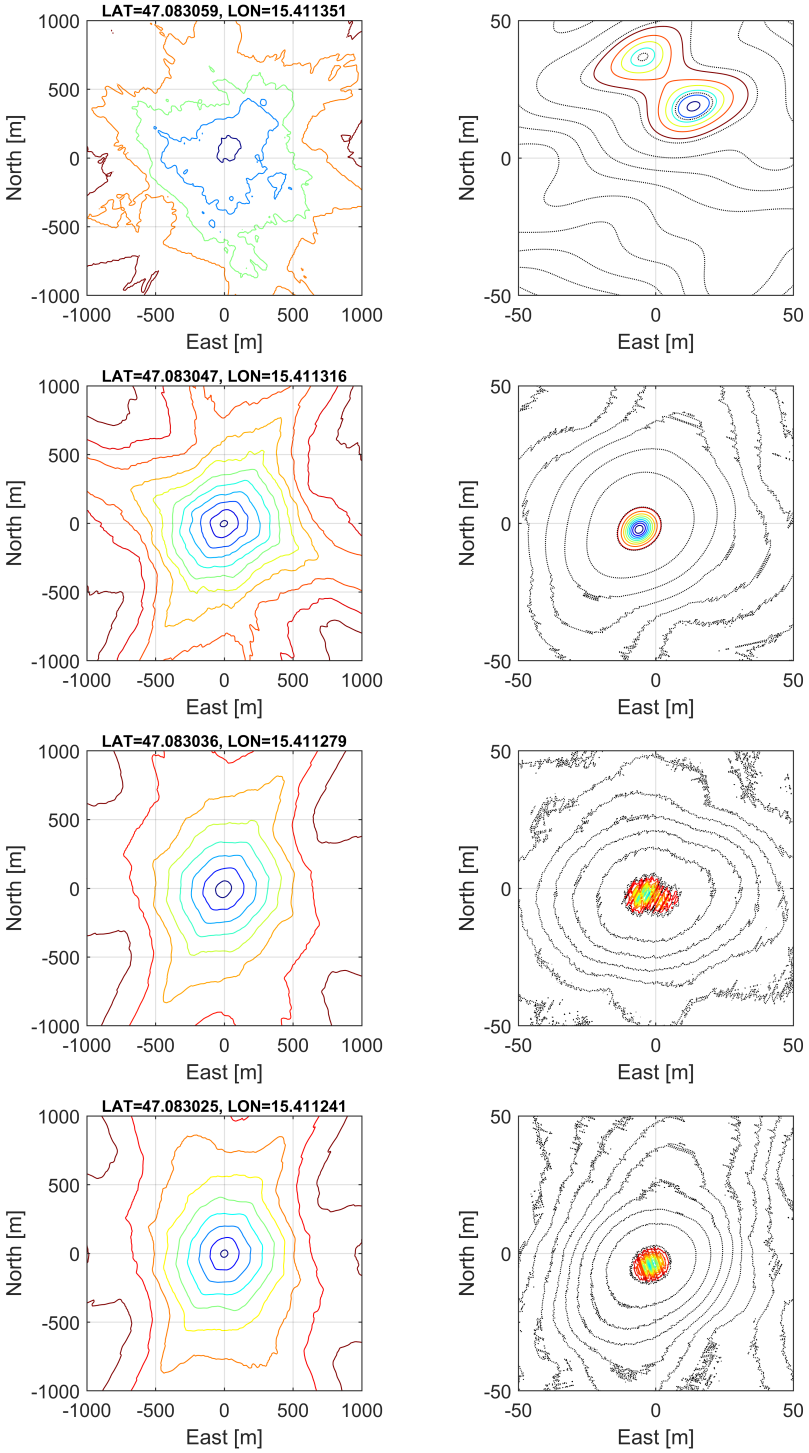

Figure D.14: PDF time series of the bridge underpass - Part 5

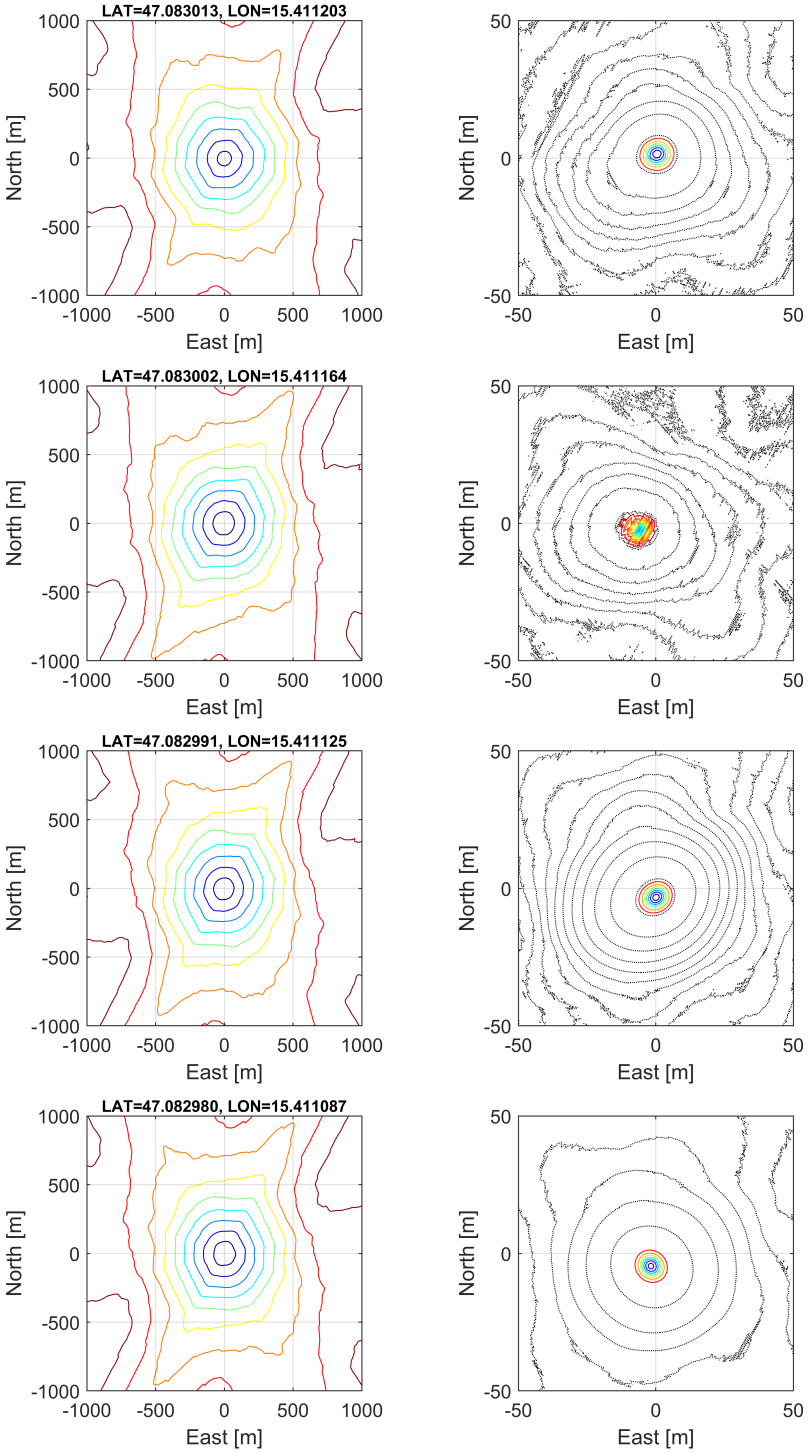

Figure D.15: PDF time series of the bridge underpass - Part 6

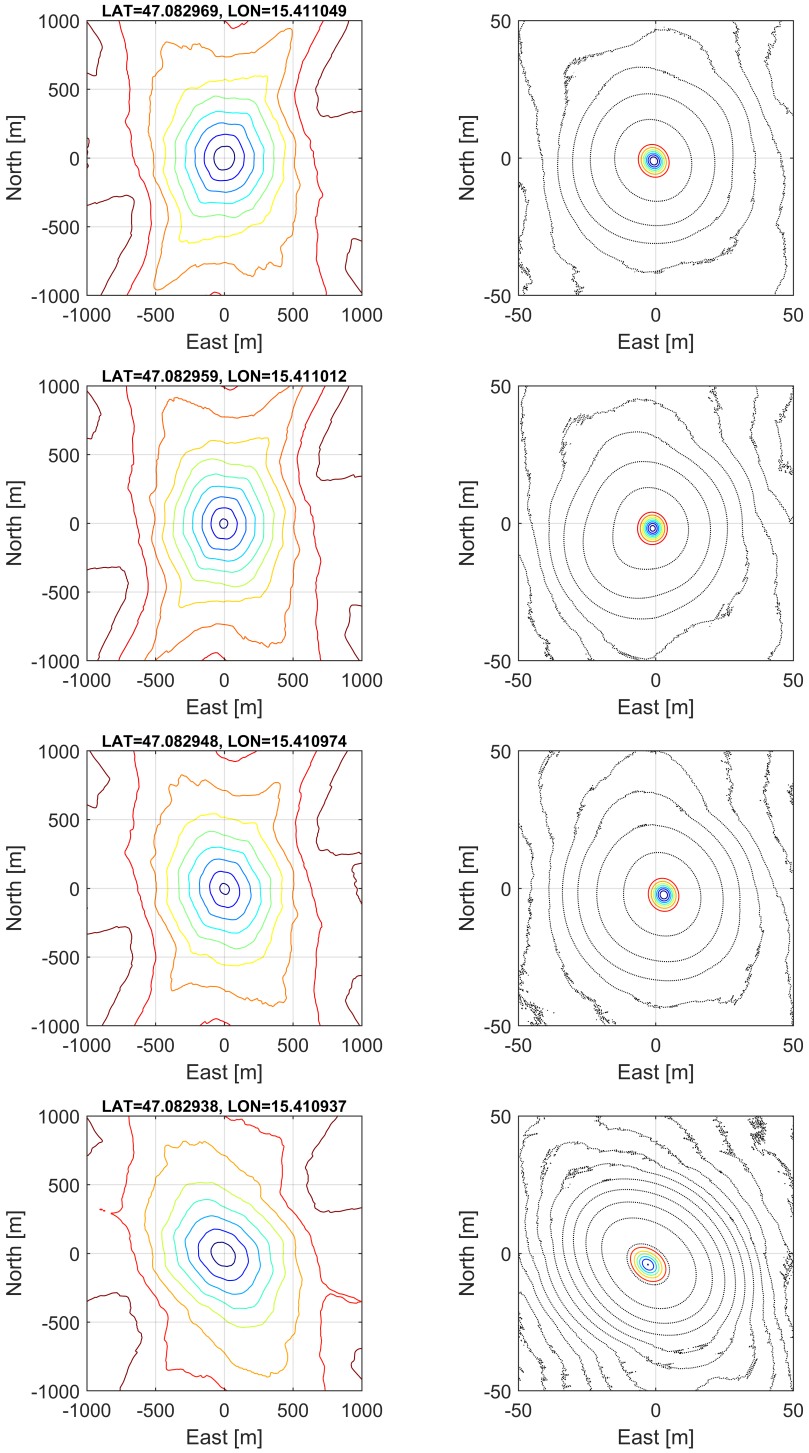

Figure D.16: PDF time series of the bridge underpass - Part 7

Indoor Environment

The indoor scenario was recorded at the Impulszentrum, Reininghausstrasse, Graz, Austria. The trajectory is shown in the figure below.

Figure D.17: Indoor trajecotry corresponding to the time series in the Impulszentrum, Reininghausstraße, Graz, Austria. The red positions of the trajectory refer to the PDFs of Fig. D.18 to D.24

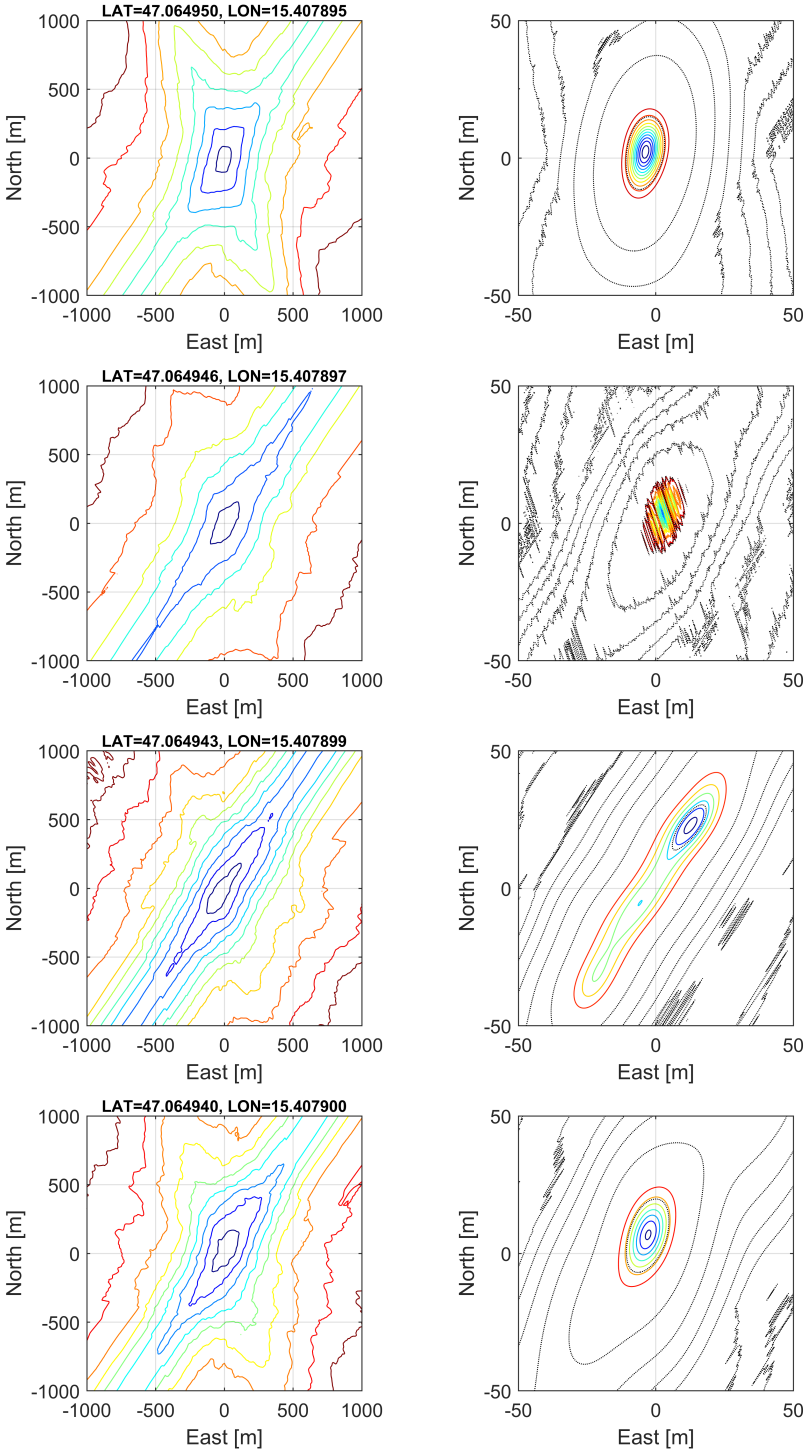

Figure D.18: PDF time series of the indoor scenario - Part 1

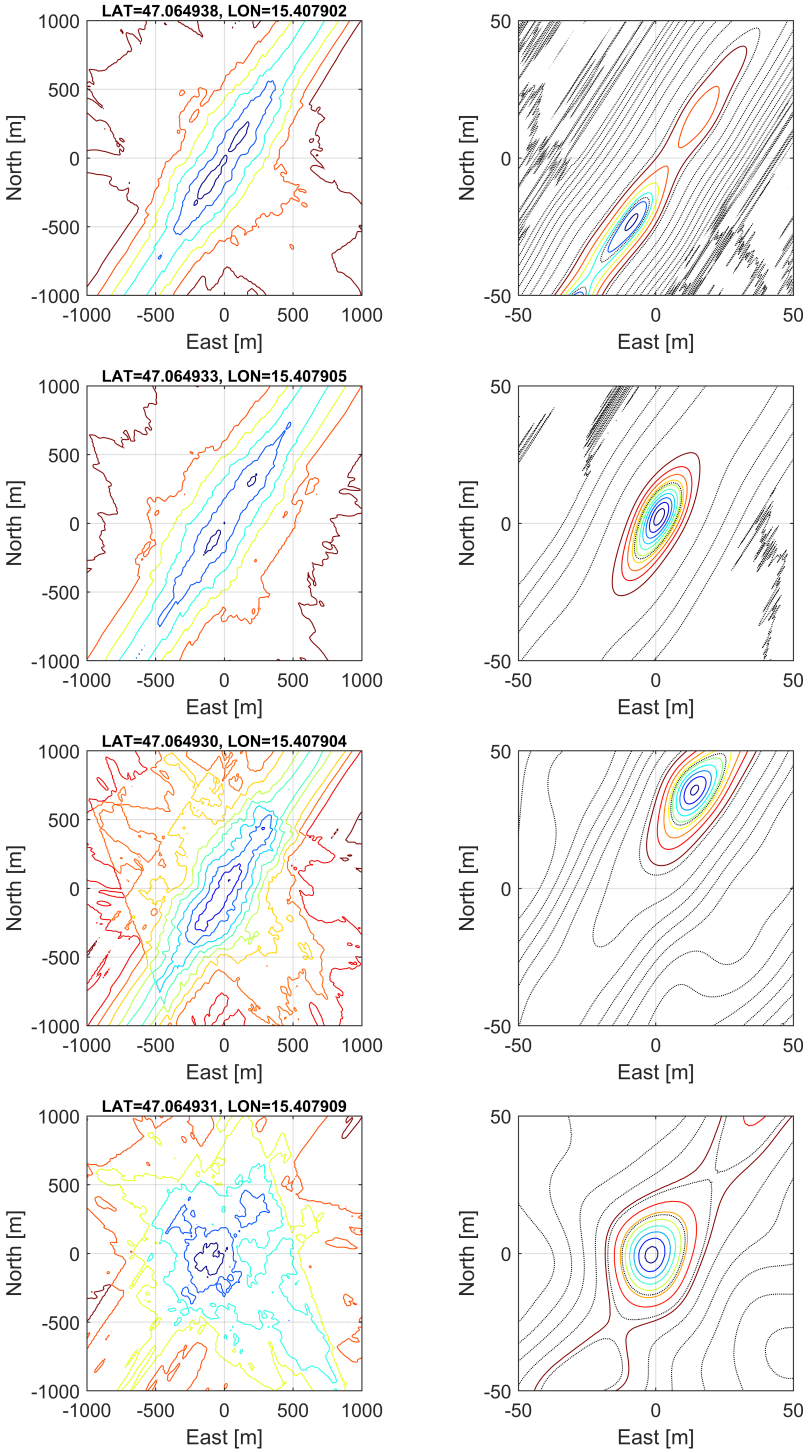

Figure D.19: PDF time series of the indoor scenario - Part 2

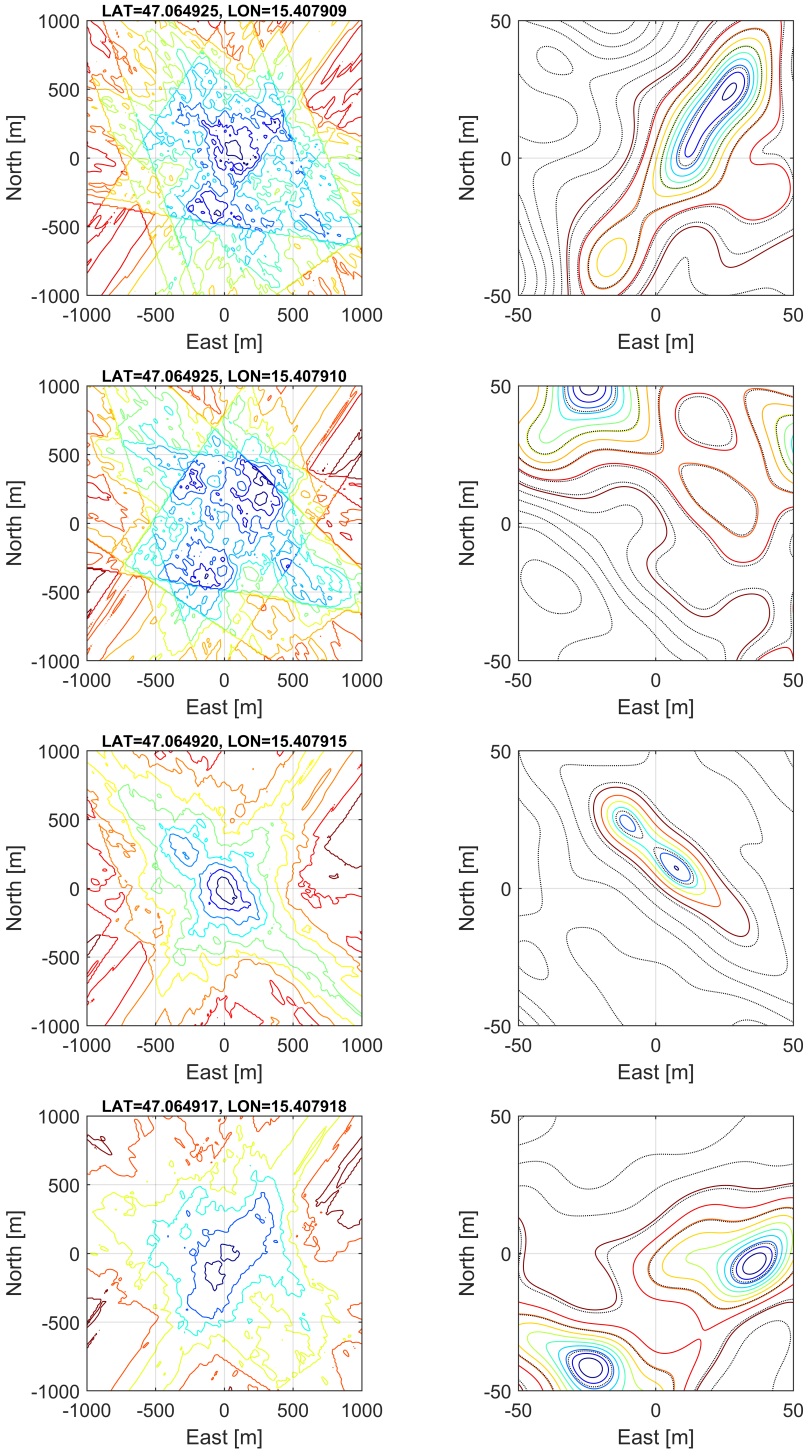

Figure D.20: PDF time series of the indoor scenario - Part 3

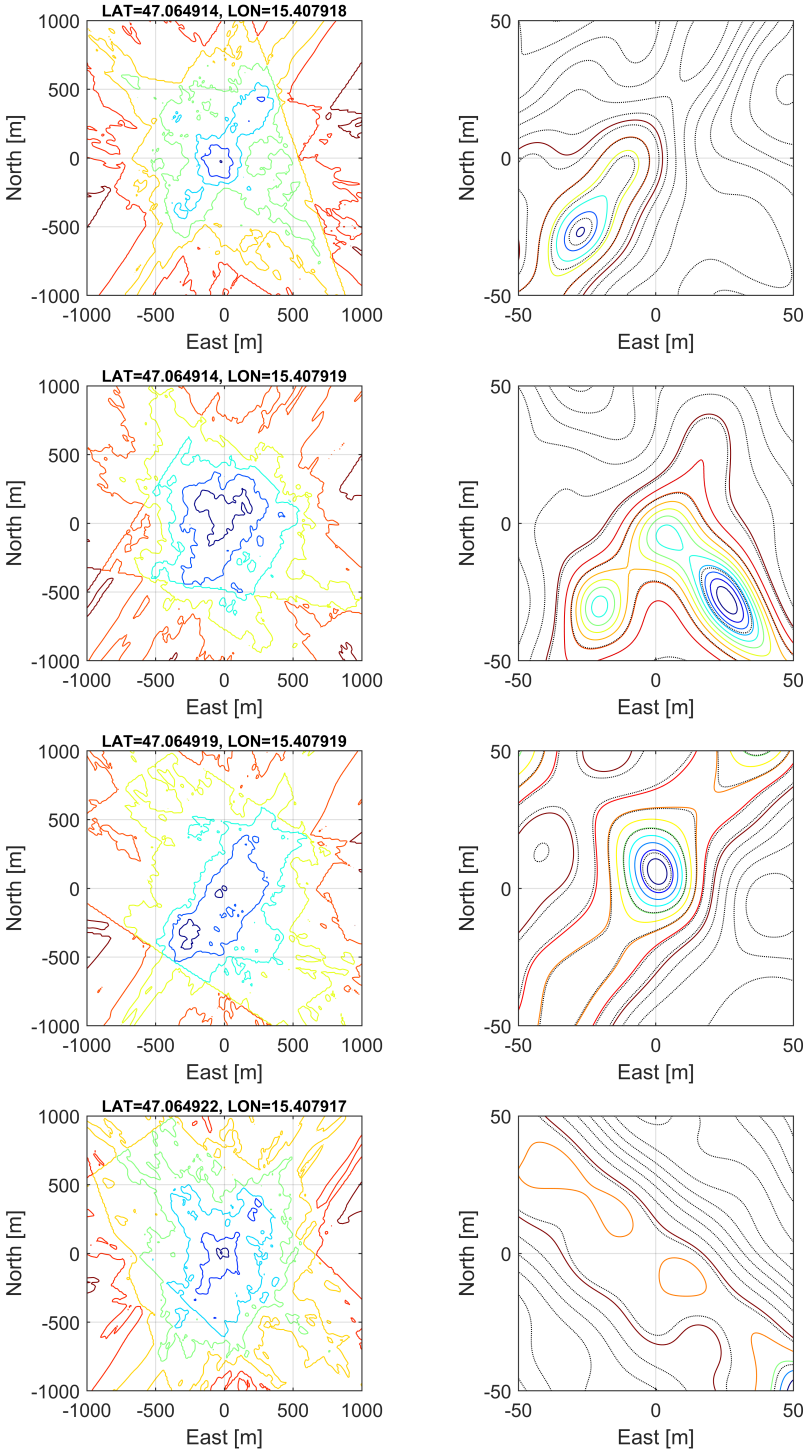

Figure D.21: PDF time series of the indoor scenario - Part 4

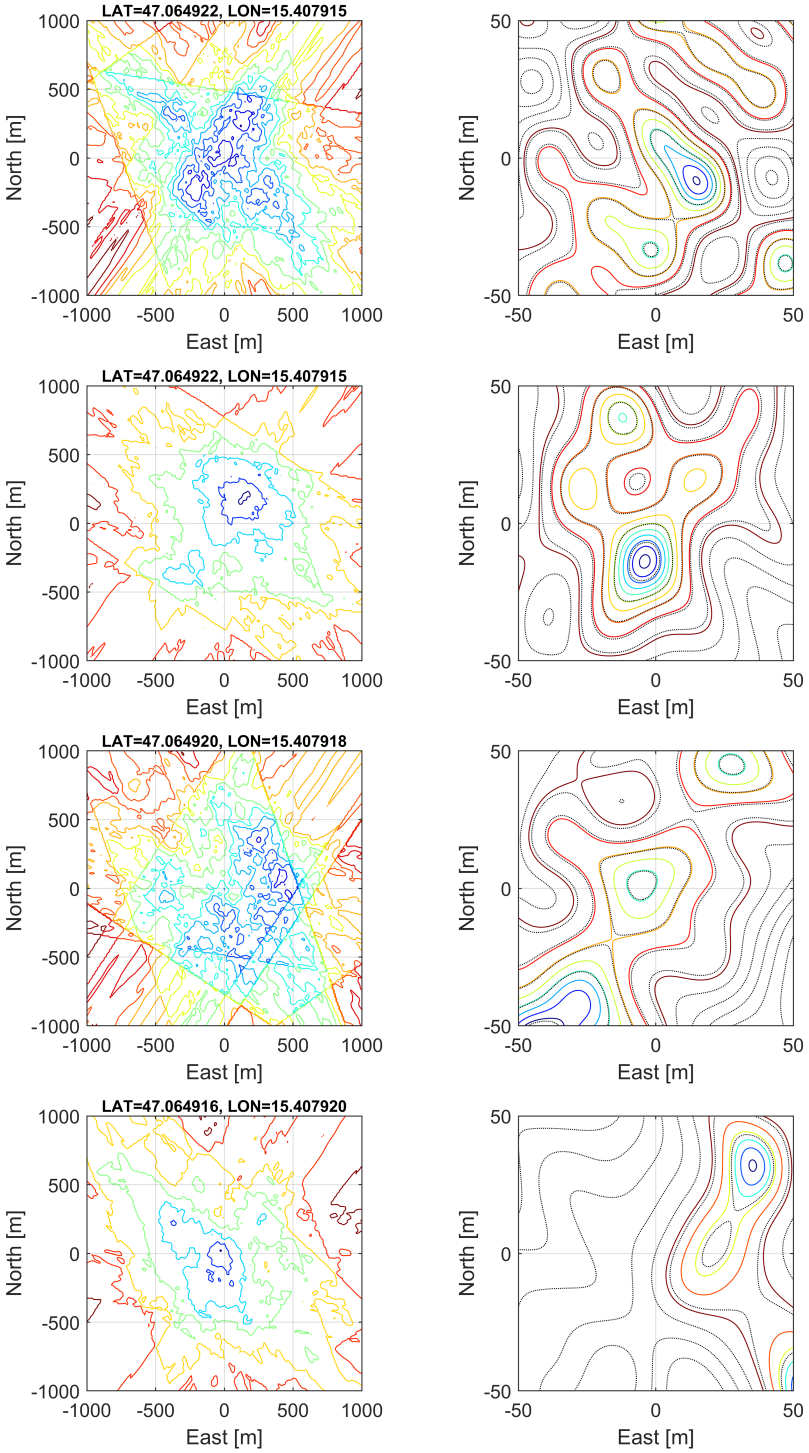

Figure D.22: PDF time series of the indoor scenario - Part 5

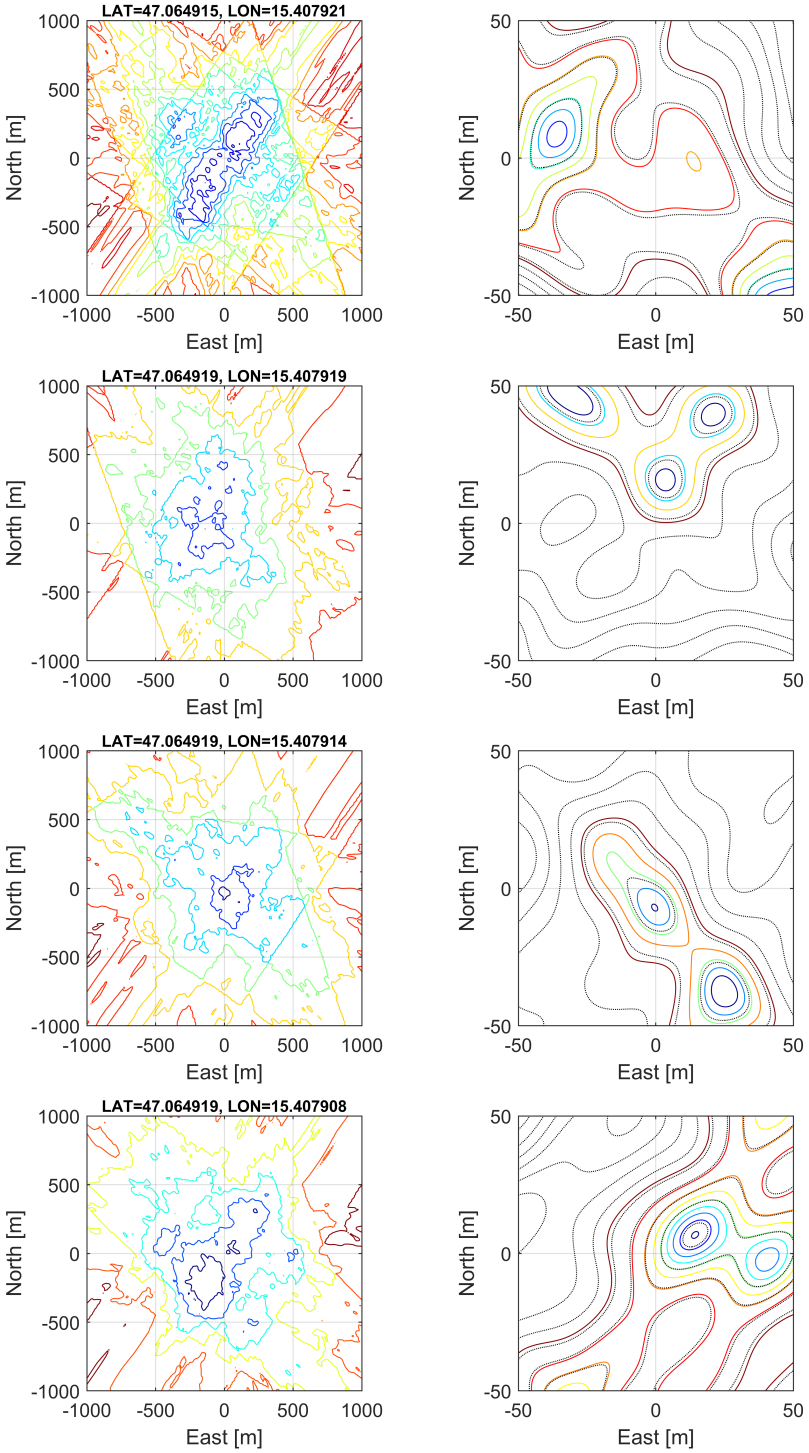

Figure D.23: PDF time series of the indoor scenario - Part 6

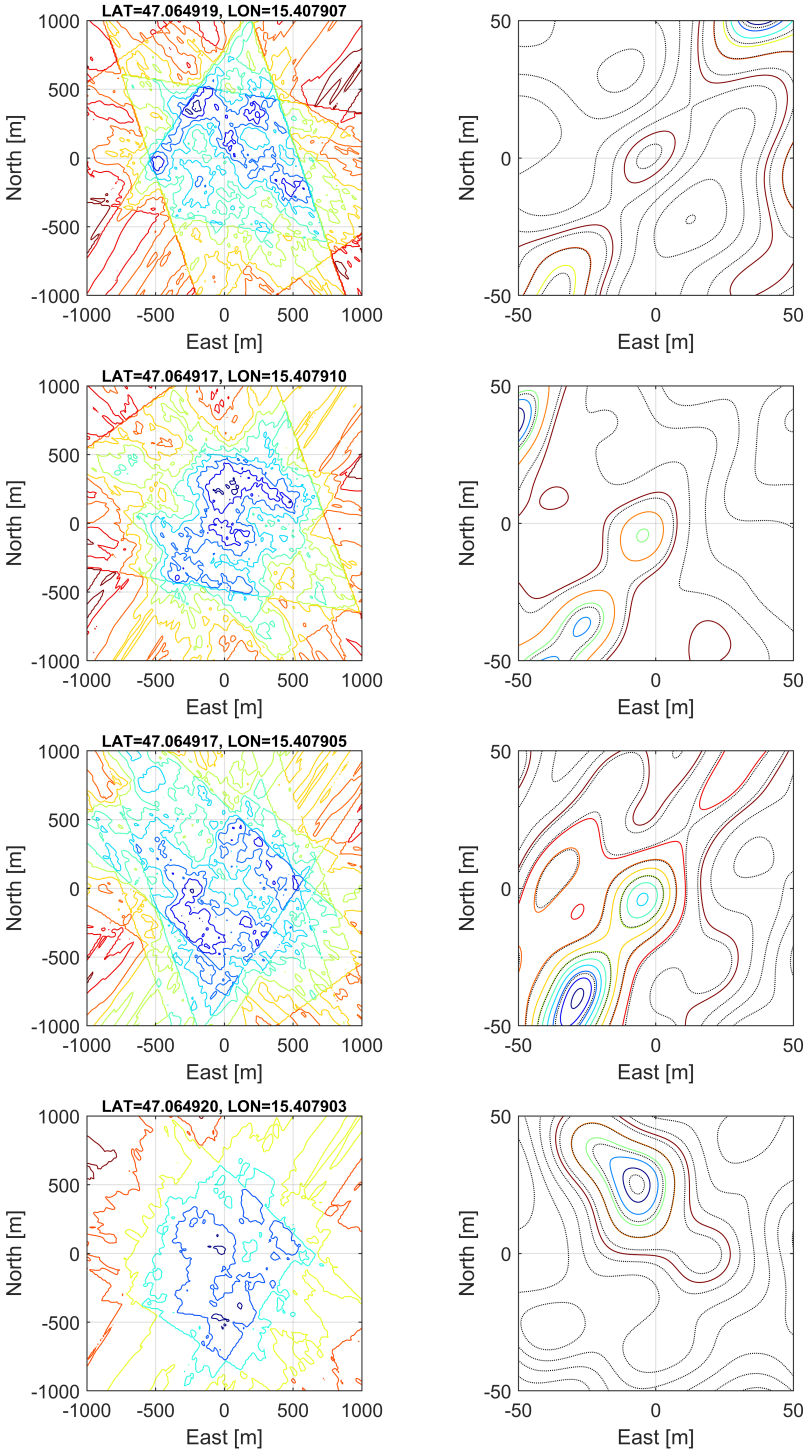

Figure D.24: PDF time series of the indoor scenario - Part 7

Appendix E

This appendix extends chapter 8.5 and shows the impact of nuisance parameters on a series of epochs, which should give evidence that the proposed approach to cover the UEREs works as expected. The plots have been generated as described in chapter 8.5. The scenario was recorded at the rooftop with open sky conditions and the epochs have an interval of 0.25 seconds. Thus, the satellite geometry is quasi the same for all epochs, and the artificial introduced error $\Delta\epsilon$ on the code pseudorange lead to a similar behavior of all presented epochs. Nevertheless, the proposed recovery works in all presented epochs as expected.

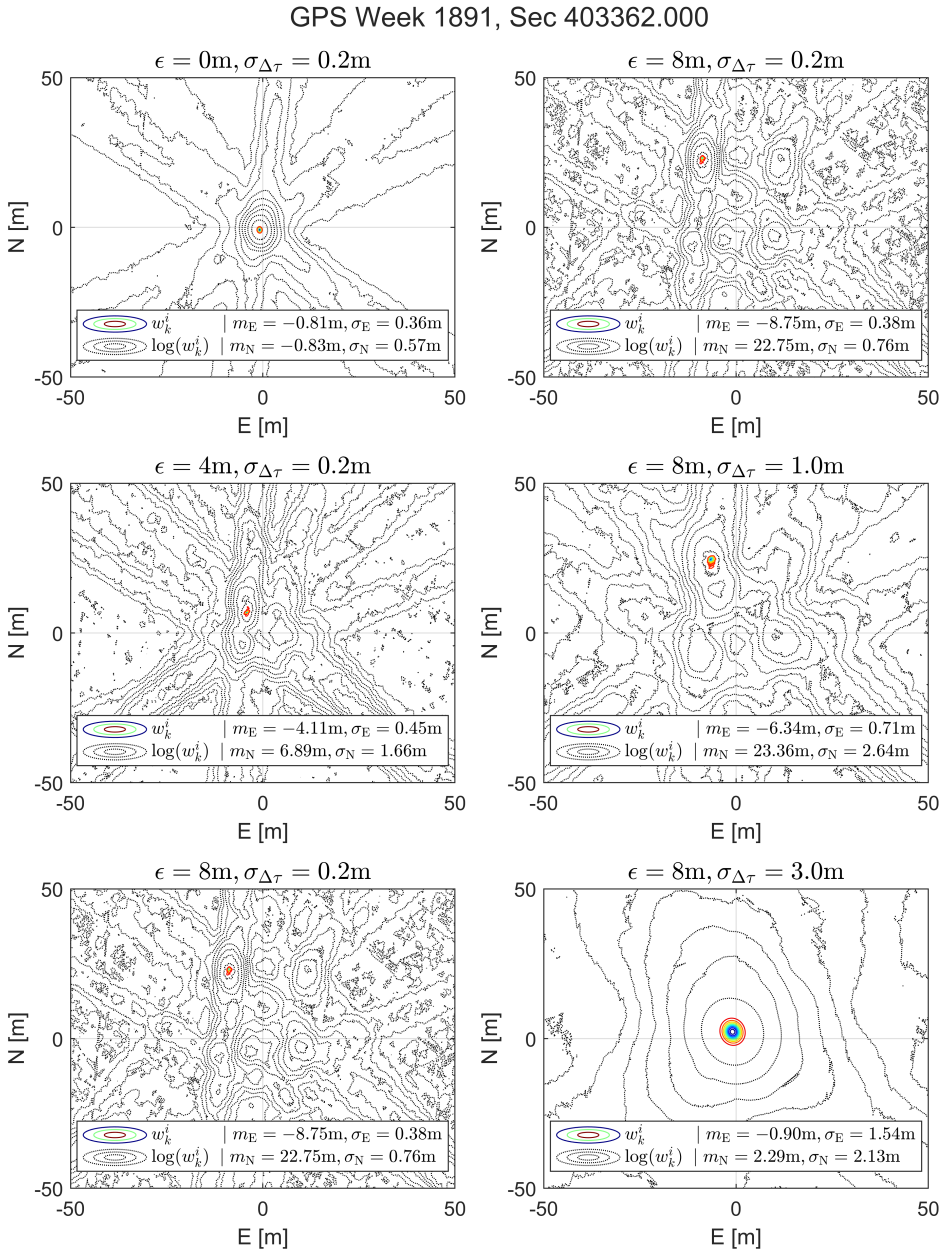

Figure E.1: Impact of Nuisance Parameters - Part 1

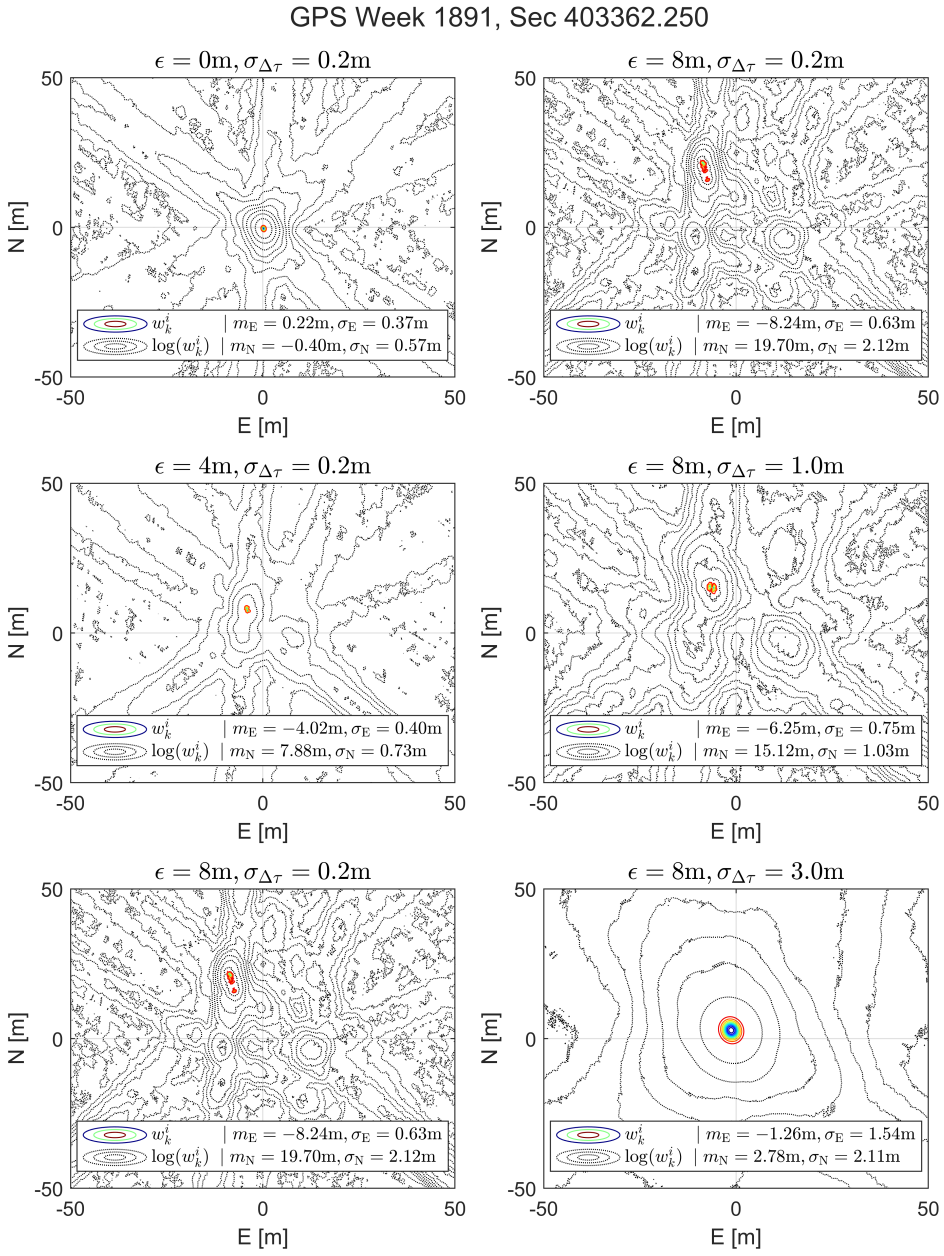

Figure E.2: Impact of Nuisance Parameters - Part 2

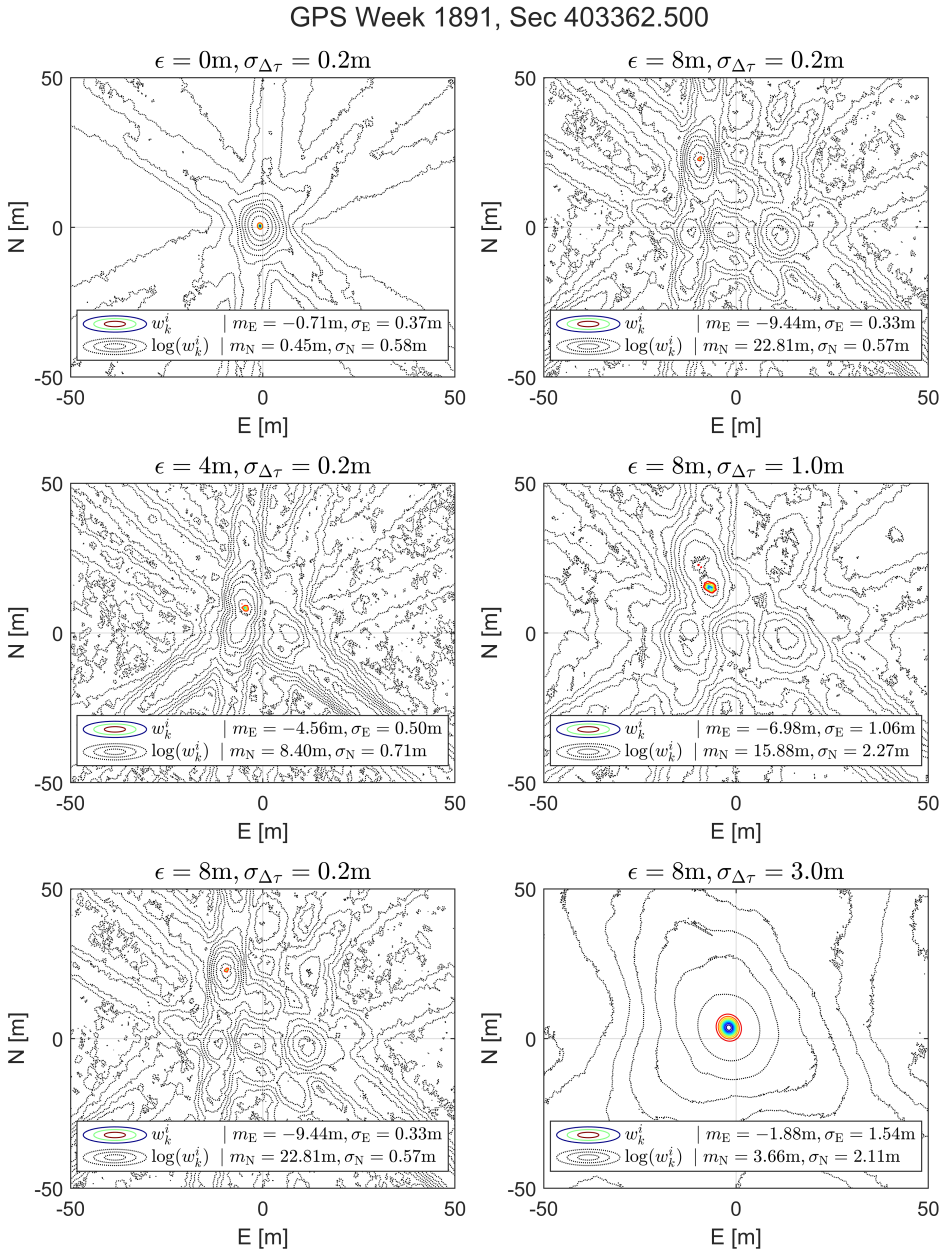

Figure E.3: Impact of Nuisance Parameters - Part 3

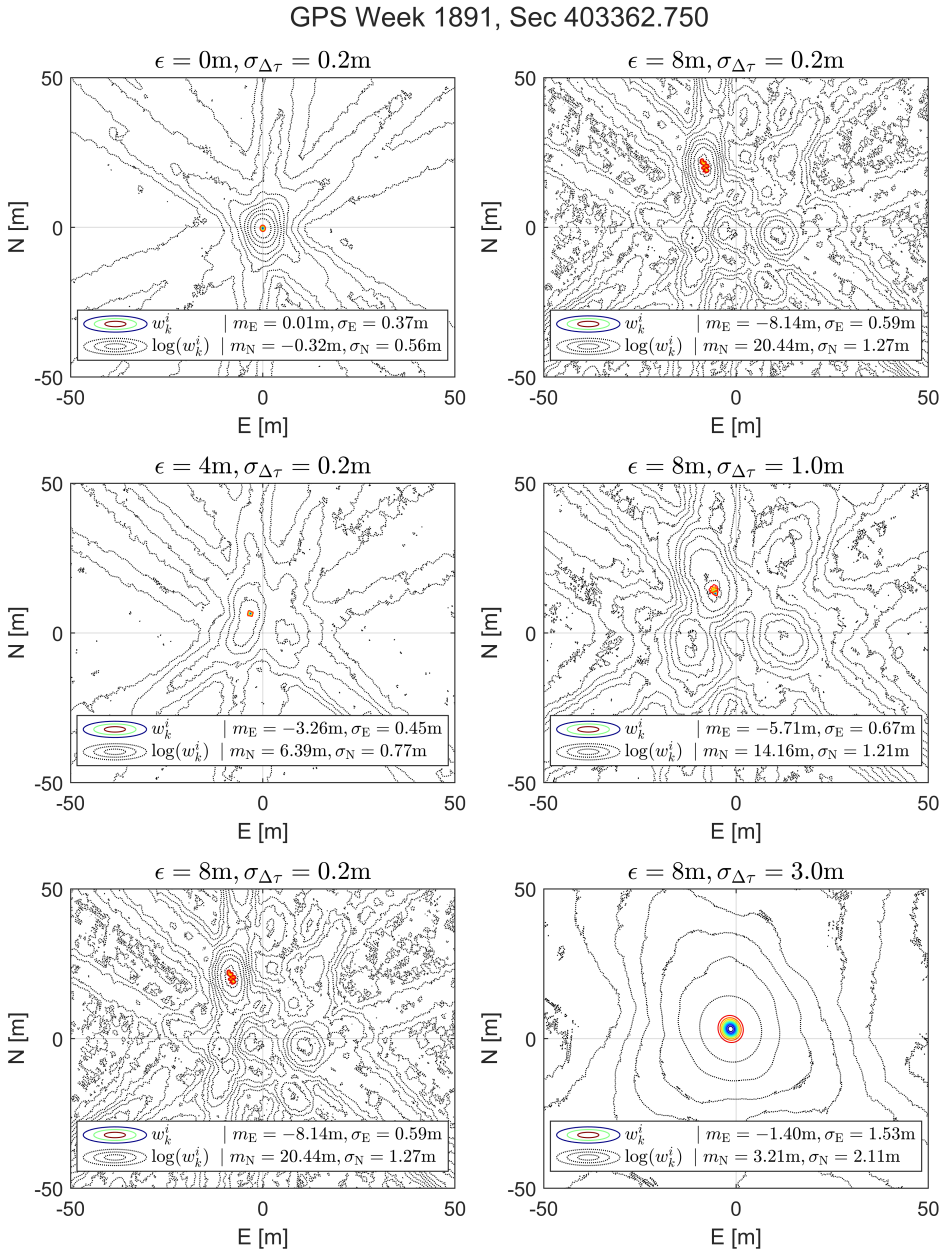

Figure E.4: Impact of Nuisance Parameters - Part 4

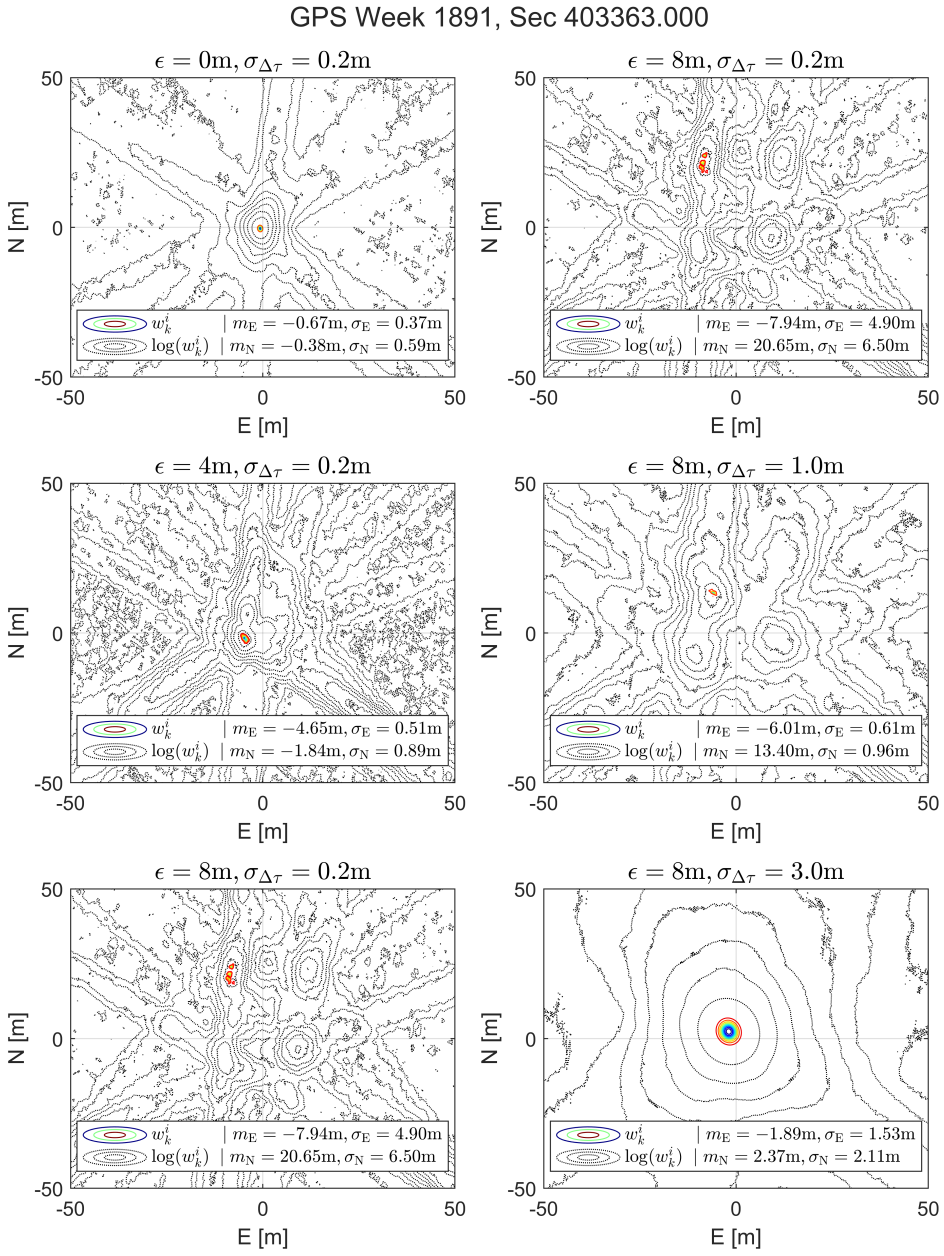

Figure E.5: Impact of Nuisance Parameters - Part 5

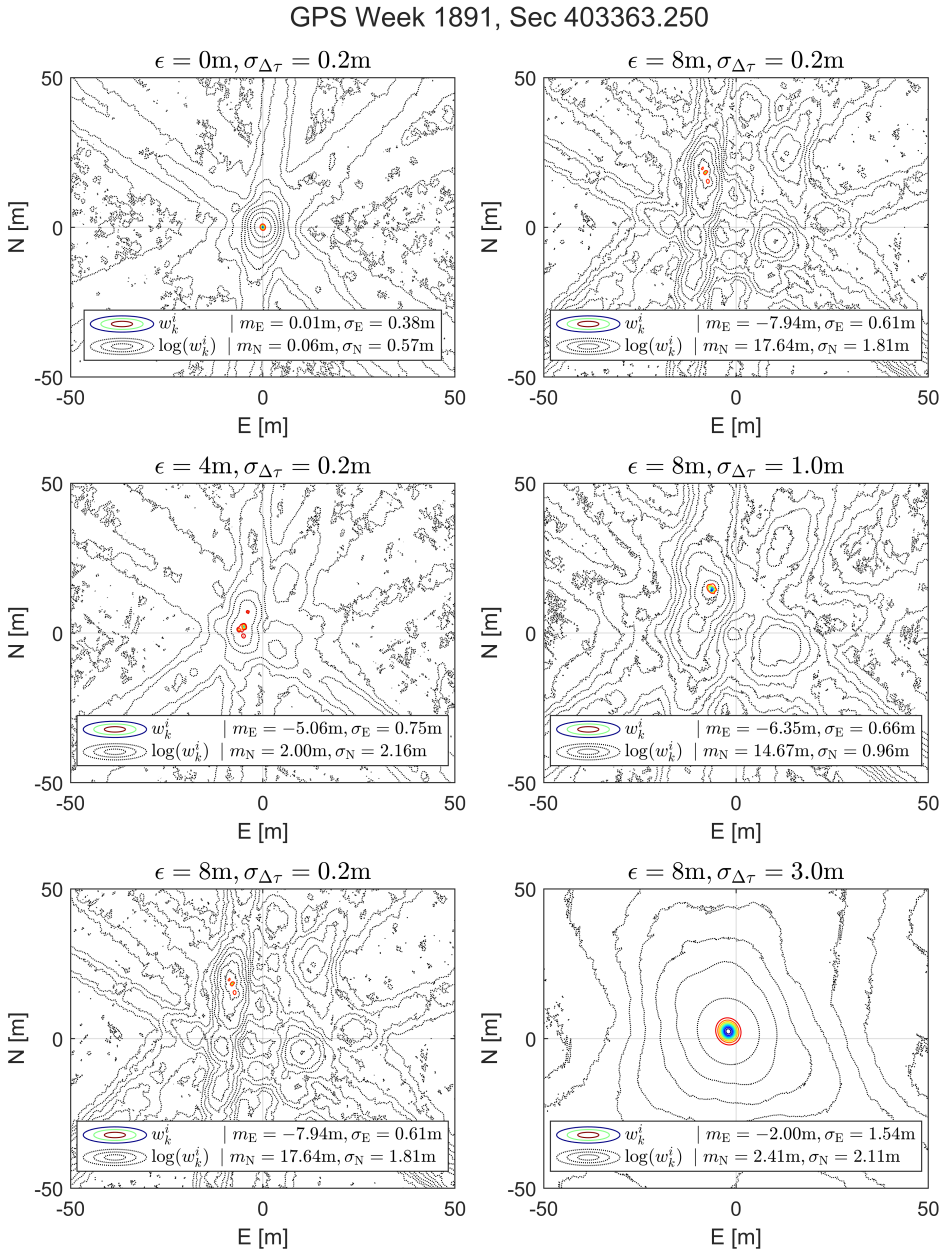

Figure E.6: Impact of Nuisance Parameters - Part 6

List of Figures

List of Tables

Bibliography

Arulampalam, M. Sanjeev et al. (2002). "A Tutorial on Particle Filters for Online Nonlinear/Non-Gaussian Bayesian Tracking." In: *IEEE Transactions on Signal Processing* 50.2, pp. 174–188. ISSN: 1053587X. DOI: 10.1109/78.978374 (cit. on pp. 38, 40, 42–44, 46–49).

Avila-Rodriguez, Jose-Angel et al. (2007). *A vision on new frequencies , signals and concepts for future GNSS systems*. URL: https://www.academia.edu/18819705/A%7B%5C_%7Dvision%7B%5C_%7Don%7B%5C_%7Dnew%7B%5C_%7Dfrequencies%7B%5C_%7Dsignals%7B%5C_%7Dand%7B%5C_%7Dconcepts%7B%5C_%7Dfor%7B%5C_%7Dfuture%7B%5C_%7DGNSS%7B%5C_%7Dsystems (visited on 10/20/2020) (cit. on p. 8).

Ávila-Rodríguez, José-Ángel (2008). "On Generalized Signal Waveforms for Satellite Navigation." PhD thesis. Universität der Bundeswehr München, p. 408 (cit. on p. 147).

Axelrad, Penina et al. (2011). "Collective Detection and Direct Positioning Using Multiple GNSS Satellites." In: ISSN: 00281522 (cit. on pp. 106, 107, 151–153, 164).

Ban, Yalong et al. (2014). "Low-end MEMS IMU can contribute in GPS/INS deep integration." In: *Record - IEEE PLANS, Position Location and Navigation Symposium* 41174028, pp. 746–752. DOI: 10.1109/PLANS.2014.6851440 (cit. on p. 35).

Basile, Francesco et al. (2018). "Multi–Frequency Precise Point Positioning Using GPS and Galileo Data with Smoothed Ionospheric Corrections." In: pp. 1388–1398 (cit. on p. 35).

Bergman, N (1999). "Recursive Bayesian Estimation for Navigation and Tracking Applications." PhD thesis. Linköping University, pp. 1–219. ISBN: 9172194731 (cit. on p. 49).

Bin Ahmad, Khairol Amali, Mohamed Sahmoudi, and Christophe Macabiau (2014). "Characterization of GNSS Receiver Position Errors for User Integrity Monitoring in Urban Environments." In: *ENC-GNSS 2014, European Navigation Conference* (cit. on p. 38).

Borre, Kai et al. (2007). *A software-defined GPS and Galileo receiver*. Boston: Birkhäuser, pp. 1–189. ISBN: 9780817643904 (cit. on pp. 51, 58, 60, 63).

Broderick, James B. and Maple Grove (2006). *Vector tracking loop operability through oscillator micro-jump event* (cit. on p. 36).

C4ADS (2019). *Above Us Only Stars - Exposing GPS Spoofing in Russia and Syria*. Tech. rep. University of Texas at Austin, pp. 1–66. URL: https://www.c4reports.org/ (cit. on p. 106).

Carpenter, J., P. Clifford, and P. Fearnhead (1999). "Improved particle filter for nonlinear problems." In: *IEE Proceedings - Radar, Sonar and Navigation* 146.1, p. 2. ISSN: 13502395. DOI: 10.1049/ip-rsn:19990255 (cit. on pp. 47, 49).

Chen, Xaoming et al. (2011). "Trimble RTX, an innovative new approach for network RTK." In: *24th International Technical Meeting of the Satellite Division of the Institute of Navigation 2011, ION GNSS 2011* 3, pp. 2214–2219 (cit. on p. 35).

Chien, Ying Ren (2015). "Design of GPS Anti-Jamming Systems Using Adaptive Notch Filters." In: *IEEE Systems Journal* 9.2, pp. 451–460. ISSN: 19379234. DOI: 10.1109/JSYST.2013.2283753 (cit. on p. 105).

China Satellite Navigation Office (2017a). *BeiDou Navigation Satellite System Signal in Space Interface Control Document (BDS-SIS-ICD-B1C-B2a-beta)*. Tech. rep. Beta. China Satellite Navigation Office (cit. on pp. 21, 23).

China Satellite Navigation Office (2017b). *BeiDou Navigation Satellite System Signal in Space Interface Control Document (BDS-SIS-ICD-B2a-1.0)*. Tech. rep. Version 1.0. China Satellite Navigation Office, pp. 1–81 (cit. on p. 23).

China Satellite Navigation Office (2018). *BeiDou Navigation Satellite System Signal in Space Interface Control Document (BDS-SIS-ICD-B3I-1.0)*. Tech. rep. Version 1.0. China Satellite Navigation Office, pp. 1–89 (cit. on p. 24).

China Satellite Navigation Office (2019a). *BeiDou Navigation Satellite System Signal in Space Interface Control Document (BDS-SIS-ICD-B1I-3.0)*. Tech. rep. Version 3.0. China Satellite Navigation Office, pp. 1–89 (cit. on p. 23).

China Satellite Navigation Office (2019b). *BeiDou Navigation Satellite System Signal in Space Interface Control Document (BDS-SIS-ICD-B2b-beta)*. Tech. rep. Beta. China Satellite Navigation Office, pp. 1–58 (cit. on p. 23).

China Satellite Navigation Office (2019c). *BeiDou Navigation Satellite System Signal in Space Interface Control Document (BDS-SIS-ICD-B2b-PPP-beta)*. Tech. rep. China Satellite Navigation Office, pp. 1–51 (cit. on p. 24).

China Satellite Navigation Office (2019d). *Development of the BeiDou Navigation Satellite System*. Tech. rep. Version 4.0. China Satellite Navigation Office, pp. 1–34 (cit. on p. 22).

Closas, Pau (2009). "Bayesian Signal Processing Techniques for GNSS Receivers." PhD thesis. Universitat Politècnica de Catalunya, pp. 1–254 (cit. on pp. 37, 86, 88, 106, 152, 153, 164).

Closas, Pau, Carles Fernández-Prades, D. Bernal, et al. (2008). "Bayesian direct position estimation." In: *Proceedings of the 21st International Technical Meeting of the Satellite Division of The Institute of Navigation (ION GNSS 2008)* September, pp. 183–190 (cit. on pp. 37, 84–86, 106).

Closas, Pau, Carles Fernández-Prades, and J.A. Fernández–Rubio (2007). "Maximum Likelihood Estimation of Position in GNSS." In: *IEEE Signal Processing Letters* 14.May, pp. 359–362 (cit. on pp. 37, 84, 106).

Closas, Pau and Adrià Gusi-Amigó (2017). "Direct Position Estimation of GNSS Receivers: Analyzing main results, architectures, enhancements, and challenges." In: *IEEE Signal Processing Magazine* 34.5, pp. 72–84. ISSN: 10535888. DOI: 10.1109/MSP.2017.2718040 (cit. on pp. 37, 81–83, 86, 92, 107, 151, 153, 154, 163).

Dampf, Jürgen, Kathrin Frankl, and Thomas Pany (2018). "Optimal Particle Filter Weight for Bayesian Direct Position Estimation in a GNSS Receiver." In: *Sensors* 18.8, p. 2736. ISSN: 1424-8220. DOI: 10.3390/s18082736 (cit. on pp. 37, 90, 91, 107–111, 113, 121, 129–132, 134–136, 138, 140–144, 156, 176, 181).

Dampf, Jürgen, Johannes Gruber, and Thomas Pany (2013). *Synthtic Aperture Processing for Deep GNSS / INS Integration*. Tech. rep. IFEN Gmbh, Alte Gruber Straße 6, 85586 Poing (cit. on p. 36).

Dampf, Jürgen, Christian Lichtenberger, and Thomas Pany (2019). "Probability Analysis for Bayesian Direct Position Estimation in a Real-Time GNSS Software Receiver." In: *Proceedings of 32th International Meeting of the Satellite Division of The Institute of Navigation (ION GNSS+ 2019)* (cit. on pp. 100, 114, 117, 121, 123, 128, 145–148, 150, 153, 155–161).

Dampf, Jürgen and Thomas Pany (2018). "Nuisance Parameters for Bayesian Direct Position Estimation Targeting Improved Stability." In: *Proceedings of 31th International Meeting of the Satellite Division of The Institute of Navigation (ION GNSS+ 2018)* (cit. on pp. 107, 108, 111, 112, 115, 121, 181).

Dampf, Jürgen, Thomas Pany, Wolfgang Baer, et al. (2016). "Real World Direction of Arrival Estimation and Mitigation of Spoofing Signals with a Synthetic Aperture Antenna." In: *8th ESA Workshop on Satellite Navigation Technologies and European Workshop on GNSS Signals and Signal Processing (NAVITEC)*. 1. Noordwijk, Netherlands (cit. on p. 36).

Dampf, Jürgen, Thomas Pany, Wolfgang Bär, et al. (2017). "Real World Spoofing Trials and Mitigation" (cit. on p. 36).

Dampf, Jürgen, Norbert Witternigg, et al. (2017). "Particle Filter Algorithms and Experiments for High Sensitivity GNSS Receivers." In: *6th International Colloquium - Scientific and Fundamental Aspects of GNSS / Galileo*. 1. Valencia, Spain (cit. on pp. 89, 107, 164).

Dennis, Jed (2015). "Refinement of Broadcast Integrity Methods for Space Based Augmentation System Selection." In: *Proceedings of the 2015 International Technical Meeting of The Institute of Navigation*. Dana Point, California, pp. 404–414 (cit. on p. 29).

Doucet, Arnaud, Simon Godsill, and Christophe Andrieu (2000). "On sequential Monte Carlo sampling methods for Bayesian filtering." In: *Statistics and Computing* 10.3, pp. 197–208. ISSN: 09603174. DOI: 10.1023/A:1008935410038 (cit. on pp. 48, 49).

ESA (2018). *Navipedia*. URL: https://gssc.esa.int/navipedia/index.php (cit. on pp. 13–20, 22, 24–26, 28, 30, 31, 33, 96).

Esteves, Paulo, Sahmoudi Mohamed, and Lionel Ries (2014). "Collective Detection of Multi-GNSS Signals" (cit. on p. 106).

EU (2016). *Galileo OS SIS ICD*. Tech. rep. 1.3. European Union, pp. 1–88 (cit. on pp. 19, 20).

EU (2019). *Galileo E6-B / C Codes Technical Note*. Tech. rep. European Union (cit. on p. 20).

EU (2020). *SAR/GALILEO SERVICE DEFINITION DOCUMENT*. Tech. rep. European Union, pp. 1–64 (cit. on p. 19).

FAA (2020). *Satellite Navigation - WAAS - How It Works*. URL: https://www.faa.gov/about/office_org/headquarters_offices/ato/service_units/techops/navservices/gnss/waas/howitworks/ (visited on 01/31/2021) (cit. on p. 29).

Faragher, Ramsey (2018). "Supercorrelation : Enhancing the Accuracy and Sensitivity of Consumer GNSS Receivers with a DSP Upgrade Consumer GNSS data types - how raw is raw?" In: September, pp. 357–375 (cit. on p. 166).

Faragher, Ramsey, Nicolas Couronneau, and Robert Mark Crockett (2017). *Method, Apparatus, Computer Program, Chip Set, or data structure for correlating a digital signal and a correlation code* (cit. on p. 37).

Fernández, Antonio et al. (2010). "GNSS / INS / LiDAR Integration in Urban Environment : Algorithm Description and Results from ATENEA Test Campaign." In: (cit. on p. 35).

Fernández-Prades, Carles, Javier Arribas, and Pau Closas (2016). "Robust GNSS Receivers by Array Signal Processing: Theory and Implementation." In: *Proceedings of the IEEE* 104.6, pp. 1207–1220. ISSN: 0018-9219. DOI: 10.1109/JPROC.2016.2532963 (cit. on p. 36).

Garc, Omar (2018). "Tightly Coupled GNSS / INS Integration based on Robust M-Estimators." In: pp. 1554–1561 (cit. on p. 35).

Garcia-Molina, Jose Avilia and Jose Avilia Fernandez-Rubio (2020). "MIMO-GNSS Signal Processing for Precise Indoor Timing." In: *Inside GNSS* May/June, pp. 34–41 (cit. on p. 107).

Gentner, Christian et al. (2012). "Hybrid Positioning with 3GPP-LTE and GPS employing Particle Filters." In: *Proceedings ION GNSS 2012, Nashville, TN, USA*, pp. 473–481 (cit. on p. 38).

Gordon, N.J., D.J. Salmond, and A.F.M. Smith (1993). "Novel approach to nonlinear/non-Gaussian Bayesian state estimation." In: *IEE Proceedings F Radar and Signal Processing* 140.2, p. 107. ISSN: 0956375X. DOI: 10.1049/ip-f-2.1993.0015 (cit. on pp. 38, 47).

GPS World (2016). "Galileo declares Initial Services." In: *GPS World*, pp. 1–4 (cit. on p. 18).

GPSoft (2020). *GPS-only Kalman Filters*. URL: https://gpsoftnav.com/products/nsi-kalman-filter-toolbox-2-0-matlab/gps-kalman-filters/ (visited on 02/22/2020) (cit. on p. 72).

Groves, Paul D. (2013). *Principles of GNSS, Inertial, and Multisensor Integrated Navigation Systems*. 2nd. Boston, London: Artech House. ISBN: 978-1-60807-005-3 (cit. on pp. 35, 73).

GSA (2015). *EGNOS LPV-200 Enables Safer Aircraft Landings*. URL: https://www.gsa.europa.eu/news/egnos-lpv-200-enables-safer-aircraft-landings (visited on 01/31/2021) (cit. on p. 30).

GSA (2017). *GNSS Market Report 2017*. 5, p. 100. DOI: 10.2878/0426. URL: https://www.gsa.europa.eu/2017-gnss-market-report (cit. on pp. 3–6, 92).

GSA (2019). *GSA EGNOS Service Provider call*. URL: https://www.gsa.europa.eu/newsroom/news/egnos-service-provider-call-now-open (cit. on p. 30).

Gustafsson, Fredrik and Gustaf Hendeby (2012). "Some relations between extended and unscented Kalman filters." In: *IEEE Transactions on Signal Processing* 60.2, pp. 545–555. ISSN: 1053587X. DOI: 10.1109/TSP.2011.2172431 (cit. on p. 45).

Hafner, Petra (2015). "Development of a Positioning Filter for the Smartphone-based Navigation of Visually Impaired People." PhD thesis. Graz University of Technology, pp. 1–144 (cit. on pp. 38, 41).

He, Zhe and Mark Petovello (2014). "Joint Detection and Estimation of Weak GNSS Signals with Application to Coarse Time Navigation." In: *Proceedings of the 27th International Technical Meeting of The Satellite Division of the Institute of Navigation (ION GNSS+ 2014)*, pp. 1554–1567 (cit. on pp. 106, 110).

Henkel, Patrick, Ulrich Mittmann, and Michele Iafrancesco (2016). "Real-time kinematic positioning with GPS and GLONASS." In: *European Signal Processing Conference* 4, pp. 1063–1067. ISSN: 22195491. DOI: 10.1109/EUSIPCO.2016.7760411 (cit. on p. 34).

Henkel, Patrick and Andreas Sperl (2016). "Real-time kinematic positioning for unmanned air vehicles." In: *IEEE Aerospace Conference Proceedings*. ISSN: 1095323X. DOI: 10.1109/AERO.2016.7500933 (cit. on p. 34).

Ho, Y. and R. Lee (1964). "A Bayesian approach to problems in stochastic estimation and control." In: *IEEE Transactions on Automatic Control* 9.4, pp. 333–339. ISSN: 0018-9286. DOI: 10.1109/TAC.1964.1105763. URL: http://ieeexplore.ieee.org/document/1105763/ (cit. on p. 43).

Hwang, D. B. et al. (2011). "Unified approach to ultra-tightly-coupled GPS/INS integrated navigation system." In: *IEEE Aerospace and Electronic Systems Magazine* 26.3, pp. 30–38. ISSN: 08858985. DOI: 10.1109/MAES.2011.5746183 (cit. on p. 35).

IFEN GmbH (2019a). *NavX-NCS Essential GNSS Simulator*. Poing, Germany (cit. on p. 139).

IFEN GmbH (2019b). *SX3 GNSS Software Receiver, Version 3.3.0*. Poing, Germany (cit. on pp. 121, 137).

Indian Space Research Organization (2017). *Indian Regional Navigation Satellite System Signal in Space Interface Control Document for the Standard Positionig Service (ISRO-IRNSS-ICD-SPS-1.1)*. Tech. rep. Bangalore: Indian Space Research Organization, pp. 1–72 (cit. on pp. 27, 28).

Intel Corporation (2020). *Intel Integrated Performance Primitives (IPP), V2017.4.210*. Santa Clara, California, US (cit. on pp. 116, 118, 165).

Japanese Cabinet Office (2018a). *Quasi-Zenith Satellite System Interface Specification Centimeter Level Augmentation Service*. Tech. rep. Japanese Cabinet Office, pp. 1–98 (cit. on pp. 25, 26).

Japanese Cabinet Office (2018b). *Quasi-Zenith Satellite System Interface Specification Positioning Technology Verification Service (IS-QZSS-TV-002)*. Tech. rep. Japanese Cabinet Office, pp. 1–16 (cit. on p. 25).

Japanese Cabinet Office (2018c). *Quasi-Zenith Satellite System Interface Specification Satellite Positioning, Navigation and Timing Service (IS-QZSS-PNT-003)*. Tech. rep. Japanese Cabinet Office, pp. 1–151 (cit. on pp. 25, 26).

Japanese Cabinet Office (2019a). *Quasi-Zenith Satellite System Interface Specification Centimeter Level Augmentation Service (IS-QZSS-L6-002)*. Tech. rep. Japanese Cabinet Office, pp. 1–110 (cit. on pp. 25, 26).

Japanese Cabinet Office (2019b). *Quasi-Zenith Satellite System Interface Specification DC Report Service (IS-QZSS-DCR-007)*. Tech. rep. Japanese Cabinet Office, pp. 1–128 (cit. on p. 25).

Japanese Cabinet Office (2019c). *Quasi-Zenith Satellite System Interface Specification Positioning Technology Verification Service (IS-QZSS-TV-003)*. Tech. rep. Japanese Cabinet Office, pp. 1–16 (cit. on p. 25).

Japanese Cabinet Office (2019d). *Quasi-Zenith Satellite System Interface Specification Sub-meter Level Augmentation Service (IS-QZSS-L1S-004)*. Tech. rep. Japanese Cabinet Office, pp. 1–44 (cit. on pp. 25, 26).

Joseph, Angelo (2010). "GNSS Solutions: Measuring GNSS Signal Strength." In: *Inside GNSS* Nov/Dec, pp. 20–25 (cit. on p. 58).

Kanazawa, Keiji, Daphne Koller, and Stuart Russell (1995). "Stochastic simulation algorithms for dynamic probabilistic networks." In: *Proc. Eleventh Annu. Conf. Uncertainty AI*, pp. 346–351 (cit. on pp. 38, 47).

Kang, Chang Ho, Sun Young Kim, and Chan Gook Park (2014). "A GNSS interference identification using an adaptive cascading IIR notch filter." In: *GPS Solutions* 18.4, pp. 605–613. ISSN: 15211886. DOI: 10.1007/s10291-013-0358-0 (cit. on p. 105).

Kaplan, Elliott and Christopher Hegarty (2006). *Understanding GPS: Principles and Applications*. Artech House. ISBN: 1580538940 (cit. on pp. 32, 33, 51, 58, 60, 63, 66, 67, 70–72).

Kitagawa, Genshiro (1996). "Monte Carlo Filter and Smoother for Non-Gaussian Nonlinear State Space Models." In: *Journal of Computational and Graphical Statistics* 5.1, pp. 1–25 (cit. on p. 38).

Kotz, Samuel, Tomaz J. Kozubowski, and Krzysztof Podgórski (2001). *The Laplace Distribution and Generalizations*. January. ISBN: 9781461201731. DOI: 10.1007/978-1-4612-0173-1 (cit. on p. 125).

Kwan, Philip (2019a). *NAVST AR GPS Space Segment/User Segment L1C Interfaces* (cit. on p. 13).

Kwan, Philip (2019b). *NAVSTAR GPS Space Segment/Navigation User Segment L1 and L2 Interfaces* (cit. on pp. 13, 14).

Kwan, Philip (2019c). *NAVSTAR GPS Space Segment/User Segment L5 Interfaces* (cit. on p. 15).

Lashley, Matthew and David M. Bevly (2009). "GNSS Solutions: What are vector tracking loops, and what are their benefits and drawbacks?" In: *Inside GNSS* May/June 2009, pp. 16–21 (cit. on pp. 36, 76, 163).

Leandro, Rodrigo et al. (2011). "RTX Positioning : The Next Generation of cm-accurate Real-Time GNSS Positioning." In: *Proceedings of the 24th International Technical Meeting of The Satellite Division of the Institute of Navigation (ION GNSS 2011)*, pp. 1460–1475 (cit. on p. 35).

Liu, Jun S and Rong Chen (1998). "Sequential Monte Carlo Methods for Dynamic Systems." In: *Journal of the American Statistical Association* 93.443, pp. 1032–1044 (cit. on p. 49).

Lu, Mingquan and Zheng Yao (2014). "New Signal Structures for BeiDou Navigation Satellite System." Tsinghua (cit. on p. 24).

MacCormick, J and A Blake (1999). "A probabilistic exclusion principle for tracking multiple objects." In: *Proc. of the Seventh IEEE Inernational Conference on Computer Vision(ICCV99)* 1, pp. 572–578. DOI: 10.1109/ICCV.1999.791275 (cit. on pp. 38, 47).

McMichael, Ian T. et al. (2016). "Horizon ring nulling shorted annular patch GNSS antenna with shunted stubs." In: *2016 IEEE Antennas and Propagation Society International Symposium, APSURSI 2016 - Proceedings* 2.2, pp. 1101–1102. DOI: 10.1109/APS.2016.7696258 (cit. on p. 105).

Menegaz, Henrique M T et al. (2015). "A Systematization of the Unscented Kalman Filter Theory." In: *IEEE Transactions on Automatic Control* 60.10, pp. 2583–2598. ISSN: 0018-9286. DOI: 10.1109/TAC.2015.2404511 (cit. on p. 45).

Microsoft Cooperation (2018). *Microsoft Developer Network (MSDN)*. Washington, DC, USA (cit. on p. 178).

Misra, P. and P. Enge (2010). *Global Positioning Systems: Signals, Measurements, and Performance*. Second. Massachusetts: Ganga-Jamuna Press. ISBN: 0970954425 (cit. on pp. 2, 9, 15, 33, 34, 38, 51–53, 58, 60, 63, 68, 69, 94, 97, 148, 178).

Ng, Yuting and Grace Xingxin Gao (2016a). "Joint GPS and vision direct position estimation." In: *Proceedings of the IEEE/ION Position, Location and Navigation Symposium, PLANS 2016*, pp. 380–385. DOI: 10.1109/PLANS.2016.7479724 (cit. on p. 106).

Ng, Yuting and Grace Xingxin Gao (2016b). "Mitigating jamming and meaconing attacks using direct GPS positioning." In: *Proceedings of the IEEE/ION Position, Location and Navigation Symposium, PLANS 2016*, pp. 1021–1026. DOI: 10.1109/PLANS.2016.7479804 (cit. on p. 107).

Ng, Yuting and Grace Xingxin Gao (2017). "GNSS Multireceiver Vector Tracking." In: *IEEE Transactions on Aerospace and Electronic Systems* 53.5, pp. 2583–2593. ISSN: 00189251. DOI: 10.1109/TAES.2017.2705338 (cit. on p. 76).

Ng, Yuting, Student Member, et al. (2012). "Robust GPS-Based Direct Time Estimation for PMUs." In: pp. 1–5 (cit. on p. 106).

Niedermeier, Herbert et al. (2010). "DINGPOS: High sensitivity GNSS platform for deep indoor scenarios." In: *International Conference on Indoor Positioning and Indoor Navigation, IPIN 2010 - Conference Proceedings* September, pp. 15–17. DOI: 10.1109/IPIN.2010.5647542 (cit. on p. 35).

OpenMP ARB (2020). *OpenMP, Version 5.0* (cit. on pp. 116, 118).

Oran Brigham, E. (1990). *The Fast Fourier Transform and its Applications*. Englewood Cliffs, New Jersey 07632: Prentice Hall, pp. 1–448. ISBN: 0-13-307505-2 (cit. on pp. 78, 117).

Pany, Thomas (2010). *Navigation Signal Processing for GNSS Software Receivers*. 1st. Artech House, pp. 1–352. ISBN: 978-1608070275 (cit. on pp. 51, 58, 60, 63, 108, 110, 169, 171).

Pany, Thomas and Bernd Eissfeller (2006). "Use of a Vector Delay Lock Loop Receiver for GNSS Signal Power Analysis in Bad Signal Conditions." In: *IEEE/ION Position, Location, And Navigation Symposium*, pp. 893–903. DOI: 10.1109/PLANS.2006.1650689 (cit. on pp. 36, 75, 122).

Pany, Thomas, Nico Falk, et al. (2013). "GNSS Synthetic Aperture Processing with Artificial Antenna Motion." In: *Proceedings of the 26th International Technical Meeting of The Satellite Division of the Institute of Navigation (ION GNSS+ 2013)*. September. Nashville (cit. on pp. 75, 166).

Pany, Thomas, Jón Winkel, et al. (2010). "Experimental results from an ultra-tightly coupled GPS/Galileo/WiFi/ZigBee/ MEMS-IMU indoor navigation test system featuring coherent integration times of several seconds." In: *Programme and Abstract Book - 5th ESA Workshop on Satellite Navigation Technologies and European Workshop on GNSS Signals and Signal Processing, NAVITEC 2010* 1. DOI: 10.1109/NAVITEC.2010.5708020 (cit. on p. 35).

Peretic, Matthew and Grace X Gao (2020a). "Design of a Parallelized Direct Position Estimation-Based GNSS Receiver – Part I : Techniques and Algorithms." In: *Standford University*, pp. 1–13 (cit. on pp. 98, 107, 167).

Peretic, Matthew and Grace X Gao (2020b). "Design of a Parallelized Direct Position Estimation-Based GNSS Receiver – Part II : Analysis and Results." In: pp. 1–14 (cit. on p. 107).

PhysOrg (2019). "China to complete Beidou competitor to GPS with new launches." In: *PhysOrg* December 2019 (cit. on p. 21).

Ripley, Brian D (1987). *Stochastic Simulation*. New York: John Wiley & Sons. ISBN: 9780470316726. DOI: 10.1002/9780470316726 (cit. on p. 49).

Roi, Yozevitch and Moshe Boaz Ben (2014). "A Robust Shadow Matching Algorithm for GNSS Positioning." In: *NAVIGATION, Journal of the Institute of Navigation* 62.October, pp. 95–109 (cit. on p. 38).

Russian Space Systems (2016a). *GLONASS CDMA Open Service Interface Control Document L1*. Moscow: Russian Space Systems, JSC, pp. 1–60 (cit. on p. 17).

Russian Space Systems (2016b). *GLONASS CDMA Open Service Interface Control Document L2*. Tech. rep. Moscow (cit. on p. 17).

Russian Space Systems (2016c). *GLONASS CDMA Open Service Interface Control Document L3*. Moscow: Russian Space Systems, JSC (cit. on p. 17).

Russian Space Systems (2016d). *ICD General Description of Code Division Multiple Access Signal System*. Tech. rep. Moscow: Russian Space Systems, pp. 1–119 (cit. on pp. 16, 17).

Saito, Susumu (2019). *MSAS System Development*. Tech. rep. Seoul: GBAS/SBAS International Workshop, pp. 1–15 (cit. on p. 31).

Sánchez, Daniela E and Harvey C Gómez (2018). "Modeling and Understanding LiDAR Data for Absolute and Relative Positioning." In: *Proceedings of the 31th International Technical Meeting of The Satellite Division of the Institute of Navigation (ION GNSS+ 2018)* (cit. on p. 35).

Smith III, Julius O. (2011). *Spectral Audio Signal Processing*, pp. 1–674. ISBN: 978-0-9745607-3-1 (cit. on p. 124).

State Council Information Office Republic of China (2016). "China 's BeiDou Navigation Satellite System." Beijing (cit. on p. 21).

Stöber, Carsten et al. (2011). "Analysis and Verification of Synthetic Multicorrelators." In: *Proceedings of the 24th International Technical Meeting of The Satellite Division of the Institute of Navigation (ION GNSS 2011)*. Portland, OR, pp. 2060–2069. ISBN: 9781618394750 (cit. on pp. 76, 79).

Stupak, Grigoriy (2010). "Russia to Put 8 CDMA Signals on 4 GLONASS Frequencies." In: *Inside GNSS*, p. 1 (cit. on p. 18).

Stupak, Grigory (2012). *SDCM status and plans*. Tech. rep. Russian Space Systems (JSC), pp. 1–15 (cit. on p. 30).

Test and Assessment Research Center of China Satellite Navigation Office (2020). *Beidou Constellation Status*. (Visited on 10/20/2020) (cit. on p. 21).

Teunissen, P J G (2014). "Least-Squares Estimation of the Integer GPS Ambiguities." In: February (cit. on p. 34).

Teunissen, Peter and Oliver Montenbruck (2017). *Handbook of Global Navigation Satellite Systems*. Ed. by Peter J .G. Teunissen and Oliver Montenbruck. Springer International Publishing AG, p. 1328. ISBN: 978-3-319-42926-7 (cit. on pp. 9, 10, 12–20, 23, 26–28, 30, 31, 51–53, 55, 56, 58–65, 73–75, 77).

The MathWorks Inc. (2019). *MATLAB, Release 2019a*. Natick, MA, USA (cit. on pp. 112, 121, 129).

Tian, Anhong et al. (2013). "GPS single point positioning algorithm based on least squares." In: *Proceedings - 6th International Symposium on Computational Intelligence and Design, ISCID 2013* 2.4, pp. 16–19. DOI: 10.1109/ISCID.2013.119 (cit. on p. 122).

Van Diggelen, Frank (1998). "GPS Accuracy: Lies, Damn Lies, and Statistics." In: *GPS World*. URL: http://gpsworld.com/gpsgnss-accuracy-lies-damn-lies-and-statistics-1134/ (cit. on p. 38).

Viandier, N. et al. (2008). "GNSS Performance Enhancement in Urban Environment Based on Pseudo-range Error Model." In: *IEEE/ION Position, Location and Navigation Symposium (PLANS)*, pp. 377–382. DOI: 10.1109/PLANS.2008.4570093 (cit. on pp. 36, 38).

Vollath, Ulrich et al. (2000a). "Long-Range RTK Positioning Using Virtual Reference Stations." In: *Proceedings of ION GPS*, pp. 1143–1147 (cit. on p. 34).

Vollath, Ulrich et al. (2000b). "Multi-Base RTK Positioning Using Virtual Reference Stations." In: *Proceedings of the 13th International Technical Meeting of the Satellite Division of The Institute of Navigation (ION GPS 1998)*, pp. 123–131 (cit. on p. 34).

Vu, Bac Nghia and Milos Andrle (2014). "Implementation of vector tracking loop algorithm in modern GPS receiver." In: *AIAA/IEEE Digital Avionics Systems Conference - Proceedings*, 3E11–3E19. ISSN: 21557209. DOI: 10.1109/DASC.2014.6979458 (cit. on p. 76).

Wan, E.a. A and R. Van Der Merwe (2000). "The unscented Kalman filter for nonlinear estimation." In: *Oregon Graduate Institute of Science and Technology*, pp. 153–158. ISSN: 15270297. DOI: 10.1109/ASSPCC.2000.882463 (cit. on p. 45).

Wang, Jian et al. (2017). "Evaluation on loosely and tightly coupled GNSS/INS vehicle navigation system." In: *Proceedings of the 2017 19th International Conference on Electromagnetics in Advanced Applications, ICEAA 2017*, pp. 892–895. DOI: 10.1109/ICEAA.2017.8065396 (cit. on p. 35).

Wendel, Jan (2007). *Integrierte Navigationssysteme*. Munich, Vienna: De Gruyter Oldenbourg (cit. on pp. 35, 70, 73).

Witternigg, Norbert et al. (2017). "Particle Filter Algorithms and Experiments for High Sensitivity GNSS Receivers." In: *International Navigation Conference (INC)*. Brighton, United Kingdom (cit. on pp. 89, 107, 164).

Wolfram Research Inc. (2018). *Mathematica, Version 11.3*. Champaign, IL, USA (cit. on p. 177).

Won, Jong Hoon, Bernd Eissfeller, and Thomas Pany (2011). "Implementation, Test and Validation of a Vector-Tracking-Loop with the ipex Software Receiver." In: *Proceedings of the 24th International Technical Meeting of The Satellite Division of the Institute of Navigation (ION GNSS 2011)*, pp. 795–802 (cit. on pp. 73, 122).

Yuri, Urlichich et al. (2011). "GLONASS Modernization." In: *GPS World*. URL: https://www.gpsworld.com/glonass-modernization-12232/ (cit. on pp. 16, 18).

Zang, Nan, Bofeng Li, and Yunzhong Shen (2017). "PPP augmentation with current Galileo and BeiDou constellations." In: *Forum on Cooperative Posi-*

tioning and Service, CPGPS 2017, pp. 213–218. DOI: 10.1109/CPGPS.2017.8075127 (cit. on p. 35).

Zhang, Xiaoming, Zheng Yao, and Mingquan Lu (2011). "Optimizing the Gabor Bandwidth of satellite navigation signals by MCS signal expression." In: *Science China: Physics, Mechanics and Astronomy* 54.6, pp. 1077–1082. ISSN: 16747348. DOI: 10.1007/s11433-011-4329-6 (cit. on p. 14).

Zhodzishsky, Mark and Javad Ashjaee (2001). *Joint tracking of the carrier phases of the signals received from different satellites*. URL: https://www.freepatentsonline.com/6313789.html (cit. on p. 36).

Zhu, Ni et al. (2018). "GNSS Position Integrity in Urban Environments: A Review of Literature." In: *IEEE Transactions on Intelligent Transportation Systems*, pp. 1–17. ISSN: 15249050. DOI: 10.1109/TITS.2017.2766768 (cit. on p. 38).